FAST IONIC CONDUCTORS AND SOLID-SOLID INTERFACES DESIGNED FOR NEXT GENERATION SOLID-STATE BATTERIES

EDITED BY: Fuminori Mizuno, Jeff Sakamoto and Shyue Ping Ong
PUBLISHED IN: Frontiers in Energy Research

frontiers Research Topics

ISSN 1664-8714
ISBN 978-2-88945-647-5
DOI 10.3389/978-2-88945-647-5

About Frontiers

Frontiers is more than just an open-access publisher of scholarly articles: it is a pioneering approach to the world of academia, radically improving the way scholarly research is managed. The grand vision of Frontiers is a world where all people have an equal opportunity to seek, share and generate knowledge. Frontiers provides immediate and permanent online open access to all its publications, but this alone is not enough to realize our grand goals.

Frontiers Journal Series

The Frontiers Journal Series is a multi-tier and interdisciplinary set of open-access, online journals, promising a paradigm shift from the current review, selection and dissemination processes in academic publishing. All Frontiers journals are driven by researchers for researchers; therefore, they constitute a service to the scholarly community. At the same time, the Frontiers Journal Series operates on a revolutionary invention, the tiered publishing system, initially addressing specific communities of scholars, and gradually climbing up to broader public understanding, thus serving the interests of the lay society, too.

Dedication to Quality

Each Frontiers article is a landmark of the highest quality, thanks to genuinely collaborative interactions between authors and review editors, who include some of the world's best academicians. Research must be certified by peers before entering a stream of knowledge that may eventually reach the public - and shape society; therefore, Frontiers only applies the most rigorous and unbiased reviews.

Frontiers revolutionizes research publishing by freely delivering the most outstanding research, evaluated with no bias from both the academic and social point of view. By applying the most advanced information technologies, Frontiers is catapulting scholarly publishing into a new generation.

What are Frontiers Research Topics?

Frontiers Research Topics are very popular trademarks of the Frontiers Journals Series: they are collections of at least ten articles, all centered on a particular subject. With their unique mix of varied contributions from Original Research to Review Articles, Frontiers Research Topics unify the most influential researchers, the latest key findings and historical advances in a hot research area! Find out more on how to host your own Frontiers Research Topic or contribute to one as an author by contacting the Frontiers Editorial Office: researchtopics@frontiersin.org

FAST IONIC CONDUCTORS AND SOLID-SOLID INTERFACES DESIGNED FOR NEXT GENERATION SOLID-STATE BATTERIES

Topic Editors:
Fuminori Mizuno, Toyota Motor Corporation, Japan
Jeff Sakamoto, University of Michigan, United States
Shyue Ping Ong, University of California, San Diego, United States

Citation: Mizuno, F., Sakamoto, J., Ong, S. P., eds (2018). Fast Ionic Conductors and Solid-Solid Interfaces Designed for Next Generation Solid-State Batteries. Lausanne: Frontiers Media. doi: 10.3389/978-2-88945-647-5

Table of Contents

frontiers
in Energy Research

ORIGINAL RESEARCH
published: 07 December 2016
doi: 10.3389/fenrg.2016.00038

Lithium Superionic Conductor $Li_{9.42}Si_{1.02}P_{2.1}S_{9.96}O_{2.04}$ with $Li_{10}GeP_2S_{12}$-Type Structure in the $Li_2S–P_2S_5–SiO_2$ Pseudoternary System: Synthesis, Electrochemical Properties, and Structure–Composition Relationships

*Satoshi Hori[1], Kota Suzuki[1,2], Masaaki Hirayama[1,2], Yuki Kato[1,3,4] and Ryoji Kanno[1,2]**

[1]Department of Electronic Chemistry, Interdisciplinary Graduate School of Science and Engineering, Tokyo Institute of Technology, Yokohama, Japan, [2]Department of Chemical Science and Engineering, School of Materials and Chemical Technology, Tokyo Institute of Technology, Yokohama, Japan, [3]Battery Research Division, Higashifuji Technical Center, Toyota Motor Corporation, Susono, Shizuoka, Japan, [4]Battery AT, Advanced Technology 1, Toyota Motor Europe NV/SA, Zaventem, Belgium

Lithium superionic conductors with the $Li_{10}GeP_2S_{12}$ (LGPS)-type structure are promising materials for use as solid electrolytes in the next-generation lithium batteries. A novel member of the LGPS family, $Li_{9.42}Si_{1.02}P_{2.1}S_{9.96}O_{2.04}$ (LSiPSO), and its solid solutions were synthesized by quenching from 1273 K in the $Li_2S–P_2S_5–SiO_2$ pseudoternary system. The material exhibited an ionic conductivity as high as 3.2×10^{-4} S cm^{-1} at 298 K, as well as the high electrochemical stability to lithium metal, which was improved by the introduction of oxygen into the LGPS-type structure. An all-solid-state cell with a lithium metal anode and LSiPSO as the separator showed excellent performance with a high reversibility of 100%. Thus, oxygen doping is an effective way of improving the electrochemical stability of LGPS-type structure.

Keywords: $Li_{10}GeP_2S_{12}$, lithium conductor, solid-state battery, solid electrolyte, superionic conductor, ionic conductor, sulfides

OPEN ACCESS

Edited by:
Jeff Sakamoto,
University of Michigan, USA

Reviewed by:
Kazunori Takada,
National Institute for Materials Science, Japan
Yoon Seok Jung,
Ulsan National Institute of Science and Technology, South Korea

****Correspondence:***
Ryoji Kanno
kanno@echem.titech.ac.jp

Specialty section:
This article was submitted to Energy Storage, a section of the journal Frontiers in Energy Research

Received: *19 August 2016*
Accepted: *15 November 2016*
Published: *07 December 2016*

Citation:
Hori S, Suzuki K, Hirayama M, Kato Y and Kanno R (2016) Lithium Superionic Conductor $Li_{9.42}Si_{1.02}P_{2.1}S_{9.96}O_{2.04}$ with $Li_{10}GeP_2S_{12}$-Type Structure in the $Li_2S–P_2S_5–SiO_2$ Pseudoternary System: Synthesis, Electrochemical Properties, and Structure–Composition Relationships. Front. Energy Res. 4:38. doi: 10.3389/fenrg.2016.00038

INTRODUCTION

Lithium batteries have become pervasive in our daily lives, powering portable electronics and power tools, and are expected to play an important role in a vast range of energy storage applications, such as purely electric vehicles and power back-up devices, as well as the grid-level storage of renewably generated energy (Armand and Tarascon, 2008; Scrosati and Garche, 2010; Dunn et al., 2011). These advanced applications will inevitably require batteries that exhibit higher energy and power densities, as well as the ability to be scaled-up. As such batteries undergo improvements in terms of their energy and power densities and size, high-performance electrolytes become essential; a new class of electrolytes must provide high ionic conductivity over a broad range of ambient temperatures and also be thermally/electrochemically stable and compatible with the more reactive electrodes used in the batteries to ensure higher energy and power densities (Jow et al., 2014).

After the discovery of $Li_{10}GeP_2S_{12}$ (LGPS) (Kamaya et al., 2011), which is a new type of lithium superionic conductor, solid electrolytes are expected to satisfy the abovementioned stringent requirements. Consequently, all-solid-state lithium batteries that are based on inorganic solid electrolytes have emerged as attractive options for the next-generation energy storage systems, as they exhibit fewer safety concerns in comparison to battery systems based on flammable organic liquids (Robinson and Janek, 2014; Dudney et al., 2015). Note that the superionic conductor LGPS exhibits a conductivity of 1.2×10^{-2} S cm^{-1} at room temperature, which is comparable to or even higher than that of the liquid electrolytes. The high ionic conductivity is attributable to the unique structure of LGPS, in which lithium ions are distributed along the *c*-axis in a three-dimensional framework composed of an octahedral LiS_6 unit and tetrahedral PS_4 and GeS_4 units (Kwon et al., 2015; Wang et al., 2015).

So far, a number of studies motivated by this attractive feature of LGPS have investigated the charge/discharge performances of all-solid-state cells based on LGPS and have suggested that developing other LGPS-type solid electrolytes would be a significant step toward the realization of all-solid-state batteries with higher power and energy densities (Kato et al., 2012, 2016). However, the following two obstacles need to be overcome before LGPS finds wide application as a solid electrolyte in batteries: the fact that it contains germanium, which is relatively rare and hence expensive, and its low electrochemical stability when in contact with lithium metal. Note that lithium metal exhibits the lowest theoretical potential and a capacity as large as 3860 mAh g^{-1}, which contributes to the increase in the energy density of batteries.

Therefore, the development of LGPS-type solid electrolytes with a high electrochemical stability, reasonably good conductivity, and low cost is desirable. Although previous studies have reported LGPS-type phases in the Li_2S–P_2S_5–SiS_2 and Li_2S–P_2S_5–SnS_2 pseudoternary systems (Bron et al., 2013; Hori et al., 2014; Kuhn et al., 2014; Whiteley et al., 2014), the electrochemical stability of these LGPS-type materials needs to be improved further. To achieve this goal, we doped oxygen atoms into the LGPS-type structure. The Li_2S–P_2S_5–SiO_2 pseudoternary system – $Li_{9.42}Si_{1.02}P_{2.1}S_{9.96}O_{2.04}$ (LSiPSO) was reported as an LGPS-type phase with promising preliminary results (Kato et al., 2016) – was selected for investigation since SiO_2 is a relatively inexpensive and abundant material. We investigated in detail the properties and characteristics of the LSiPSO phase, such as its crystal structure, conductivity, and performance as a solid electrolyte in all-solid-state cell. We found that the oxygen atoms are introduced at specific sites in the LGPS-type structure and that the electrochemical stability is improved significantly but at the expense of a tolerable decrease in the lithium conductivity.

MATERIALS AND METHODS

Material Synthesis and Characterization

The starting materials, Li_2S (Idemitsu Kosan, >99.9% purity) and SiO_2 (Kanto Chemical Co. Ltd., >99% purity) powders, were milled to obtain fine particles using a ball-milling apparatus. These starting materials were then weighed together with P_2S_5 (Aldrich, >99.9% purity) in the appropriate molar ratios in an Ar-filled glove box, placed in a stainless steel pot, and mixed for 90 min using a vibrating mill (CMT, Tl-100). The specimens were then pressed into pellets, placed into a carbon crucible, and then sealed at 10 Pa in a carbon-coated quartz tube. After being heated at a reaction temperature of 1273 K for 5 h, the tube was quenched into ice water. The X-ray diffraction (XRD) patterns of the samples were collected with an X-ray diffractometer (Rigaku, SmartLab) with Cu$K\alpha_1$ radiation (λ = 1.5405 Å). The high-temperature XRD patterns were obtained using a high-flux synchrotron X-ray source with a wavelength of 0.5 Å at the B19B2 beamline at the SPring-8 facility in Hyogo, Japan. The measurements were made at temperatures of 300–873 K using a Debye–Scherrer diffraction camera; the specimens were sealed under vacuum in a quartz capillary (*ca.* 0.5 mm in diameter). Neutron diffraction data were collected using a time-of-flight diffractometer (SPICA) installed on the BL09 beamline at the Japan Proton Accelerator Research Complex in Tokai, Japan. The specimens were sealed in a vanadium cell (*ca.* 6 mm in diameter) with an indium ring. The software program Z-Rietveld was used to refine the structural and profile parameters (Oishi et al., 2009). Differential thermal analysis (DTA) was performed using a Rigaku Thermo plus TG8120 system at temperatures between room temperature and 1173 K.

Electrochemical Measurements

The test cell used in this study for the electrochemical measurements has been described previously (Kobayashi et al., 2008). The ionic conductivity was measured by the AC impedance method in an Ar atmosphere at temperatures of 248–373 K. A signal with an amplitude of 100 mV and frequencies between 1 Hz and 10 MHz was applied using a frequency response analyzer (Solartron, 1260). The sample powder was pressed into a pellet in a cylinder. The electrodes were prepared by pressing an Au powder at 444 MPa onto both sides of the pellet. The electrochemical window of the solid electrolyte was evaluated using cyclic voltammetry. The asymmetric Li/solid electrolyte/stainless steel cell was examined with a scan rate of 1 mV s^{-1} and voltages between −0.1 and 5 V using a Solartron 1287 electrochemical interface. The solid-state cells were constructed using the synthesized solid electrolyte as the separator, a mixture of $LiNbO_3$-coated $LiCoO_2$ and LGPS as the composite cathode (7:3 in weight ratio), and Li metal (thickness: 0.3 mm, diameter: 5 mm) as the anode (Ohta et al., 2007; Li et al., 2016). Besides LSiPSO, three LGPS-type materials (such as LGPS, $Li_{10.35}Si_{1.35}P_{1.65}S_{12}$, and $Li_{9.81}Sn_{0.81}P_{2.19}S_{12}$) were used as separators for comparison purpose. Each of these electrolyte powders of 200 mg was pressed into a pellet in an insulator tube. The composite cathode of 2–3 mg was then pressed onto one side of the separator-pellet, and Li metal foil was attached onto the other side. Cycling tests were performed at 2.55–4.25 V using a charge/discharge testing machine (TOSCAT-3100, Toyo System). The current applied to the cell was 7.25 mAh g^{-1} (0.05 C rate), which corresponded to current densities of 0.015–0.019 mA cm^{-2}. The specific capacities of the cells were calculated based on the weight of the $LiNbO_3$-coated $LiCoO_2$ sample.

RESULTS AND DISCUSSION

Synthesis

Figure 1 shows the Li_2S–P_2S_5–SiO_2 pseudoternary diagram along with the compositions at which the samples were obtained. Since the solid-solution ranges for the LGPS-type phases have been reported to exist in the Li_4MS_4–Li_3PS_4 system (M = Si, Ge, Sn) (Hori et al., 2014, 2015a), we investigated the compositions on the $Li_4SiS_2O_2$–Li_3PS_4 tie line (samples #2–4) and those surrounding the tie line (samples #1 and #5–10).

The XRD patterns of the synthesized samples are shown in **Figure 2**. All the diffraction lines for the sample with the nominal composition, LSiPSO (sample #1), which was synthesized as described in Section "Materials and Methods," were indexed to the same space group as that of the original LGPS phase [$P4_2/nmc$ (137)], indicating that the LSiPSO phase had a LGPS-type structure. We tested various synthesis conditions and found that although the optimized mixing procedures and cooling rates are important for obtaining monophasic LSiPSO (see Figure S1 and Table S1 in Supplementary Material), the composition is more relevant with respect to the phase that appears in the samples. In the case of the compositions on the $Li_4SiS_2O_2$–Li_3PS_4 tie line, the LSiPSO phase was not obtained as a pure phase; the main phases were a β-Li_3PS_4-derived phase in samples #2 and #3, a LSiPSO phase along with the Li_7PS_6 phase with an argyrodite-like structure in sample #4, and a Si-based LGPS-type phase in sample #5 (Kong et al., 2010; Homma et al., 2011). For compositions derived from the $Li_4SiS_2O_2$–Li_3PS_4 tie line, the phases that appeared changed with the amount of SiO_2 in the composition; for the samples with smaller amounts of SiO_2 compared to the case for sample #4, the Li_7PS_6 phase and a β-Li_3PS_4 modification were observed as the main primary phases in the samples #6 and #7, respectively. When the amount of SiO_2 in the compositions was increased from that in sample #4, the volume fraction of the LSiPSO phase also increased (samples #8–11). Since samples #8 and #11 exhibited impurity phases such as γ-Li_3PS_4 and a crystalline SiO_2 phase, it was concluded that the solid-solution range for the LSiPSO phase exists for compositions very similar to LSiPSO in the Li_2S–P_2S_5–SiO_2 pseudoternary system. The detected phases for each sample are listed in **Table 1** along with the synthesis parameters.

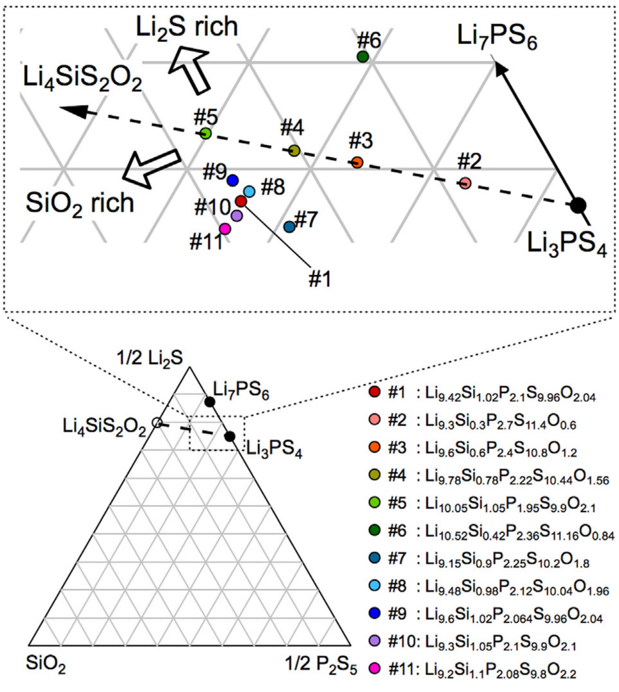

FIGURE 1 | Composition diagram for the Li_2S–P_2S_5–SiO_2 pseudoternary system. The compositions synthesized in this study are indicated along with the related label numbers in the magnified view of the diagram. The compositional formulas corresponding to these label numbers are also shown on the lower right-hand side.

Ionic Conductivity

The conductivity was measured by the AC impedance method using a pressed sample of powdered LSiPSO. The highest temperature during the measurement was restricted to 373 K, owing to experimental limitations; however, the thermal and high-temperature XRD analyses indicated that LSiPSO was stable at even 573 K (see Figure S2 in Supplementary Material). **Figure 3** shows the Nyquist and Arrhenius plots for LSiPSO. The impedance plots at and below 298 K consisted of a semicircle in the high-frequency range and a spike in the low-frequency range. The spike is considered due to formation of a double layer in the electrolyte/Au electrode interface (Irvine et al., 1990). The inset in **Figure 3A** shows the equivalent circuit used for simulating the data at and below 298 K. It consists of a resistance and constant-phase element (CPE) in parallel, with the two being in series with a CPE; these, respectively, represent the combined effects of the bulk and the grain boundaries and the effect of double-layer capacitance. The capacitance value for the high-frequency semicircle was calculated to be $1.2–1.5 \times 10^{-10}$ F (see Table S2 in Supplementary Material). Since the bulk and grain-boundary capacitances are empirically considered to be of the order of 10^{-12} and 10^{-9} F, respectively, the capacitance values indicated that the observed semicircles were ascribable to the fact that the grain boundaries contributed more to the resistance than did the bulk (West, 1984; Irvine et al., 1990). The shape of the impedance plots above 298 K was no longer semicircular, and the spike from the electrode contribution was observed; the intercept to the real axis was used for calculating the electrical conductivity. The ionic conductivity of LSiPSO was 3.2×10^{-4} S cm^{-1} at room temperature. This value is one order of magnitude smaller than that of LGPS, which shows the ionic conductivity of 1.2×10^{-2} S cm^{-1} for a sintered pellet (Kamaya et al., 2011) or $6–8 \times 10^{-3}$ S cm^{-1} for a cold-pressed pellet (Kato et al., 2012; Shin et al., 2014; Han et al., 2015). Nevertheless, the ionic conductivity value of LSiPSO meets the conductivity criterion ($>10^{-4}$ S cm^{-1}) proposed for practical electrolytes in lithium batteries (Goodenough and Kim, 2010). The activation energy was calculated as being 33.7 kJ mol^{-1}, which is larger than that for other LGPS-type phases reported previously (25–26 kJ mol^{-1}) (Kato et al., 2016). In general, oxides show larger grain-boundary resistances than do sulfides; we assume that the higher activation energy observed for the LSiPSO phase is

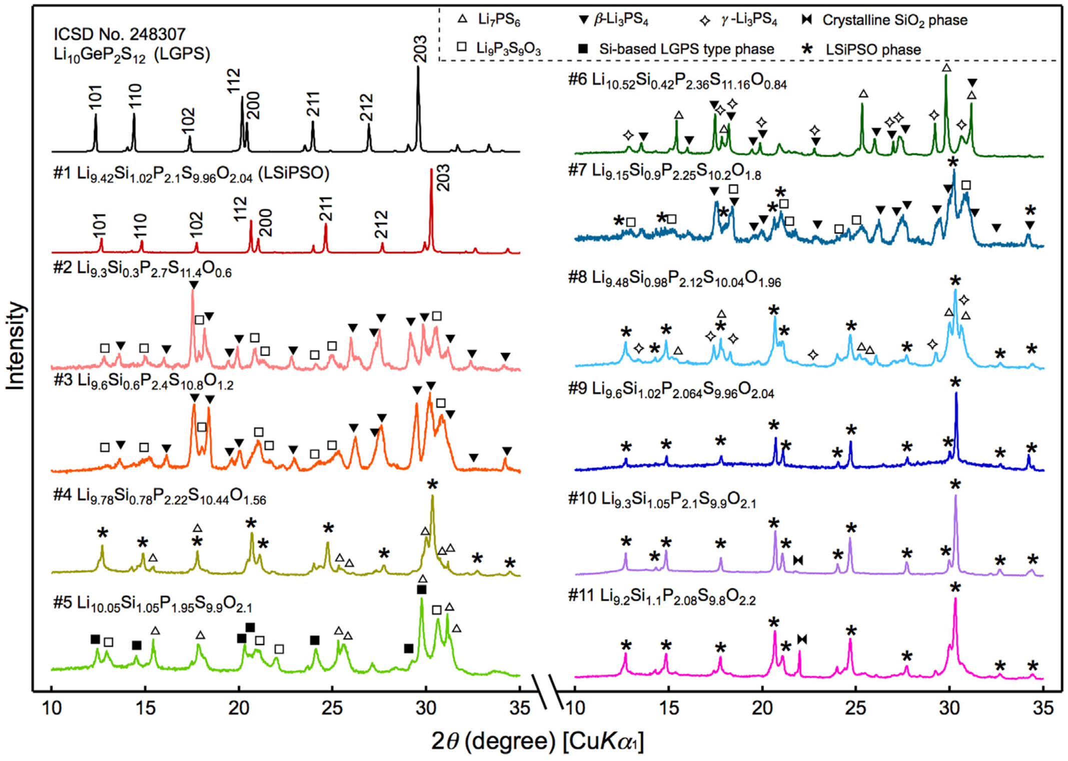

FIGURE 2 | X-ray diffraction patterns for the synthesized samples and that of the original LGPS phase. The sample numbers and compositions correspond to those shown in **Figure 1**.

TABLE 1 | Methods used to prepare the various samples in the Li_2S–P_2S_5–SiO_2 system synthesized in this study.

No.	Composition	Vibrational milling (min)	Preparation process	Identified phases[a]
1	$Li_{9.42}Si_{1.02}P_{2.1}S_{9.96}O_{2.04}$	90	5 h at 1000°C, quench in water	LSiPSO
2	$Li_{9.3}Si_{0.3}P_{2.7}S_{11.4}O_{0.6}$	90	5 h at 1000°C, quench in water	β-Li_3PS_4, LPSO
3	$Li_{9.6}Si_{0.6}P_{2.4}S_{10.8}O_{1.2}$	90	5 h at 1000°C, quench in water	β-Li_3PS_4, LSiPSO, Li_7PS_6
4	$Li_{9.78}Si_{0.78}P_{2.22}S_{10.44}O_{1.56}$	60	1 h at 940°C, slow cooling	LSiPSO, Li_7PS_6, β-Li_3PS_4
5	$Li_{10.05}Si_{1.05}P_{1.95}S_{9.9}O_{2.1}$	60	1 h at 965°C, slow cooling	LSiPS, Li_7PS_6, LPSO
6	$Li_{10.52}Si_{0.42}P_{2.36}S_{11.16}O_{0.84}$	60	1.5 h at 1000°C, slow cooling	Li_7PS_6, β-Li_3PS_4, γ-Li_3PS_4
7	$Li_{9.15}Si_{0.9}P_{2.25}S_{10.2}O_{1.8}$	90	1 h at 1000°C, slow cooling	LSiPSO, LPSO, β-Li_3PS_4
8	$Li_{9.48}Si_{0.98}P_{2.12}S_{10.04}O_{1.96}$	60	1.5 h at 1000°C, slow cooling	LSiPSO, Li_7PS_6, γ-Li_3PS_4
9	$Li_{9.6}Si_{1.02}P_{2.064}S_{9.96}O_{2.04}$	90	5 h at 1000°C, quench in water	LSiPSO
10	$Li_{9.3}Si_{1.05}P_{2.1}S_{9.9}O_{2.1}$	90	5 h at 1000°C, quench in water	LSiPSO, SiO_2
11	$Li_{9.2}Si_{1.1}P_{2.08}S_{9.8}O_{2.2}$	60	1.5 h at 1000°C, slow cooling	LSiPSO, SiO_2

[a] *LPSO, $Li_9P_3S_9O_3$ (Takada et al., 2005); LSiPS, Si-based LGPS-type phase (Hori et al., 2014).*

ascribable to the larger resistance of the grain boundaries, which is the result of the oxide doping. This assumption was consistent with the fact that the capacitance value observed at 298 K was closer to the typical value of the grain-boundary capacitance than that of the bulk capacitance. The ionic conductivity would potentially be increased by the optimization of the annealing conditions, which would reduce the grain-boundary resistance.

Electrochemical Stability

In the present study, we studied in detail the electrochemical stability of LSiPSO, which had been explored briefly in a previous study (Kato et al., 2016). The charge/discharge performance of a solid-state cell using LSiPSO and examined at 298 K is shown in **Figure 4**. The inset in **Figure 4A** shows a schematic drawing of the cell used in this study. The cell consists of the synthesized solid electrolyte as the separator, a composite of $LiNbO_3$-coated $LiCoO_2$ with LGPS as the cathode composite material, and Li metal as the anode. **Figure 4A** shows the charge/discharge curves of the cells using a different LGPS-type solid electrolyte such as the original LGPS phase (LGPS) and Si-/Sn-based isostructural phases such as $Li_{10.35}Si_{1.35}P_{1.65}S_{12}$ (LSiPS), $Li_{9.81}Sn_{0.81}P_{2.19}S_{12}$ (LSnPS), and LSiPSO. The capacity was calculated based on the

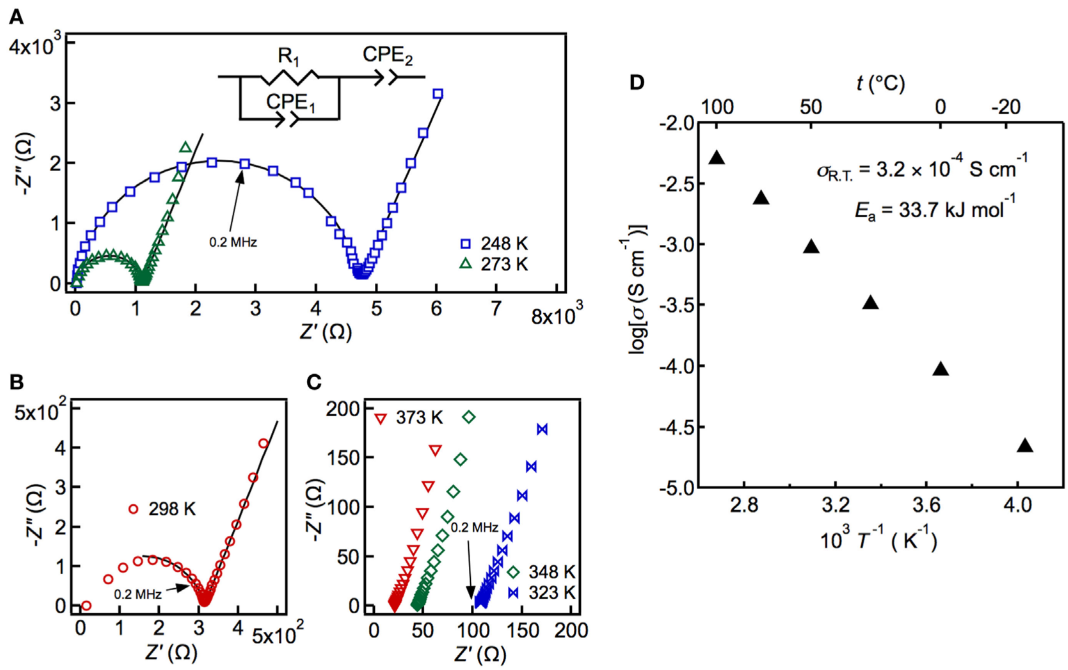

FIGURE 3 | **Impedance plots (A–C) and Arrhenius plots of the conductivity data (D) measured at 248–373 K**. The solid line in the left panel shows the fit obtained using the equivalent circuit (inset), which was composed of the total resistance and the constant-phase elements (CPEs), which, in turn, represent the combined response of the bulk and the grain boundaries, and the electrode response.

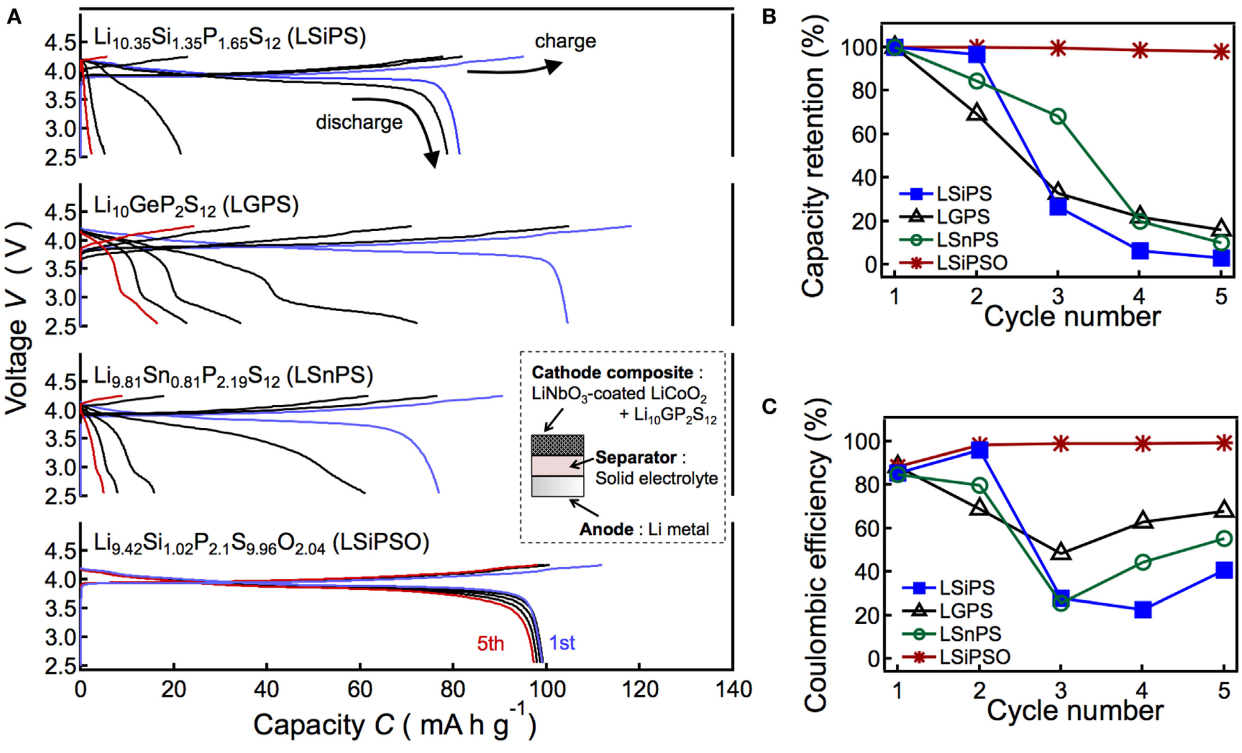

FIGURE 4 | **Results of the charge/discharge tests of the all-solid-state cell consisting of a $LiNbO_2$-coated $LiCoO_2$ cathode, $Li_{9.42}Si_{1.02}P_{2.1}S_{9.96}O_{2.04}$ (LSiPSO) as the electrolyte, and a Li metal anode**. The figure also shows the data for cells with Si-, Sn-, and Ge-based LGPS-type solid electrolytes as the separator. The left panel shows charge–discharge curves **(A)** and right panels show the capacity retention **(B)** and coulombic efficiency **(C)** as functions of the cycle number.

weight of $LiCoO_2$ powder in the cathode composite. The plateau regions of the charge/discharge curves during the first cycle at approximately 3.9 V for all the cells probably correspond to the lithium extraction/insertion reaction of $LiCoO_2$. The test cell with LSiPSO exhibited an initial discharge capacity of *ca.* 100 mAh g^{-1}, which is larger than those reported for all-solid-state cells using a sulfide-based electrolyte and cathode and anode materials similar to those used in the present study (Takahara et al., 2004). Furthermore, LSiPSO exhibited high electrochemical stability during cycling. The discharge capacity of the LSiPSO cell remained higher than 95 mAh g^{-1} (>98% of the initial capacity), whereas the L*M*PS (*M* = Si, Ge, Sn) cell showed a rapid capacity fading, with the capacity eventually dropping to less than 20% of the initial discharge capacity, as shown in **Figure 4B**. Moreover, the charge/discharge reversibility calculated from the discharge/charge capacity ratio, which is given in **Figure 4C**, also confirmed the better performance of the cell with LSiPSO; the efficiency of the LSiPSO cell reached almost 100% after the second cycle while L*M*PS showed much lower efficiency.

Previous studies have proposed that the performance of all-solid-state cell using Li anode is closely related to the continuous growth of the interphase formed by reductive decomposition of the solid electrolyte on the Li electrode (Kanno et al., 2004; Takahara et al., 2004). We presume that the capacity fading of the L*M*PS cell is due to overpotentials during charge–discharge processes, which could be observed when an interphase with low ionic conductivity continuously grows with cycling (Kanno et al., 2004; Whiteley et al., 2014). The irreversibility of the L*M*PS cell can be ascribed to the larger overpotential during discharge process than that during charge process (Whiteley et al., 2014); the cell voltage was dropped down to the cut-off voltage by the overpotential before the discharge of the cell was completed.

On the other hand, charge–discharge characteristics can be improved by generating stable interphase between anode and solid electrolyte, as demonstrated in previous studies (Kanno et al., 2004; Takahara et al., 2004). The excellent performance of the cell with LSiPSO suggests that the LSiPSO phase has stability to reductive decomposition on Li electrode and/or forms a stable interphase on Li electrode and, therefore, is expected to find application in high-energy density all-solid-state batteries using Li metal electrodes. Charge–discharge tests at high temperatures to demonstrate rate capabilities of the all-solid-state cell with LSiPSO are planned for future works.

To elucidate why the solid-state cell with LSiPSO exhibited better performance than those with the other LGPS-type solid electrolytes, the electrochemical window was examined by cyclic voltammetry using a lithium metal electrode as the reference. **Figure 5** displays current–voltage curves for LSiPSO as well as the other LGPS-type electrolytes. No significant current was observed till voltages of up to 5 V (vs. Li^+/Li) with respect to all the solid electrolytes. In addition, the shapes of the CV curves at 3–5 V did not change significantly over five cycles, indicating electrochemical stability with respect to oxidation when in contact with cathode materials having a high electrochemical potential (4–5 V vs. Li/Li^+). This experimentally observable stability toward oxidation is considered due to formation of

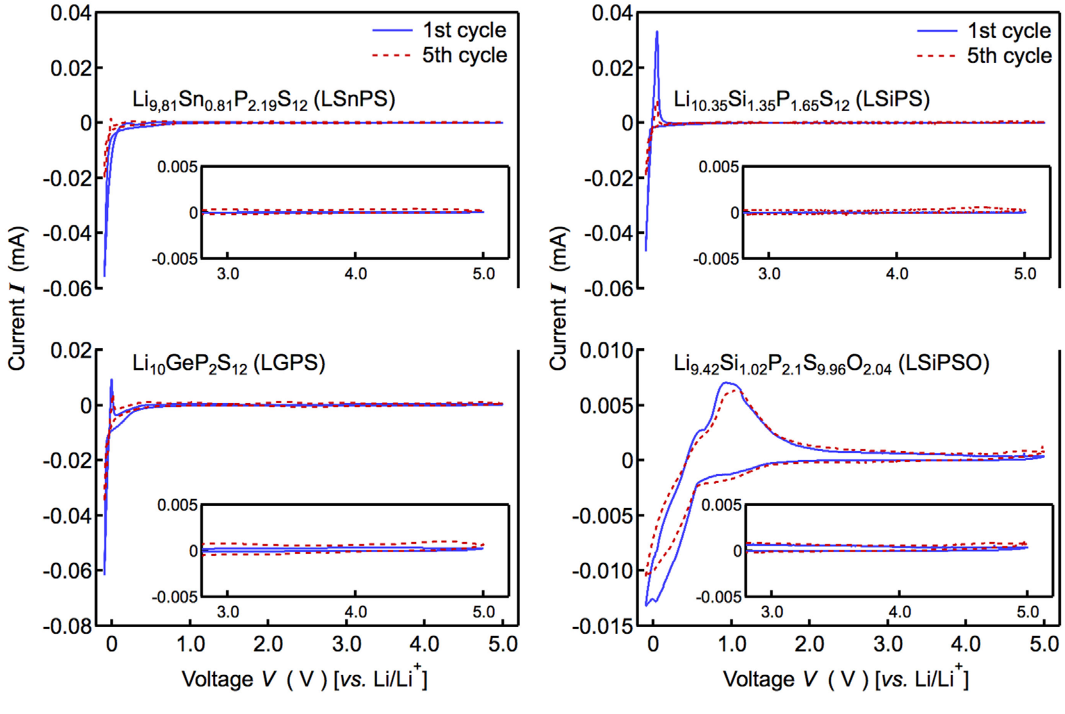

FIGURE 5 | Current–voltage curves of the Li/$Li_{9.42}Si_{1.02}P_{2.1}S_{9.96}O_{2.04}$/stainless steel cell. The figure also shows the data corresponding to the Si-, Sn-, and Ge-based LGPS-type solid electrolytes.

a passivation layer between a solid electrolyte and electrode (Han et al., 2015; Richards et al., 2016). Cathodic and anodic currents were observed near 0 V (vs. Li^+/Li), these were partly owing to the lithium deposition reaction ($Li^+ + e^- \rightarrow Li$) and the dissolution reaction ($Li \rightarrow Li^+ + e^-$), respectively. However, the cathodic current near 0 V could also be ascribed to the reductive decomposition of the solid electrolyte or the interfacial reactions that occur on the Li electrode, while the anodic current was probably attributable to the corresponding reverse reactions. In the case of LSiPSO, the cathodic current was observed at below 1.5 V, suggesting a reaction of LSiPSO at the electrolyte/electrode interface starts at this voltage. On the other hand, the ratio of the peak areas of anodic/cathodic current, which potentially indicates reversibility of the deposition–dissolution reaction (Kondo et al., 1992), was much higher than that in the case of the other LGPS-type electrolytes. Moreover, while the shapes of the CV curves of the other LGPS-type materials changed significantly near 0 V over five cycles, the CV curves of LSiPSO underwent no significant change. These observations suggested the interfacial reaction of LSiPSO, and Li deposition–dissolution reactions were more reversible than those corresponding reactions in the case of the other LGPS-type materials. This assumption is consistent with our observation that the all-solid-state cell with the LSiPSO phase showed greater performance than those with the other LGPS-type materials.

Structure Analysis

The crystal structure of LSiPSO was analyzed based on the neutron diffraction data using the Rietveld refinement. In this study, the structure of LSiPSO was analyzed based on the original LGPS composition; $Li_{10}SiP_2S_{10}O_2$ was used for the structural analysis.

Figure 6 shows a schematic drawing of the crystal structure based on the analysis. The details of the refinement results are described in Figure S3 and Tables S3 and S4 in Supplementary Material along with the refinement process. The lattice parameters for LSiPSO were calculated to be a = 8.43126 (4) Å and c = 12.3666 (9) Å; these are smaller than those of the LGPS and LGPS-type phases in the Li–Si–P–S system, indicating that all the Ge (ionic radii r = 0.39 Å) atoms and some of the S atoms (r = 1.84 Å) were substituted with Si (r = 0.26 Å) and O atoms (r = 1.40 Å), respectively (Shannon, 1976; Hori et al., 2014). The Li ions were in the Li1 and Li3 sites distributed along the c-axis; this was in keeping with the original LGPS model. Moreover, these sites showed larger atomic displacement parameters than those of the Li2 and Li4 sites, suggesting that, in the case of LSiPSO, the Li1 and Li3 sites play an important role in lithium conduction, which is the conduction mechanism of LGPS as observed experimentally and suggested by previous theoretical studies. The O atoms were found to selectively occupy one of the three 8g sites (the site for S1); 76% of the total O atoms in the structure occupied the vertices of the $P2[S/O]_4$ tetrahedra, which

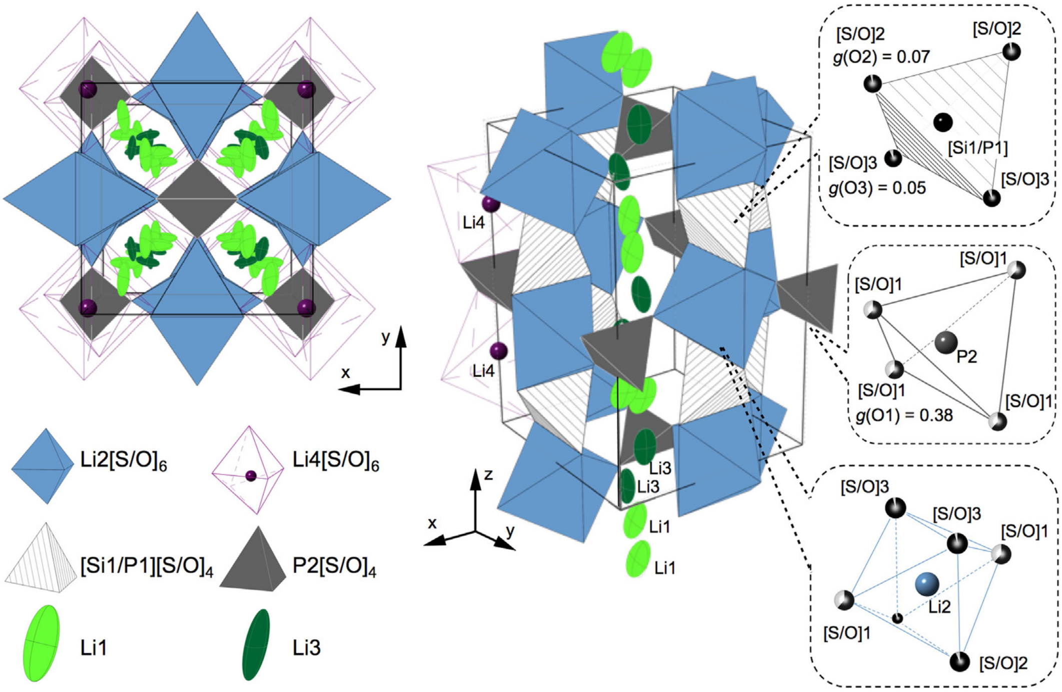

FIGURE 6 | Schematic drawings of the LSiPSO crystal structure determined by Rietveld analysis. The structure is represented by polyhedrons and ellipsoids; the blue and purple octahedra represent $Li2(4d)[S/O]_6$ and $Li4(4c)[S/O]_6$, respectively; the hatched and dark gray tetrahedra represent $[Si1/P1][S/O]_4$ and $P2[S/O]_4$, respectively; Li1(16h) and Li3(16h), which show large atomic displacement parameters, are drawn with a 50% probability as light- and dark-green ellipsoids, respectively. Li1 and Li3 are distributed along the c-axis in the framework composed of $Li2[S/O]_6$ octahedra, $[Si1/P1][S/O]_4$ tetrahedra, and $P2[S/O]_4$ tetrahedra. The left side shows the top view from the c-direction. The right side shows a perspective view, in which parts of Li1, Li3, and Li4 are not drawn for simplicity. The coordination of the sulfide/oxide atoms in the polyhedral is indicated in the dotted rectangles along with the occupation parameters, g, for the oxide atoms.

connect the polyhedral chains along the Li1 and Li3 sites. The average [Si1/P1]–[S/O] distance in the [Si1/P1][S/O]$_4$ tetrahedra (: 2.046 Å) was smaller than that for Si-based LGPS-type phase (: 2.094 Å) (Hori et al., 2015b), indicating the introduction of O atoms, which possess a smaller ionic radius than S atoms. The average P2–[S/O]$_4$ distance (: 1.789 Å) showed a significant decrease in comparison to the corresponding P2–S distance for the Si-based LGPS-type phase (: 2.005 Å); this corresponded to the selective substitution of oxygen atoms at the S1 site.

The doping of O atoms caused a decrease in the lattice parameters, which is often unfavorable for lithium conduction. The doped O atoms occupied vertices of the tetrahedra located at the centers of the tunnels along the *c*-axis, in which lithium atoms are distributed (**Figure 6**). These positions of the doped O atoms and the lowering of the conductivity of LSiPSO in comparison to that of the original LGPS phase supported the assumption that the tubes along the *c*-axis are the primary conduction pathways for lithium ions, as has also been proposed by experimental research as well as theoretical studies (Kwon et al., 2015; Wang et al., 2015). With respect to electrochemical stability, the doped oxygen is expected to increase it. A recent computational study has proposed that the inherent electrochemical stability of oxides is higher than that of sulfides (Richards et al., 2016). The oxygen doping might provide inherent electrochemical stability of the LSiPSO phase as well as enable formation of a stable interphase at the LSiPSO/Li electrode interface.

CONCLUSION

We doped oxygen atoms into the LGPS-type structure to improve its electrochemical stability. The Li_2S–P_2S_5–SiO_2 pseudoternary system was investigated, and the monophasic LGPS-type phase was obtained at the composition of LSiPSO. The LSiPSO phase showed a lower ionic conductivity (3.2×10^{-4} S cm^{-1}) and higher activation energy (33.7 kJ mol^{-1}) than those of the original LGPS phase. Impedance analysis indicated that the grain boundaries contributed more to the total resistance than did the bulk; the decreased conductivity and increased activation energy were attributable to the increase in the grain-boundary resistance, which was the result from oxygen doping. Based on the crystal structure analysis, we assume that the doped oxygen also affected the ionic conduction in bulk crystal; the doped oxygen atoms made the lattice size smaller, which caused the shortening of the primary lithium conduction pathway. On the other hand, the electrochemical stability was improved significantly by the oxygen doping. The LSiPSO phase showed higher electrochemical stability when in contact with lithium relative to those of the other LGPS-type phases without oxygen doping, based on cyclic voltammetry and charge/discharge measurements performed using an all-solid-state cell with Li metal as an anode and the synthesized solid electrolyte as the separator. Therefore, we suggest that oxygen doping is an effective technique for increasing the electrochemical stability of sulfide superionic conductors. Since similar relationships between compositions and structures have been reported previously for the superionic conductors in the Li–*M*–P–S system (*M* = Si, Sn, and Ge) (see Figure S4 in Supplementary Material), the results of this study demonstrate that the Li–*M*–P–S–O system is a promising compositional space to investigate for electrochemically stable superionic conductors.

AUTHOR CONTRIBUTIONS

SH, KS, and MH designed the experimental work. SH performed the experiments. SH, KS, MH, and YK analyzed the experimental data. SH and RK wrote the manuscript. YK and RK directed this work.

ACKNOWLEDGMENTS

This study was supported by the Post-LiEAD project of the New Energy and Industry Technology Development Organization (NEDO), Japan. The synchrotron radiation experiments were carried out as projects approved by the Japan Synchrotron Radiation Institute (JASRI) (proposal No. 2013B1630). The neutron scattering experiment was approved by the Neutron Scattering Program Advisory Committee of IMSS, KEK (Proposal No. 2014S10). The neutron experiment (Proposal no. 2014S10) was performed at BL09 Special environment neutron powder diffractometer (SPICA) developed by the Research and Development Initiative for Scientific Innovation of New Generation Batteries (RISING) project of the New Energy and Industrial Technology Development Organization (NEDO).

SUPPLEMENTARY MATERIAL

The Supplementary Material for this article can be found online at http://journal.frontiersin.org/article/10.3389/fenrg.2016.00038/full#supplementary-material.

REFERENCES

Armand, M., and Tarascon, J. M. (2008). Building better batteries. *Nature* 451, 652–657. doi:10.1038/451652a

Bron, P., Johansson, S., Zick, K., Schmedt auf der Günne, J., Dehnen, S., and Roling, B. (2013). $Li_{10}SnP_2S_{12}$: an affordable lithium superionic conductor. *J. Am. Chem. Soc.* 135, 15694–15697. doi:10.1021/ja407393y

Dudney, N. J., West, W. C., and Nanda, J. (eds). (2015). “Front matter,” in *Handbook of Solid State Batteries*, 2nd Edn (Singapore: World Scientific), i–xii.

Dunn, B., Kamath, H., and Tarascon, J.-M. (2011). Electrical energy storage for the grid: a battery of choices. *Science* 334, 928–935. doi:10.1126/science.1212741

Goodenough, J. B., and Kim, Y. (2010). Challenges for rechargeable Li batteries. *Chem. Mater.* 22, 587–603. doi:10.1021/cm901452z

Han, F., Gao, T., Zhu, Y., Gaskell, K. J., and Wang, C. (2015). A battery made from a single material. *Adv. Mater.* 27, 3473–3483. doi:10.1002/adma.201500180

Homma, K., Yonemura, M., Kobayashi, T., Nagao, M., Hirayama, M., and Kanno, R. (2011). Crystal structure and phase transitions of the lithium ionic conductor Li_3PS_4. *Solid State Ionics.* 182, 53–58. doi:10.1016/J.Ssi.2010.10.001

Hori, S., Kato, M., Suzuki, K., Hirayama, M., Kato, Y., and Kanno, R. (2015a). Phase diagram of the Li_4GeS_4-Li_3PS_4 quasi-binary system containing the superionic conductor $Li_{10}GeP_2S_{12}$. *J. Am. Ceram. Soc.* 98, 3352–3360. doi:10.1111/jace.13694

Hori, S., Taminato, S., Suzuki, K., Hirayama, M., Kato, Y., and Kanno, R. (2015b). Structure-property relationships in lithium superionic conductors having a $Li_{10}GeP_2S_{12}$-type structure. *Acta Crystallogr. B Struct. Sci. Cryst. Eng. Mater.* 71, 727–736. doi:10.1107/S2052520615022283

Hori, S., Suzuki, K., Hirayama, M., Kato, Y., Saito, T., Yonemura, M., et al. (2014). Synthesis, structure, and ionic conductivity of solid solution, $Li_{10+\delta}M_{1+\delta}P_{2-\delta}S_{12}$ (M = Si, Sn). *Faraday Discuss.* 176, 83–94. doi:10.1039/c4fd00143e

Irvine, J. T. S., Sinclair, D. C., and West, A. R. (1990). Electroceramics: characterization by impedance spectroscopy. *Adv. Mater.* 2, 132–138. doi:10.1002/adma.19900020304

Jow, R. T., Xu, K., Borodin, O., and Ue, M. (2014). *Electrolytes for Lithium and Lithium-Ion Batteries*. New York: Springer.

Kamaya, N., Homma, K., Yamakawa, Y., Hirayama, M., Kanno, R., Yonemura, M., et al. (2011). A lithium superionic conductor. *Nat. Mater.* 10, 682–686. doi:10.1038/nmat3066

Kanno, R., Murayama, M., Inada, T., Kobayashi, T., Sakamoto, K., Sonoyama, N., et al. (2004). A self-assembled breathing interface for all-solid-state ceramic lithium batteries. *Electrochem. Solid-State Lett.* 7, A455–A458. doi:10.1149/1.1809553

Kato, Y., Hori, S., Saito, T., Suzuki, K., Hirayama, M., Mitsui, A., et al. (2016). High-power all-solid-state batteries using sulfide superionic conductors. *Nat. Energy* 1, 16030. doi:10.1038/nenergy.2016.30

Kato, Y., Kawamoto, K., Hirayama, M., and Kanno, R. (2012). Discharge performance of all-solid-state battery using a lithium superionic conductor $Li_{10}GeP_2S_{12}$. *Electrochemistry* 80, 749–751. doi:10.5796/electrochemistry.80.749

Kobayashi, T., Yamada, A., and Kanno, R. (2008). Interfacial reactions at electrode/electrolyte boundary in all solid-state lithium battery using inorganic solid electrolyte, thio-LISICON. *Electrochim. Acta* 53, 5045–5050. doi:10.1016/j.electacta.2008.01.071

Kondo, S., Takada, K., and Yamamura, Y. (1992). New lithium ion conductors based on Li_2S–SiS_2 system. *Solid State Ionics* 53–56, Part 2, 1183–1186. doi:10.1016/0167-2738(92)90310-L

Kong, S. T., Gün, Ö, Koch, B., Deiseroth, H. J., Eckert, H., and Reiner, C. (2010). Structural characterisation of the Li argyrodites Li_7PS_6 and Li_7PSe_6 and their solid solutions: quantification of site preferences by MAS-NMR spectroscopy. *Chemistry* 16, 5138–5147. doi:10.1002/chem.200903023

Kuhn, A., Gerbig, O., Zhu, C., Falkenberg, F., Maier, J., and Lotsch, B. V. (2014). A new ultrafast superionic Li-conductor: ion dynamics in $Li_{11}Si_2PS_{12}$ and comparison with other tetragonal LGPS-type electrolytes. *Phys. Chem. Chem. Phys.* 16, 14669–14674. doi:10.1039/c4cp02046d

Kwon, O., Hirayama, M., Suzuki, K., Kato, Y., Saito, T., Yonemura, M., et al. (2015). Synthesis, structure, and conduction mechanism of the lithium superionic conductor $Li_{10+\delta}Ge_{1+\delta}P_{2-\delta}S_{12}$. *J. Mater. Chem. A* 3, 438–446. doi:10.1039/c4ta05231e

Li, W. J., Hirayama, M., Suzuki, K., and Kanno, R. (2016). Fabrication and electrochemical properties of a $LiCoO_2$ and $Li_{10}GeP_2S_{12}$ composite electrode for use in all-solid-state batteries. *Solid State Ionics.* 285, 136–142. doi:10.1016/j.ssi.2015.05.007

Ohta, N., Takada, K., Sakaguchi, I., Zhang, L., Ma, R., Fukuda, K., et al. (2007). $LiNbO_3$-coated $LiCoO_2$ as cathode material for all solid-state lithium secondary batteries. *Electrochem. Commun.* 9, 1486–1490. doi:10.1016/j.elecom.2007.02.008

Oishi, R., Yonemura, M., Nishimaki, Y., Torii, S., Hoshikawa, A., Ishigaki, T., et al. (2009). Rietveld analysis software for J-PARC. *Nucl. Instrum. Methods Phys. Res.* 600, 94–96. doi:10.1016/j.nima.2008.11.056

Richards, W. D., Miara, L. J., Wang, Y., Kim, J. C., and Ceder, G. (2016). Interface stability in solid-state batteries. *Chem. Mater.* 28, 266–273. doi:10.1021/acs.chemmater.5b04082

Robinson, A. L., and Janek, J. (2014). Solid-state batteries enter EV fray. *MRS Bull.* 39, 1046–1047. doi:10.1557/mrs.2014.285

Scrosati, B., and Garche, J. (2010). Lithium batteries: status, prospects and future. *J. Power Sources* 195, 2419–2430. doi:10.1016/j.jpowsour.2009.11.048

Shannon, R. D. (1976). Revised effective ionic radii and systematic studies of interatomic distances in halides and chalcogenides. *Acta Crystallogr. A* 32, 751–767. doi:10.1107/S0567739476001551

Shin, B. R., Nam, Y. J., Oh, D. Y., Kim, D. H., Kim, J. W., and Jung, Y. S. (2014). Comparative study of TiS_2/Li-In all-solid-state lithium batteries using glass-ceramic Li_3PS_4 and $Li_{10}GeP_2S_{12}$ solid electrolytes. *Electrochim. Acta* 146, 395–402. doi:10.1016/j.electacta.2014.08.139

Takada, K., Osada, M., Ohta, N., Inada, T., Kajiyama, A., Sasaki, H., et al. (2005). Lithium ion conductive oxysulfide, Li_3PO_4—Li_3PS_4. *Solid State Ionics* 176, 2355–2359. doi:10.1016/j.ssi.2005.03.023

Takahara, H., Tabuchi, M., Takeuchi, T., Kageyama, H., Ide, J., Handa, K., et al. (2004). Application of lithium metal electrodes to all-solid-state lithium secondary batteries using Li_3PO_4-Li_2S-SiS_2 glass. *J. Electrochem. Soc.* 151, A1309–A1313. doi:10.1149/1.1773712

Wang, Y., Richards, W. D., Ong, S. P., Miara, L. J., Kim, J. C., Mo, Y., et al. (2015). Design principles for solid-state lithium superionic conductors. *Nat. Mater.* 14, 1026–1031. doi:10.1038/nmat4369

West, A. R. (1984). "Ionic conductivity and solid electrolytes," in *Solid State Chemistry and Its Application* (Chichester: John Wiley and Sons), 452–496.

Whiteley, J. M., Woo, J. H., Hu, E., Nam, K.-W., and Lee, S.-H. (2014). Empowering the lithium metal battery through a silicon-based superionic conductor. *J. Electrochem. Soc.* 161, A1812–A1817. doi:10.1149/2.0501412jes

Conflict of Interest Statement: The authors declare that the research was conducted in the absence of any commercial or financial relationships that could be construed as a potential conflict of interest.

frontiers
in Energy Research

ORIGINAL RESEARCH
published: 30 August 2016
doi: 10.3389/fenrg.2016.00032

Fabrication of All-Solid-State Lithium-Ion Cells Using Three-Dimensionally Structured Solid Electrolyte $Li_7La_3Zr_2O_{12}$ Pellets

*Mao Shoji, Hirokazu Munakata and Kiyoshi Kanamura**

Department of Applied Chemistry, Graduate School of Urban Environmental Sciences, Tokyo Metropolitan University, Tokyo, Japan

All-solid-state lithium-ion batteries using Li^+-ion conducting ceramic electrolytes have been focused on as attractive future batteries for electric vehicles and renewable energy conversion systems because high safety can be realized due to non-flammability of ceramic electrolytes. In addition, a higher volumetric energy density than that of current lithium-ion batteries is expected since the all-solid-state lithium-ion batteries can be made in bipolar cell configurations. However, the special ideas and techniques based on ceramic processing are required to construct the electrochemical interface for all-solid-state lithium-ion batteries since the battery development has been done so far based on liquid electrolyte system over 100 years. As one of the promising approaches to develop practical all-solid-state batteries, we have been focusing on three-dimensionally (3D) structured cell configurations such as an interdigitated combination of 3D pillars of cathode and anode, which can be realized by using solid electrolyte membranes with hole-array structures. The application of such kinds of 3D structures effectively increases the interface between solid electrode and solid electrolyte per unit volume, lowering the internal resistance of all-solid-state lithium-ion batteries. In this study, $Li_{6.25}Al_{0.25}La_3Zr_2O_{12}$ (LLZAl), which is a Al-doped $Li_7La_3Zr_2O_{12}$ (LLZ) with Li^+-ion conductivity of ~10^{-4} S ·cm^{-1} at room temperature and high stability against lithium-metal, was used as a solid electrolyte, and its pellets with 700 μm depth holes in 700 μm × 700 μm area were fabricated to construct 3D-structured all-solid-state batteries with $LiCoO_2$/LLZAl/lithium-metal configuration. It is expected that the $LiCoO_2$–LLZAl interface is formed by point-to-point contact even when the LLZAl pellet with 3D hole-array structure is applied. Therefore, Li_3BO_3, which is a mechanically soft solid electrolyte with a low melting point at around 700°C was also applied as a supporting Li^+-ion conductor to improve the $LiCoO_2$–LLZAl interface.

Keywords: all-solid-state lithium-ion battery, solid electrolyte, $Li_{6.25}Al_{0.25}La_3Zr_2O_{12}$, three-dimensional structure, Li_3BO_3

Edited by:
Fuminori Mizuno,
Toyota Research Institute of North America, USA

Reviewed by:
Chunming Zhang,
National Engineering Research Center for Nanotechnology, China
Pengjian Zuo,
Harbin Institute of Technology, China

****Correspondence:***
Kiyoshi Kanamura
kanamura@tmu.ac.jp

Specialty section:
This article was submitted to Energy Storage, a section of the journal Frontiers in Energy Research

Received: *29 February 2016*
Accepted: *17 August 2016*
Published: *30 August 2016*

Citation:
Shoji M, Munakata H and Kanamura K (2016) Fabrication of All-Solid-State Lithium-Ion Cells Using Three-Dimensionally Structured Solid Electrolyte $Li_7La_3Zr_2O_{12}$ Pellets. Front. Energy Res. 4:32. doi: 10.3389/fenrg.2016.00032

INTRODUCTION

In recent years, the application of lithium-ion batteries has been expanded from portable electronic devices to large devices such as electric vehicles and energy storage systems on an industrial scale. According to this movement, higher battery performance, particularly safety is being required (Tarascon and Armand, 2001). However, it is basically difficult to realize high safety in current lithium-ion batteries because of the use of liquid electrolytes including flammable organic solvents, which also demands the massive battery package to avoid the electrolyte leakage. Therefore, the replacement of liquid electrolytes with solid electrolytes is an important issue to contribute the improvement of both safety and energy density of lithium-ion batteries. Actually, these advantages can be confirmed in polymer lithium-ion batteries, however, in which gel-type electrolytes including liquid electrolytes have been still used owing to low conductivity of true polymer electrolytes. On the other hand, inorganic solid electrolytes have attracted much attention in recent decade since those materials are non-flammable and thermally stable (Knauth, 2009). So far, many kinds of inorganic solid electrolytes including both glass- and crystal-based materials have been developed. They are categorized into two major groups. One is sulfide-based solid electrolyte group, which mainly consists of glass materials with relatively high plasticity. In the recent development, the Li^+-ion conductivity of sulfide materials is approaching the value of liquid electrolytes. For example, 1.2×10^{-2} S cm^{-1} at room temperature has been reported for the composition of $Li_{10}GeP_2S_{12}$ by Kanno et al. (Kamaya et al., 2011). However, there is a serious problem to be solved. The sulfide-based solid electrolytes, particularly those with high Li^+-ion conductivity, easily react with water and generate toxic hydrogen sulfide gas. The other group consists of oxide-based solid electrolytes such as $Li_{0.35}La_{0.55}TiO_3$ (LLT), $Li_{1+x}Al_xTi_{2-x}(PO_4)_3$ (LATP), and $Li_7La_3Zr_2O_{12}$ (LLZ). Compared to the sulfide-based solid electrolytes, these kinds of solid electrolytes have good thermal and chemical stability and high mechanical strength. LATP has a NASICON-type (Na super ion conductor) structure and exhibits a total (bulk + grain-boundary) ionic conductivity of 7×10^{-4} S cm^{-1} at 25°C when the composition is $Li_{1.3}Al_{0.3}Ti_{1.7}(PO_4)_3$ (Aono et al., 1989, 1990). LLT is a perovskite-type oxide Li^+-ion conductor with a high bulk ionic conductivity of 1×10^{-3} S cm^{-1} at 25°C, but its total ionic conductivity is as low as 7.5×10^{-5} S cm^{-1} (Inaguma et al., 1993). These are not stable against Li-metal due to the reduction of Ti^{4+} to Ti^{3+} at 1.8 V vs. Li/Li^+, resulting in the appearance of electronic conduction (Knauth, 2009). Therefore, if lithium-metal is used as an anode in all-solid-state lithium-ion batteries to realize high energy density, a Li^+-conducting protective layer such as poly(methyl methacrylate) (PMMA) gel-electrolyte has to be formed as a buffer layer to prevent the direct contact of those solid electrolytes with Li-metal (Hoshina et al., 2005).

Recently, many research groups including our group are focusing on $Li_7La_3Zr_2O_{12}$ (LLZ) as one of promising solid electrolytes for all-solid-state lithium-ion batteries using Li-metal anode (Murugan et al., 2007a). LLZ has a wider electrochemical window than LLT due to the stability against Li-metal. The total ionic conductivity of LLZ with a cubic structure is 7.7×10^{-4} S cm^{-1} at 25°C, which is larger than that of LLT and also those of other Li^+-ion conducting garnet-like oxides (Thangadurai et al., 2003; Murugan et al., 2007b). In addition to the cubic phase, LLZ has a tetragonal phase, whose ionic conductivity is as low as ~10^{-6} S cm^{-1}. Therefore, it is necessary to use cubic LLZ for battery applications. The cubic phase is stable above 640°C and is easily transformed to the tetragonal phase as decreasing the temperature. Therefore, many approaches have been done to stabilize the cubic phase at room temperature. The Al^{3+} substitution of Li^+ sites in LLZ (Al-doping) is an effective way to improve the stability of cubic phase at room temperature. For example, $Li_{6.25}Al_{0.25}La_3Zr_2O_{12}$ ($x = 0.25$ in $Li_{7-3x}Al_xLa_3Zr_2O_{12}$) has been known as a stable cubic LLZ (Matsuda et al., 2015). These kinds of Al-doped LLZs are usually denoted as LLZAls and show a relatively high bulk ionic conductivity such as 3.1×10^{-4} S cm^{-1} at 25°C in $Li_{6.25}Al_{0.25}La_3Zr_2O_{12}$. Although the Li^+-ion conductivity of oxide-based solid electrolytes is still one order of magnitude lower than that of liquid electrolytes, a practical Li^+-ion conductivity similar to that of liquid electrolytes in a separator can be realized if those solid electrolytes are formed in the thickness of less than 50 μm since their Li^+-ion transport number is almost unity. In order to fabricate such thin solid electrolyte membranes with both high density and high mechanical strength, special fabrication techniques are required.

In our previous study, we fabricated a $LiCoO_2$ cathode layer on a LLZ pellet by a simple sintering process using $LiCoO_2$ powder at 800°C for 1 h. However, the electrochemical performance was very poor with the specific discharge capacity of as small as 0.27 mAh g^{-1} (Kotobuki et al., 2010). From the scanning electron microscopic observation, it was found that the contact between $LiCoO_2$ cathode and LLZ solid electrolyte was poor. This problem can be improved by applying the precursor sol of $LiCoO_2$. When the mixture of $LiCoO_2$ particles and its precursor sol is applied, the better electrode–electrolyte contact can be formed, resulting in the lower internal resistance of all-solid-state lithium-ion batteries (Kotobuki et al., 2011). A similar approach to improve the electrode–electrolyte contact in all-solid-state lithium-ion batteries has been carried out by Ohta et al. (2013). They applied Li_3BO_3 as a supporting electrolyte to improve the contact between $LiCoO_2$ cathode and LLZ solid electrolyte, in which the mixture of Li_3BO_3 and $LiCoO_2$ was sintered onto a LLZ pellet with the composition of $Li_{6.75}La_3(Zr_{1.75}Nb_{0.25})O_{12}$ optimized by them (Ohta et al., 2011). Consequently, the total resistance including $LiCoO_2$/LLZ and Li-metal/LLZ interfacial resistances was improved from 700 to 230 Ω cm^{-2}. This result suggests that the use of Li^+-ion conducting supporting electrolytes is effective to improve the solid (electrode)–solid (electrolyte) contact. However, the capacity of all-solid-state lithium-ion batteries cannot be increased only by the improvement of interfacial contact. It is basically needed to make thick electrodes to obtain high capacity in batteries. The Li^+-ion conductivity of cathode materials used in lithium-ion batteries are not so high. Therefore, thicker cathode layer for higher capacity cannot be used due to limit of the lithium-ion migration length. One of the ideas to realize practically high capacity in all-solid-state lithium-ion batteries is to make 3D-structured electrodes. Of course, this idea is applicable to current lithium-ion batteries using liquid electrolytes to improve their electrochemical performance. For example, the energy density of battery can be increased without losing the power density in the combination of interdigitated pillar-arrays of anode and cathode since the Li^+-ion diffusion length between anode and cathode can be maintained even when the electrodes are made thicker (higher) to increase the battery capacity. Namely, the trade-off problem between energy and power density in batteries can be solved. Actually, we had reported this advantage by making some 3D-structured electrodes for current lithium-ion batteries (Izumi et al., 2012). The similar approach is also effective to increase the practical capacity of all-solid-state lithium-ion batteries. However, unlike liquid electrolytes, solid electrolytes have no fluidity, which makes it difficult to introduce them into the space between 3D-strucutrued electrodes. Oxide-based solid electrolytes have high mechanical strength compared to other electrolytes, so that their various 3D structures can be formed. When a solid electrolyte membrane with a hole-array structure is formed, 3D batteries can be fabricated by introduction of electrode active materials into the holes. In 3D-structured solid electrolyte membranes, the electrode–electrolyte contact area per unit volume is increased. Therefore, the application of 3D structures is particularly effective to improve the electrochemical performance of all-solid-state lithium-ion batteries. In addition, the electrolyte thickness in the bottom of holes can be thin for short Li^+-ion diffusion length since the other parts maintain the mechanical strength of electrolyte membrane. So far, we have tried to prepare LLZ solid electrolyte membranes with hole-array structures (**Figure 1**) by several methods. One is a micro-stereolithography using a LLZ slurry including a photo-curable resin. This method can make LLZ membranes with several tenths of micrometer-scale patterns precisely. However, their densification was difficult by simple sintering process (**Figure 2**). Consequently, the resulting LLZ membranes were porous and had high resistance. More simply, we recently have applied a press method using a die with a pillar-array structure to make LLZ pellets with a hole-array structure (Shoji et al., 2014). Compared to the micro-stereolithography, the fineness of patterns is slightly lost but dense LLZ pellets with 3D hole-array structures can be formed reproducibly. In this study, we apply this press method to make LLZAl pellets with 3D hole-array structures and present their effectiveness on improvement of electrochemical performance of all-solid-state lithium-ion batteries.

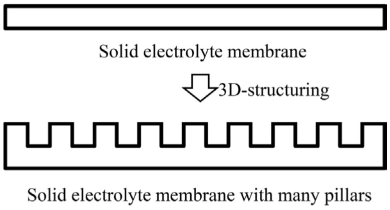

FIGURE 1 | **Schematics of 3D-structured solid electrolyte membrane**.

MATERIALS AND METHODS

LLZAl powder was synthesized by a solid state reaction (Kotobuki et al., 2011). $LiOH{\cdot}H_2O$, $La(OH)_3$, ZrO_2 (7.7:3:2: in molar ratio) were mixed by planetary ball-milling and then calcined at 900°C for 6 h. The calcined powder was mixed with γ-Al_2O_3 powder by planetary ball-milling, and then a binder was added to make a pellet with a hole-array structure, i.e., 3D-structured pellet, by using a special punch, which has many small and short pillars (**Figure 3**). For comparison, a flat LLZAl pellet was also fabricated using binder-free powder. The 3D-structured pellet was sintered by two sintering steps of 900°C for 3 h and then 1200°C for 12 h. Although a sintering mechanism of LLZ is complicate, the two sintering steps can prevent to remain impurity phases such as $La_2Zr_2O_7$ and Li_2CO_3, which behave as an inhibitor of densifying LLZ (Chen et al., 2014).

The characterization of sintered 3D-structured LLZAl pellets was performed by X-ray diffraction (XRD) analysis, scanning electron microscopy (SEM), and impedance measurement from 0.1 to 10^6 Hz at 30°C. To estimate Li^+-ion conductivity of LLZAl, the 3D-structured LLZAl pellet was polished to be a flat pellet for removing the effect of 3D structure from the estimation of its Li^+-ion conductivity.

For the assembly of all-solid-state battery using the 3D-structured LLZAl pellet, $LiCoO_2$ cathode with and without Li_3BO_3 was filled into the holes of the 3D-structured LLZAl pellet. The detailed procedures are as follows: $LiCoO_2$ sol was prepared by mixing $LiNO_3$, $Co(NO_3)_2{\cdot}6H_2O$, CH_3COOH, 2-propanol, H_2O, and polyvinylpyrrolidone (PVP) in a molar ratio of 1.1:1:10:1:0.06. Li_3BO_3 powder was synthesized by a solid state reaction using Li_2CO_3 and B_2O_3 in a molar ratio of 3:1 (Ohta et al., 2013). For the case of $LiCoO_2/Li_3BO_3$ composite cathode, the mixture of $LiCoO_2$ sol and Li_3BO_3 in a weight ratio of 7:3 was injected into the holes of the 3D-structured LLZAl pellet. Then, it was calcination at 400°C for 5 min and then 700°C for

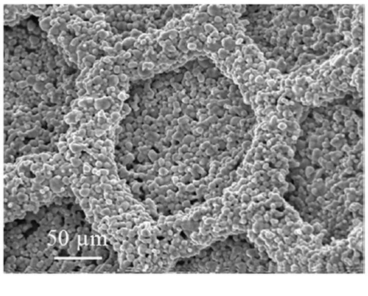

FIGURE 2 | **SEM image of 3D-structured LLZ membrane**.

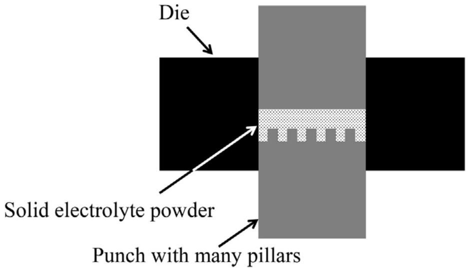

FIGURE 3 | **Schematics of pelletization for 3D-structured pellet**.

30 min to form an intermediate layer for making good contact between $LiCoO_2/Li_3BO_3$ composite cathode and LLZAl solid electrolyte. After that, the mixture of Li_3BO_3 powder and commercially available $LiCoO_2$ powder in a weight ratio of 3:7 was filled in holes of the 3D-structured LLZAl pellet, and then the Li_3BO_3-added $LiCoO_2$ sol denoted above was also dropped into the mixed powder-filled holes of the 3D-structured LLZAl pellet. This pellet was finally heated at 400°C for 5 min and then 700°C for 30 min. For comparison, Li_3BO_3-free sample was also prepared according to the same procedure except the use of Li_3BO_3. Their characterizations were performed by XRD, SEM, energy dispersive X-ray spectrometry (EDS), impedance measurement, and charge-discharge test.

RESULTS AND DISCUSSION

Figure 4 shows a photograph of sintered 3D-structured LLZAl pellet with a diameter of about 10 mm. The XRD pattern of the 3D-structured LLZAl pellet shown in **Figure 5** is attributed to the cubic crystal. From an impedance spectrum, the ionic conductivity of LLZAl estimated from its polished flat pellet was 3.5×10^{-4} S cm^{-1} at 30°C, which is a typical ionic conductivity of LLZ-type electrolytes. **Figure 6** shows surface and cross sectional SEM images of the 3D-structured LLZAl pellet. A pore size of holes on the 3D-structuerd LLZAl pellet was estimated to be about 700 μm × 700 μm. A thickness of the thick parts of 3D-structuerd LLZAl pellet and a depth of holes was about 1 mm and 700 μm, respectively. The electrolyte thickness in the bottom of holes was approximately 300 μm. This hole-array structure was very coarse. However, the surface area of the 3D-structuerd LLZAl pellet was approximately 2.5 times as large as flat pellet. In the 3D-structuerd LLZAl pellet, some large pores of about 100 μm and many small pores of about 10 μm were observed. The relative density of the 3D-structured LLZAl pellet was estimated to be 88.2%. A flat LLZAl pellet prepared from binder-free calcined powder had no large pores. Therefore, these large pores were formed by the use of calcined powder containing the binder. To get the large pores to disappear and improve the relative density, it is required to decrease the binder containing calcined powder and optimize a dewaxing process during the sintering. Only a few grain boundaries were observed in the 3D-structured LLZAl pellet. In our previous study (Shoji et al., 2014), we prepared a 3D-structured LLZAl pellet that contained many grain boundaries, and the all-solid-state battery using the 3D-structured LLZAl pellet did not work as a rechargeable

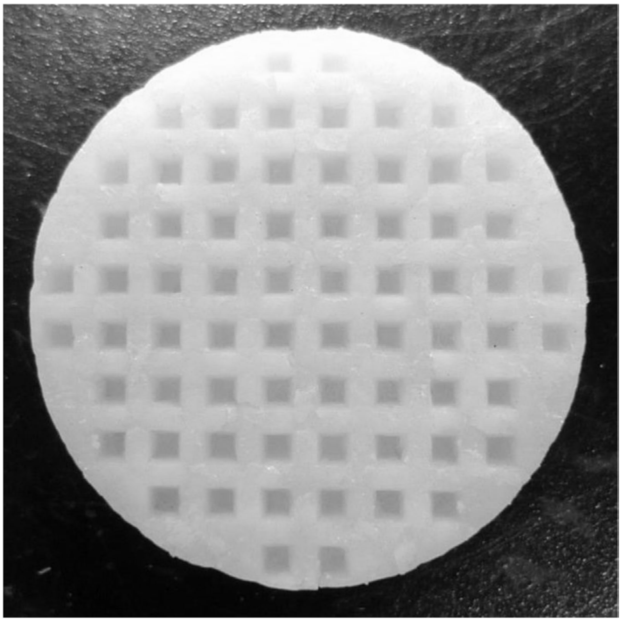

FIGURE 4 | Photograph of sintered 3D-structured LLZAl pellet with diameter of 10 mm.

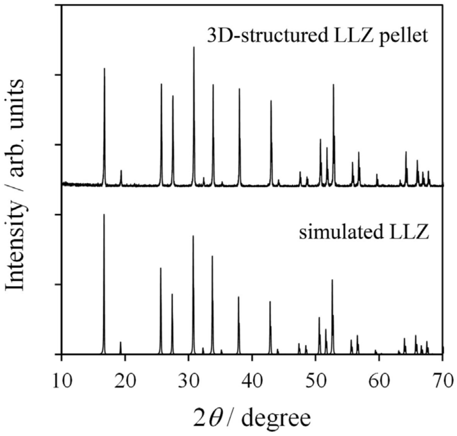

FIGURE 5 | XRD pattern of sintered 3D-structured LLZAl pellet and simulated cubic LLZ.

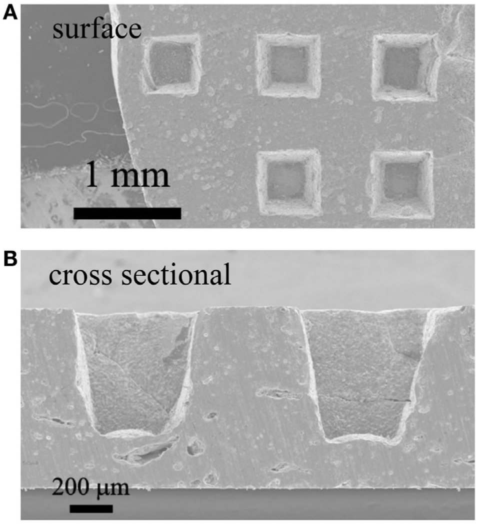

FIGURE 6 | (A) Surface and **(B)** cross sectional SEM images of 3D-structured LLZAl pellet.

battery. A two-sintering step process has not been adopted in the previous study. Therefore, the two-sintering step process has an effect on the decrement of grain boundaries by preventing impurity phases to remain. As a result, prepared 3D-structured LLZAl pellet in this study had no penetration. It was regarded that the 3D-structured LLZAl pellet can be used to fabricate the all-solid-state battery.

For improvement of contact between the $LiCoO_2$ layer and the 3D-structured LLZAl pellet, we used a Li_3BO_3 additive as a supporting electrolyte. Cross sections of each pellet were observed by SEM and EDS. These results are shown in **Figure 7**. By comparing these, large voids were not observed in the Li_3BO_3-added $LiCoO_2$ layer. However, the volumes of Li_3BO_3-added $LiCoO_2$ or Li_3BO_3-free $LiCoO_2$ layer except the voids were estimated to about the same, which were estimated from the amount of weight increment of the 3D-structured LLZAl pellets. The Li_3BO_3 additive has no work in densifying the $LiCoO_2$ layer. However, the Li_3BO_3-added $LiCoO_2$ layer was more uniformly distributed in the holes than Li_3BO_3-free $LiCoO_2$ layer. These results have indicated that the fluidity of $LiCoO_2$ layer emerged due to melting Li_3BO_3 around 700°C during the heat treatment, and then, $LiCoO_2$ in the holes was uniformly distributed. SEM images shown in **Figures 8B,C** clearly indicated that clay-like adhering material is attached around $LiCoO_2$ particles. Probably, this adhering material is Li_3BO_3 that is melted once during the heat treatment, and the Li_3BO_3 was connected to each $LiCoO_2$ particle and between $LiCoO_2$ particles and LLZAl. To confirm an effect of the Li_3BO_3 additive, an impedance measurement of each sample was carried out. Impedance spectra are showed in **Figure 9**. These spectra indicated a resistance of LLZAl (bulk and grain boundary) and interfacial resistances between LLZAl and electrodes (Li-metal and $LiCoO_2$), LLZAl and Li_3BO_3, and $LiCoO_2$ and Li_3BO_3. The resistances of bulk and grain boundary of LLZAl had no significant difference between each sample, about 0.2 kΩ. On the other hand, the interfacial resistances of the 3D-structured LLZAl pellet injected Li_3BO_3-added $LiCoO_2$ was lower than injected Li_3BO_3-free $LiCoO_2$. Since a Li-metal was not involved with Li_3BO_3, an interfacial resistance between LLZAl and Li-metal had no difference between each sample. Thus, $LiCoO_2$ and the Li_3BO_3 additive attributed to the decrement of the interfacial resistances, because the Li_3BO_3 additive can form a better contact in interface (Ohta et al., 2013).

Charge-discharge tests of all-solid-state lithium-ion batteries using the 3D-structured LLZAl pellets injected Li_3BO_3-free $LiCoO_2$ or Li_3BO_3-added $LiCoO_2$ were performed under a constant current density of 14 μA cm^{-2} in cutoff voltages of 2.5 and 4.2 V at 60°C. **Figure 10** shows charge–discharge curves of each sample. Both all-solid-state lithium-ion batteries were

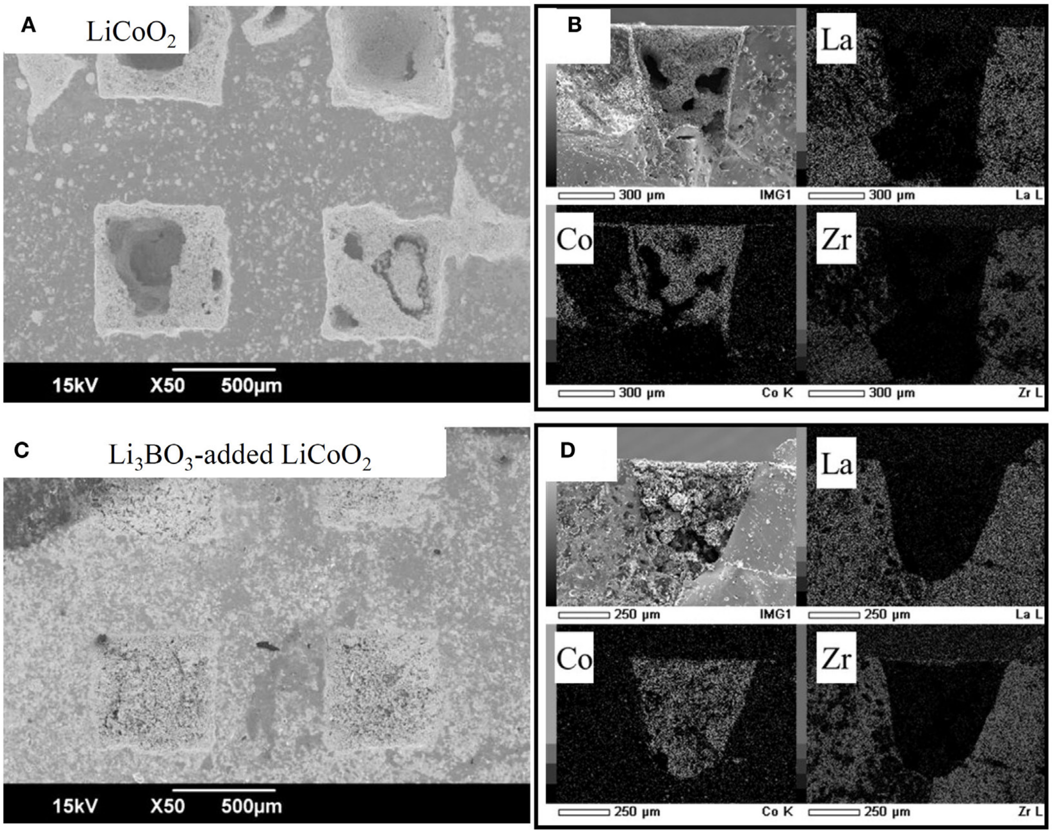

FIGURE 7 | SEM images and EDS mappings of 3D-structured LLZAl pellets injected Li_3BO_3-free $LiCoO_2$ (A,B) and $LiCoO_2$-Li_3BO_3 composite (C,D), respectively.

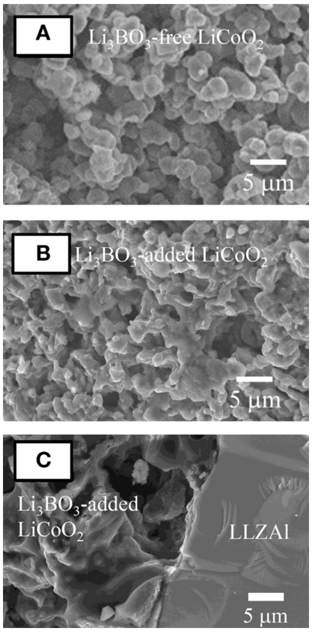

FIGURE 8 | **SEM images (A) Li_3BO_3-free $LiCoO_2$, (B) Li_3BO_3-added $LiCoO_2$, and (C) interface between Li_3BO_3-added $LiCoO_2$ and LLZAl.**

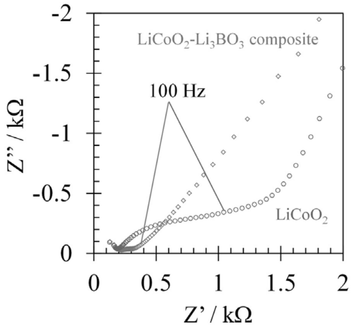

FIGURE 9 | **Impedance spectra of $LiCoO_2$/flat LLZAl/Li-metal and $LiCoO_2$/3D-structured LLZAl/Li-metal batteries.**

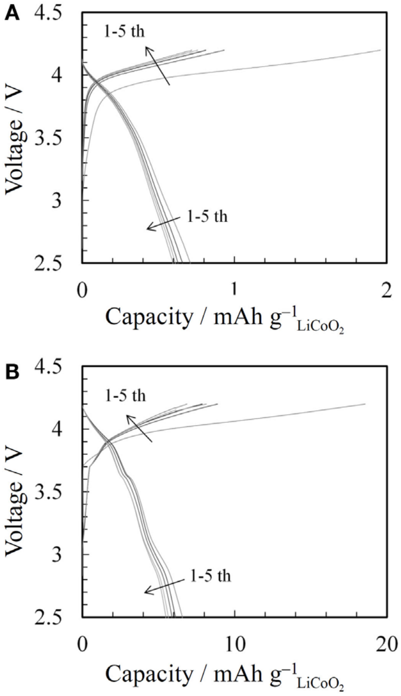

FIGURE 10 | **Charge–discharge curves of (A) $LiCoO_2$/flat LLZAl/Li-metal and (B) $LiCoO_2$/3D-structured LLZAl/Li-metal batteries.**

worked as rechargeable batteries, exhibiting very low discharge capacities between 0.6 ~ 7 mAh g^{-1}. On the other hand, the utilization of Li_3BO_3-added $LiCoO_2$ was larger than Li_3BO_3-free $LiCoO_2$. In the SEM images of **Figure 8**, each $LiCoO_2$ particle and $LiCoO_2$ and LLZAl pellet were connected by the Li_3BO_3 additive. It is considered that the improvement of the utilization was attributed to Li_3BO_3, which worked as ionic migration path. However, the utilization was still very low. It is attributed that the contact area between LLZAl and $LiCoO_2$ was still small. To improve the utilization, a denser Li_3BO_3-added $LiCoO_2$ layer is required. In addition, holes of the 3D-strucutred LLZAl pellet were too large for the Li^+-ion diffusion length. $LiCoO_2$ around the center of this large size holes could not be utilized as active materials due to too long of a distance between $LiCoO_2$ and LLZAl. It is necessary to design finer hole with size of about 100 µm or less.

CONCLUSION

In this report, we reported about a concept of 3D-structuring of LLZAl solid electrolyte to realize high capacity density and high mechanical strength of all-solid-state lithium-ion batteries. Since densification of LLZAl membranes was difficult by simple sintering process, we made dense LLZAl pellets with 3D-structure (a hole-array structure). An ionic conductivity of the 3D-structured LLZAl was estimated to 3.5×10^{-4} S cm^{-1}, which is a sufficient ionic conductivity as a LLZ electrolyte. And it was confirmed that the all-solid-state battery using the 3D-structured LLZAl pellet was operated as a rechargeable battery. Also, addition of Li_3BO_3 to $LiCoO_2$ layer was an effective way to improve contact between each $LiCoO_2$ particles or $LiCoO_2$ and LLZAl. However, this battery could not exhibit high utilization of $LiCoO_2$ due to low density of $LiCoO_2$ layer and coarse holes of the 3D-structured LLZAl pellet. Finer hole-array structure with size of about 100 µm or less is required to improve a utilization of $LiCoO_2$. Of course, high mechanical strength is also needed. However, to realize the 3D-structured LLZAl membranes, it is necessary to establish techniques to mold using the punch with many finer pillars. Moreover, the optimization of sintering processes for preparation of dense LLZAl membranes must be studied.

AUTHOR CONTRIBUTIONS

KK conceived the conception and design of the study, MS performed the experiments and acquired the data, MS, HM and KK analyzed the data, MS and HM drafted and revised the manuscript.

ACKNOWLEDGMENTS

This work was supported by Advanced Low Carbon Technology Research and Development Program – Specially Promoted Research for Innovative Next Generation Batteries (ALCA-SPRING) from Japan Science and Technology Agency (JST).

REFERENCES

Aono, H., Sugimoto, E., Sadaoka, Y., Imanaka, N., and Adachi, G. (1989). Ionic conductivity of the lithium titanium phosphate ($Li_{1+x}M_xTi_{2-x}(PO_4)_3$, M = Al, Sc, Y, and La) systems. *J. Eectrochem. Soc.* 136, 590–591. doi:10.1149/1.2096693

Aono, H., Sugimoto, E., Sadaoka, Y., Imanaka, N., and Adachi, G. (1990). Ionic conductivity of solid electrolytes based on lithium titanium phosphate. *J. Eectrochem. Soc.* 137, 1023–1027. doi:10.1149/1.2086597

Chen, R.-J., Huang, M., Huang, W.-Z., Shen, Y., Lin, Y.-H., and Nan, C.-W. (2014). Effect of calcining and Al doping on structure and conductivity of $Li_7La_3Zr_2O_{12}$. *Solid State Ion.* 265, 7–12. doi:10.1016/j.ssi.2014.07.004

Hoshina, K., Dokko, K., and Kanamura, K. (2005). Investigation on electrochemical interface between $Li_4Ti_5O_{12}$ and $Li_{1+x}Al_xTi_{2-x}(PO_4)_3$ NASICON-type solid electrolyte. *J. Electrochem. Soc.* 152, A2138–A2142. doi:10.1149/1.2041967

Inaguma, Y., Liquan, C., Itoh, M., Nakamura, T., Uchida, T., Ikuta, H., et al. (1993). High ionic conductivity in lithium lanthanum titanate. *Solid State Commun.* 86, 689–693. doi:10.1016/0038-1098(93)90841-A

Izumi, A., Sanada, M., Furuichi, K., Teraki, K., Matsuda, T., Hiramatsu, K., et al. (2012). Development of high capacity lithium-ion battery applying three-dimensionally patterned electrode. *Electrochim. Acta* 79, 218–222. doi:10.1016/j.electacta.2012.07.001

Kamaya, N., Homma, K., Yamakawa, Y., Hirayama, M., Kanno, R., Yonemura, M., et al. (2011). A lithium superionic conductor. *Nat. Mater.* 10, 682–686. doi:10.1038/nmat3066

Knauth, P. (2009). Inorganic solid Li ion conductors: an overview. *Solid State Ion.* 180, 911–916. doi:10.1016/j.ssi.2009.03.022

Kotobuki, M., Munakata, H., Kanamura, K., Sato, Y., and Yoshida, T. (2010). Compatibility of $Li_7La_3Zr_2O_{12}$ solid electrolyte to all-solid-state battery using Li metal anode. *J. Electrochem. Soc.* 157, A1076–A1079. doi:10.1149/1.3474232

Kotobuki, M., Suzuki, Y., Munakata, H., Kanamura, K., Sato, Y., Yamamoto, K., et al. (2011). Effect of sol composition on solid electrode/solid electrolyte interface for all-solid-state lithium ion battery. *Electrochim. Acta* 56, 1023–1029. doi:10.1016/j.electacta.2010.11.008

Matsuda, Y., Sakamoto, K., Matsui, M., Yamamoto, O., Takeda, Y., and Imanishi, N. (2015). Phase formation of a garnet-type lithium-ion conductor $Li_{7-3x}Al_xLa_3Zr_2O_{12}$. *Solid State Ion.* 277, 23–29. doi:10.1016/j.ssi.2015.04.011

Murugan, R., Thangadurai, V., and Weppner, W. (2007a). Fast lithium ion conduction in garnet-type $Li_7La_3Zr_2O_{12}$. *Angew. Chem. Int. Ed.* 46, 7778–7781. doi:10.1002/anie.200701144

Murugan, R., Thangadurai, V., and Weppner, W. (2007b). Lithium ion conductivity of $Li_{5+x}Ba_xLa_{3-x}Ta_2O_{12}$ (x=0–2) with garnet-related structure in dependence of the barium content. *Ionics* 13, 195–203. doi:10.1007/s11581-007-0097-8

Ohta, S., Kobayashi, T., and Asaoka, T. (2011). High lithium ionic conductivity in the garnet-type oxide $Li_{7-X}La_3(Zr_{2-X}, Nb_X)O_{12}$ (X = 0–2). *J. Power Sources* 196, 3342–3345. doi:10.1016/j.jpowsour.2010.11.089

Ohta, S., Komagata, S., Seki, J., Saeki, T., Morishita, S., and Asaoka, T. (2013). All-solid-state lithium ion battery using garnet-type oxide and Li_3BO_3 solid electrolytes fabricated by screen-printing. *J. Power Sources* 238, 53–56. doi:10.1016/j.jpowsour.2013.02.073

Shoji, M., Wakasugi, J., Osone, R., Nishioka, T., Munakata, H., and Kanamura, K. (2014). "Design and fabrication of all-solid-state rechargeable lithium batteries for future applications," in *Proceedings of the 38th International Conference on Advanced Ceramics and Composites Jan 26–31* (Daytona Beach, FL: The American Ceramic Society).

Tarascon, J.-M., and Armand, M. (2001). Issues and challenges facing rechargeable lithium batteries. *Nature* 414, 359–367. doi:10.1038/35104644

Thangadurai, V., Kaack, H., and Weppner, W. J. F. (2003). Novel fast lithium ion conduction in garnet-type $Li_5La_3M_2O_{12}$ (M = Nb, Ta). *J. Am. Ceram. Soc.* 86, 437–440. doi:10.1111/j.1151-2916.2003.tb03318.x

frontiers
in Energy Research

ORIGINAL RESEARCH
published: 28 July 2016
doi: 10.3389/fenrg.2016.00030

Grain Boundary Analysis of the Garnet-Like Oxides $Li_{7+X-Y}La_{3-X}A_XZr_{2-Y}Nb_YO_{12}$ (A = Sr or Ca)

Shingo Ohta*, Yuki Kihira and Takahiko Asaoka

Battery & Cell Division, Toyota Central R&D Labs. Inc., Nagakute, Japan

Garnet-like oxides having the formula $Li_{7+X-Y}La_{3-X}A_XZr_{2-Y}Nb_YO_{12}$ (A = Sr or Ca) were synthesized using a solid-state reaction, and their bulk and grain boundary resistivities were assessed by AC impedance measurements. A difference in grain boundary resistivity was identified between Sr and Ca materials, and so the grain boundaries were examined using electron probe microanalysis (EPMA). The difference in the grain boundary resistivities was attributed to the core–shell structure of the Sr-substituted samples. In contrast, the Ca-substituted materials exhibited accumulations of impurities at the grain boundaries.

Keywords: solid electrolytes, oxide, ion conductivity, grain boundary, all-solid-state, lithium ion battery

Edited by:
Shyue Ping Ong,
University of California,
San Diego, USA

Reviewed by:
Liqiang Mai,
Wuhan University of Technology,
China
Lincoln James Miara,
Samsung Electronics America,
Inc. (SEA)

****Correspondence:***
Shingo Ohta
shingo_ohta@mail.toyota.co.jp,
sohta@mosk.tytlabs.co.jp

Specialty section:
This article was submitted
to Energy Storage,
a section of the journal
Frontiers in Energy Research

Received: *30 January 2016*
Accepted: *11 July 2016*
Published: *28 July 2016*

Citation:
Ohta S, Kihira Y and Asaoka T (2016) Grain Boundary Analysis of the Garnet-Like Oxides $Li_{7+X-Y}La_{3-X}A_XZr_{2-Y}Nb_YO_{12}$ (A = Sr or Ca). Front. Energy Res. 4:30. doi: 10.3389/fenrg.2016.00030

INTRODUCTION

It is increasingly important to ensure the safety of lithium ion batteries as they are considered for use as power sources in electric vehicles or airplanes. These batteries typically use flammable organic liquids as the electrolyte, and so to improve the safety of lithium ion batteries, solid-state electrolytes have been developed to allow the fabrication of incombustible all-solid-state devices. Solid oxide electrolytes are believed to potentially have advantages over other inorganic electrolytes, such as sulfides, in terms of their chemical stability and lack of toxic degradation products (Ohtomo et al., 2013a,b). The garnet-like oxide $Li_7La_3Zr_2O_{12}$ (LLZ), which was reported by Prof. Murugan in 2007, is one of the most promising oxide electrolytes because of its excellent lithium ion conductivity ($\geq 10^{-4}$ Scm^{-1}) and wide potential window (Murugan et al., 2007). Following the discovery of LLZ, there were extensive efforts to improve its lithium ion conductivity, especially by elemental substitution leading to structural modification of the framework atoms (Rangasamy et al., 2013; Jalem et al., 2013; Thompson et al., 2014). This substitution modifies the lithium ion pathway by varying the bulk lithium ion conductivity, and many researchers have focused on improving the bulk lithium ion conductivity of garnet as a means of enhancing the conductivity of LLZ (Nyman et al., 2010; Ohta et al., 2011; Logeat et al., 2012; Allen et al., 2012). However, practical all-solid-state lithium ion batteries are likely to be fabricated by typical solid-state reactions, such that the primary contributor to the internal resistance of the solid oxide electrolyte will not be the bulk resistance, but rather the grain boundary resistivity (R_{gb}) of the polycrystalline electrolyte. As such, the total resistivity (R_{total}) of the electrolyte, including the R_{gb}, is important. Generally, the grain boundary resistance of a solid oxide electrolyte is high, meaning that the total ion conductivity has almost the same value as the grain boundary ion conductivity. Lithium lanthanum titanate, for example, is known to exhibit high ionic conductivity along with a high bulk conductivity of $\sigma_{bulk} = 1 \times 10^{-3}$ Scm^{-1}. However, the two-dimensional lithium ion paths in this material are interrupted by grain boundaries, resulting in a high R_{gb} with $\sigma_{grain\ boundary} \approx \sigma_{total} = 2 \times 10^{-5}$ Scm^{-1} (Inaguma et al., 1993; Stramare et al., 2003;

Yashima et al., 2005; Gao et al., 2014; Moriwake et al., 2015). In contrast, the grain boundary resistance of garnet-like oxides is relatively low compared to other ion-conducting oxides because of the good lithium ion connection between grains, forming three dimensional lithium ion paths. These materials thus show total lithium ion conductivity values as high as the bulk lithium ion conductivity (that is, $\sigma_{total} \approx \sigma_{bulk}$) (Ohta et al., 2011; Allen et al., 2012). However, the R_{gb} values of garnet-like oxides vary widely, from several percent to 40% of the R_{total}, depending on the composition (Li et al., 2012; Kihira et al., 2013). These differences in R_{gb} are believed to arise from the effects of substances at the grain boundaries. For this reason, the grain boundary resistivities induced by substitution with other elements should be assessed as a means of minimizing the R_{gb} and to determine the optimum substitution elements for garnet-like oxides.

In the present study, we simultaneously made substitutions at both the Zr and La sites to synthesize $Li_{7+X-Y}(La_{3-X}A_X)(Zr_{2-Y}Nb_Y)O_{12}$ (A-LLZNb; A = Ca, Sr). This was done to determine the optimum composition with regard to obtaining the highest lithium ion conductivity, based on differences in valency and ionic size: Nb^{5+} (0.64 Å), Zr^{4+} (0.72 Å), Ca^{2+} (1.34 Å), La^{3+} (1.36 Å), and Sr^{2+} (1.44 Å) (Shannon, 1976). Through these investigations, we found that the R_{gb} showed different characteristics between Ca and Sr substitutions. This study clarified that the ionic size and valency of the substitution element affect the grain and grain boundary morphology, and consequently the total lithium ion conductivity. This effect is discussed herein based on the grain boundaries of A-LLZNb incorporating Sr and Ca, as assessed *via* electron probe microanalysis (EPMA).

MATERIALS AND METHODS

$Li_{7+X-Y}(La_{3-X}A_X)(Zr_{2-Y}Nb_Y)O_{12}$ (A-LLZNb; A = Ca or Sr) bulk ceramic samples were synthesized by a conventional solid-state reaction in alumina crucibles. The starting materials were Li_2CO_3 (a 10% excess was added to allow for lithium losses by evaporation at high temperatures), $La(OH)_3$, ZrO_2, Nb_2O_5, and alkali earth metals in the form of carbonates.

The electrical conductivity of each sample was measured in air using a two-probe AC impedance method with an Agilent 4294A instrument over the frequency range of 110 MHz to 40 Hz at 25°C. Au electrodes were applied to both sides of the sample pellets using Au paste prior to these measurements, and the pellet and paste were subsequently annealed at 800°C for 0.5 h. The morphologies and the elemental distributions of the Ca or Sr-LLZNb bulk ceramics were measured by EPMA (JEOL Ltd. JXA-8500F). The crystal structures and impurity phases of the samples were determined by X-ray diffraction (XRD, Rigaku Co., Ltd., Ultima IV) using Cu Kα radiation.

RESULTS AND DISCUSSION

Figure 1 shows the AC impedance plots (Nyquist plots) of the synthesized A-LLZNb (A = Sr or Ca) bulk ceramic samples, where a = $Li_7La_2Sr_1Zr_1Nb_1O_{12}$ (1.0Sr-LLZNb), b = $Li_7La_{2.25}Ca_{0.75}Zr_{1.25}Nb_{0.75}O_{12}$ (0.75Ca-LLZNb), and c = $Li_7La_2Ca_1Zr_1Nb_1O_{12}$ (1.0Ca-LLZNb). When analyzing the impedance plot of a garnet oxide, there will be two semi-circles indicating the bulk resistivity (R_{bulk}) at higher frequencies (each terminal frequencies are 0.3M ~ 0.1 MHz) and the R_{gb} at lower frequencies (each terminal frequencies are 5000 ~ 50 Hz), the sum of which results in the R_{total}. The R_{bulk} and R_{gb} of the A-LLZNb (A = Sr or Ca) specimens are listed in **Table 1**. The R_{bulk} values and terminal frequencies of all samples were almost similar (~10^3 Ωcm and ~0.1 MHz), indicating that the R_{bulk} was not significantly affected by the substitution element. In contrast, the R_{gb} values of samples a, b, and c demonstrate that the substitution element makes a large difference with regard to the R_{gb} range. Each terminal frequencies are different by two orders of magnitude (5000 ~ 50 Hz). As shown in **Figure 1D**, the R_{gb} to R_{total} ratio in the Sr-LLZNb series increased gradually upon elevating the substitution level. In contrast, the ratios of the Ca-LLZNb series remained low until the substitution level reached 0.75, after which the ratio value increased significantly, eventually becoming quite large at higher substitution levels. These results suggest three discussion points: (i) the cause of the sudden jump in the R_{gb} values of the Ca-LLZNb series, (ii) the reason for the gradual increase in the R_{gb} values of the Sr-LLZNb series upon adding more Sr and Nb, and (iii) the reason why the R_{gb} values of the Sr-LLZNb series are higher than those of the Ca-LLZNb. In order to clarify the above points, we investigated the morphologies at grain boundaries and the relationship between these morphologies and composition, using EPMA.

Figure 2A shows the Ca, Al, La, Zr, and Nb EPMA maps obtained from a 0.75Ca-LLZNb sample. Al was not a constituent element but was identified as a contaminant in the sample, likely originating from the Al_2O_3 crucible during the sintering process, and so the Al distribution was assessed. The linear analysis results obtained along the red line in the back scattered electron (BSE) map in **Figure 2A** are provided in **Figure 2B**. The distributions of the elements and the linear analysis results indicate that Al and Ca were located at the grain boundary triple points in the sample. In contrast, no segregation and no elemental concentration gradients were observed in garnet grains, suggesting that the composition of the garnet grains was uniform. In order to clarify the composition of the impurity in the Ca-LLZNb series, XRD patterns were acquired, as shown in **Figure 2C**. The Ca-LLZNb for which $X < 0.5$ generated only diffraction peaks corresponding to the garnet phase, indicating that a small amount of Ca can be substituted at the La sites. Conversely, impurity peaks assigned to CaO, $LiAlO_2$, and $CaAl_2O_4$ were produced by heavily Ca-substituted samples ($X \geq 0.5$). Thus, the solid solubility limit of Ca in LLZNb appears to coincide with an X value of ~0.5, after

TABLE 1 | R_{bulk} and R_{gb} values of the A-LLZNb (A = Sr or Ca, X = 0.25, 0.5, 0.75, or 0.1) series.

	$Li_7(La_{3-X}Ca_X)(Zr_{2-X}Nb_X)_{12}$		$Li_7(La_{3-X}Sr_X)(Zr_{2-X}Nb_X)_{12}$	
	R_{buik} (Ω)	R_{gb} (Ω)	R_{buik} (Ω)	R_{gb} (Ω)
$X = 0.25$	2.1×10^3	2.7×10^2	8.5×10^3	1.4×10^3
$X = 0.5$	3.4×10^3	1.8×10^2	5.2×10^3	1.9×10^3
$X = 0.75$	5.8×10^3	2.5×10^2	5.3×10^3	4.6×10^3
$X = 0.1$	2.7×10^4	2.7×10^5	7.5×10^3	1.0×10^4

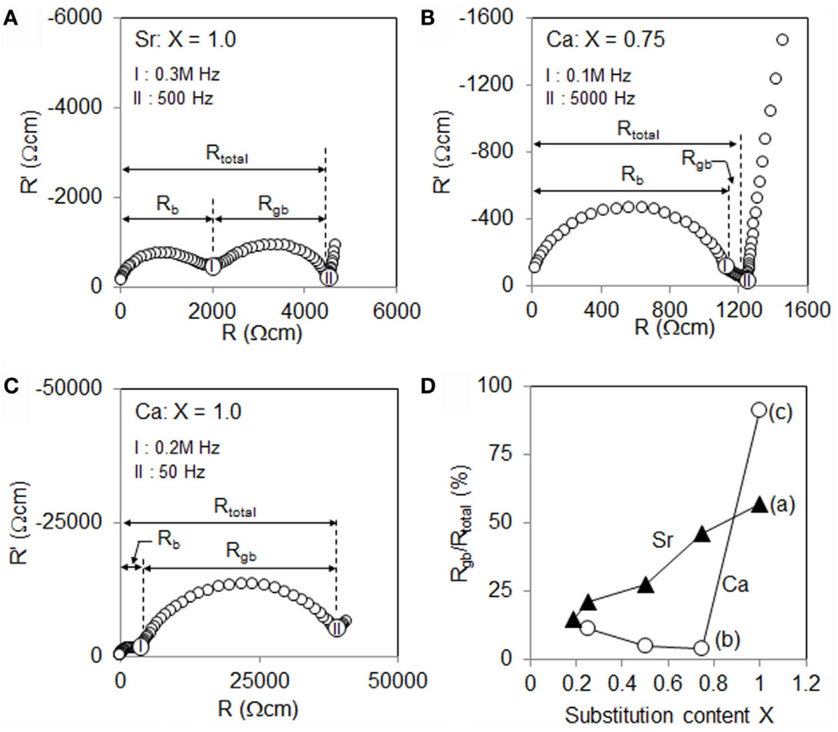

FIGURE 1 | Nyquist plots for Li_{7+X-Y} $(La_{3-X}A_X)(Zr_{2-Y}Nb_Y)O_{12}$ (A-LLZNb, A = Sr or Ca) in which (A) A = Sr, $X = 1.0$, (B) A = Ca, $X = 0.75$, (C) A = Ca, $X = 1.0$, and (D) the ratios of resistance due to grain boundaries to total resistance (R_{gb}/R_{total}) as functions of X. The terminal frequencies of both resistances are shown in the graph.

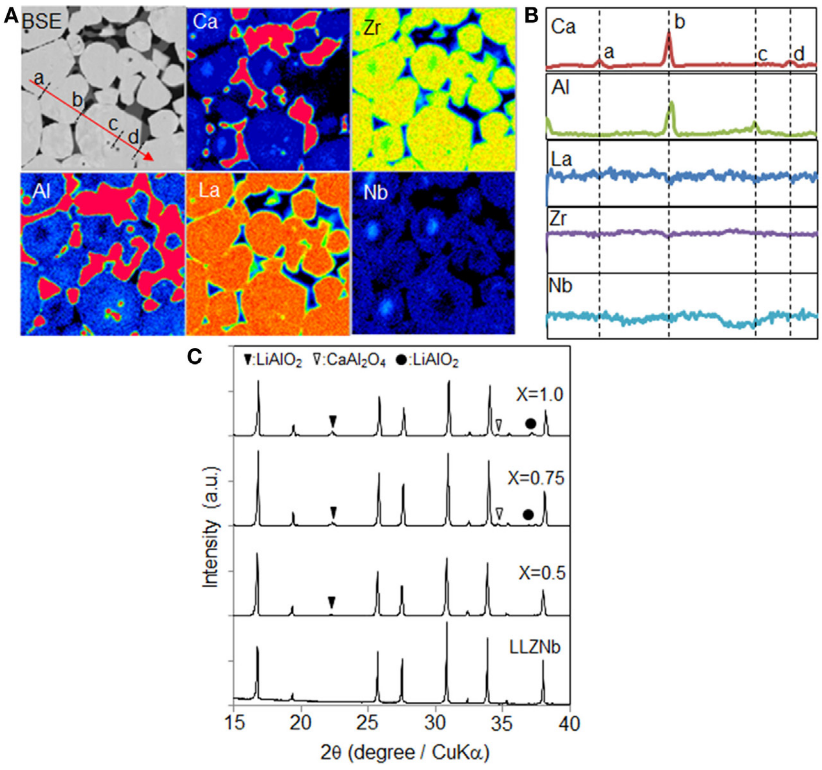

FIGURE 2 | (A) Cross-sectional EPMA mapping images of Ca-LLZNb, **(B)** linear analysis of Ca, Al, La, Zr, and Nb, and **(C)** XRD pattern obtained from Ca-LLZNb.

which the excess Ca accumulates at the grain boundaries. Based on this finding, an Al introduction mechanism can be proposed. In this mechanism, disproportionation of the garnet phase is induced upon the addition of Ca in excess of its solubility limit, after which excess Ca and Li accumulate at the grain boundaries. The excess Li reacts with the Al_2O_3 crucible such that Al is introduced into the sample, and $LiAlO_2$ and $CaAl_2O_4$ are subsequently formed during the sintering process.

Figure 3A presents the Sr, Al, La, Zr, and Nb EPMA maps generated by the 1.0Sr-LLZNb sample, while the linear analysis results obtained along the red line in the BSE map in **Figure 3A** are shown in **Figure 3B**. The garnet grains were determined to have a core–shell structure. The line scans show that, within the shell region and close to the grain boundaries at points a, b, c, and d in the BSE map in **Figure 3A**, there were higher concentrations of Sr and Nb and lower concentrations of La and Zr compared to the core region. Although the segregation of both Sr and Zr was observed in this field of view, $SrZrO_3$ diffraction peaks were not detected by XRD (**Figure 3C**). This result would suggest that the concentration of $SrZrO_3$ as an impurity was very low, and so we believe that the solubility limit of Sr in LLZNb is high compared to that of Ca. Al appears to have diffused into the grain boundaries of the sample from the Al_2O_3 crucible during sintering just as in the case of the Ca-LLZNb. A mechanism for this Al introduction can be proposed based on elemental distribution analysis, since this analysis found that there was an elemental concentration gradient inside the Sr-LLZNb grains. It thus appears that $LiAlO_2$ formation was induced by Li release due to structural disorder, just as is thought to have occurred with the Ca-LLZNb.

The elemental distribution and linear analysis results clearly show that the state of the grains and grain boundaries result from the effects of Sr or Ca substitution in the LLZNb. **Figure 4** presents schematic images of the grains and grain boundaries of Ca- or Sr-substituted LLZNb that appear at different R_{gb} ratios. Based on these schematics, we propose a reason for the gradual increase in the R_{gb} value of Sr-LLZNb with increasing Sr content. As greater amounts of Sr are added, the Sr will be forced out toward the boundaries to form a Sr-rich layer. The ionic radius of Sr^{2+} (1.44 Å) is greater than that of La^{3+} (1.36 Å), and their valence numbers are also different, and so the appearance of the Sr-rich layer must be balanced through an adjustment of both the structure and valency to form a garnet structure. Interestingly, Nb^{5+} (0.64 Å), which has a smaller ionic radius than Zr^{4+} (0.72 Å), and whose valence number is larger rather than smaller (as is the case with Sr^{2+} and La^{3+}), allows a balance to be maintained such that the Sr-rich garnet structure is unchanged (**Table 2**). Hence, although the solid solubility limit of Sr in LLZNb is higher than that of Ca, the gradual increase in the R_{gb} ratio in the Sr-LLZNb series is attributed to a Sr,Nb-rich layer that becomes increasingly thick as the amount of Sr added is increased (**Figures 4A,B**).

It is also possible to explain the lower solid solubility limit of Ca in LLZNb compared to that of Sr. The ionic radii of both Ca^{2+} (1.34 Å) and Nb^{5+} (0.64 Å) are smaller than those of La^{3+} (1.36 Å) and Zr^{4+} (0.72 Å), so the garnet structure cannot be

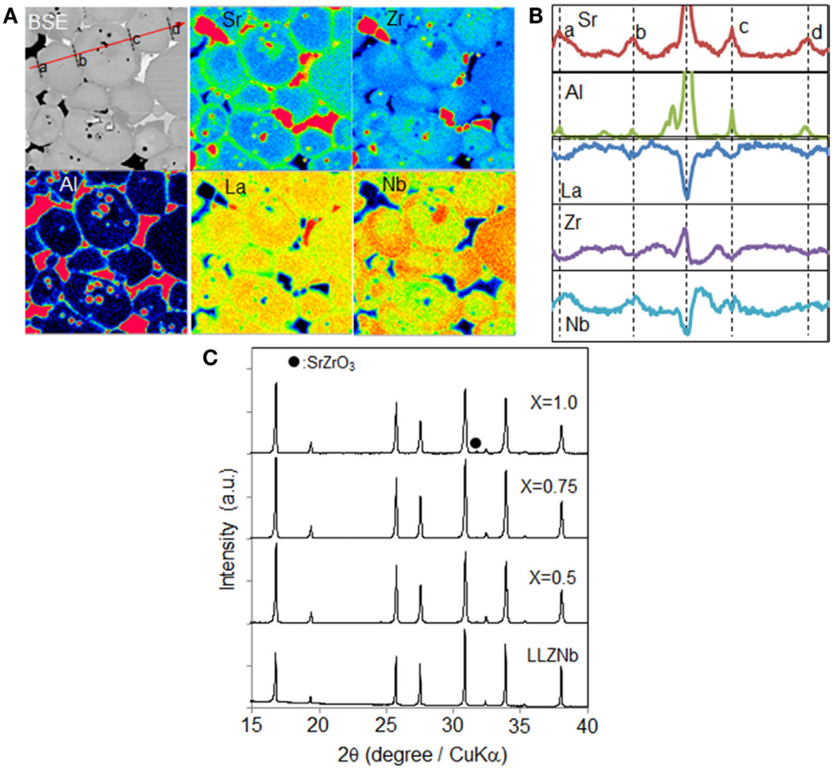

FIGURE 3 | **(A)** Cross-sectional EPMA mapping images of Sr-LLZNb, **(B)** linear analysis of Sr, Al, La, Zr, and Nb, and **(C)** XRD pattern obtained from Sr-LLZNb.

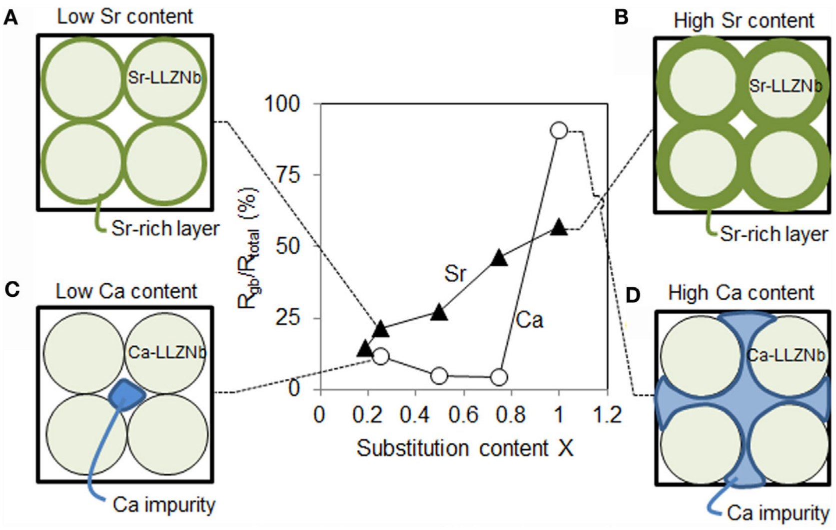

FIGURE 4 | Schematic images of the grains and grain boundaries of (A) low Sr and (B) high Sr-substituted LLZNb, and (C) low Ca and (B) high Ca-substituted LLZNb. (D) R_{gb}/R_{total} ratios as functions of *X*.

TABLE 2 | Valence numbers and ionic radii of elements substituted into the A-LLZNb (A = Sr or Ca) series.

	Sr-LLZN						Ca-LLZN					
	La site			ZR site			La site			ZR site		
	La		Sr	Zr		Nb	La		Ca	Zr		Nb
Charge	3+	$\xrightarrow{\text{down}}$	2+	4+	$\xrightarrow{\text{up}}$	5+	3+	$\xrightarrow{\text{down}}$	2+	4+	$\xrightarrow{\text{up}}$	5+
Radii	1.36	$\xrightarrow{\text{up}}$	1.44	0.72	$\xrightarrow{\text{down}}$	0.64	1.36	$\xrightarrow{\text{down}}$	1.34	0.72	$\xrightarrow{\text{down}}$	0.64

adjusted, although the relationship of their valance number is same as is possible in the case of Sr-LLZNb (**Table 2**). When the Ca substitution level is close to the solid solubility limit, although small amounts of Ca and Al impurities are accumulated at the grain boundary triple points, a Li conduction pathway can form due to sufficient contact between grains, such that the R_{gb} of the LLZNb remains low (**Figure 4C**). When the Ca substitution level is above the solid solubility limit, significant concentrations of Ca and Al impurities are accumulated at the grain boundaries, leading to insufficient contact between grains (**Figure 4D**). This is the reason why the R_{gb} of the LLZNb suddenly increases when high concentrations of Ca are substituted.

CONCLUSION

We successfully fabricated Li_{7+X-Y} $(La_{3-X}A_X)(Zr_{2-Y}Nb_Y)O_{12}$ (A-LLZNb; A = Ca, Sr) by solid-state reaction. The observed variations in the R_{gb} ratio between Sr-LLZNb and Ca-LLZNb are considered to result from the different substitution elements. Three issues were addressed in this work: (i) the sudden jump in the R_{gb} values of the Ca-LLZNb series, (ii) the higher R_{gb} values of the Sr-LLZNb series, and (iii) the gradual increase in the R_{gb} values of the Sr-LLZNb upon adding increasing amounts of Sr and Nb.

With regard to issue (i), EPMA analysis found Ca and Al at the grain boundaries of the Ca-LLZNb at $X = 1.0$, explaining the very high R_{gb} ratio. Point (ii) was elucidated by results showing a Sr,Nb-rich layer on the surfaces of garnet grains. The effect in point (iii) is thought to result from this Sr,Nb-rich layer, which would be balanced by variations in ionic size and valence. In the case of Sr-Nb or Ca-Nb combinations, the larger Sr^{2+} ions at the La^{3+} sites would be balanced by smaller Nb^{5+} ions at Zr^{4+} sites to form a Sr,Nb-rich layer, while Ca^{2+} will not form a Ca-rich layer because of its mismatch in ionic size and valence with Nb^{5+}. Thus, the gradual increase in the R_{gb} ratio in the Sr-LLZNb series with increasing Sr content is considered to result from the Sr,Nb-rich layer that becomes increasingly thick as the amount of Sr rises. These results also demonstrate that the solid solubility limit of Sr in LLZNb is apparently higher than that of Ca. In the case of Ca, the elemental concentration gradient seen with Sr was not observed, and the Ca and other elements were distributed evenly inside the grains. Even though Ca and Ca–Zr accumulations were found at grain boundaries, the grains were connected with one another, which might have led to the low R_{gb} ratios in the Ca-LLZNb.

AUTHOR CONTRIBUTIONS

SO: conception and design of the study; YK: collection and assembly of data; TA: approval of this study.

REFERENCES

Allen, J. L., Wolfenstine, J., Rangasamy, E., and Sakamoto, J. (2012). Effect of substitution (Ta, Al, Ga) on the conductivity of Li7La3Zr2O12. *J. Power Sources* 206, 315–319. doi:10.1016/j.jpowsour.2012.01.131

Gao, X., Fisher, C. A. J., Kimura, T., Ikuhara, Y. H., Kuwabara, A., Moriwake, H., et al. (2014). Domain boundary structures in lanthanum lithium titanates. *J. Mater. Chem. A.* 2, 843–852. doi:10.1039/c3ta13726k

Inaguma, Y., Chen, L. Q., Itoh, M., Nakamura, T., Uchida, T., Ikuta, H., et al. (1993). High ionic-conductivity in lithium lanthanum titanate. *Solid State Commun.* 86, 689–693. doi:10.1016/0038-1098(93)90841-A

Jalem, R., Yamamoto, Y., Shiiba, H., Nakayama, M., Munakata, H., Kasuga, T., et al. (2013). Concerted migration mechanism in the Li ion dynamics of garnet-type Li7La3Zr2O12. *Chem. Mater.* 25, 425–430. doi:10.1021/cm303542x

Kihira, Y., Ohta, S., Imagawa, H., and Asaoka, T. (2013). Effect of simultaneous substitution of alkali earth metals and Nb in Li7La3Zr2O12 on lithium-ion conductivity. *ECS Electrochem. Lett.* 2, A56–A59. doi:10.1149/2.001307eel

Li, Y. T., Han, J. T., Wang, C. A., Xie, H., and Goodenough, J. B. (2012). Optimizing Li+ conductivity in a garnet framework. *J. Mater. Chem.* 22, 15357–15361. doi:10.1039/c2jm31413d

Logeat, A., Koohler, T., Eisele, U., Stiaszny, B., Harzer, A., Tovar, M., et al. (2012). From order to disorder: the structure of lithium-conducting garnets Li7-xLa3TaxZr2-xO12 (x=0-2). *Solid State Ionics.* 206, 33–38. doi:10.1016/j.ssi.2011.10.023

Moriwake, H., Gao, X., Kuwabara, A., Fisher, C. A. J., Kimura, T., Ikuhara, Y. H., et al. (2015). Domain boundaries and their influence on Li migration in solid-state electrolyte (La,Li)TiO3. *J. Power Sources* 276, 203–207. doi:10.1016/j.jpowsour.2014.11.139

Murugan, R., Thangadurai, V., and Weppner, W. (2007). Fast lithium ion conduction in garnet-type Li7La3Zr2O12. *Angew. Chem. Int. Ed.* 46, 7778–7781. doi:10.1002/anie.200701144

Nyman, M., Alam, T. M., McIntyre, S. K., Bleier, G. C., and Ingersoll, D. (2010). Alternative approach to increasing Li mobility in Li-La-Nb/Ta garnet electrolytes. *Chem. Mater.* 22, 5401–5410. doi:10.1021/cm101438x

Ohta, S., Kobayashi, T., and Asaoka, T. (2011). High lithium ionic conductivity in the garnet-type oxide Li7-X La-3(Zr2-X, Nb-X)O-12 (X=0-2). *J. Power Sources* 196, 3342–3345. doi:10.1016/j.jpowsour.2010.11.089

Ohtomo, T., Hayashi, A., Tatsumisago, M., and Kawamoto, K. (2013a). Suppression of H2S gas generation from the 75Li(2)S center dot 25P(2)S(5) glass electrolyte by additives. *J. Mater. Sci.* 48, 4137–4142. doi:10.1007/s10853-013-7226-8

Ohtomo, T., Hayashi, A., Tatsumisago, M., and Kawamoto, K. (2013b). Glass electrolytes with high ion conductivity and high chemical stability in the system LiI-Li2O-Li2S-P2S5. *Electrochemistery* 81, 428–431. doi:10.5796/electrochemistry.81.428

Rangasamy, E., Wolfenstine, J., Allen, J., and Sakamoto, J. (2013). The effect of 24c-site (A) cation substitution on the tetragonal-cubic phase transition in Li(7-x)La(3-x)A(x)Zr(2)O(12) garnet-based ceramic electrolyte. *J. Power Sources* 230, 261–266. doi:10.1016/j.jpowsour.2012.12.076

Shannon, R. D. (1976). Revised effective ionic radii and systematic studies of interatomic distances in halides and chalcogenides. *Acta Crystallograph. Sect. A* A32, 751–767. doi:10.1107/S0567739476001551

Stramare, S., Thangadurai, V., and Weppner, W. (2003). Lithium lanthanum titanates: are view. *Chem. Mater.* 15, 3974–3990. doi:10.1088/0953-8984/22/40/404203

Thompson, T., Wolfenstine, J., Allen, J. L., Johannes, M., Huq, A., David, I. N., et al. (2014). Tetragonal vs. cubic phase stability in Al – free Ta doped Li7La3Zr2O12 (LLZO). *J. Mater. Chem. A* 2, 13431–13436. doi:10.1039/c4ta02099e

Yashima, M., Itoh, M., Inaguma, Y., and Morii, Y. (2005). Crystal structure and diffusion path in the fast lithium-ion conductor La0.62Li0.16TiO3. *J. Am. Chem. Soc.* 127, 3491–3495. doi:10.1021/ja0449224

ACKNOWLEDGMENTS

This study was partly supported by the project "Applied and Practical LiB Development for Automobile and Multiple Application" of the New Energy and Industrial Technology Development Organization (NEDO), Japan and Toyota Motor Corp.

Conflict of Interest Statement: The authors declare that the research was conducted in the absence of any commercial or financial relationships that could be construed as a potential conflict of interest.

frontiers
in Energy Research

ORIGINAL RESEARCH
published: 20 July 2016
doi: 10.3389/fenrg.2016.00028

Development of Lithium-Stuffed Garnet-Type Oxide Solid Electrolytes with High Ionic Conductivity for Application to All-Solid-State Batteries

Ryoji Inada*, Satoshi Yasuda, Masaru Tojo, Keiji Tsuritani, Tomohiro Tojo and Yoji Sakurai

Department of Electrical and Electronic Engineering, Toyohashi University of Technology, Toyohashi, Japan

All-solid-state lithium-ion batteries are expected to be one of the next generations of energy storage devices because of their high energy density, high safety, and excellent cycle stability. Although oxide-based solid electrolyte (SE) materials have rather lower conductivity and poor deformability than sulfide-based ones, they have other advantages, such as their chemical stability and ease of handling. Among the various oxide-based SEs, lithium-stuffed garnet-type oxide, with the formula of $Li_7La_3Zr_2O_{12}$ (LLZ), has been widely studied because of its high conductivity above 10^{-4} S cm^{-1} at room temperature, excellent thermal performance, and stability against Li metal anode. Here, we present our recent progress for the development of garnet-type SEs with high conductivity by simultaneous substitution of Ta^{5+} into the Zr^{4+} site and Ba^{2+} into the La^{3+} site in LLZ. Li^+ concentration was fixed to 6.5 per chemical formulae, so that the formula of our Li garnet-type oxide is expressed as $Li_{6.5}La_{3-x}Ba_xZr_{1.5-x}Ta_{0.5+x}O_{12}$ (LLBZT) and Ba contents x are changed from 0 to 0.3. As a result, all LLBZT samples have a cubic garnet structure without containing any secondary phases. The lattice parameters of LLBZT decrease with increasing Ba^{2+} contents $x \leq 0.10$ while increase with x from 0.10 to 0.30, possibly due to the simultaneous change of Ba^{2+} and Ta^{5+} substitution levels. The relative densities of LLBZT are in a range between 89 and 93% and are not influenced in any significant way by the compositions. From the AC impedance spectroscopy measurements, the total (bulk + grain) conductivity at 27°C of LLBZT shows its maximum value of 8.34×10^{-4} S cm^{-1} at $x = 0.10$, which is slightly higher than the conductivity ($= 7.94 \times 10^{-4}$ S cm^{-1}) of LLZT without substituting Ba ($x = 0$). The activation energy of the conductivity tends to become lower by Ba substation, while excess Ba substitution degrades the conductivity in LLBZT. LLBZT has a wide electrochemical potential window of 0–6 V vs. Li^+/Li, and Li^+ insertion and extraction reactions of $TiNb_2O_7$ film electrode formed on LLBZT by aerosol deposition are demonstrated at 60°C. The results indicate that LLBZT can potentially be used as a SE in all-solid-state batteries.

Keywords: garnet-type oxide, solid electrolyte, ionic conductivity, all-solid-state battery, aerosol deposition

OPEN ACCESS

Edited by:
Jeff Sakamoto,
University of Michigan, USA

Reviewed by:
Hui Xia,
Nanjing University of Science and Technology, China
Candace K. Chan,
Arizona State University, USA

****Correspondence:***
Ryoji Inada
inada@ee.tut.ac.jp

Specialty section:
This article was submitted to Energy Storage, a section of the journal Frontiers in Energy Research

Received: *09 February 2016*
Accepted: *06 July 2016*
Published: *20 July 2016*

Citation:
Inada R, Yasuda S, Tojo M, Tsuritani K, Tojo T and Sakurai Y (2016) Development of Lithium-Stuffed Garnet-Type Oxide Solid Electrolytes with High Ionic Conductivity for Application to All-Solid-State Batteries. Front. Energy Res. 4:28. doi: 10.3389/fenrg.2016.00028

INTRODUCTION

Lithium-ion batteries (LIBs) consist of a graphite negative electrode, organic liquid electrolyte, and lithium transition-metal oxide. They were first commercialized in 1991, and since then such batteries have been widely distributed globally as a power source for mobile electronic devices, such as cell phones and laptop computers. Nowadays, large-scale LIBs have been developed for application to automotive propulsion and stationary load-leveling for intermittent power generation from solar or wind energy (Tarascon and Armand, 2001; Armand and Tarascon, 2008; Scrosati and Garche, 2010; Goodenough and Kim, 2011). However, increasing battery size creates more serious safety issues for LIBs; one reason being the increased amount of flammable organic liquid electrolytes.

All-solid-state LIBs are expected to be one of the next generations of energy storage devices because of their high energy density, high safety, and excellent cycle stability (Fergus, 2010; Takada, 2013; Tatsumisago et al., 2013). The materials used for solid electrolyte (SE) must have not only high lithium-ion conductivity above 10^{-3} S cm^{-1} at room temperature but also possess chemical stability against electrode materials, air, and moisture. Although oxide-based SE materials have rather lower conductivity and poor deformability compared to sulfide-based ones, they have other advantages such as their chemical stability and ease of handling (Knauth, 2009; Ren et al., 2015a). Furthermore, the formation of solid–solid interface with low resistance between SE and electrode is another challenging issue in order to achieve better electrochemical performance in solid-state batteries with an oxide-based SE.

Among the various oxide-based SE materials, lithium-stuffed garnet-type oxide with the formula of $Li_7La_3Zr_2O_{12}$ (LLZ) has been widely studied because of its high conductivity above 10^{-4} S cm^{-1} at room temperature, excellent thermal performance, and stability against Li metal anode (Murugan et al., 2007a). LLZ has two different crystal phases, one is the cubic phase (Awaka et al., 2011) and the other is tetragonal (Awaka et al., 2009a; Geiger et al., 2011), but high conductivity above 10^{-4} S cm^{-1} at room temperature is mostly confirmed in cubic phase sintered at high temperature (1100–1200°C) in Al_2O_3 crucible or with Al_2O_3 substitution (Murugan et al., 2007a; Jin and McGinn, 2011; Kotobuki et al., 2011; Kumazaki et al., 2011; Li et al., 2012a; Rangasamy et al., 2012). During high temperature sintering, Al^{3+} enters from the crucible and/or substituted Al_2O_3 into the LLZ pellet and works as sintering aid. In addition, it has been pointed out that some amount of Al^{3+} enters into the LLZ lattice, occupies the part of Li^+ site and modifies the Li^+ vacancy concentration for charge compensation, and stabilizes the cubic phase. Ga^{3+} has a similar effect as Al^{3+} for cubic phase stabilization and enhancement of ionic conducting properties (Wolfenstine et al., 2012; Shinawi and Janek, 2013; Bernuy-Lopez et al., 2014; Jalem et al., 2015).

Partial substitution of the Zr^{4+} site in LLZ by other higher valence cations, such as Nb^{5+} (Ohta et al., 2011; Kihira et al., 2013), Ta^{5+} (Buschmann et al., 2012; Li et al., 2012b; Logéat et al., 2012; Wang and Wei, 2012; Inada et al., 2014a; Thompson et al., 2014, 2015; Ren et al., 2015a,b), W^{6+} (Dhivya et al., 2013; Li et al., 2015), and Mo^{6+} (Bottke et al., 2015) is also reported to be effective in stabilizing the cubic garnet phase, and their conductivity at room temperature is greatly enhanced up to ~1×10^{-3} S cm^{-1} by controlling the contents of dopants and optimizing Li^+ concentration in the garnet framework. Although a demonstration of a solid-state battery with Nb-doped LLZ as SE has been already reported (Ohta et al., 2012, 2013, 2014), it has also been reported that the chemical stability against a Li metal electrode of Ta-doped LLZ is much superior to a Nb-doped one (Nemori et al., 2015). Partially substituted W^{6+} in LLZ could potentially become a redox center as well as Nb^{5+} at relatively high potential against Li^+/Li (Xie et al., 2012).

In this paper, we synthesized garnet-type SEs with simultaneous substitution of Ta^{5+} into the Zr^{4+} site and Ba^{2+} into the La^{3+} site in LLZ, by a conventional solid state reaction method. Li^+ concentration was fixed to 6.5 per chemical formulae to stabilize the cubic garnet phase, so that the chemical formula of our samples is expressed as $Li_{6.5}La_{3-x}Ba_xZr_{1.5-x}Ta_{0.5+x}O_{12}$ (LLBZT) and Ba contents x are changed from 0 to 0.30. Many researchers have pointed out that the Li^+ conducting property in cubic garnet-type oxide is influenced not only by the Li^+ concentration but also by the lattice constant (Thangadurai and Weppner, 2005; Murugan et al., 2007b; Awaka et al., 2009b; Kihira et al., 2013; Thangadurai et al., 2014, 2015). Since the ionic radii of Ba^{2+} (142 pm) is greater than La^{3+} (116 pm), the lattice sizes of LLBZT with fixed Li^+ concentration per chemical formulae will be changed by the Ba substitution level, which will modify the ionic conducting property. Although it has been already confirmed that LLZ with substitution of both Ta and Ba can be fabricated (Tong et al., 2015), the influence of Ba substitution levels on the properties have not been fully discussed. In our study, the influence of Ba substitution level on the crystal phase, microstructure, and ionic conductivity for LLBZT was investigated. Furthermore, in order to investigate the feasibility for all-solid-state battery application, a $TiNb_2O_7$ film electrode was formed on garnet-type LLBZT without any thermal treatment by an aerosol deposition (AD) method (Akedo, 2006) and its electrochemical properties were evaluated.

MATERIALS AND METHODS

Synthesis and Characterization of LLBZT

LLBZT oxides with fixed Li content of 6.5 but different Ba content $x = 0$, 0.05, 0.1, 0.20, and 0.30 were prepared by a conventional solid state reaction method. It should be noted that, in this work, we did not use an Al_2O_3 crucible for sample synthesis because Al^{3+} contamination from the crucible into the LLBZT lattice during high temperature sintering may have an influence on Li^+ concentration and that this contamination level is very difficult to control. In addition, we had already succeeded in obtaining cubic garnet-type Ta-doped LLZ without containing Al by using a Pt–Au alloy crucible and sintering at 1100°C for 15 h. The highest room temperature conductivity attains to 6.1×10^{-4} S cm^{-1} at Li^+ concentration of 6.5 (Inada et al., 2014a), so we believe that Al^{3+} is not always required to stabilize the cubic phase and achieve high ionic conductivity.

Stoichiometric amounts of $LiOH{\cdot}H_2O$ (Kojundo chemical laboratory, 99%, 10% excess was added to account for the evaporation of lithium at high temperatures), $La(OH)_3$ (Kojundo chemical laboratory, 99.99%), $BaCO_3$ (Kojundo chemical laboratory, 99.9%), ZrO_2 (Kojundo chemical laboratory, 98%), and Ta_2O_5 (Kojundo chemical laboratory, 99.9%) were ground and mixed by planetary ball milling (Nagao System, Planet M2-3F) with zirconia balls and ethanol for 3 h and then calcined at 900°C for 6 h in a Pt–Au 5% alloy crucible. The calcined powders were ground again by planetary ball milling for 1 h, and then pressed into pellets at 300 MPa by cold isostatic pressing (CIP). Finally, all LLBZT pellets were sintered at 1150°C for 15 h in air using a Pt–Au 5% alloy crucible. During the sintering stage, the pellet was covered with the same mother powder to suppress excess Li loss and the formation of secondary phase, such as $La_2Zr_2O_7$.

As the characterization of obtained LLBZT samples, the crystal structure of the samples was evaluated by X-ray diffraction (XRD, Rigaku Multiflex) using Cu$K\alpha$ radiation ($\lambda = 0.15418$ nm), with a measurement range of $2\theta = 5$–$90°$ and a step interval of 0.004°. Using the XRD data for all LLBZT samples, the lattice constants were calculated by Rigaku PDXL XRD analysis software. Scanning electron microscope (SEM) observation and energy dispersive X-ray (EDX) analysis were performed using a field-emission SEM (SU8000 Type II, Hitachi) to investigate the fractured surface microstructure of sintered LLBZT and the distribution of La, Ba, Zr, Ta, and O elements.

The conductivity of each LLBZT sample was evaluated with AC impedance measurements using a chemical impedance meter (3532-80, Hioki) and an LCR tester (3532-50, Hioki) at a temperature from 27 to 100°C, a frequency from 5 Hz to 5 MHz, and an applied voltage amplitude of 0.1 V. The former was used for measurement from 5 Hz to 1 MHz while the latter was used for measurement above 1 MHz, respectively. Both parallel surfaces of the pellet were sputtered with Li^+ blocking Au electrodes for the conductivity measurement. The electrochemical windows of the samples were evaluated by cyclic voltammetry (CV) using a potentio-galvanostat (VersaSTAT 3, Princeton Applied Research) at a scanning rate of 0.2 mV s^{-1} between −0.4 and 6 V vs. Li^+/Li. An Au electrode and lithium metal were attached to both faces of the pellet as working and counter electrodes, respectively.

TNO Film Electrode Fabrication on LLBZT and Its Characterization

In order to study the feasibility of LLBZT for application to solid state batteries, $TiNb_2O_7$ (TNO) film electrode was formed on LLBZT pellet by AD method (Akedo, 2006). AD has several advantages compared to other conventional thin film deposition methods, including the deposition of a crystallized film without any heat treatments and a fast deposition rate. A film is deposited through impact and adhesion of fine particles on substrate at room temperature. This phenomenon is known as "room temperature impact consolidation (RTIC)." Consequently, as-deposited film has similar properties to the raw powder material, such as its crystal structure, composition, and physical property. By addressing these features, several papers have been reported for the feasibility of the AD method as a battery electrode or SE fabrication process (Popovici et al., 2011; Kim et al., 2013; Inada et al., 2014b, 2015; Iwasaki et al., 2014; Ahn et al., 2015; Kato et al., 2016).

TNO is known to be an insertion-type electrode material operating at a potential around 1.6–1.7 V vs. Li^+/Li and shows reversible charge and discharge capacities of around 250 mAh g^{-1} and reasonably good cycle stability (Han et al., 2011; Guo et al., 2014; Ashisha et al., 2015), so that we considered TNO as suitable for the feasibility study for an all-solid-state battery application. TNO powders used in this work were prepared by a conventional solid-state reaction method. Stoichiometric amount of anatase TiO_2 (Kojundo Chemical Laboratory Co., Ltd., 99%) and Nb_2O_5 (Kojundo Chemical Laboratory Co., Ltd., 99.9%) were ground and mixed in ethanol by planetary ball milling (Nagao System, Planet M2-3F) with zirconia balls for 1 h. The mixture was annealed at 1100°C for 24 h in air. From the XRD measurements, we confirmed that TNO was successfully obtained without forming any impurity phases.

It has been reported that both the size and morphology of raw powder are important factors for the structure and property of the film formed by AD (Akedo, 2006; Popovici et al., 2011; Inada et al., 2014b, 2015). In order to prepare TNO powder with suitable particle size for dense film fabrication by AD, TNO powder was pulverized using planetary ball milling (Nagao System, Planet M2-3F) with ethanol and zirconia balls. The rotation speed of planetary ball milling was fixed to 300 rpm but milling time was changed in order to control particle size.

The AD apparatus consists of a carrier gas supply system, an aerosol chamber, a deposition chamber equipped with a motored X–Y–Z stage, and a nozzle with a thin rectangular shaped-orifice with a size of 10 mm × 0.5 mm (Inada et al., 2014b, 2015). Deposition starts with evacuating the deposition chamber. A pressure difference between the carrier gas system and the deposition chamber is generated as a power source for film deposition. A carrier N_2 gas flows out from the gas supply system to the aerosol chamber. In the aerosol chamber, powder is dispersed into carrier gas and then the aerosol flows into the deposition chamber through a tube and is sprayed onto LLBZT as substrate. The deposition chamber was evacuated to a low vacuum state around 30 Pa, and deposition was carried out for several periods of 10 min. During the deposition process, the stage was moved uni-axially with a back-and-forth motion length of 50 mm. Distance between the tip of the nozzle and the LLBZT substrate was set to be 10 mm, and mass flow of N_2 carrier gas was fixed at 20 L min^{-1}. Before depositing the film electrode, an end surface of the LLBZT pellet was polished using sandpaper in order to form a smooth interface with the electrolyte.

Scanning Electron Microscope observation was performed using a field-emission SEM (SU8000 Type II, Hitachi) to reveal the morphology of the TNO powder and both the surface and cross-sectional microstructure of the TNO film electrode formed on LLBZT. EDX analysis was also performed during SEM observation to investigate the distribution of Ti and Nb elements contained in the film electrode.

An all-solid-state cell was fabricated by attaching a Li metal foil on the opposite end surface of a LLBZT pellet covered by a TNO film electrode in an Ar-filled grove box. TNO film is used as the working electrode and Li metal foil as the counter one. CV measurements (three cycles) of TNO film/LLBZT/Li all-solid-state cell were carried out using a potentio-galvanostat (VersaSTAT 3, Princeton Applied Research) at a temperature of 60°C and a scanning rate of 0.1 mV s^{-1} between 1.0 and 2.5 V vs. Li^+/Li. After the CV measurement, the solid-state cell was charged and discharged over a cell voltage range between 1.0 and 2.5 V at a constant current density of 2 μA cm^{-2} (corresponding to 5 mA g^{-1} per TNO film) and 60°C, using a battery test system (TOSCAT-3100, Toyo System).

RESULTS AND DISCUSSION

Characterization of LLBZT with Different Ba Contents

Figure 1 shows the XRD patterns of sintered LLBZT with different Ba content $x = 0$–0.30. Calculated diffraction peak patterns for cubic LLZ are also plotted as the reference (Awaka et al., 2011). All of the peaks for each LLBZT sample are well indexed as cubic garnet-type structures with a space group $Ia\bar{3}d$, and no other secondary phases were observed. Enlarged XRD patterns at $2\theta = 50.0$–$54.5°$ are shown in **Figure 2**. As can be seen, the peaks shifted toward a higher angle as x increases from 0 to 0.10, while at $x \geq 0.10$, the peaks shifted toward a lower angle with increasing x. It is worth noting that this trend is confirmed in other diffraction peaks, indicating that the lattice constants of LLBZT are not changed monotonically with x.

Using measured XRD data, we calculated the lattice constant for each LLBZT, and the results are summarized in **Table 1**. Among all the samples, LLBZT with $x = 0.10$ has the smallest lattice constant (=12.944 Å). As confirmed in the chemical formulae of LLBZT prepared in this work, Ta contents $y = 0.5 + x$ increase with Ba contents x and the ionic radii of Ta^{5+} (64 pm) is smaller than Zr^{4+} (78 pm). Therefore, the complex change of the lattice constants in LLBZT, depending on the composition, could be caused by the simultaneous change of Ba and Ta substitution levels. At $x \leq 0.10$, increase of Ta^{5+} substitution contents influences more on the lattice size of LLBZT, but at $x > 0.10$, the influence of Ba^{2+} substitution contents on the lattice size become dominant. Consequently, the lattice constants of LLBZT are decreased with $x \leq 0.10$, while increased with x from 0.10 to 0.30.

The calculated lattice constants for all LLBZT are also plotted as a function of Ba contents x (lower horizontal axis) and Ta contents $y = 0.5 + x$ (upper horizontal axis) in **Figure 3**. For comparison, the calculated lattice constants for Ba-free $Li_{7-y}La_3Zr_{2-y}Ta_yO_{12}$ (LLZT) with $y = 0.50$, 0.75, and 1.00 prepared in our previous work (Inada et al., 2014a) are also plotted against Ta contents y, which is almost linearly decreased with y. With increasing x, it is expected that the volume expansion of dodecahedral $(La/Ba)O_8$ and the volume contraction of octahedral $(Ta/Zr)O_6$ occur in a garnet framework of LLBZT, resulting in complex change of lattice constants depending on x. At Ba contents $x \leq 0.10$ and Ta contents $y \leq 0.60$, the lattice constants for LLBZT nearly fall on the y dependence of lattice constants in LLZT, so that, for LLBZT with $x \leq 0.10$ and $y \leq 0.60$, the contribution of a smaller Ta^{5+} substitution to the Zr^{4+} site is dominant. On the other hand, the lattice constants for LLBZT with $x = 0.20$ and 0.30 and $y = 1.70$ and 1.80 become larger than those for LLZT with the same y levels and the deviation becomes more remarkable with increasing x, suggesting that the contribution of a larger Ba^{2+} substitution to the La^{3+} site becomes dominant.

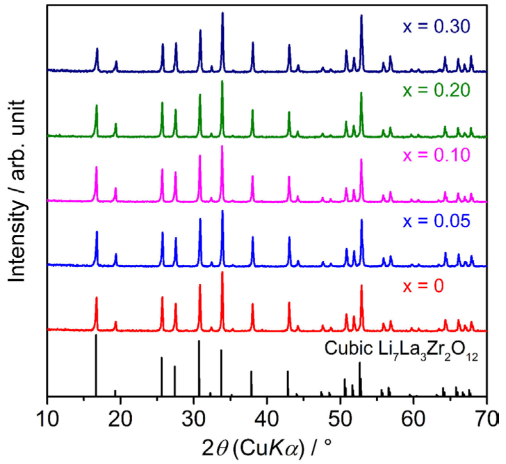

FIGURE 1 | **XRD patterns for sintered LLBZT with different Ba contents *x*.**

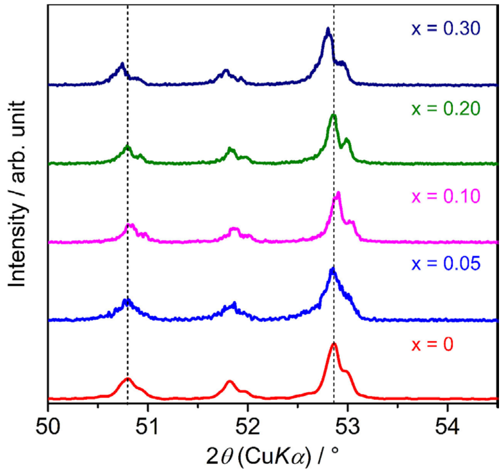

FIGURE 2 | **Enlarged XRD patterns for sintered LLBZT with different Ba contents *x*.**

TABLE 1 | **Expected compositions, lattice constants, relative densities of sintered LLZT and LLBZT with different Ba contents *x*.**

Ba content *x*	Expected composition	Lattice constant/Å	Relative density %
0	$Li_{6.5}La_3Zr_{1.5}Ta_{0.5}O_{12}$	12.954	92.8
0.05	$Li_{6.5}La_{2.95}Ba_{0.05}Zr_{1.45}Ta_{0.55}O_{12}$	12.949	92.6
0.10	$Li_{6.5}La_{2.9}Ba_{0.1}Zr_{1.4}Ta_{0.6}O_{12}$	12.944	90.4
0.20	$Li_{6.5}La_{2.8}Ba_{0.2}Zr_{1.3}Ta_{0.7}O_{12}$	12.952	88.8
0.30	$Li_{6.5}La_{2.7}Ba_{0.3}Zr_{1.2}Ta_{0.8}O_{12}$	12.964	92.0

Figure 4 shows the comparison of SEM images for fractured cross sections of all LLBZT. Average grain size in the sintered LLBZT samples was confirmed to be around 5 μm, and all grains are in good contact with each other. The density of each sintered pellet was determined from their weight and physical dimensions. The relative density (measured density normalized by the theoretical one) of LLBZT with different compositions are summarized in **Table 1**. Here, the theoretical density for each sample was calculated from the lattice constant and expected compositions also shown in **Table 1**. The relative density of each sample was estimated to be in a range between 89 and 93%, indicating that the difference in relative density among the sintered LLBZT with different composition is not so large. Enlarged SEM images and corresponding elementary mapping for La, Ba, Zr, and Ta and O in LLBZT with different Ba contents $x = 0.05–0.30$ are also shown in **Figure 5**. It can be seen that all elements show similar distribution in the sample, indicating that La^{3+} and Zr^{4+} are successfully substituted by Ba^{2+} and Ta^{5+}, respectively.

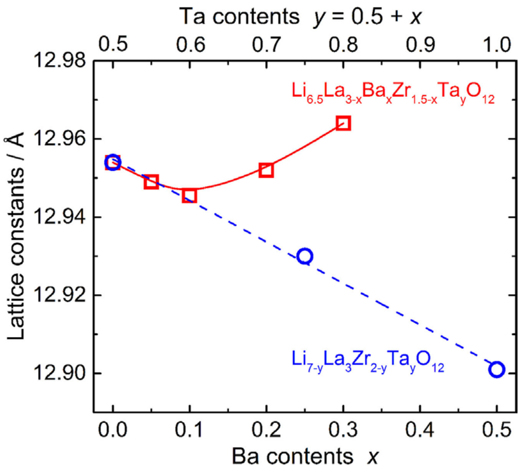

FIGURE 3 | Lattice constants of cubic garnet-type LLBZT plotted against Ba contents *x* and Ta contents $y = 0.5 + x$. Lattice constants of cubic garnet-type $Li_{7-y}La_3Zr_{2-y}Ta_yO_{12}$ without Ba substitution (Inada et al., 2014a,b) are plotted as a function of Ta contents *y* for comparison.

Ionic Conductivity and Electrochemical Stability of LLBZT

The conductivity of LLBZT with different compositions was examined by AC impedance spectroscopy using a Li-ion-blocking Au electrode. **Figure 6** shows Nyquist plots of AC impedance measured at 27 and 50°C for all samples. For direct comparison among the samples with different sizes, real and imaginary parts of impedance Z and Z'' multiplied by a factor of AL^{-1} are plotted, where A and L are surface area and thickness of each pellet. For all samples, a part of the semicircle and linear portion data were obtained in high and low frequency regions, indicating that the conducting nature is primarily ionic. Only a part of one semicircle was confirmed and the intercept point of the linear tail in the low frequency range with a real axis corresponding to the sum of the bulk- and grain-boundary resistance. Total conductivity σ for each sample can be calculated by the inverse of the total (bulk and grain boundary) resistance.

The lattice constant and conductivity σ at 27°C of LLBZT are plotted against Ba contents *x* in **Figures 7A,B**. The sample without Ba substitution shows $\sigma = 7.94 \times 10^{-4}$ S cm^{-1}, which is higher than LLZT with the same composition reported in our previous work (Inada et al., 2014a). This is mainly due to the higher sintering temperature (=1150°C) used in this work than that used in previous work (=1100°C). At $x \leq 0.1$, σ of LLBZT slightly increases, while the lattice constants slightly decrease with

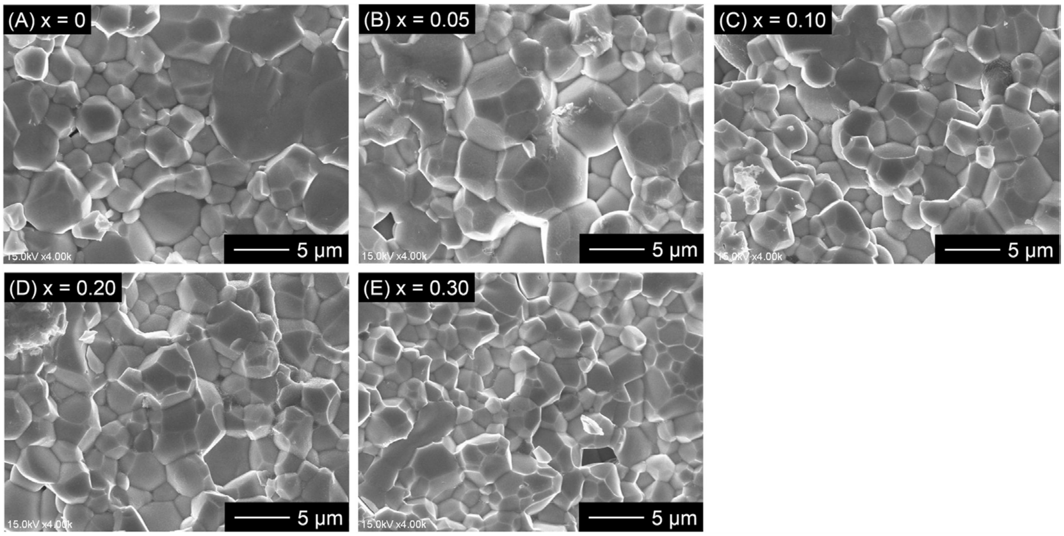

FIGURE 4 | Comparison of SEM images for fractured cross section of LLBZT with different Ba contents *x*: (A) $x = 0$, (B) $x = 0.05$, (C) $x = 0.10$, (D) $x = 0.20$, and (E) $x = 0.30$.

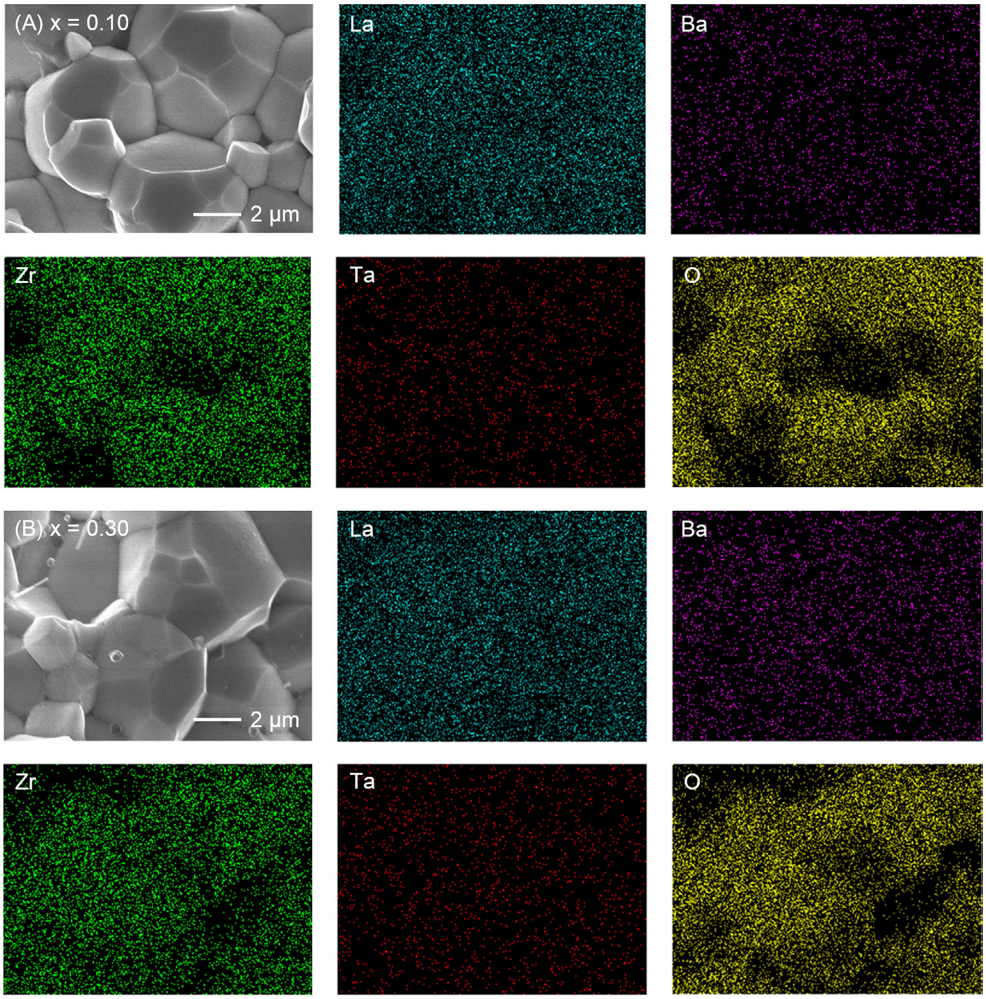

FIGURE 5 | **SEM images and corresponding elementary mapping for La, Ba, Zr, Ta, and O for LLBZT with (A) $x = 0.10$ and (B) $x = 0.30$.**

increasing x. The highest $\sigma = 8.34 \times 10^{-4}$ S cm^{-1} was obtained in LLBZT with $x = 0.1$ and the smallest lattice constant (=12.944 Å) among all samples. The relative density of LLBZT with $x = 0.1$ is slightly smaller than that for the sample with $x = 0$ and 0.05. Unfortunately, we could not obtain the bulk ionic conductivity of LLBZT, quantitatively, because of the limitation of frequency ranges in our experimental set-up, but it is expected that the bulk conductivity of LLBZT shows its maximum at $x = 0.1$. At $x > 0.1$, σ monotonically decreases while the lattice constants increase with x. The lowest $\sigma = 4.92 \times 10^{-4}$ S cm^{-1} was confirmed in LLBZT with $x = 0.3$ and the largest lattice constant among all samples.

The conductivity of LLBZT with fixed Li$^+$ concentration (=6.5) shows its maximum at a lattice constant of around 12.94–12.95 Å. Kihira et al. (2013) have reported their systematical investigation for the properties of cubic garnet-type LLZ with substituting Nb^{5+} to Zr^{4+} site and alkali earth metal cations, such as Sr^{2+} and Ca^{2+}, to La^{3+} site simultaneously, to modify the lattice constant. They also tried to substitute Mg^{2+} and Ba^{2+} to La^{3+} site in Nb-doped LLZ but some impurity phases, such as MgO and BaZrO$_3$, were formed. Interestingly, regardless of the substitution element, the highest conductivity in their samples is observed at nearly the same lattice constant of 12.94–12.96 Å, which is close to our results for LLBZT with $x = 0$–0.10. However, LLBZT with $x = 0.20$ has lower room temperature conductivity than LLBZT with $x = 0.05$, although both samples have nearly the same lattice size.

Since the difference in the relative densities among all samples is not so large, the contribution of grain-boundary resistivity to the total ionic conductivity does not depend on the composition of LLBZT. We believe that the composition dependence of σ is mainly caused by the change of Li$^+$ conduction property in LLBZT bulk. The bulk Li$^+$ conductivity σ_{Li} is described as $\sigma_{Li} = ne\mu$, where n is the number of carriers, e is the charge and μ is the carrier mobility. Since the charge value will be constant, σ_{Li} will be influenced by the number of carriers and the mobility. As mentioned above, it is expected that in LLBZT garnet, the volume of the dodecahedral (La/Ba)O$_8$ is expanded while the volume of octahedral (Ta/Zr)O$_6$ is contracted with increasing Ba contents x. These polyhedrons are adjacent to the tetrahedral LiO$_4$ and the

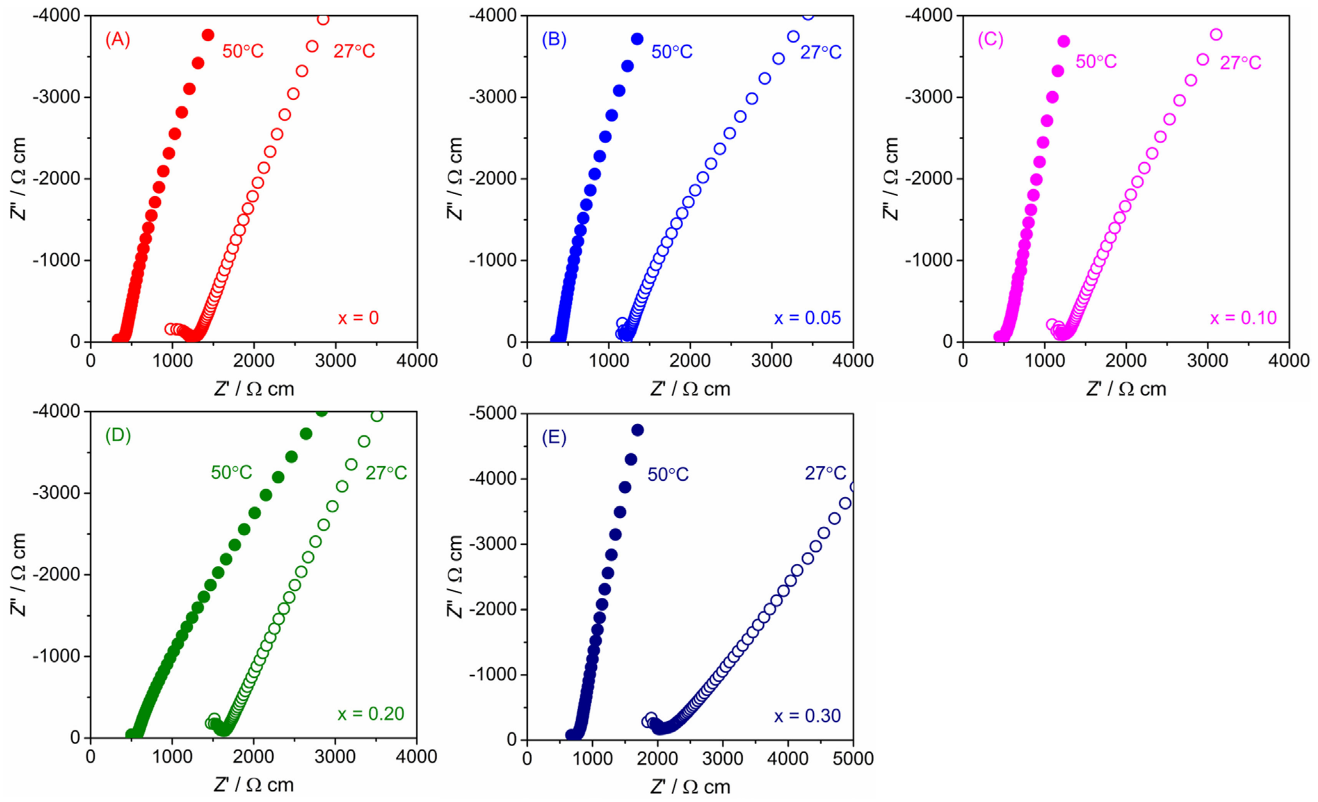

FIGURE 6 | **Nyquist plot of AC impedance for LLBZT with different Ba contents *x* at 27 and 50°C: (A) *x* = 0, (B) *x* = 0.05, (C) *x* = 0.10, (D) *x* = 0.20, and (E) *x* = 0.30**.

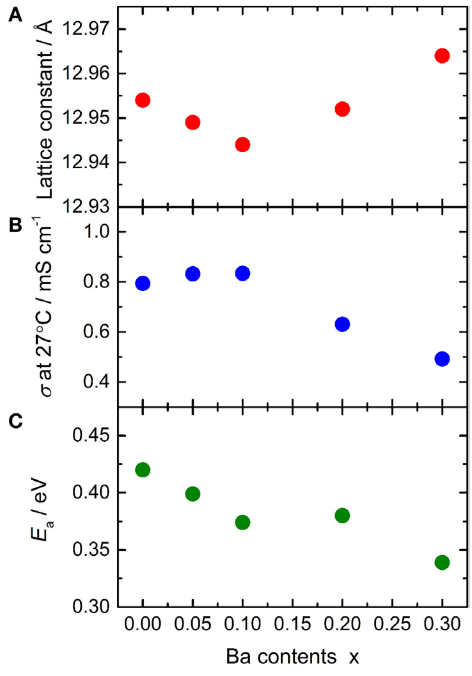

FIGURE 7 | **(A) Lattice constant, (B) total conductivity σ at 27°C and (C) its activation energy E_a for LLBZT plotted against Ba contents *x***.

octahedral LiO_6 in a garnet framework, so that the volumes of the LiO_4 and LiO_6 polyhedrons also show complex change depending on *x*. It has been pointed out that the Li^+ conductivity of garnet-type oxides is strongly influenced by the site occupancy in both LiO_4 (24*d* site) and LiO_6 (96*h* site) polyhedrons. The 24*d* and 96*h* site occupancies effect on the number of carriers, and higher σ_{Li} is achieved by well-balanced site occupancy (Li et al., 2012b; Kihira et al., 2013; Thangadurai et al., 2014, 2015). We believe that the 24*d* and 96*h* site occupancies are influenced not only by the Li^+ contents in a garnet framework but also by the sizes of both LiO_4 and LiO_6 polyhedrons. The highest conductivity at room temperature for LLBZT with *x* from 0.05 to 0.10 would be attributed to the well-balanced 24*d* and 96*h* site occupancies, while the deterioration of the conductivity with increasing $x > 0.20$ would be caused by the change in the site occupancies depending on the sizes of both LiO_4 and LiO_6 polyhedrons.

Temperature dependence of the conductivity for all LLBZT was also evaluated in the temperature range from 27 to 100°C. **Figure 8** shows the variation of σ for all sintered samples as a function of an inverse of temperature $1000T^{-1}$. The temperature dependence of σ is expressed by the Arrhenius equation as $\sigma = \sigma_0 \exp[-E_a/(k_B T)]$, where σ_0 is constant, E_a is activation energy of conductivity, and k_B is Boltzmann constant ($= 1.381 \times 10^{-23}$ J/K). The E_a of each sample are estimated from the slope of σT data plotted in **Figure 8** and summarized in **Table 2**, together with σ at 27°C. The sample without Ba

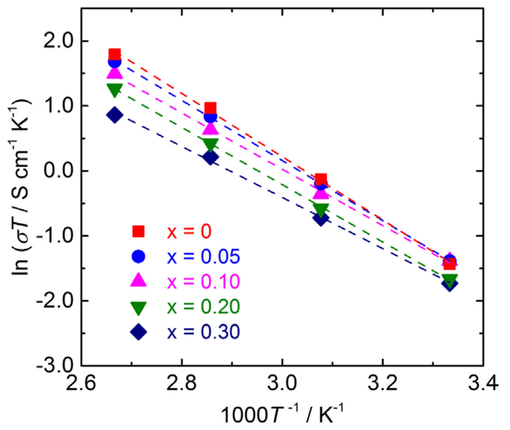

FIGURE 8 | Arrhenius plot of the conductivity σ for LLBZT with different Ba contents *x* = 0–0.30 plotted against the inverse of measurement temperature.

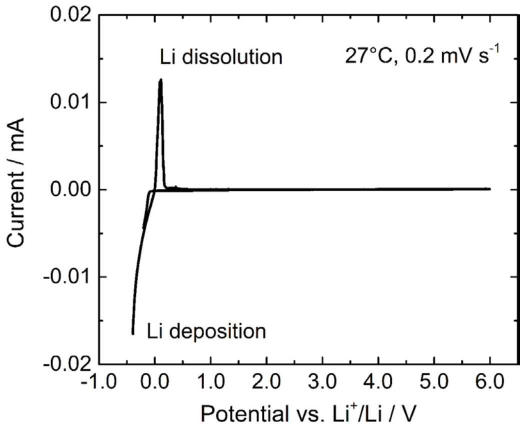

FIGURE 9 | A cyclic voltammogram of LLBZT with Ba contents *x* = 0.20 measured at a scanning rate of 0.2 mV s^{-1} at 27°C.

TABLE 2 | Total conductivity σ at different measurement temperature and activation energy E_a for LLBZT with different Ba contents *x* = 0–0.30.

Ba content *x*	Total conductivity σ/S cm^{-1}				E_a/eV
	27°C	50°C	75°C	100°C	
0	7.94×10^{-4}	2.70×10^{-3}	7.5×10^{-3}	16.0×10^{-3}	0.420
0.05	8.32×10^{-4}	2.50×10^{-3}	6.6×10^{-3}	14.4×10^{-3}	0.399
0.10	8.34×10^{-4}	2.20×10^{-3}	5.40×10^{-3}	11.9×10^{-3}	0.374
0.20	6.31×10^{-4}	1.80×10^{-3}	4.50×10^{-3}	10.6×10^{-3}	0.380
0.30	4.92×10^{-4}	1.30×10^{-3}	3.10×10^{-3}	5.40×10^{-3}	0.339

substitution has the highest $E_a = 0.42$ eV, which is higher than an Al-doped LLZT sample with a similar composition (Li et al., 2012b) but nearly the same as the Al-free sample prepared by hot pressing (Thompson et al., 2015). The E_a of LLBZT is in the range of 0.34–0.40 eV and tends to decrease with increasing Ba substitution levels as shown in **Figure 7C**.

Ba substitution levels influence on both the ionic conductivity and its activation energy. At $x \leq 0.10$, the lattice size of LLBZT is reduced with increasing *x*, while σ at room temperature is increased slightly, suggesting that the number of carriers for Li^+ conduction in LLBZT are increased with *x* from 0 to 0.10. Therefore, the reduction of E_a by Ba substitution at $x \leq 0.10$ would be mainly attributed to the increase in the number of carriers by the slight modification of the 24*d* and 96*h* site occupancies. On the other hand, the lattice size of LLBZT is increased with *x*, while σ at room temperature is lowered with increasing *x* from 0.10 to 0.30, suggesting that the number of carriers for Li^+ conduction is decreased with *x* while the bottleneck size for Li^+ conduction expands. It is expected that the expansion of bottleneck size result in enhancing the mobility, so the reduction of E_a at $x > 0.10$ would be mainly caused by the enhancement of the mobility.

In order to evaluate the electrochemical stability of LLBZT, a cyclic voltammogram of LLBZT is shown in **Figure 9**. Li deposition and dissolution peaks near 0 V vs. Li^+/Li are clearly observed, but no other reactions are confirmed up to 6 V vs. Li^+/Li. Therefore, LLBZT has a wide electrochemical potential window and various electrode materials can potentially be used to construct all-solid-state batteries with LLBZT as the SE.

Characterization of TNO Film Electrode Formed on LLBZT

For the feasibility study of all-solid-state battery application, TNO film electrode was formed on the surface of sintered LLBZT pellet by the AD method, and its electrochemical property was evaluated. We used pulverized TNO powder by planetary ball milling as raw material for fabrication of the film electrode. As can be seen in **Figure 10A**, raw TNO powder dominantly includes particles with a size of 0.5–0.8 μm. SEM images of the surface and cross section of TNO film electrode are shown in **Figures 10B,C**, together with a schematic illustration of the film formation by AD in **Figure 10D**. It is confirmed that strongly deformed and/or fractured TNO particles form a dense film electrode on LLBZT without any thermal treatment. The thickness of the TNO film electrode is confirmed to be ~1.5 μm. The interface morphology between the TNO film and the LLBZT pellet seems to be very smooth. **Figure 11** shows elementary mapping results of Ti and Nb on the surface and the cross section of the TNO film electrode formed on LLBZT. On the film surface, both Ti and Nb are detected in the whole observed area, while in the cross section, Ti and Nb are dominantly detected in the film electrode area.

A cyclic voltammogram of a TNO film/LLBZT/Li solid-state cell measured at 60°C and a scan rate of 0.1 mV s^{-1} is shown in **Figure 12**. After the cell construction, the open-circuit voltage of the cell was confirmed to be around 1.7 V. Except for the first scanning toward anodic direction, both the oxidation and reduction reaction of the TNO film electrode on LLBZT seems to be reversible. Broad oxidation and reduction reaction peaks are confirmed at the cell voltages (nearly corresponding to the potential vs. Li^+/Li) of 1.8 V and 1.6 V, which corresponds to the Li^+ extraction and insertion reaction potential for TNO (Ashisha et al., 2015). **Figure 13** shows the charge and discharge properties of a TNO film/LLBZT/Li solid-state cell measured at

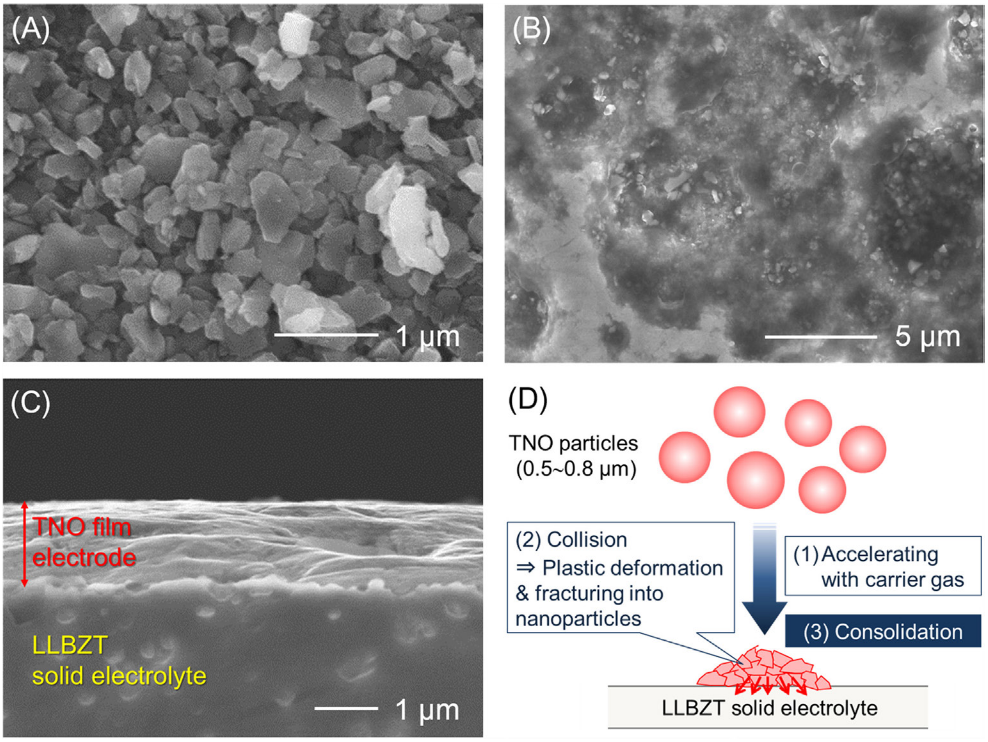

FIGURE 10 | SEM images for (A) TNO powder used as raw materials for film electrode fabrication by AD, (B) the surface of TNO film electrode, and (C) polished cross section of TNO film electrode. Plastically deformed and/or fractured TNO particles form the dense film on LLBZT *via* impact consolidation as shown in **(D)**.

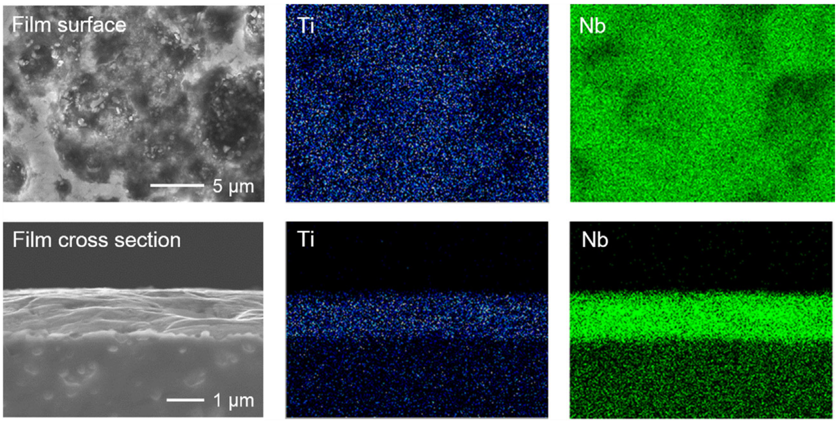

FIGURE 11 | SEM images and corresponding elementary mapping for Ti and Nb on the surface and polished cross section of TNO film electrode formed on LLBZT.

60°C and a current density of 2 µA cm^{-2}. As can be seen, TNO film electrode formed on LLBZT by AD showed capacities of 220 mAh g^{-1} for Li^+ insertion reaction and 170 mAh g^{-1} for Li^+ extraction reaction. Electrode reactions occur at an averaged cell voltage of 1.6 V, which is nearly the same as the TNO composite electrode with conducting additive and binder in an organic liquid electrolyte (Han et al., 2011; Guo et al., 2014; Ashisha et al., 2015). Although the coulombic efficiency of TNO film electrode is far below 100% at present, the results shown in **Figures 12** and **13** indicate that LLBZT works as the Li^+ conduction path between the TNO film as the working electrode and the Li metal foil as the counter one.

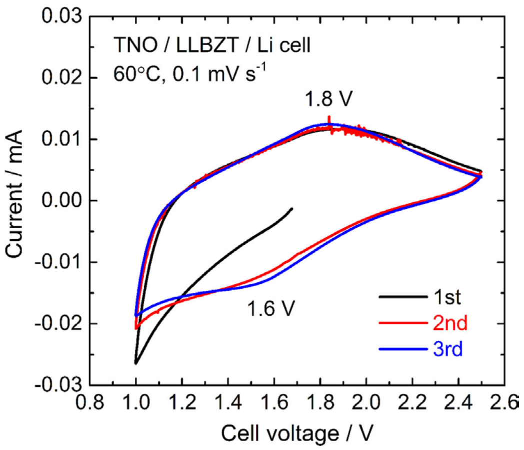

FIGURE 12 | A cyclic voltammogram measured at 60°C and a scanning rate of and 0.1 mV s^{-1} for TNO film electrode/LLBZT/Li all-solid-state cell.

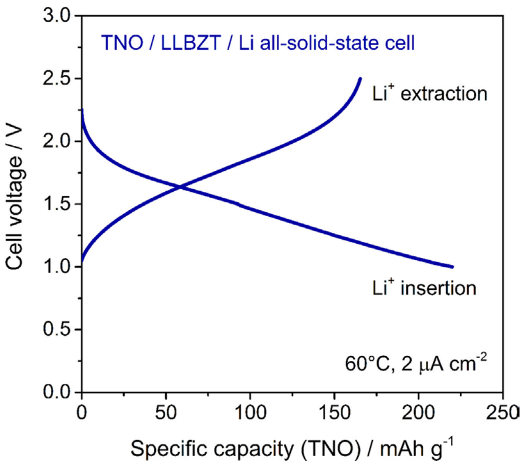

FIGURE 13 | Charge and discharge curves measured at 60°C and current density of 2 μA cm^{-2} for TNO film electrode/LLBZT/Li all-solid-state cell.

As a future prospect for solid state battery development with garnet-type LLBZT SE, both increasing the thickness of the electrode and reducing the thickness of the SE layer should be indispensable for enhancing the volumetric energy density of a solid-state battery. In a thicker electrode layer with a thickness of several 10 μm, a composite structure with electrode active material and SE must be needed to increase the solid–solid interface among them for the high utilization of active material in a composite electrode. We are considering that AD is one of the potential processing methods to form composite electrode on LLBZT sheet because composite powders with active material and Li^+ conducting SE can be directly used (Iwasaki et al., 2014; Kato et al., 2016) as raw material to form the composite electrode on SE sheet. Since thermal treatment is not always needed to form the electrode on SE sheet by AD, undesired reactions between the electrode and SE can be greatly suppressed. In addition, AD is also potentially applicable to the fabrication of film-shaped SE layer, which has been already demonstrated in NASICON-type Li^+ conducting oxide-based SE (Popovici et al., 2011; Inada et al., 2015). We are now trying to fabricate composite thick film electrode on LLBZT by AD, and progress on this will be reported in a forthcoming paper.

CONCLUSION

In this paper, we investigate the properties of garnet-type Li^+ conducting oxide SEs with simultaneous substitution of Ta^{5+} into the Zr^{4+} site and Ba^{2+} into the La^{3+} site in LLZ. Li^+ concentration was fixed to 6.5 per chemical formulae, so that the composition of our samples is expressed as $Li_{6.5}La_{3-x}Ba_xZr_{1.5-x}Ta_{0.5+x}O_{12}$ (LLBZT), and Ba contents x are changed from 0 to 0.30. As a result, all LLBZT samples have a cubic garnet-type structure without any secondary phases. The lattice constants of LLBZT decrease with increasing Ba^{2+} contents $x \leq 0.10$ while increase with x from 0.10 to 0.30, possibly caused by the simultaneous change of smaller Ta^{5+} and larger Ba^{2+} substitution levels. On the other hand, the relative densities of LLBZT are not influenced greatly by x. The total conductivity at 27°C of LLBZT has its maximum value of 8.34×10^{-4} S cm^{-1} at $x = 0.10$, which is slightly higher than the conductivity of LLZT without substituting Ba (= 7.94×10^{-4} S cm^{-1}). This improvement would be attributed to the modification of the number of carriers by tuning the 24*d* and 96*h* site occupancies. A larger lattice size created by excess Ba substitution is not suitable to achieve high ionic conductivity in LLBZT. The activation energy of the conductivity tends to become lower than the sample without Ba substitution. However, the influence of Ba contents on the Li^+ occupation site and carrier concentration in garnet-type LLBZT cannot be examined at present so that a detailed structural analysis would be necessary to clarify the ionic conducting property in LLBZT.

LLBZT is confirmed to be electrochemically stable at the potential range of 0–6 V vs. Li^+/Li so that various kinds of electrode materials can potentially be used for constructing an all-solid-state battery. In order to investigate the feasibility for solid-state battery application, TNO film electrode was formed on LLBZT without any thermal treatment by an AD method, and its electrochemical properties were evaluated. The Li^+ insertion and extraction reaction of the film electrode formed on LLBZT could be confirmed, indicating that LLBZT can be used as a SE in an all-solid-state battery.

AUTHOR CONTRIBUTIONS

RI was in charge of planning and performing all the experiment (containing both material preparation and characterization) in this work, together with summarizing the paper preparation. SY and KT were in charge of the preparation and characterization of oxide solid electrolyte samples. MT was in charge of the fabrication of the film-type electrode on solid electrolyte material and its characterization. TT and YS were in charge of the discussion for all experimental results.

ACKNOWLEDGMENTS

RI would like to thank Prof. Dr. Venkataraman Thangadurai of University of Calgary, Prof. Dr. Jeff Sakamoto of University of Michigan, Prof. Dr. Palani Balaya of National University of Singapore, and Prof. Dr. Ashutosh Tiwari of The University of Utah for their kind and technical advices in our sample preparation and characterization during his visiting in their laboratory on March 2015. This work was partly supported by JSPS KAKENHI [Challenging Exploratory Research and Scientific Research (C)] grant numbers 26630111 and 16K06218 from the Japan Society for the Promotion of Science (JSPS), Research Foundation for the Electrotechnology of Chubu (R-25209) and TOYOAKI Scholarship Foundation.

REFERENCES

Ahn, C.-W., Choi, J.-J., Ryu, J., Hahn, B.-D., Kim, J.-W., Yoon, W.-Ha, et al. (2015). Microstructure and electrochemical properties of iron oxide film fabricated by aerosol deposition method for lithium ion battery. *J. Power Sources* 275, 336–340. doi:10.1016/j.jpowsour.2014.11.033

Akedo, J. (2006). Aerosol deposition of ceramic thick films at room temperature: densification mechanism of ceramic layers. *J. Am. Ceramic Soc.* 89, 1834–1839. doi:10.1111/j.1551-2916.2006.01030.x

Armand, M., and Tarascon, J.-M. (2008). Building better batteries. *Nature* 451, 652–657. doi:10.1038/451652a

Ashisha, A. G., Arunkumara, P., Babua, B., Manikandana, P., Saranga, S., and Shaijumon, M. M. (2015). $TiNb_2O_7$/graphene hybrid material as high performance anode for lithium-ion batteries. *Electrochim. Acta* 176, 285–292. doi:10.1016/j.electacta.2015.06.122

Awaka, J., Kijima, N., Hayakawa, H., and Akimoto, J. (2009a). Synthesis and structure analysis of tetragonal $Li_7La_3Zr_2O_{12}$ with the garnet-related type structure. *J. Solid State Chem.* 182, 2046–2052. doi:10.1016/j.jssc.2009.05.020

Awaka, J., Kijima, N., Takahashi, Y., Hayakawa, H., and Akimoto, J. (2009b). Synthesis and crystallographic studies of garnet-related lithium-ion conductors $Li_6CaLa_2Ta_2O_{12}$ and $Li_6BaLa_2Ta_2O_{12}$. *Solid State Ionics.* 180, 602–606. doi:10.1016/j.ssi.2008.10.022

Awaka, J., Takashima, A., Kataoka, K., Kijima, N., Idemoto, Y., and Akimoto, J. (2011). Crystal structure of fast lithium-ion-conducting cubic $Li_7La_3Zr_2O_{12}$. *Chem. Lett.* 40, 60–62. doi:10.1246/cl.2011.60

Bernuy-Lopez, C., Manalastas, W. Jr., Lopez, J. M., Aguadero, A., Aguesse, F., and Kilner, J. A. (2014). Atmosphere controlled processing of Ga-substituted garnets for high Li-ion conductivity ceramics. *Chem. Mater.* 26, 3610–3617. doi:10.1021/cm5008069

Bottke, P., Rettenwander, D., Schmidt, W., Amthauer, G., and Wilkening, M. (2015). Ion dynamics in solid electrolytes: NMR reveals the elementary steps of Li^+ hopping in the garnet $Li_{6.5}La_3Zr_{1.75}Mo_{0.25}O_{12}$. *Chem. Mater.* 27, 6571–6582. doi:10.1021/acs.chemmater.5b02231

Buschmann, H., Berendts, S., Mogwitz, B., and Janek, J. (2012). Lithium metal electrode kinetics and ionic conductivity of the solid lithium ion conductors "$Li_7La_3Zr_2O_{12}$" and $Li_{7-x}La_3Zr_{2-x}Ta_xO_{12}$ with garnet-type structure. *J. Power Sources* 206, 236–244. doi:10.1016/j.jpowsour.2012.01.094

Dhivya, L., Janani, N., Palanivel, B., and Murugan, R. (2013). Li^+ transport properties of W substituted $Li_7La_3Zr_2O_{12}$ cubic lithium garnets. *AIP Adv.* 3, 082115. doi:10.1063/1.4818971

Fergus, J. W. (2010). Ceramic and polymeric solid electrolytes for lithium-ion batteries. *J. Power Sources* 195, 4554–4569. doi:10.1016/j.jpowsour.2010.01.076

Geiger, C. A., Alekseev, E., Lazic, B., Fisch, M., Armbruster, T., Langner, R., et al. (2011). Crystal chemistry and stability of "$Li_7La_3Zr_2O_{12}$" garnet: a fast lithium-ion conductor. *Inorg. Chem.* 50, 1089–1097. doi:10.1021/ic101914e

Goodenough, J. B., and Kim, Y. (2011). Challenges for rechargeable batteries. *J. Power Sources* 196, 6688–6694. doi:10.1016/j.jpowsour.2010.11.074

Guo, B. K., Yu, X. Q., Sun, X. G., Chi, M. F., Qiao, Z. A., Liu, J., et al. (2014). A long-life lithium-ion battery with a highly porous $TiNb_2O_7$ anode for large-scale electrical energy storage. *Energy Environ. Sci.* 7, 2220–2226. doi:10.1039/C4EE00508B

Han, J.-T., Huan, Y.-H., and Goodenough, J. B. (2011). New anode framework for rechargeable lithium batteries. *Chem. Mater.* 23, 2027–2029. doi:10.1021/cm200441h

Inada, R., Ishida, K., Tojo, M., Okada, T., Tojo, T., and Sakurai, Y. (2015). Properties of aerosol deposited NASICON-type $Li_{1.5}Al_{0.5}Ge_{1.5}(PO_4)_3$ solid electrolyte thin films. *Ceramics Int.* 41, 11136–11142. doi:10.1016/j.ceramint.2015.05.062

Inada, R., Kusakabe, K., Tanaka, T., Kudo, S., and Sakurai, Y. (2014a). Synthesis and properties of Al-free $Li_{7-x}La_3Zr_{2-x}Ta_xO_{12}$ garnet related oxides. *Solid State Ionics.* 262, 568–572. doi:10.1016/j.ssi.2013.09.008

Inada, R., Shibukawa, K., Masada, C., Nakanishi, Y., and Sakurai, Y. (2014b). Characterization of as-deposited $Li_4Ti_5O_{12}$ thin film electrode prepared by aerosol deposition method. *J. Power Sources* 244, 646–651. doi:10.1016/j.jpowsour.2013.12.084

Iwasaki, S., Hamanaka, T., Yamakawa, T., West, W. C., Yamamoto, K., Motoyama, M., et al. (2014). Preparation of thick-film $LiNi_{1/3}Co_{1/3}Mn_{1/3}O_2$ electrodes by aerosol deposition and its application to all-solid-state batteries. *J. Power Sources* 272, 1086–1090. doi:10.1016/j.jpowsour.2014.09.038

Jalem, R., Rushton, M. J. D., Manalastas, W. Jr., Nakayama, M., Kasuga, T., Kilner, J. A., et al. (2015). Effects of Gallium doping in garnet-type $Li_7La_3Zr_2O_{12}$ solid electrolytes. *Chem. Mater.* 27, 2821–2831. doi:10.1021/cm5045122

Jin, Y., and McGinn, P. J. (2011). Al-doped $Li_7La_3Zr_2O_{12}$ synthesized by a polymerized complex method. *J. Power Sources* 196, 8683–8687. doi:10.1016/j.jpowsour.2011.05.065

Kato, T., Iwasaki, S., Ishii, Y., Motoyama, N., West, W. C., Yamamoto, Y., et al. (2016). Preparation of thick-film electrode-solid electrolyte composites on $Li_7La_3Zr_2O_{12}$ and their electrochemical properties. *J. Power Sources* 303, 65–72. doi:10.1016/j.jpowsour.2015.10.101

Kihira, Y., Ohta, S., Imagawa, H., and Asaoka, T. (2013). Effect of simultaneous substitution of alkali earth metals and Nb in $Li_7La_3Zr_2O_{12}$ on lithium-ion conductivity. *ECS Electrochem. Lett.* 2, A56–A59. doi:10.1149/2.001307eel

Kim, I., Park, J., Nam, T.-H., Kim, K.-W., Ahn, J.-H., Park, D.-S., et al. (2013). Electrochemical properties of an as-deposited $LiFePO_4$ thin film electrode prepared by aerosol deposition. *J. Power Sources* 243, 181–186. doi:10.1016/j.jpowsour.2012.12.108

Knauth, P. (2009). Inorganic solid Li ion conductors: an overview. *Solid State Ionics.* 180, 911–916. doi:10.1016/j.ssi.2009.03.022

Kotobuki, M., Kanamura, K., Sato, Y., and Yoshida, T. (2011). Fabrication of all-solid-state lithium battery with lithium metal anode using Al_2O_3-added $Li_7La_3Zr_2O_{12}$ solid electrolyte. *J. Power Sources* 196, 7750–7754. doi:10.1016/j.jpowsour.2011.04.047

Kumazaki, S., Iriyama, Y., Kim, K.-H., Murugan, R., Tanabe, K., Yamamoto, K., et al. (2011). High lithium ion conductive $Li_7La_3Zr_2O_{12}$ by inclusion of both Al and Si. *Electrochem. commun.* 13, 509–512. doi:10.1016/j.elecom.2011.02.035

Li, Y., Han, J.-T., Wang, C.-A., Vogel, S. C., Xie, H., Xu, M., et al. (2012a). Ionic distribution and conductivity in lithium garnet $Li_7La_3Zr_2O_{12}$. *J. Power Sources* 209, 278–281. doi:10.1016/j.jpowsour.2012.02.100

Li, Y., Han, J.-T., Wang, C.-A., Xie, H., and Goodenough, J. B. (2012b). Optimizing Li^+ conductivity in a garnet framework. *J. Mater. Chem.* 22, 15357–15361. doi:10.1039/C2JM31413D

Li, Y., Wang, Z., Cao, Y., Du, F., Chen, C., Cui, Z., et al. (2015). W-doped $Li_7La_3Zr_2O_{12}$ ceramic electrolytes for solid state Li-ion batteries. *Electrochim. Acta* 180, 37–42. doi:10.1016/j.electacta.2015.08.046

Logéat, A., Köhler, T., Eisele, U., Stiaszny, B., Harzer, A., Tovar, M., et al. (2012). From order to disorder: the structure of lithium-conducting garnets $Li_{7-x}La_3Ta_xZr_{2-x}O_{12}$ (x = 0–2). *Solid State Ionics.* 206, 33–38. doi:10.1016/j.ssi.2011.10.023

Murugan, R., Thangadurai, V., and Weppner, W. (2007a). Fast lithium ion conduction in garnet-type $Li_7La_3Zr_2O_{12}$. *Angew. Chem. Int. Ed.* 46, 7778–7781. doi:10.1002/anie.200701144

Murugan, R., Weppner, W., Schmid-Beurmann, P., and Thangadurai, V. (2007b). Structure and lithium ion conductivity of bismuth containing lithium garnets $Li_5La_3Bi_2O_{12}$ and $Li_6SrLa_2Bi_2O_{12}$. *Mater. Sci. Eng. B* 143, 14–20. doi:10.1016/j.mseb.2007.07.009

Nemori, H., Matsuda, Y., Mitsuoka, S., Matsui, M., Yamamoto, O., Takeda, Y., et al. (2015). Stability of garnet-type solid electrolyte $Li_xLa_3A_{2-y}B_yO_{12}$ (A=Nb or Ta, B = Sc or Zr). *Solid State Ionics.* 282, 7–12. doi:10.1016/j.ssi.2015.09.015

Ohta, S., Kobayashi, T., and Asaoka, T. (2011). High lithium ionic conductivity in the garnet-type oxide $Li_{7-X}La_3(Zr_{2-X}, Nb_X)O_{12}$ (X = 0–2). *J. Power Sources* 196, 3342–3345. doi:10.1016/j.jpowsour.2010.11.089

Ohta, S., Komagata, S., Seki, J., and Asaoka, T. (2012). Electrochemical performance of an all-solid-state lithium ion battery with garnet-type oxide electrolyte. *J. Power Sources* 202, 332–335. doi:10.1016/j.jpowsour.2011.10.064

Ohta, S., Komagata, S., Seki, J., Saeki, T., Morishita, S., and Asaoka, T. (2013). All-solid-state lithium ion battery using garnet-type oxide and Li_3BO_3 solid electrolytes fabricated by screen-printing. *J. Power Sources* 238, 53–56. doi:10.1016/j.jpowsour.2013.02.073

Ohta, S., Seki, J., Yagi, Y., Kihira, Y., Tani, T., and Asaoka, T. (2014). Co-sinterable lithium garnet-type oxide electrolyte with cathode for all-solid-state lithium ion battery. *J. Power Sources* 265, 40–44. doi:10.1016/j.jpowsour.2014.04.065

Popovici, D., Nagai, H., Fujisima, S., and Akedo, J. (2011). Preparation of lithium aluminum titanium phosphate electrolytes thick films by aerosol deposition method. *J. Am. Ceramic Soc.* 94, 3847–3850. doi:10.1111/j.1551-2916.2011.04551.x

Rangasamy, E., Wolfenstine, J., and Sakamoto, J. (2012). The role of Al and Li concentration on the formation of cubic garnet solid electrolyte of nominal composition $Li_7La_3Zr_2O_{12}$. *Solid State Ionics.* 206, 28–32. doi:10.1016/j.ssi.2011.10.022

Ren, Y., Chen, K., Chen, R., Liu, T., Zhang, Y., and Nan, C.-W. (2015a). Oxide electrolytes for lithium batteries. *J. Am. Ceramic Soc.* 98, 3603–3623. doi:10.1111/jace.13844

Ren, Y., Deng, H., Chen, R., Shen, Y., Lin, Y., and Nan, C.-W. (2015b). Effects of Li source on microstructure and ionic conductivity of Al-contained $Li_{6.75}La_3Zr_{1.75}Ta_{0.25}O_{12}$ ceramics. *J. Eur. Ceramic Soc.* 35, 561–572. doi:10.1016/j.jeurceramsoc.2014.09.007

Scrosati, B., and Garche, J. (2010). Lithium batteries: status, prospects and future. *J. Power Sources* 195, 2419–2430. doi:10.1016/j.jpowsour.2009.11.048

Shinawi, H. E., and Janek, J. (2013). Stabilization of cubic lithium-stuffed garnets of the type "$Li_7La_3Zr_2O_{12}$" by addition of gallium. *J. Power Sources* 225, 13–19. doi:10.1016/j.jpowsour.2012.09.111

Takada, K. (2013). Progress and prospective of solid-state lithium batteries. *Acta Mater.* 61, 759–770. doi:10.1016/j.actamat.2012.10.034

Tarascon, J.-M., and Armand, M. (2001). Issues and challenges facing rechargeable lithium batteries. *Nature* 414, 359–367. doi:10.1038/35104644

Tatsumisago, M., Nagao, M., and Hayashi, A. (2013). Recent development of sulfide solid electrolytes and interfacial modification for all-solid-state rechargeable lithium batteries. *J. Asian Ceramic Soc.* 1, 117–125. doi:10.1016/j.jascer.2013.03.005

Thangadurai, V., Narayanan, S., and Pinzaru, D. (2014). Garnet-type solid-state fast Li ion conductors for Li batteries: critical review. *Chem. Soc. Rev.* 43, 4714–4727. doi:10.1039/c4cs00020j

Thangadurai, V., Pinzaru, D., Narayanan, S., and Baral, A. K. (2015). Fast solid-state Li ion conducting garnet-type structure metal oxides for energy storage. *J. Phys. Chem. Lett.* 6, 292–299. doi:10.1021/jz501828v

Thangadurai, V., and Weppner, W. (2005). $Li_6ALa_2Ta_2O_{12}$ (A = Sr, Ba): novel garnet-like oxides for fast lithium ion conduction. *Adv. Funct. Mater.* 15, 107–112. doi:10.1002/adfm.200400044

Thompson, T., Sharafi, A., Johannes, M. D., Huq, A., Allen, J. L., Wolfenstine, J., et al. (2015). Tale of two sites: on defining the carrier concentration in garnet-based ionic conductors for advanced Li batteries. *Adv. Energy Mater.* 5: 1500096. doi:10.1002/aenm.201500096

Thompson, T., Wolfenstine, J., Allen, J. L., Johannes, M., Huq, A., Davida, I. N., et al. (2014). Tetragonal vs. cubic phase stability in Al-free Ta doped $Li_7La_3Zr_2O_{12}$ (LLZO). *J. Mater. Chem. A* 2, 13431–13436. doi:10.1039/c4ta02099e

Tong, X., Thangadurai, V., and Wachslnan, E. D. (2015). Highly conductive Li garnets by a multielement doping strategy. *Inorg. Chem.* 54, 3600–3607. doi:10.1021/acs.inorgchem.5b00184

Wang, Y., and Wei, L. (2012). High ionic conductivity lithium garnet oxides of $Li_{7-x}La_3Zr_{2-x}Ta_xO_{12}$ compositions. *Electrochem. Solid State Lett.* 15, A68–A71. doi:10.1149/2.024205esl

Wolfenstine, J., Ratchford, J., Rangasamy, E., Sakamoto, J., and Allen, J. L. (2012). Synthesis and high Li-ion conductivity of Ga-stabilized cubic $Li_7La_3Zr_2O_{12}$. *Mater. Chem. Phys.* 134, 571–575. doi:10.1016/j.matchemphys.2012.03.054

Xie, H., Park, K.-S., Song, J., and Goodenough, J. B. (2012). Reversible lithium insertion in the garnet framework of $Li_3Nd_3W_2O_{12}$. *Electrochem. commun.* 19, 135–137. doi:10.1016/j.elecom.2012.03.014

Conflict of Interest Statement: The authors declare that the research was conducted in the absence of any commercial or financial relationships that could be construed as a potential conflict of interest.

frontiers
in Energy Research

REVIEW
published: 15 July 2016
doi: 10.3389/fenrg.2016.00025

Development of Sulfide Solid Electrolytes and Interface Formation Processes for Bulk-Type All-Solid-State Li and Na Batteries

Akitoshi Hayashi[1]*, *Atsushi Sakuda*[1,2] *and Masahiro Tatsumisago*[1]

[1] *Department of Applied Chemistry, Graduate School of Engineering, Osaka Prefecture University, Sakai, Osaka, Japan,* [2] *Department of Energy and Environment, Research Institute of Electrochemical Energy, National Institute of Advanced Industrial Science and Technology (AIST), Ikeda, Osaka, Japan*

OPEN ACCESS

Edited by:
Shyue Ping Ong,
University of California,
San Diego, USA

Reviewed by:
Liqiang Mai,
Wuhan University of
Technology, China
Xiao-Liang Wang,
Seeo Inc., USA

***Correspondence:**
Akitoshi Hayashi
hayashi@chem.osakafu-u.ac.jp

Specialty section:
This article was submitted
to Energy Storage,
a section of the journal
Frontiers in Energy Research

Received: *01 March 2016*
Accepted: *16 June 2016*
Published: *15 July 2016*

Citation:
Hayashi A, Sakuda A and
Tatsumisago M (2016) Development
of Sulfide Solid Electrolytes and
Interface Formation Processes
for Bulk-Type All-Solid-State
Li and Na Batteries.
Front. Energy Res. 4:25.
doi: 10.3389/fenrg.2016.00025

All-solid-state batteries with inorganic solid electrolytes (SEs) are recognized as an ultimate goal of rechargeable batteries because of their high safety, versatile geometry, and good cycle life. Compared with thin-film batteries, increasing the reversible capacity of bulk-type all-solid-state batteries using electrode active material particles is difficult because contact areas at solid–solid interfaces between the electrode and electrolyte particles are limited. Sulfide SEs have several advantages of high conductivity, wide electrochemical window, and appropriate mechanical properties, such as formability, processability, and elastic modulus. Sulfide electrolyte with $Li_7P_3S_{11}$ crystal has a high Li^+ ion conductivity of 1.7×10^{-2} S cm^{-1} at 25°C. It is far beyond the Li^+ ion conductivity of conventional organic liquid electrolytes. The Na^+ ion conductivity of 7.4×10^{-4} S cm^{-1} is achieved for $Na_{3.06}P_{0.94}Si_{0.06}S_4$ with cubic structure. Moreover, formation of favorable solid–solid interfaces between electrode and electrolyte is important for realizing solid-state batteries. Sulfide electrolytes have better formability than oxide electrolytes. Consequently, a dense electrolyte separator and closely attached interfaces with active material particles are achieved *via* "room-temperature sintering" of sulfides merely by cold pressing without heat treatment. Elastic moduli for sulfide electrolytes are smaller than that of oxide electrolytes, and Na_2S–P_2S_5 glass electrolytes have smaller Young's modulus than Li_2S–P_2S_5 electrolytes. Cross-sectional SEM observations for a positive electrode layer reveal that sulfide electrolyte coating on active material particles increases interface areas even with a minimum volume of electrolyte, indicating that the energy density of bulk-type solid-state batteries is enhanced. Both surface coating of electrode particles and preparation of nanocomposite are effective for increasing the reversible capacity of the batteries. Our approaches to form solid–solid interfaces are demonstrated.

Keywords: all-solid-state battery, lithium battery, sodium battery, sulfide, solid electrolyte, electrode–electrolyte interface

INTRODUCTION

All-solid-state batteries using inorganic solid electrolytes (SEs), used in place of conventional organic liquid electrolytes, have been studied because of their high safety (non-flammability with no liquid leakage), long cycle life, and versatile geometries (Takada, 2013; Tatsumisago et al., 2013; Tatsumisago and Hayashi, 2014). These features are important for large rechargeable lithium batteries with high energy density for application to eco-cars, such as electric vehicles and plug-in hybrid vehicles. Rechargeable sodium batteries are also attractive for large-scale applications for stationary load-leveling because sodium is expected to be the next targeted element after lithium based on its atomic weight, standard potential, and natural abundance (Yabuchi et al., 2015b; Yamada, 2014).

A key material to realize all-solid-state rechargeable batteries is a superior SE. In lithium ion conductors, sulfide electrolytes of $Li_{10}GeP_2S_{12}$ and $Li_7P_3S_{11}$ have high room-temperature conductivity of more than 10^{-2} S cm^{-1}, which is as high as the conductivity of conventional organic liquid electrolytes (Kamaya et al., 2011; Seino et al., 2014). The lithium ion transport number of liquid electrolytes is below 0.5, whereas that of SE is 1. It is noteworthy that the conductivity of lithium ions of sulfide SEs already exceeds that of organic liquid electrolytes. Very recently, $Li_{9.54}Si_{1.74}P_{1.44}S_{11.7}Cl_{0.3}$ has been reported to show the highest conductivity of 2.5×10^{-2} S cm^{-1}. Using this superior electrolyte, high power competing with that of supercapacitors can be achieved in all-solid-state rechargeable lithium batteries (Kato et al., 2016b). Sulfide SEs have several important benefits of high conductivity, wide electrochemical window, and appropriate mechanical properties, such as formability and elastic modulus. A shortcoming of sulfide electrolytes is its low air stability. To realize bulk-type all-solid-state batteries, the formation of favorable solid–solid interfaces between electrode and electrolyte is important in addition to the development of superior sulfide electrolytes. Direct coating of sulfide electrolytes on active material particles instead of adding electrolyte particle is effective for forming a close solid–solid interface with large contact area. Insulative active materials, such as sulfur and Li_2S, should be blended not only with SE but also with carbon-conductive additive to form ion and electron conduction paths to active materials. Nanocomposites of the three components are useful by preparation with high-energy ball milling, which pulverizes and combines them. Transition metal sulfides (MS_x) with high conductivity have good compatibility with sulfide SEs having the same sulfide anions. Especially, sulfur-rich compounds, such as TiS_3, are attractive active materials with high reversible capacity. Lithium metal is a supremely negative electrode, but issues related to lithium dendrites prevent its commercialization. Combination with a SE is a promising solution. Interface modification between Li metal and the SE is important.

As described in this paper, the recent development of sulfide SEs and interface formation processes for bulk-type all-solid-state Li and Na batteries are reviewed. Significant properties as SEs of conductivity, chemical stability, and mechanical property for Li$^+$ or Na$^+$ ion conducting sulfides are reported. Procedures for preparing sulfide electrolytes, such as mechanical milling and liquid-phase synthesis, are also described. Several approaches to form favorable solid–solid interfaces developed by our research group are demonstrated. Processes for the coating of sulfide electrolytes *via* gas-phase or liquid-phase process on $LiCoO_2$ or graphite particles have been developed. Preparation of nanocomposite electrodes with sulfur, Li_2S, and Li_3PS_4 (as a bifunctional material of electrolyte and electrode) particles is described, along with the use of MS_x active materials. Formation of a solid–solid interface for using lithium metal negative electrodes is also discussed.

DEVELOPMENT OF SULFIDE SOLID ELECTROLYTES

Sulfide SEs with Li$^+$ or Na$^+$ ion conductivity have been developed during the past three decades. Recently, chemical stability and mechanical properties as well as conductivity for sulfide electrolytes have attracted much attention. Sulfide electrolytes are prepared using several techniques with solid-phase reaction, melt-quenching, mechanical milling, crystallization of mother glasses, and liquid-phase reaction. Detailed information related to electrolyte properties will be presented in the following sections of this report.

Conductivity

Inorganic sulfide SEs with high Li$^+$ or Na$^+$ ion conductivities have been developed. Sulfide electrolytes with high conductivities are presented in **Table 1**. In Li$^+$ ion conducting sulfide electrolytes, crystalline $Li_{10}GeP_2S_{12}$ (LGPS; Kamaya et al., 2011) and glass–ceramic $Li_7P_3S_{11}$ (Seino et al., 2014) have considerably high conductivity of more than 10^{-2} S cm^{-1} at 25°C, which is beyond the Li$^+$ ion conductivity of conventional organic liquid electrolytes. Very recently, $Li_{9.54}Si_{1.74}P_{1.44}S_{11.7}Cl_{0.3}$ with LGPS structure has been reported to show the highest conductivity of 2.5×10^{-2} S cm^{-1} (Kato et al., 2016b). Studies investigating new electrolytes with much higher conductivity are in progress. Several crystals, such as $Li_{10}SnP_2S_{12}$ (Boron et al., 2013) and Li_6PS_5Cl (Boulineau et al., 2012), have high conductivity of more than 10^{-3} S cm^{-1}. This conductivity is also achieved by the addition of lithium halides to sulfide glass and glass–ceramic electrolytes (Wada et al., 1983; Ujiie et al., 2014).

The Na$^+$ ion conductivity is lower than Li$^+$ ion conductivity in glassy electrolytes. Ionic conduction of Na$^+$ ion with ionic radius larger than Li$^+$ ion is unfavorable in glasses (Souquet et al., 1981). For sodium ion conductors, sulfides with high conductivity had not been found since this report described Na_3PS_4 glass–ceramic electrolytes in 2012. A cubic Na_3PS_4 phase is precipitated by crystallization of a mother Na_3PS_4 glass. The prepared glass–ceramic electrolyte shows Na$^+$ ion conductivity of greater than 10^{-4} S cm^{-1} at 25°C (Hayashi et al., 2012b). Furthermore, partial substitution of Si for P in Na_3PS_4 is useful for increasing conductivity (Tanibata et al., 2014). **Figure 1** presents the composition dependence of conductivities at 25°C for Na_3PS_4–Na_4SiS_4 glass–ceramic electrolytes. The replacement of 6 mol% Na_3PS_4 by Na_4SiS_4 increases the conductivity from 4.6×10^{-4} to 7.4×10^{-4} S cm^{-1}. The electron density distribution of the cubic Na_3PS_4 structure obtained using the maximum entropy method is shown in the inset of **Figure 1**. Na_3PS_4 has three-dimensional

TABLE 1 | Li^+ ion and Na^+ ion conductivities for sulfide solid electrolytes.

Composition	Conductivity at 25°C (S cm^{-1})	Classification	Reference
$Li_{9.54}Si_{1.74}P_{1.44}S_{11.7}Cl_{0.3}$	2.5×10^{-2}	Crystal	(Kato et al. 2016b)
$Li_{10}GeP_2S_{12}$	1.2×10^{-2}	Crystal	Kamaya et al. (2011)
$Li_{10}SnP_2S_{12}$	4×10^{-3}	Crystal	Boron et al. (2013)
$Li_{3.833}Sn_{0.833}As_{0.166}S_4$	1.4×10^{-3}	Crystal	Sahu et al. (2014)
Li_6PS_5Cl	1.3×10^{-3}	Crystal	Boulineau et al. (2012)
$70Li_2S{\cdot}30P_2S_5$ ($Li_7P_3S_{11}$)	1.7×10^{-2}	Glass–ceramic	Seino et al. (2014)
$63Li_2S{\cdot}27P_2S_5{\cdot}10LiBr$	8.4×10^{-3}	Glass–ceramic	Ujiie et al. (2014)
$80Li_2S{\cdot}20P_2S_5$	1.3×10^{-3}	Glass–ceramic	Mizuno et al. (2006)
$30Li_2S{\cdot}26B_2S_3{\cdot}44LiI$	1.7×10^{-3}	Glass	Wada et al. (1983)
$50Li_2S{\cdot}17P_2S_5{\cdot}33LiBH_4$	1.6×10^{-3}	Glass	Yamauchi et al. (2013)
$63Li_2S{\cdot}36SiS_2{\cdot}1Li_3PO_4$	1.5×10^{-3}	Glass	Aotani et al. (1994)
$70Li_2S{\cdot}30P_2S_5$	1.6×10^{-4}	Glass	Zhang and Kennedy (1990)
Na_3PSe_4	1.2×10^{-3}	Crystal	Zhang et al. (2015)
Na_3PS_4 (tetragonal)	1×10^{-6}	Crystal	Jansen and Henseler (1992)
$94Na_3PS_4{\cdot}6Na_4SiS_4$	7.4×10^{-4}	Glass–ceramic	Tanibata et al. (2014)
Na_3PS_4 (cubic)	2×10^{-4}	Glass–ceramic	Hayashi et al., (2012b)
$60Na_2S{\cdot}40GeS_2$	7.3×10^{-6}	Glass	Souquet et al. (1981)

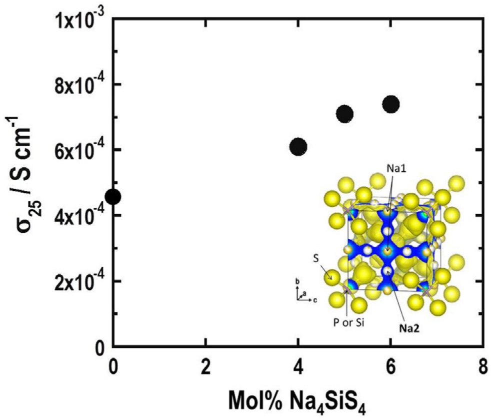

FIGURE 1 | Composition dependence of conductivity at 25°C for (100-*x*)$Na_3PS_4{\cdot}xNa_4SiS_4$ (mol%) glass–ceramic electrolytes. The inset shows the electron density distribution of the cubic Na_3PS_4 structure.

Na^+ ion conduction paths along Na1 and Na2 sites. Increased Na^+ ion concentration is presumed as the reason for the enhancement of conductivity. Very recently, high conductivity of more than 10^{-3} S cm^{-1} has been reported in crystalline Na_3PSe_4 (Zhang et al., 2015). However, studies of new sulfide Na^+ ion conductors are few. A first-principles calculation indicates that Sn-doped cubic Na_3PS_4 is predicted to have a higher Na^+ ion conductivity of 10^{-2} S cm^{-1} (Zhu et al., 2015). Synthesis of SEs with a favorable structure for Na^+ ion conduction based on calculation results is important for finding new Na^+ ion conducting SEs.

Chemical Stability

A shortcoming of sulfide electrolytes is their lower chemical stability in air atmosphere. Sulfides tend to be decomposed by hydrolysis, generating harmful H_2S. Suppression of hydrolysis of sulfides is an important task for developing sulfide electrolytes. Based on our early experiments, the selection of compositions in sulfide electrolytes gives moderate stability in air to sulfide electrolytes (Muramatsu et al., 2011). The chemical stability of sulfide glass electrolytes in the binary system $Li_2S–P_2S_5$ was examined by exposing them to air atmosphere. Amounts of generated H_2S from the sulfides depend on the composition of the glasses; H_2S generation is minimized at the composition $75Li_2S{\cdot}25P_2S_5$ (mol%). The glass comprises Li^+ and PS_4^{3-} ions. An isolated anion PS_4^{3-} without bridging sulfurs is useful for high tolerance for hydrolysis. Li_3PS_4-based SEs with both good chemical stability and high conductivity have been prepared by the combination of oxides (Li_2O or P_2O_5) and iodides (LiI) (Ohtomo et al., 2013a,b). The addition of metal oxides, such as ZnO, which act as an absorbent for H_2S, is also effective for decreasing H_2S (Hayashi et al., 2013). It is noteworthy that the use of a favorable M_xO_y (M_xO_y: Fe_2O_3, ZnO, and Bi_2O_3) with a larger negative Gibbs energy change (ΔG) for the reaction with H_2S is effective for improving the chemical stability of sulfide electrolytes. Another approach is the use of sulfide compositions based on the hard and soft acids and bases theory (HSAB; Sahu et al., 2014). Lithium tin thiophosphate, Li_4SnS_4, has better air stability than that of Li_3PS_4. Actually, as-substituted Li_4SnS_4 has good features of both high conductivity of 10^{-3} S cm^{-1} and high air stability.

The chemical stability of SEs tends to affect battery performance. The electrochemical performance of all-solid-state C/$LiCoO_2$ cells using Li_3PS_4 glass or $Li_7P_3S_{11}$ glass–ceramic as a SE is compared. The cell with Li_3PS_4 glass electrolytes exhibits better cycle performance, although Li_3PS_4 glass has lower conductivity than $Li_7P_3S_{11}$ electrolyte (Ohtomo et al., 2013c). High performance of the battery would be based on the higher chemical stability of Li_3PS_4 electrolytes. Chemical stability as well as conductivity is an important factor of SEs for developing superior solid-state batteries.

Mechanical Property

Adhesion of the solid–solid interface is a key to the utilization of electrode active materials in all-solid-state batteries. Formability or processability of SEs is examined by the molding pressure dependence of the relative density of compressed powder pellets.

Figure 2A shows the dependence of the relative density of $75Li_2S{\cdot}25P_2S_5$ and $75Na_2S{\cdot}25P_2S_5$ (mol%) glass electrolytes on molding pressure. The relative densities increase gradually with an increase in molding pressure in both glasses at the same alkali compositions of 75 mol% M_2S (M = Li or Na), whereas the relative density for the Na_2S system is higher than that for the Li_2S

system (Sakuda et al., 2013a,b; Nose et al., 2015). Cross-sectional SEM images of the 75 mol% M_2S pellets pressed at 360 MPa are shown in the inset. Grain boundaries and voids in the pellets are more decreased in the $75Na_2S\cdot 25P_2S_5$ glass compared with the $75Li_2S\cdot 25P_2S_5$ glass. Sulfide glasses are densified by cold pressing without heat treatment, and this densification phenomenon is called "room-temperature pressure sintering" (Sakuda et al., 2013a,b). It is noteworthy that the $75Na_2S\cdot 25P_2S_5$ glass has better formability than the $75Li_2S\cdot 25P_2S_5$ glass. Both the glasses comprise Li^+ or Na^+ ion and PS_4^{3-} ion, which are thought to diffuse at the particle boundaries on pressing at room temperature. Na^+ ion with a larger ionic radius than Li^+ ion has a weaker interaction with PS_4^{3-} ion. Therefore, both Na^+ and PS_4^{3-} ions would diffuse readily by cold press, leading to better densification.

Retaining solid–solid contacts between active materials and SEs during charge–discharge processes brings about long cycle lives of all-solid-state batteries. Young's moduli of SEs are important for keeping favorable contacts even at volume changes of active materials. Those for densified sulfide electrolytes prepared by hot-pressing are determined by an ultrasonic pulse-echo technique and the uniaxial compression tests (Sakuda et al., 2013a,b; Nose et al., 2015). Young's moduli of the sulfide glasses in the systems Li_2S–P_2S_5 and Na_2S–P_2S_5 are presented in **Figure 2B**. They are increased gradually with the increase in the alkali content in both systems. The Na_2S–P_2S_5 glasses have smaller Young's moduli of 15–19 GPa than the Li_2S–P_2S_5 glasses (18–25 GPa). The difference on Young's modulus is understood based on the Coulomb force and the mean atomic volume of the glasses. These sulfide glasses have an intermediate Young's modulus between oxide glasses and organic polymers. Sulfide electrolytes deforming elastically are expected to act as a buffer in response to volume changes of active materials during charge–discharge processes. In fact, most all-solid-state batteries that use sulfide SEs exhibit good cycle performance.

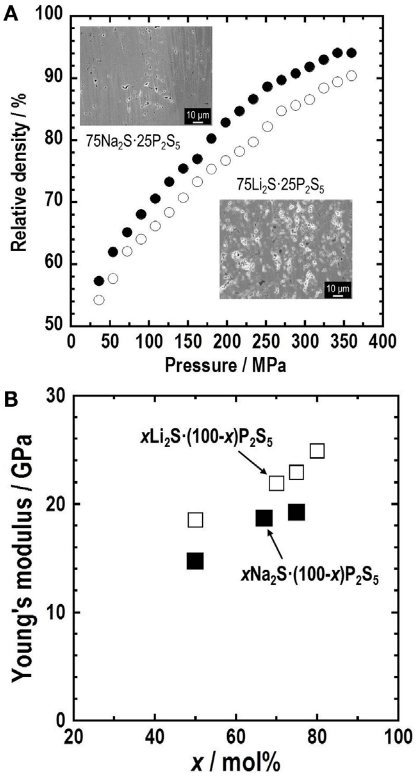

FIGURE 2 | **(A)** Molding pressure dependence of relative density of $75M_2S\cdot 25P_2S_5$ (M = Li or Na, mol%) glass electrolyte. Cross-sectional SEM images of these glass pellets prepared by pressing at 360 MPa are also shown in the inset. **(B)** Composition dependence of Young's modulus for the $xM_2S\cdot(100\text{-}x)P_2S_5$ glasses.

Preparation Process

Sulfide SEs were prepared *via* various techniques. Crystalline electrolytes are prepared *via* solid-phase reaction, whereas glass electrolytes are obtained using the melt-quenching method. In general, sulfide starting materials are sealed in a carbon-coated quartz tube under vacuum and then heat-treated because of high vapor pressure of sulfides at high temperatures. Heating temperatures and cooling rates at preparation process affect precipitated crystals. A phase diagram in ternary system Li_2S–GeS_2–P_2S_5 is complicated (Hori et al., 2015), and crystalline $Li_{10}GeP_2S_{12}$ with a conductivity of 10^{-2} S cm^{-1} is prepared by selecting experimental conditions. Another preparation technique of sulfide electrolytes is mechanical milling using a high-energy planetary ball mill apparatus. This technique is fundamentally a room-temperature process. Therefore, sulfides are reacted at ordinary temperature and pressure. Electrolyte particles are obtained directly by milling. They are applicable to all-solid-state batteries without additional pulverization of electrolytes. Crystallization of glass electrolyte tends to precipitate a metastable phase, such as high-temperature phase, which generally has high ionic conductivity (Tatsumisago et al., 1991; Hayashi et al., 2003). Crystalline $Li_7P_3S_{11}$ (a high-temperature phase at the composition) is precipitated as a primary phase by heat treatment of a corresponding mother glass, and the obtained glass–ceramic electrolytes show conductivities of 10^{-3}–10^{-2} S cm^{-1}, which depend on the degree of crystallinity and the grain boundary of $Li_7P_3S_{11}$ (Mizuno et al., 2005, 2006; Seino et al., 2014). Cubic Na_3PS_4 is crystallized from the Na_3PS_4 glass prepared by mechanical milling. The prepared glass–ceramic electrolytes with Na_3PS_4 show Na^+ ion conductivity of 10^{-4} S cm^{-1} at 25°C (Hayashi et al., 2012b).

Electrolyte preparation *via* liquid phase is a suitable process for cost-effective quantity synthesis without using a special reaction apparatus. In general, this process has benefits of lowering the reaction temperature, shortening the reaction time, and controlling the particle morphology and size. Prepared electrolyte solutions are also useful for the coating of active material particles. Very recently, liquid-phase synthesis of sulfide SEs has been reported. The reaction processes for sulfides are divided into two categories: one uses suspension and the other uses a homogeneous solution. For the former synthesis, β-Li_3PS_4 synthesized in tetrahydrofuran (Liu et al., 2013) or dimethyl carbonate (Phuc et al., 2016) as reaction medium and $Li_7P_3S_{11}$ synthesized in 1,2-dimethoxyethane (Ito et al., 2014) are reported. In these reactions, precursors with precipitates are obtained. Compressed pellets of the heat-treated sulfide electrolytes show conductivity of greater than 10^{-4} S cm^{-1} at 25°C. As the latter one *via* homogeneous liquid, Li_3PS_4 is synthesized from a mixture of Li_2S and P_2S_5 with *N*-methlyformamide (NMF) (Teragawa et al., 2014a). The Li_3PS_4 SEs can also be prepared using a dissolution–reprecipitation process in NMF from $80Li_2S{\cdot}20P_2S_5$ (mol%) glass prepared in advance using mechanical milling (Teragawa et al., 2014b). The prepared Li_3PS_4 electrolyte shows low conductivity of 10^{-6} S cm^{-1} at the present stage, but conductivity can be enhanced by selecting electrolyte compositions. Argyrodide-type Li_6PS_5Cl is dissolved into ethanol. Then, the argyrodite phase is reprecipitated by removing ethanol at 80°C under vacuum for 3 h (Yubuchi et al., 2015a,b). A pellet of the product shows conductivity of 10^{-5} S cm^{-1} at 25°C, which is somewhat lower than that of the original Li_6PS_5Cl. Grain boundary resistance, which is affected by surface structure and morphology, might be greater in the prepared Li_6PS_5Cl. Optimization of posttreatments for the prepared powders will enhance the Li_6PS_5Cl conductivity. Furthermore, the combination of sulfide SEs and ionic liquids produces pseudo-SEs (Minami et al., 2010; Oh et al., 2015). The prepared electrolytes give a new category of electrolytes having both high conductivity and good formability.

Sodium-ion conducting sulfide electrolytes with cubic Na_3PS_4 are also synthesized *via* a liquid-phase process from the mixture of Na_2S and P_2S_5 in NMF solvent (Yubuchi et al., 2015a). The room-temperature conductivity of the obtained electrolyte is 10^{-6} S cm^{-1}, which is lower than the conductivity of the electrolyte prepared by mechanical milling. Studies investigating sulfide SEs with Na^+ ion conductivity are extremely few at present. New electrolytes produced *via* a simple liquid-phase process will be researched widely.

PREPARATION OF SOLID–SOLID INTERFACE IN ALL-SOLID-STATE BATTERIES

Sulfide glasses are well-balanced SEs with high conductivity, good formability, appropriate Young's modulus, and moderate chemical stability. They are therefore highly promising SEs for use in all-solid-state batteries. A schematic diagram of bulk-type all-solid-state batteries is depicted in **Figure 3**. A positive electrode layer is composed not only of active material particles but also of SE ones. The Li^+ ion is supplied from SEs attached to active materials. Electrons are mobile through active materials. To enhance the rate of performance of the batteries, conductive additives of nanocarbons are added to the electrode layer. A lithium alloy or lithium metal is used as the negative electrode. A SE layer as a separator is sandwiched with the positive and negative electrode layers. Then, because of good formability of sulfide SEs, it can be pressed uniaxially at room temperature to fabricate bulk-type all-solid-state batteries.

An all-solid-state In/$LiCoO_2$ or Li-In/$Li_4Ti_5O_{12}$ cell with Li_2S–P_2S_5 glass–ceramic electrolytes exhibits good cycle performance for hundreds of times at 25°C (Tatsumisago and Hayashi, 2008; Tatsumisago et al., 2013). These cells operate at a high temperature of 100°C, where it is difficult for a liquid electrolyte cell to be used. The all-solid-state cell with $Li_4Ti_5O_{12}$ shows a discharge–charge capacity of about 140 mAh g^{-1}. It retains the capacity for 700 cycles with no degradation under a high current density of more than 10 mA cm^{-2} (Minami et al., 2011).

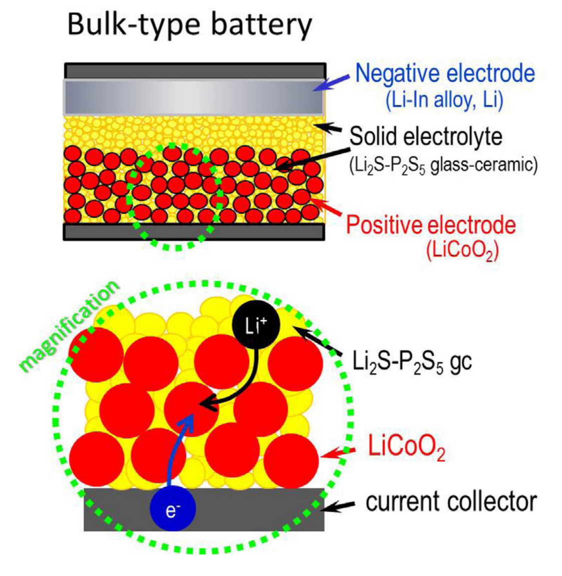

FIGURE 3 | **Schematic diagram of bulk-type all-solid-state batteries.**

Coating of Sulfide Electrolytes on $LiCoO_2$ and Graphite Particles

Direct coating of sulfide SEs on $LiCoO_2$ particles, instead of mixing electrolyte particles, is effective for forming good electrolyte–$LiCoO_2$ interfaces with a wide contact area. Pulsed laser deposition (PLD) was first used as a coating technique (Sakuda et al., 2010, 2011). In this study, $LiNbO_3$-coated $LiCoO_2$ particles were fluidized with a vibrator to ensure uniform coating of sulfide electrolytes on the particles.

Figure 4 presents cross-sectional SEM images of positive electrodes with (a) a conventional mixture of $LiCoO_2$ and Li_2S–P_2S_5 SE particles with the weight ratio of 70/30 and (b) SE-coated $LiCoO_2$ particles, where the weight ratio of $LiCoO_2$ and SE coatings was 90/10. **Figure 2A** shows that solid–solid contacts between $LiCoO_2$ and SE are formed by cold pressing of the mixture electrode because SE particles are deformed easily by pressing. **Figure 4A** shows that the aggregation of $LiCoO_2$ particles engenders less utilization of $LiCoO_2$ because many voids and less contact with SE are observed among $LiCoO_2$ particles. A close-packed electrode layer is formed using only SE-coated $LiCoO_2$ (**Figure 4B**). Its enlarged figure, which will be displayed in **Figure 7D** later, shows that a close solid–solid interface with fewer voids appears, and Li^+ ion conduction paths are therefore formed among $LiCoO_2$ particles. It is noteworthy that SE amounts in the electrode are decreased considerably by SE coating on $LiCoO_2$ particles. The use of minimum amounts of SE in an electrode layer contributes to enhanced energy density of all-solid-state batteries.

A cross-sectional high-angle annular dark field (HAADF)-STEM image and EDX mappings of O, P, S, Co, and Nb elements for the SE-coated $LiCoO_2$ electrodes are presented in **Figure 5**. A SE coating layer is observed between two $LiCoO_2$ particles,

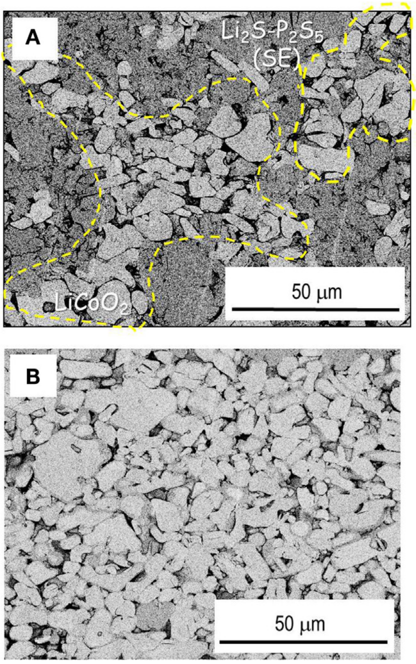

FIGURE 4 | Cross-sectional SEM images of $LiCoO_2$ positive electrode layers consisting of (A) mixture electrode with $LiCoO_2$ and Li_2S–P_2S_5 electrolyte particles and (B) electrolyte-coated $LiCoO_2$ particles.

where one particle has several cracks. The EDX mapping of Nb element reveals that a $LiNbO_3$ coating layer exists on the surface of $LiCoO_2$, but the layer is missing at the cracks. The EDX mappings of P and S elements indicate that SE penetrates into the cracks as a liquid electrolyte does. Favorable formability of sulfide SE is effective for forming good contacts with the surface of active materials and using active materials even at newly formed crystal faces with cracks.

Solid electrolyte coatings were also done for graphite particles using PLD. The mixture of SE-coated graphite and SE particles was used as a negative electrode. The weight ratio of graphite and SE was 90/10. All-solid-state cells with Li_2S–P_2S_5 SE as a separator layer were charged and discharged at a constant current density of 0.064 mA cm^{-2} (*ca.* 0.05 C) for voltages of 2.8–4.3 or 4.6 V at room temperature (Sakuda et al., 2013b). **Figure 6** shows charge–discharge curves for all-solid-state SE-coated graphite/SE-coated $LiCoO_2$ batteries. The battery with a cutoff voltage of 4.6 V at the charge process shows a higher discharge capacity than that of 4.3 V. Battery has a discharge capacity of 133 mAh g^{-1}, as calculated from the total mass of the composite positive electrode.

Figure 7 shows cross-sectional SEM images of SE-coated $LiCoO_2$ positive electrodes; **Figure 7A** as-prepared, **Figure 7B** after the initial charge-discharge (cutoff voltage: 4.3 V), and **Figure 7C** after the initial charge–discharge (cutoff voltage: 4.6 V). **Figures 7D–F**, respectively, portray enlarged images of **Figures 7A–C**. Closely attached SE–$LiCoO_2$ interfaces with large contact area are achieved by PLD coating, as shown in **Figures 7A,D**. The electrode morphology (**Figure 7B**) does not change greatly after the initial charge–discharge process at the cutoff of 4.3 V. SE coatings still attach on the $LiCoO_2$ particles (**Figure 7E**), and empty spaces among particles observed in panel (**Figure 7B**) are similar to those observed in the as-prepared electrode (**Figure 7A**). **Figure 7C** shows that voids among $LiCoO_2$ particles increase after the charge–discharge process at a higher cutoff voltage of 4.6 V. A $LiCoO_2$ particle charged to 4.6 V suffers from deterioration. Many cracks are formed in the particle, as shown in the magnified image of panel (**Figure 7F**). This morphological change is attributable to (1) reduction of mechanical strength and (2) excess strain at the solid–solid interfaces among $LiCoO_2$ particles during their large volume expansion and/or phase transition.

Figure 8 shows cross-sectional SEM images of SE-coated graphite negative electrodes; **Figure 8A** as-prepared and **Figure 8B** after the initial charge–discharge (cutoff voltage: 4.3 V). Graphite particles are close-packed in a negative electrode layer. SE coatings are observed around graphite particles. They form Li^+ ion conduction paths through the electrode layer. After the initial charge–discharge, no obvious void is observed in the negative electrode. The close-packed electrode is present. Good solid–solid interfaces are also retained between the graphite layer and an electrolyte separator layer.

As described in Section "Preparation Process," liquid-phase synthesis of sulfide electrolytes is also useful for forming favorable electrode–electrolyte solid–solid interfaces, which can be achieved by removing solvents from electrolyte solutions. An all-solid-state cell using $LiCoO_2$ coated with Li_3PS_4 electrolyte *via* an NMF solution operates as rechargeable batteries without the addition of SE and carbon-conductive additive particles to the positive electrodes (Teragawa et al., 2014a,b). However, the cell capacities are lower than those of the cells using $LiCoO_2$ coated with Li_3PS_4 electrolytes by PLD, because the electrolytes synthesized *via* the liquid-phase has lower ionic conductivities than those prepared by PLD. The $LiCoO_2$ particles coated with Li_6PS_5Cl electrolytes *via* ethanol solution with a higher conductivity than Li_3PS_4 were therefore applied to all-solid-state cells. The weight ratio of $LiCoO_2$/SE layer was 92.5/7.5 in SE-coated $LiCoO_2$ particles. An all-solid-state cell using the electrolyte-coated $LiCoO_2$ shows an initial discharge capacity of 45mAh g^{-1}, which is greater than that of cells using Li_3PS_4-coated $LiCoO_2$ (Yubuchi et al., 2015b). SE coating *via* electrolyte liquids is a simple and cost-effective process. Increasing conductivity of SE at lower temperatures is necessary to improve battery performance.

Sulfur-Based Nanocomposite Positive Electrodes

Sulfur is a fascinating positive electrode with high energy density because it is an abundant resource with high theoretical capacity of 1672 mAh g^{-1} and environmental friendliness. Lithium polysulfides (Li_2S_x), which are formed during discharge (lithiation process), are readily dissolved in organic liquid electrolytes, leading to lack of a sulfur positive electrode. Dissolution of lithium polysulfides is suppressed by absorbing sulfurs in nanocarbon pores. This approach has been studied extensively (Ji and Nazar, 2010). The use of inorganic SEs fundamentally resolves the problem.

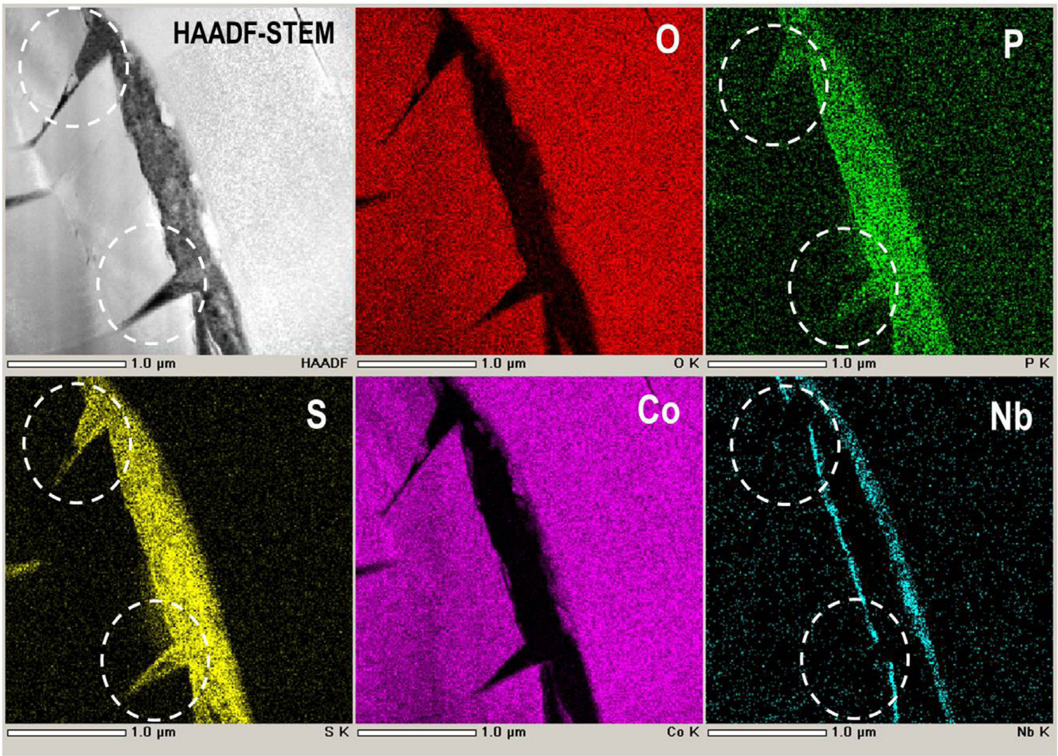

FIGURE 5 | **Cross-sectional high-angle annular dark field (HAADF)-TEM image and EDX mappings of O, P, S, Co, and Nb elements for the SE-coated $LiCoO_2$ electrodes**.

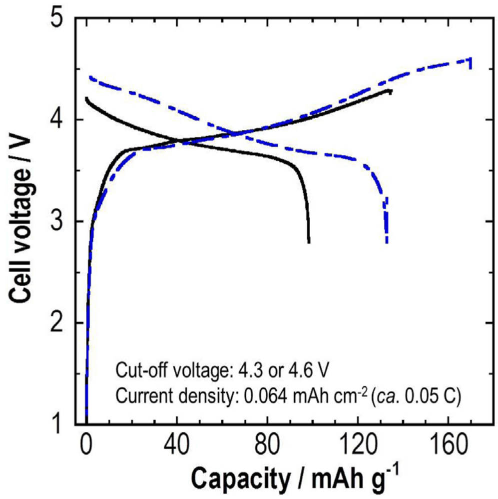

FIGURE 6 | **Initial charge–discharge curves for an all-solid-state SE-coated graphite/SE-coated $LiCoO_2$ battery**.

Composite sulfur electrodes consisting of S, acetylene black (AB), and $Li_2S–P_2S_5$ SE powders with a weight ratio of 25/25/50 were prepared using high-energy planetary ball milling to produce favorable contacts among the three components (Nagao et al., 2011). The Li-In/S cell exhibits a large reversible capacity of greater than 1500 mAh g^{-1} of sulfur with average potential of ca. 2.1 V (vs. Li^+/Li). The cell with sulfur electrode shows 15 times higher capacity than the cell with $LiCoO_2$, although the operating potential of the former cell is almost half that of the latter cell.

Application of Li_2S as a discharge product of sulfur active material offers the important benefits of high theoretical capacity of 1167 mAh g^{-1} and versatility of negative electrode materials without lithium sources. Because of the insulative nature of Li_2S, composite electrodes, Li_2S mixed with conductive additives, such as nanocarbons and SEs, should be prepared for the use of Li_2S as an active material. Composite Li_2S electrodes were prepared by mechanical milling. A typical weight ratio of Li_2S/AB/$Li_2S–P_2S_5$ SE is 25/25/50. The prepared composite gives broad peaks attributable to Li_2S in X-ray diffraction patterns. An all-solid-state cell of In/Li_2S composites is charged and then discharged at 25°C. The initial reversible capacity is 800 mAh g^{-1} at the current density of 0.064 mA cm^{-2} (Nagao et al., 2012b). The cell retained 750 mAh g^{-1} for 10 cycles. Charge–discharge reaction mechanisms were examined using high-resolution TEM observation (Nagao et al., 2015). **Figure 9** shows TEM images for the Li_2S electrodes; **Figure 9A** before charge–discharge test, **Figure 9B** after the initial charge, and **Figure 9C** after the initial discharge. **Figure 9A** shows that nanoparticles of *ca.* 5 nm in size with different crystal orientations are distributed randomly in the matrix consisting of amorphous SE and AB. Those nanoparticles are attributable to crystalline Li_2S. **Figure 9B** shows that no lattice fringes because of the crystalline Li_2S are apparent, and

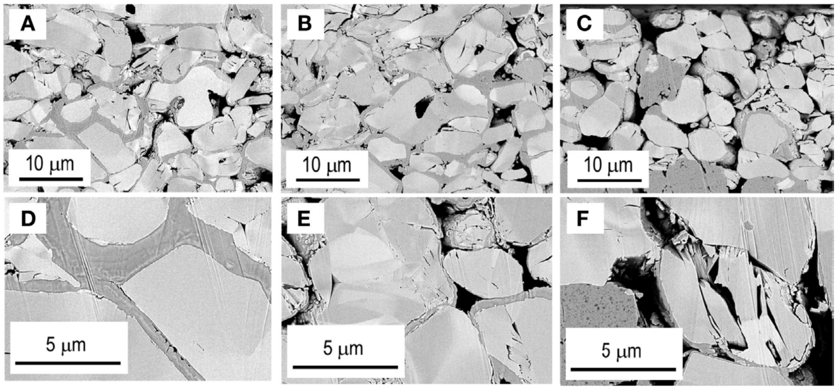

FIGURE 7 | Cross-sectional SEM images of SE-coated $LiCoO_2$ positive electrodes (A) as-prepared, (B) after the initial charge–discharge (cutoff voltage: 4.3 V), and (C) after the initial charge–discharge (cutoff voltage: 4.6 V). Images of **(D–F)**, respectively, depict enlarged images of **(A–C)**.

there exists the characteristic contrast attributable to amorphous structure in the whole region after the initial charge process. As shown in **Figure 9C**, lattice fringes with spacing of about 3.9 Å are clearly apparent after the initial discharge, suggesting that amorphous sulfur is converted into crystalline nanoparticles during discharge reaction. Reversible transformation between crystallization and amorphization of sulfur-based active nanoparticles is responsible for the high capacity and its retention.

The utilization of Li_2S is ca. 50% in the composite electrode. To increase the utilization of Li_2S, one strategy is the fundamental enhancement of ionic conductivity in Li_2S. A partial substitution of more polarizable iodide anion with larger ionic radii for sulfide anion in Li_2S is expected to increase conductivity by introducing lithium vacancies and by increasing the lattice constant. Solid solutions in the system Li_2S-LiI are therefore prepared using mechanical milling (Hakari et al., 2015a). Only the XRD peaks attributable to Li_2S are observed; LiI peaks disappear completely in the composition range of $0 < \text{LiI (mol\%)} < 20$. **Figure 10A** presents the composition dependence of lattice constant and conductivity at 25°C for the prepared Li_2S-LiI materials. The lattice constant increases monotonically with increased LiI content, suggesting that Li_2S-based solid solutions are prepared using a mechanical milling process. Conductivity is also enhanced by increasing the LiI content. The solid solution with 20 mol% LiI has conductivity of 2.2×10^{-6} S cm^{-1}, which is two orders of magnitude higher than that for Li_2S itself without the addition of LiI. A composite positive electrode with the $80Li_2S\cdot20LiI$ (mol%) solid solution, vapor-grown carbon fiber (VGCF), and Li_3PS_4 glass electrolyte with a weight ratio of 50/10/40 is applied to all-solid-state cells. **Figure 10B** shows that an all-solid-state cell (Li-In/Li_3PS_4/$80Li_2S\cdot20LiI$) is charged and discharged at a current density of 0.13 mA cm^{-2} (0.07 C) at 25°C. The cell shows a reversible capacity of 930 mAh g^{-1} for 50 cycles. The capacity corresponds to 80% utilization of Li_2S. It is noteworthy that the enhancement of conductivity of Li_2S is effective for increasing the utilization of the active material. This strategy is beneficial for the development of all-solid-state cells with a higher energy density.

A SE Li_3PS_4 is ball-milled with nanocarbon, such as AB. The prepared Li_3PS_4–AB materials as a mixed conductor are useful as positive electrode acting not only as a SE but also as an active material. An all-solid-state cell with the Li_3PS_4–AB composite positive electrode is charged and discharged. Its operation voltage of ca. 2.6 V vs. Li^+/Li is somewhat higher than that of Li_2S (Hakari et al., 2015b). Redox-active electrolytes, such as $CuCl_2$-dissolved solution in porous carbons, are also reported to apply to supercapacitors (Mai et al., 2013). The use of the SEs as an active material in electrode layers is effective at increasing the reversible capacity per gram of the total mass of positive electrodes.

Transition Metal Sulfide Positive Electrodes

Typical MS_x, such as TiS_2, are used as active materials in all-solid-state Li and Na batteries with sulfide SEs. Decreasing the particle size of MS_x and forming a wide contact area with both SEs and conductive additives are important for increasing the MS_x utilization.

Monodispersed MS_x nanoparticles are prepared using a so-called "hot-soap" technique using high-boiling point solvents as a reaction medium. Particle morphology and size can be controlled by choosing the reaction conditions and combinations of coordinating or non-coordinating solvents. NiS particles of 50 nm size were prepared using thermal decomposition of nickel acetylacetonate in a mixed solution of 1-dodecanethiol as a sulfur source and 1-octadecene as a non-coordinating solvent at 280°C for 5 h (Aso et al., 2011). The NiS nanoparticles are crystallized directly on a carbon fiber (VGCF) by adding VGCF to a liquid medium. Good adhesion between NiS and carbon is achieved (Aso et al., 2012). Sulfide electrolyte coating on NiS–VGCF was produced using the PLD method. All-solid-state cells with the prepared NiS composite electrode operate as a secondary battery at 25°C, suggesting that electron and Li^+ ion conduction paths are formed in the composite electrodes (Aso et al., 2013).

To increase the positive electrode capacity, sulfur-rich MS_x are desired. For example, titanium trisulfide TiS_3 shows a higher capacity than that of TiS_2, because additional sulfurs in TiS_3 contribute to the redox reaction that occurs during charge–discharge processes (Hayashi et al., 2012a). Amorphous NbS_x ($x = 3, 4, 5$)

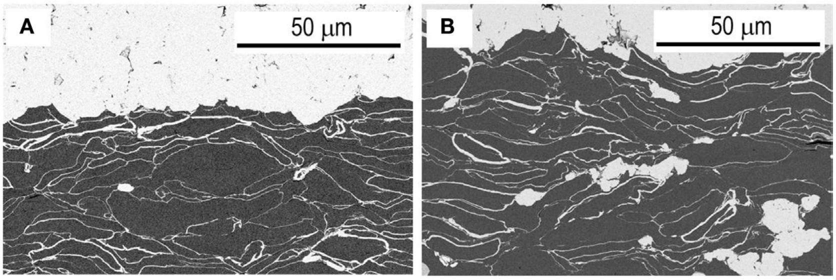

FIGURE 8 | **Cross-sectional SEM images of SE-coated graphite negative electrodes (A) as-prepared and (B) after the initial charge–discharge (cutoff voltage: 4.3 V)**.

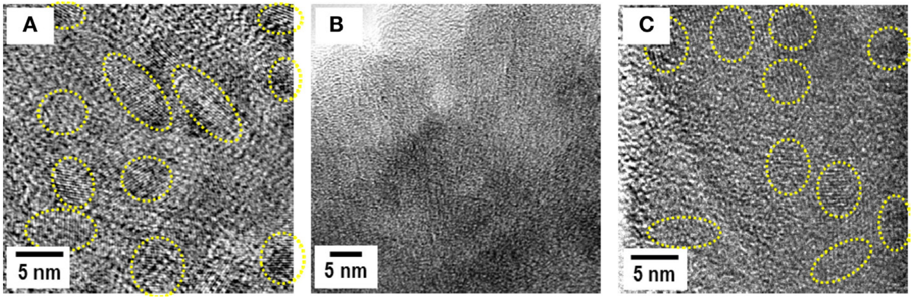

FIGURE 9 | **TEM images for the Li_2S electrodes (A) before charge–discharge test, (B) after the initial charge, and (C) after the initial discharge**.

are prepared mechanochemically. Electrochemical cells with an organic liquid electrolyte using the amorphous NbS_x ($x = 3, 4, 5$) show higher discharge capacities with an increase in the sulfur content of NbS_x (Sakuda et al., 2014). Amorphous TiS_3 (a-TiS_3) retains a higher capacity than crystalline TiS_3 in all-solid-state lithium cells. The crystal structure of TiS_3 is partially deteriorated at the initial cycle, leading to an irreversible capacity in the cell with crystalline TiS_3 (Matsuyama et al., 2016a,b). It is noteworthy that sulfur-rich amorphous MS_x with electrical conductivity are promising for use as positive electrodes instead of sulfur active materials.

Figure 11A shows the first and tenth charge–discharge curves of all-solid-state lithium cell Li-In/a-TiS_3 at 0.013 mA cm^{-2} at 25°C. The right side ordinate axis represents the electrode potential vs. Li^+/Li, as calculated based on the potential difference between the Li-In and Li electrode (0.62 V). The cell with a-TiS_3 positive electrode including no carbon-conductive additives and SEs shows a reversible capacity for 10 cycles of about 510 mAh g^{-1} of a-TiS_3, which equals the weight of the total positive electrode. The capacity corresponds to storage of about 3M Li to a-TiS_3. Electronic structural analyses using S2p XPS and S K-edge XANES reveal that a reversible sulfur redox in a-TiS_3 appears mainly during charge–discharge processes and contributes to its good capacity retention (Matsuyama et al., 2016a,b).

Amorphous TiS_3 is also applicable to all-solid-state sodium batteries. An all-solid-state sodium cell using a-TiS_3 shows capacity higher than 300 mAh g^{-1} at the first discharge process, as presented in **Figure 11B** (Tanibata et al., 2015a). The composite positive electrode consisting of a-TiS_3 and the cubic Na_3PS_4 electrolyte with a weight ratio of 40/60 is used. $Na_{15}Sn_4$ alloy and the cubic Na_3PS_4 electrolyte are used, respectively, as a negative electrode and a separator layer. The cell capacity decreases gradually during discharge–charge cycles. SEM–EDX analysis reveals that the a-TiS_3 particles aggregate after the cycles, and that resistance in the a-TiS_3 composite electrode increases during cycles. To secure electron conduction paths to a-TiS_3, 6 wt% AB is added to the positive electrode. Good capacity retention is achieved in the cell using a-TiS_3 electrode with AB. The added AB particles might prevent the shutoff of electron conduction paths in the composite electrode and give a buffer space for the volume change of a-TiS_3 particles for preserving adhesion among the particles. The addition of AB to the $Na_{15}Sn_4$ electrode also suppresses cell resistance after charge–discharge. In addition, the replacement of Na_3PS_4 glass–ceramic by $94Na_3PS_4 \cdot 6Na_4SiS_4$ (mol%) glass–ceramic with higher conductivity decreases cell resistance and increases the rate performance of all-solid-state cells (Tanibata et al., 2015b). Reversible capacity in all-solid-state Na cells is less than that in all-solid-state Li cells, as shown in **Figures 11A,B**. The lower conductivity of SEs and loss of particle contacts because of the larger volume change are responsible for a smaller capacity for the Na cells. Approaches that are used to prepare composite positive electrodes suitable for insertion/de-insertion of Na^+ ion with larger ionic radius must be developed to improve battery performance in all-solid-state Na batteries.

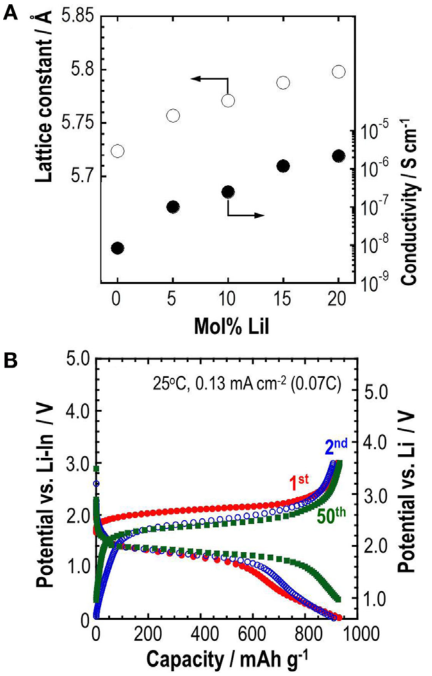

FIGURE 10 | (A) Composition dependence of lattice constant and conductivity at 25°C for prepared Li_2S-LiI solid solutions and **(B)** charge–discharge curves of an all-solid-state cell (Li-In/Li_3PS_4/$80Li_2S{\cdot}20LiI$).

Interface Modification for Li Metal Negative Electrode

To achieve high energy density of all-solid-state Li batteries, the final goal is the use of lithium metal as a negative electrode. Lithium metal is an ultimate negative electrode because of a large theoretical capacity of 3861 mAh g^{-1} and the lowest electrochemical potential of −3.04 V vs. SHE. However, a possibility of fatal problems emerged by short-circuit with dendrite formation prevent the practical use of Li metal negative electrode in lithium cells with conventional liquid and polymer electrolytes. Combination with inorganic SEs is expected to resolve the problem. In fact, thin-film solid-state batteries with Li negative electrode have excellent cycle life without capacity fading (Bates et al., 1993). The rate of utilization of Li electrodes is not high in thin-film batteries because positive electrodes such as $LiCoO_2$ have lithium sources, which are mainly used for a charge–discharge process.

Compared with thin-film batteries fabricated by gas-phase deposition, insufficient Li–SE interfaces in bulk-type all-solid-state batteries prepared by cold pressing are important issues that must be resolved. It has been revealed by *in situ* SEM observation that lithium is deposited through grain boundaries and voids in the SE (Nagao et al., 2013). Insertion of a Li-alloy thin layer at the interface between the Li electrode and SE layers brought about stable Li dissolution and deposition in the all-solid-state Li metal cells (Hiratani et al., 1988; Okita et al., 2011; Nagao et al., 2012a). These interface modifications are effective at establishing homogeneous interfaces between the Li metal and SEs.

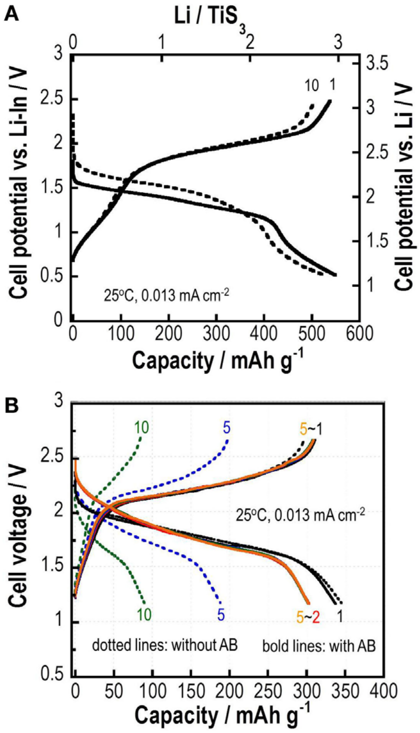

FIGURE 11 | (A) Charge–discharge curves of all-solid-state lithium cell Li-In/amorphous TiS_3 and **(B)** charge–discharge curves of all-solid-state sodium cell $Na_{15}Sn_4$/amorphous TiS_3 with or without AB.

Intensive utilization of Li is important for achieving high energy density of all-solid-state lithium metal batteries. Insertion of a Au thin film at the Li–SE interface is effective for increasing Li utilization (Kato et al., 2016a). Li and Au thin films were formed on a pelletized Li_3PS_4 glass electrolyte by vacuum evaporation. Galvanostatic cycling tests for the Li/Li_3PS_4/Li cell are presented in **Figure 12A**. At the initial cycle, the utilization of Li metal is about 40%, which is a higher rate of utilization of Li metal for thin-film batteries (about 20%). However, utilization of Li metal for the cell decreases rapidly after five cycles. The Li thin-film morphology is rough after galvanostatic cycling tests, as shown in the SEM image (**Figure 12C**), indicating that inhomogeneous Li dissolution–deposition reactions occur. The cell Li/Au/Li_3PS_4/Au/Li has about 35% Li utilization at the initial cycle and retains about 25% after the fifth cycle, as presented in **Figure 12B**. The morphology of Li metal after Li dissolution–deposition reaction became more uniform, as shown in the SEM image of panel (**Figure 12D**), compared with the cell without Au thin films. The insertion of Au film to a Li–SE interface is a first step for improving the cyclability of Li deposition–dissolution reactions with high Li utilization in all-solid-state lithium metal batteries. Intensive studies are in progress.

CONCLUDING REMARKS

We have reviewed recent developments related to sulfide SEs and interface formation processes for all-solid-state rechargeable batteries. The conductivity of sulfide Li^+ ion conductors, such as

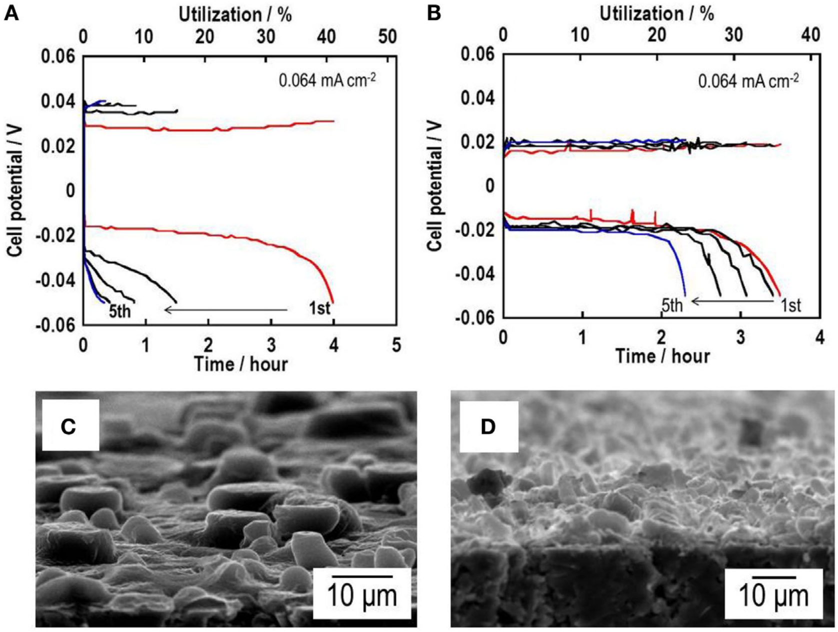

FIGURE 12 | Galvanostatic cycling tests for (A) a Li symmetric Li/Li_3PS_4/Li cell and (B) a Li/Au/Li_3PS_4/Au/Li cell. SEM images of the surface of **(C)** a Li/Li_3PS_4/Li cell and **(D)** a Li/Au/Li_3PS_4/Au/Li cell after galvanostatic cycling tests.

$Li_{10}GeP_2S_{12}$, $Li_7P_3S_{11}$, and $Li_{9.54}Si_{1.74}P_{1.44}S_{11.7}Cl_{0.3}$, has already reached 10^{-2} S cm^{-1} at room temperature. Conductivities of sulfide Na^+ ion conductors are lower than those of Li^+ ion conductors at the present stage. The highest conductivity of 10^{-3} S cm^{-1} was obtained for Na_3PSe_4. Sulfide glass electrolytes with high alkali content were prepared by high-energy ball milling process. Metastable phases, such as $Li_7P_3S_{11}$ and cubic Na_3PS_4, with high conductivity were formed by careful crystallization of the prepared glasses. Sulfide electrolytes can be synthesized *via* liquid-phase processing, which is useful for coating application. Sulfide glass electrolytes have favorable formability, and Young's modulus for forming good electrode–electrolyte interfaces achieving rapid charge transfer in bulk-type all-solid-state batteries. Chemical stability in air is a great shortcoming of using a sulfide electrolyte. The composition of Li_3PS_4 has superior chemical stability in the Li_2S–P_2S_5 binary system. The higher chemical stability is achieved by partial substitution of oxygen for sulfur. Selecting composition and designing structure for sulfide electrolytes is expected to improve conductivity, mechanical properties, and chemical stability further. As Na^+ ion conductors, higher conductivity of more than 10^{-2} S cm^{-1} is predicted for Sn-substituted cubic Na_3PS_4, but the conductivity has not been achieved experimentally. Further studies seeking new electrolytes and suitable preparation processes must be undertaken.

Coating of SE and preparation of nanocomposites are useful for forming favorable solid–solid interface in an electrode layer for bulk-type all-solid-state batteries. Coating of sulfide electrolytes on $LiCoO_2$ or graphite particles using gas-phase or liquid-phase techniques is effective for increasing solid–solid contact area using extremely small amounts of electrolytes. Preparation of nanocomposites using high-energy ball milling is useful for sulfur or Li_2S active materials with an insulative nature. Conductivity enhancement of Li_2S by combination with LiI contributes to the improvement of Li_2S utilization. Amorphous MS_x, such as amorphous TiS_3, are attractive as mixed conductors with large capacity in all-solid-state batteries. Interface modification for Li metal negative electrode with Au thin film improves the cycle performance of Li dissolution–deposition while maintaining a high rate of utilization. For further improvement of electrochemical performance of the batteries, facile approaches achieving favorable electrode–electrolyte interfaces with large contact area will be developed. Controlling the size, morphology, and dispersibility of both electrolyte and electrode particles and selecting suitable electrolytes for maintaining close solid–solid contacts during charge–discharge processes will be assessed in future studies.

AUTHOR CONTRIBUTIONS

AH contributed to the preparation of the manuscript. AS and MT contributed to the discussions about research results.

ACKNOWLEDGMENTS

This research is supported by a Grant-in-Aid for Scientific Research from the Ministry of Education, Culture, Sports, Science and Technology (MEXT) of Japan. In particular, the research about all-solid-state Li batteries was financially supported by the Japan Science and Technology Agency (JST), Advanced Low Carbon Technology Research and Development Program (ALCA), Specially Promoted Research for Innovative Next Generation Batteries (SPRING) Project, while the research about all-solid-state Na batteries was supported by the MEXT program "Elements Strategy Initiative for Catalysts and Batteries (ESICB)."

REFERENCES

Aotani, N., Iwamoto, K., Takada, K., and Kondo, S. (1994). Synthesis and electrochemical properties of lithium ion conductive glass, Li_3PO4-Li_2S-SiS_2. *Solid State Ionics.* 68, 35–39. doi:10.1016/0167-2738(94)90232-1

Aso, K., Hayashi, A., and Tatsumisago, M. (2012). Synthesis of NiS-carbon fiber composites in high-boiling solvent to improve electrochemical performance in all-solid-state lithium secondary batteries. *Electrochim. Acta* 83, 448–453. doi:10.1016/j.electacta.2012.07.088

Aso, K., Kitaura, H., Hayashi, A., and Tatsumisago, M. (2011). Synthesis of nanosized nickel sulfide in high-boiling solvent for all-solid-state lithium secondary batteries. *J. Mater. Chem.* 21, 2987–2990. doi:10.1039/c0jm02639e

Aso, K., Sakuda, A., Hayashi, A., and Tatsumisago, M. (2013). All-solid-state lithium secondary batteries using NiS-carbon fiber composite electrodes coated with Li_2S-P_2S_5 solid electrolytes by pulsed laser deposition. *ACS Appl. Mater. Interfaces* 5, 686–690. doi:10.1021/am302164e

Bates, J., Dudney, N., Gruzalski, G., Zuhr, R., Choudhury, A., and Luck, C. (1993). Fabrication and characterization of amorphous lithium electrolyte thin films and rechargeable thin-film batteries. *J. Power Sources* 4, 103–110. doi:10.1016/0378-7753(93)80106-Y

Boron, P., Johansson, S., Zick, K., Gunne, J., Dehnen, S., and Roling, B. (2013). $Li_{10}SnP_2S_{12}$: an affordable lithium superionic conductor. *J. Am. Chem. Soc.* 135, 15694–15697. doi:10.1021/ja407393y

Boulineau, S., Courty, M., Tarascon, J. M., and Viallet, V. (2012). Mechanochemical synthesis of Li-argyrodite Li_6PS_5X (X=Cl, Br, I) as sulfur-based solid electrolytes for all solid state batteries application. *Solid State Ionics.* 221, 1–5. doi:10.1016/j.ssi.2012.06.008

Hakari, T., Hayashi, A., and Tatsumisago, M. (2015a). Highly utilized lithium sulfide active material by enhancing conductivity in all-solid-state batteries. *Chem. Lett.* 44, 1664–1666. doi:10.1246/cl.150758

Hakari, T., Nagao, M., Hayashi, A., and Tatsumisago, M. (2015b). All-solid-state lithium batteries with Li_3PS_4 glass as active material. *J. Power Sources* 293, 721–725. doi:10.1016/j.jpowsour.2015.05.073

Hayashi, A., Hama, S., Minami, T., and Tatsumisago, M. (2003). Formation of superionic crystals from mechanically milled Li_2S-P_2S_5 glasses. *Electrochem. Commun.* 5, 111–114. doi:10.1016/S1388-2481(02)00555-6

Hayashi, A., Matsuyama, T., Sakuda, A., and Tatsumisago, M. (2012a). Amorphous titanium sulfide electrode for all-solid-state rechargeable lithium batteries with high capacity. *Chem. Lett.* 41, 886–888. doi:10.1246/cl.2012.886

Hayashi, A., Noi, K., Sakuda, A., and Tatsumisago, M. (2012b). Superionic glass-ceramic electrolytes for room-temperature rechargeable sodium batteries. *Nat. Commun.* 3, 1–5. doi:10.1038/ncomms1843

Hayashi, A., Muramatsu, H., Ohtomo, T., Hama, S., and Tatsumisago, M. (2013). Improvement of chemical stability of Li_3PS_4 glass electrolytes by adding M_xO_y (M=Fe, Zn, and Bi) nanoparticles. *J. Mater. Chem. A* 1, 6320–6326. doi:10.1039/c3ta10247e

Hiratani, M., Miyauchi, K., and Kudo, T. (1988). Effect of a lithium alloy layer inserted between a lithium anode and a solid electrolyte. *Solid State Ionics.* 2, 1406–1410. doi:10.1016/0167-2738(88)90394-3

Hori, S., Kato, M., Suzuki, K., Hirayama, M., Kato, Y., and Kanno, R. (2015). Phase diagram of the Li_4GeS_4-Li_3PS_4 quasi-binary system containing the superionic conductor $Li_{10}GeP_2S_{12}$. *J. Am. Ceram. Soc.* 98, 3352–3360. doi:10.1111/jace.13694

Ito, S., Nakakita, M., Aihara, Y., Uehara, T., and Machida, N. (2014). A synthesis of crystalline $Li_7P_3S_{11}$ solid electrolyte from 1, 2-dimethoxyethane solvent. *J. Power Sources* 271, 342–345. doi:10.1016/j.jpowsour.2014.08.024

Jansen, M., and Henseler, U. (1992). Synthesis, structure determination, and ionic conductivity of sodium tetrathiophosphate. *J. Solid State Chem.* 99, 110–119. doi:10.1016/0022-4596(92)90295-7

Ji, X., and Nazar, L. (2010). Advances in Li-S batteries. *J. Mater. Chem.* 20, 9821–9826. doi:10.1039/b925751a

Kamaya, N., Homma, K., Yamakawa, Y., Hirayama, M., Kanno, R., Yonemura, M., et al. (2011). A lithium superionic conductor. *Nat. Mater* 10, 682–686. doi:10.1038/nmat3066

Kato, A., Hayashi, A., and Tatsumisago, M. (2016a). Enhancing utilization of lithium metal electrodes in all-solid-state batteries by interface modification with gold thin films. *J. Power Sources* 309, 27–32. doi:10.1016/j.jpowsour.2016.01.068

Kato, Y., Hori, S., Saito, T., Suzuki, K., Hirayama, M., Mitsui, A., et al. (2016b). High-power all-solid-state batteries using sulfide superionic conductors. *Nat. Energy* 1, 16030. doi:10.1038/nenergy.2016.30

Liu, Z., Fu, W., Payzant, E., Yu, X., Wu, Z., Dudney, N., et al. (2013). Anomalous high ionic conductivity of nanoporous β-Li_3PS_4. *J. Am. Chem. Soc.* 135, 975–978. doi:10.1021/ja3110895

Mai, L. Q., Minhas-Khan, A., Tian, X., Hercule, K. M., Zhao, Y. L., Lin, X., et al. (2013). Synergistic interaction between redox-active electrolyte and binder-free functionalized carbon for ultrahigh supercapacitor performance. *Nat. Commun.* 4, 2923. doi:10.1038/ncomms3923

Matsuyama, T., Deguchi, M., Mitsuhara, K., Ohta, T., Mori, T., Orikasa, Y., et al. (2016a). Structure analyses using X-ray photoelectron spectroscopy and X-ray absorption near edge structure for amorphous MS_3 (M: Ti, Mo) electrodes in all-solid-state lithium batteries. *J. Power Sources* 313, 104–111. doi:10.1016/j.jpowsour.2016.02.044

Matsuyama, T., Hayashi, A., Ozaki, T., Mori, S., and Tatsumisago, M. (2016b). Improved electrochemical performance of amorphous TiS_3 electrodes compared to its crystal for all-solid-state rechargeable lithium batteries. *J. Ceram. Soc. Jpn.* 124, 242–246. doi:10.2109/jcersj2.15299

Minami, K., Hayashi, A., and Tatsumisago, M. (2010). Characterization of solid electrolytes prepared from Li_2S-P_2S_5 glass and ionic liquids. *J. Electrochem. Soc.* 157, A1296–A1301. doi:10.1149/1.3489352

Minami, K., Hayashi, A., Ujiie, S., and Tatsumisago, M. (2011). Electrical and electrochemical properties of glass–ceramic electrolytes in the systems Li_2S-P_2S_5-P_2S_3 and Li_2S-P_2S_5-P_2O_5. *Solid State Ionics.* 192, 122–125. doi:10.1016/j.ssi.2010.06.018

Mizuno, F., Hayashi, A., Tadanaga, K., and Tatsumisago, M. (2005). New, highly ion-conductive crystals precipitated from Li_2S-P_2S_5 glasses. *Adv. Mater.* 17, 918–921. doi:10.1002/adma.200401286

Mizuno, F., Hayashi, A., Tadanaga, K., and Tatsumisago, M. (2006). High lithium ion conducting glass-ceramics in the system Li_2S-P_2S_5. *Solid State Ionics.* 177, 2721–2725. doi:10.1016/j.ssi.2006.04.017

Muramatsu, H., Hayashi, A., Ohtomo, T., Hama, S., and Tatsumisago, M. (2011). Structural change of Li_2S-P_2S_5 sulfide solid electrolytes in the atmosphere. *Solid State Ionics.* 182, 116–119. doi:10.1016/j.ssi.2010.10.013

Nagao, M., Hayashi, A., and Tatsumisago, M. (2011). Sulfur-carbon composite electrode for all-solid-state Li/S battery with Li_2S-P_2S_5 solid electrolyte. *Electrochim. Acta* 56, 6055–6059. doi:10.1016/j.electacta.2011.04.084

Nagao, M., Hayashi, A., and Tatsumisago, M. (2012a). Bulk-type lithium metal secondary battery with indium thin layer at interface between Li electrode and Li_2S-P_2S_5 solid electrolyte. *Electrochem.* 80, 734–736. doi:10.5796/electrochemistry.80.734

Nagao, M., Hayashi, A., and Tatsumisago, M. (2012b). High-capacity Li_2S-nanocarbon composite electrode for all-solid-state rechargeable lithium batteries. *J. Mater. Chem* 22, 10015–10020. doi:10.1039/c2jm16802b

Nagao, M., Hayashi, A., Tatsumisago, M., Ichinose, T., Ozaki, T., Togawa, Y., et al. (2015). Li_2S nanocomposites underlying high-capacity and cycling stability in all-solid-state lithium-sulfur batteries. *J. Power Sources* 274, 471–476. doi:10.1016/j.jpowsour.2014.10.043

Nagao, M., Hayashi, A., Tatsumisago, M., Kanetsuku, T., Tsuda, T., and Kuwabata, S. (2013). In situ SEM study of a lithium deposition and dissolution mechanism in a bulk-type solid-state cell with a Li_2S-P_2S_5 solid electrolyte. *Phys. Chem. Chem. Phys.* 15, 18600–18606. doi:10.1039/c3cp51059j

Nose, M., Kato, A., Sakuda, A., Hayashi, A., and Tatsumisago, M. (2015). Evaluation of mechanical properties of Na_2S-P_2S_5 sulfide glass electrolytes. *J. Mater. Chem. A* 3, 22061–22065. doi:10.1039/C5TA05590C

Oh, D. Y., Nam, Y. J., Park, K. H., Jung, S. H., Cho, S. J., Kim, Y. K., et al. (2015). Excellent compatibility of solvate ionic liquids with sulfide solid electrolytes: toward favorable ionic contacts in bulk-type all-solid-state lithium-ion batteries. *Adv. Energy Mater.* 5, 1500865. doi:10.1002/aenm.201570120

Ohtomo, T., Hayashi, A., Tatsumisago, M., and Kawamoto, K. (2013a). Glass electrolytes with high ion conductivity and high chemical stability in the system LiI-Li_2O-Li_2S-P_2S_5. *Electrochemistry* 81, 428–431. doi:10.5796/electrochemistry.81.428

Ohtomo, T., Hayashi, A., Tatsumisago, M., and Kawamoto, K. (2013b). All-solid-state batteries with Li_2O-Li_2S-P_2S_5 glass electrolytes synthesized by two-step mechanical milling. *J. Solid State Chem.* 17, 2551–2557. doi:10.1007/s10008-013-2149-5

Ohtomo, T., Hayashi, A., Tatsumisago, M., and Kawamoto, K. (2013c). All-solid-state lithium secondary batteries using the $75Li_2S{\cdot}25P_2S_5$ glass and the

$70Li_2S{\cdot}30P_2S_5$ glass-ceramic as solid electrolytes. *J. Power Sources* 233, 231–235. doi:10.1016/j.jpowsour.2013.01.090

Okita, K., Ikeda, K., Sano, H., Iriyama, Y., and Sakaebe, H. (2011). Stabilizing lithium plating-stripping reaction between a lithium phosphorus oxynitride glass electrolyte and copper thin film by platinum insertion. *J. Power Sources* 196, 2135–2142. doi:10.1016/j.jpowsour.2010.10.014

Phuc, N., Morikawa, K., Totani, M., Muto, H., and Matsuda, A. (2016). Chemical synthesis of Li_3PS_4 precursor suspension by liquid-phase shaking. *Solid State Ionics.* 285, 2–5. doi:10.1016/j.ssi.2015.11.019

Sahu, G., Lin, Z., Li, J., Liu, Z., Dudney, N., and Liang, C. (2014). Air-stable, high-conduction solid electrolytes of arsenic-substituted Li_4SnS_4. *Energy Environ. Sci.* 7, 1053–1058. doi:10.1039/C3EE43357A

Sakuda, A., Hayashi, A., Ohtomo, T., Hama, S., and Tatsumisago, M. (2010). $LiCoO_2$ electrode particles coated with Li_2S-P_2S_5 solid electrolyte for all-solid-state batteries. *Electrochem. Solid-State Lett.* 13, A73–A75. doi:10.1149/1.3376620

Sakuda, A., Hayashi, A., Ohtomo, T., Hama, S., and Tatsumisago, M. (2011). All-solid-state lithium secondary batteries using $LiCoO_2$ particles with pulsed laser deposition coatings of Li_2S-P_2S_5 solid electrolytes. *J. Power Sources* 196, 6735–6741. doi:10.1016/j.jpowsour.2010.10.103

Sakuda, A., Hayashi, A., Takigawa, Y., Higashi, K., and Tatsumisago, M. (2013a). Evaluation of elastic modulus of Li_2S-P_2S_5 glassy solid electrolyte by ultrasonic sound velocity measurement and compression test. *J. Ceram. Soc. Jpn.* 121, 946–949. doi:10.2109/jcersj2.121.946

Sakuda, A., Hayashi, A., and Tatsumisago, M. (2013b). Sulfide solid electrolyte with favorable mechanical property for all-solid-state lithium battery. *Sci. Rep.* 3, 2261. doi:10.1038/srep02261

Sakuda, A., Taguchi, N., Takeuchi, T., Kobayashi, H., Sakaebe, H., Tatsumi, K., et al. (2014). Amorphous niobium sulfides as novel positive-electrode materials. *ECS Electrochem. Lett.* 3, A79–A81. doi:10.1149/2.0091407eel

Seino, Y., Ota, T., Takada, K., Hayashi, A., and Tatsumisago, M. (2014). A sulphide lithium super ion conductor is superior to liquid ion conductors for use in rechargeable batteries. *Energy Environ. Sci.* 7, 627–631. doi:10.1039/C3EE41655K

Souquet, J. L., Robinel, E., Barrau, B., and Ribes, M. (1981). Glass formation and ionic conduction in the M_2S-GeS_2 (M=Li, Na, Ag) systems. *Solid State Ionics.* 3-4, 317–321. doi:10.1016/0167-2738(81)90105-3

Takada, K. (2013). Progress and prospective of solid-state lithium batteries. *Acta Mater.* 61, 759–770. doi:10.1016/j.actamat.2012.10.034

Tanibata, N., Hayashi, A., and Tatsumisago, M. (2015a). Improvement of rate performance for all-solid-state $Na_{15}Sn_4$/amorphous TiS_3 cells using $94Na_3PS_4{\cdot}6Na_4SiS_4$ glass-ceramic electrolytes. *J. Electrochem. Soc.* 162, A793–A795. doi:10.1149/2.0011506jes

Tanibata, N., Matsuyama, T., Hayashi, A., and Tatsumisago, M. (2015b). Improvement of rate performance for all-solid-state $Na_{15}Sn_4$/amorphous TiS_3 cells using $94Na_3PS_4{\cdot}6Na_4SiS_4$ glass-ceramic electrolytes. *J. Power Sources* 275, 284–287. doi:10.1016/j.jpowsour.2014.10.193

Tanibata, N., Noi, K., Hayashi, A., Kitamura, N., Idemoto, Y., and Tatsumisago, M. (2014). X-ray crystal structure analysis of sodium-ion conductivity in $94Na_3PS_4{\cdot}6Na_4SiS_4$ glass-ceramic electrolytes. *Chem. Electro. Chem.* 1, 1130–1132. doi:10.1002/celc.201402016

Tatsumisago, M., and Hayashi, A. (2008). All-solid-state lithium secondary batteries using sulfide-based glass-ceramic electrolytes. *Funct. Mater. Lett.* 1, 31–36. doi:10.1142/S1793604708000071

Tatsumisago, M., and Hayashi, A. (2014). Sulfide glass-ceramic electrolytes for all-solid-state lithium and sodium batteries. *Int. J. Appl. Glass. Sci.* 5, 226–235. doi:10.1111/ijag.12084

Tatsumisago, M., Nagao, M., and Hayashi, A. (2013). Recent development of sulfide solid electrolytes and interfacial modification for all-solid-state rechargeable lithium batteries. *J. Asian. Ceram. Soc.* 1, 17–25. doi:10.1016/j.jascer.2013.03.005

Tatsumisago, M., Shinkuma, Y., and Minami, T. (1991). Stabilization of superionic α-AgI at room temperature in a glass matrix. *Nature* 354, 217–218. doi:10.1038/354217a0

Teragawa, S., Aso, K., Tadanaga, K., Hayashi, A., and Tatsumisago, M. (2014a). Liquid-phase synthesis of a Li_3PS_4 solid electrolyte using *N*-methylformamide for all-solid-state lithium batteries. *J. Mater. Chem. A* 2, 5095–5099. doi:10.1039/c3ta15090a

Teragawa, S., Aso, K., Tadanaga, K., Hayashi, A., and Tatsumisago, M. (2014b). Preparation of Li_2S-P_2S_5 solid electrolyte from *N*-methylformamide solution and application for all-solid-state lithium battery. *J. Power Sources* 248, 939–942. doi:10.1016/j.jpowsour.2013.09.117

Ujiie, S., Hayashi, A., and Tatsumisago, M. (2014). Preparation and electrochemical characterization of $(100\text{-}x)(0.7Li_2S{\cdot}0.3P_2S_5){\cdot}xLiBr$ glass-ceramic electrolytes. *Mater. Renew. Sustain. Energy* 3, 1–8. doi:10.1007/s40243-013-0018-x

Wada, H., Menetrier, M., Levasseur, A., and Hagenmuller, P. (1983). Preparation and ionic conductivity of new B_2S_3-Li_2S-LiI glasses. *Mater. Res. Bull.* 18, 189–193. doi:10.1016/0025-5408(83)90080-6

Yabuchi, N., Kubota, K., Dahbi, M., and Komaba, S. (2015b). Research development on sodium-ion batteries. *Chem. Rev.* 114, 11636–11682. doi:10.1021/cr500192f

Yamada, A. (2014). Iron-based materials strategies. *MRS Bull.* 39, 423–428. doi:10.1557/mrs.2014.89

Yamauchi, A., Sakuda, A., Hayashi, A., and Tatsumisago, M. (2013). Preparation and ionic conductivities of $(100\text{-}x)(0.75Li_2S{\cdot}0.25P_2S_5){\cdot}xLiBH_4$ glass electrolytes. *J. Power Sources* 244, 707–710. doi:10.1016/j.jpowsour.2012.12.001

Yubuchi, S., Hayashi, A., and Tatsumisago, M. (2015a). Sodium-ion conducting Na_3PS_4 electrolyte synthesized *via* a liquid-phase process using *N*-methylformamide. *Chem. Lett.* 44, 884–886. doi:10.1246/cl.150195

Yubuchi, S., Teragawa, S., Aso, K., Tadanaga, K., Hayashi, A., and Tatsumisago, M. (2015b). Preparation of high lithium-ion conducting Li_6PS_5Cl solid electrolyte from ethanol solution for all-solid-state lithium batteries. *J. Power Sources* 293, 941–945. doi:10.1016/j.jpowsour.2015.05.093

Zhang, L., Yang, K., Mi, J., Lu, L., Zhao, L., Wang, L., et al. (2015). Solid electrolytes: Na_3PSe_4: a novel chalcogenide solid electrolyte with high ionic conductivity. *Adv. Energy Mater* 5, 1501294. doi:10.1002/aenm.201501294

Zhang, Z., and Kennedy, J. H. (1990). Synthesis and characterization of the B_2S_3-Li_2S, the P_2S_5-Li_2S and the B_2S_3-P_2S_5-Li_2S glass systems. *Solid State Ionics.* 38, 217–224. doi:10.1016/0167-2738(90)90424-P

Zhu, Z., Chu, I.-H., Deng, Z., and Ong, S. P. (2015). Role of Na^+ interstitials and dopauts in enhancing the Na^+ conductivity of the cubic Na_3PS_4 superionic conductor. *Chem. Mater.* 27, 8318–8325. doi:10.1021/acs.chemmater.5b03656

Conflict of Interest Statement: The authors declare that the research was conducted in the absence of any commercial or financial relationships that could be construed as a potential conflict of interest.

frontiers in Energy Research

MINI REVIEW
published: 08 June 2016
doi: 10.3389/fenrg.2016.00023

Novel Solid Electrolytes for Li-Ion Batteries: A Perspective from Electron Microscopy Studies

*Cheng Ma and Miaofang Chi**

Oak Ridge National Laboratory, Center for Nanophase Materials Sciences, Oak Ridge, TN, USA

Solid electrolytes can simultaneously overcome two of the most formidable challenges of Li-ion batteries: the severe safety issues and insufficient energy densities. However, before they can be implemented in actual batteries, the ionic conductivity needs to be improved and the interface with electrodes must be optimized. The prerequisite for addressing these issues is a thorough understanding of the material's behavior at the microscopic and/or the atomic level. (Scanning) transmission electron microscopy is a powerful tool for this purpose, as it can reach an ultrahigh spatial resolution. Here, we review recent electron microscopy investigations on the ion transport behavior in solid electrolytes and their interfaces. Specifically, three aspects will be highlighted: the influence of grain interior atomic configuration on ionic conductivity, the contribution of grain boundaries, and the behavior of solid electrolyte/electrode interfaces. Based on this, the perspectives for future research will be discussed.

Keywords: lithium battery, solid electrolyte, electron microscopy, atomic resolution analysis, interface

Edited by:
Shyue Ping Ong,
University of California San Diego,
USA

Reviewed by:
Paulina Półrolniczak,
Institute of Non-Ferrous Metals
Division in Poznań Central Laboratory
of Batteries and Cells, Poland
Yan E. Wang,
MIT, USA

****Correspondence:***
Miaofang Chi
chim@ornl.gov

Specialty section:
This article was submitted
to Energy Storage,
a section of the journal
Frontiers in Energy Research

Received: *01 March 2016*
Accepted: *22 May 2016*
Published: *08 June 2016*

Citation:
Ma C and Chi M (2016) Novel Solid
Electrolytes for Li-Ion Batteries:
A Perspective from Electron
Microscopy Studies.
Front. Energy Res. 4:23.
doi: 10.3389/fenrg.2016.00023

INTRODUCTION

With the exhaustion of fossil fuels, high-performance energy storage devices have received significant attention in recent years (Quartarone and Mustarelli, 2011; Bruce et al., 2012). While the Li-ion battery (LIB) is a very promising alternative power source, the safety concerns and insufficient energy density have hindered its implementation in heavy-duty applications, e.g., electric vehicles and grid energy storage (Quartarone and Mustarelli, 2011; Bruce et al., 2012). Fortunately, these issues can be addressed by integrating novel solid electrolytes (Quartarone and Mustarelli, 2011; Takada, 2013; Wang et al., 2015). On the one hand, these solid materials are typically non-flammable and impossible to leak, which circumvents the safety issues associated with conventional organic liquid electrolytes. This is a prerequisite for large-scale application. On the other hand, the energy density can also be effectively improved. The much larger electrochemical window allows for the use of advanced electrode materials that are incompatible with conventional liquid electrolytes. In addition, by eliminating the need for bulky safety mechanisms, the battery size can be greatly reduced. Because of these advantages, solid electrolytes have received tremendous interest in recent years.

However, two grand challenges must be overcome before solid electrolytes can be used in commercial batteries. First, their ionic conductivity is typically low, preventing a fast charge and discharge (Takada, 2013; Wang et al., 2015). Second, forming a stable conductive interface between the solid electrolyte and electrode is difficult (Zhu et al., 2015 & 2016; Richards et al., 2016). Overcoming the first challenge requires a mechanistic understanding of the interplay between Li migration and the atomic framework of the material. For the second challenge, the correlation between interface structure/chemistry and ionic transport must first be systematically established. Clearly, both tasks demand structural and chemical analysis with an ultrahigh spatial resolution.

Transmission electron microscopy (TEM), most notably aberration-corrected scanning transmission electron microscopy (STEM), is an ideal tool for gaining critical atomic level insight. It is not only capable of directly visualizing the atomic configurations but can also elucidate chemical information at a sub-angstrom spatial resolution using electron energy loss spectroscopy (EELS) and energy-dispersive X-ray spectroscopy (EDS) (Pennycook, 1992; Muller et al., 2008; Chi et al., 2011; Yabuuchi et al., 2011; Wu et al., 2015). However, STEM investigations of solid electrolytes pose numerous challenges as the high Li mobility and poor electronic conductivity make these materials highly vulnerable to electron irradiation damage (Egerton et al., 2004). Fortunately, with the significantly improved capabilities for imaging and TEM specimen preparation, this issue has been greatly alleviated in recent years. Several beam-sensitive materials that could not be studied previously can now be analyzed at the atomic scale (Ma et al., 2015), and many of these studies have made significant contributions toward the research on solid electrolytes.

The present mini-review will highlight electron microscopy investigations for three important factors governing the behavior of solid electrolytes: (1) influence of grain interior atomic configuration on ionic conductivity, (2) impacts of grain boundaries, and (3) behavior of solid electrolyte–electrode interfaces. Based on this, opportunities, challenges, and perspectives for future research will be discussed.

INFLUENCE OF GRAIN INTERIOR ATOMIC CONFIGURATION ON IONIC CONDUCTIVITY

Li migration within the crystalline lattice is dictated by the atomic framework, which forms channels for Li transport. A precise understanding of the atomic structure is required to explain ionic transport within the lattice. With its ultrahigh spatial resolution and sensitivity to subtle differences in diffraction, (S)TEM not only complements X-ray and neutron scattering studies but also provides unique insights at the atomic level. Recent microscopy studies mainly focused on two systems: $Li_7La_3Zr_2O_{12}$ (LLZO) and $Li_{3x}La_{2/3-x}TiO_3$ (LLTO).

$Li_7La_3Zr_2O_{12}$ is currently the most promising oxide solid electrolyte due to the coexistence of an excellent stability against Li metal and a relatively high conductivity (Murugan et al., 2007; Cussen, 2010). It crystallizes in the garnet structure with two polymorphs (Cussen, 2010): a cubic phase with a relatively high conductivity (c-LLZO) and a less conductive tetragonal phase (t-LLZO). Distinguishing these two phases is critical to properly interpret the ionic transport behavior. The precession electron diffraction (PED) study by Buschmann et al. (2011) successfully differentiated these two phases by circumventing the influence from double diffraction. This result further confirmed that Al-doping is critical for stabilizing the cubic phase. When combined with neutron diffraction, it was found that the Li sites in c-LLZO, unlike those in t-LLZO, are partially filled. The high concentration of vacancies in c-LLZO gives rise to a higher Li mobility and superior conductivity. Besides the PED study, Buschmann et al. also tried to perform high-resolution TEM (HRTEM), but detailed analysis was prevented by the electron beam-irradiation damage. Recently, this issue was successfully alleviated by Ma et al. (2015). The careful selection of imaging and specimen preparation conditions enabled a high-quality, atomic resolution (S)TEM/EELS analysis (**Figures 1A,B**). Ma's research demonstrated that c-LLZO maintains its cubic crystal structure even in an aqueous environment with a pH >7. Such a high structural stability indicates that c-LLZO offers a robust atomic framework for Li transport. Given the high ionic conductivity, Li compatibility, and desirable structural stability against aqueous solutions with a broad range of pH values, LLZO is a promising candidate for the separator in novel aqueous Li batteries.

Another system that has been extensively interrogated by electron microscopy is LLTO, which has a perovskite-type structure (Stramare et al., 2003). By varying the composition and/or processing conditions, multiple polymorphs with different ionic conductivity may be obtained. Regardless, most of them exhibit an alternate stacking between La-rich and La-poor A-site layers, and Li migration is favored by the La-poor layers. The highest bulk conductivity is 10^{-3} S cm^{-1}, approaching that of conventional liquid electrolytes (10^{-2} S cm^{-1}) (Takada, 2013). Therefore, an in-depth understanding of the origin for such exceptional performances is crucial for designing highly conductive solid electrolytes. The (S)TEM studies made important contributions toward this cause. Taking advantage of the sensitivity of annular-bright-field (ABF) STEM imaging to light elements such as Li, Gao et al. (2013) directly visualized the variation of Li positions in different LLTO polymorphs. Li was observed to reside at the O4 window for the Li-poor composition $La_{0.62}Li_{0.16}TiO_3$, but near the A-site position for the Li-rich composition $La_{0.56}Li_{0.33}TiO_3$. The Li content, valence state of cations, and geometry of the oxygen octahedra in the La-rich and La-poor layers were also revealed by EELS. Furthermore, domain structures associated with the ordering between La-rich and La-poor layers were examined (Gao et al., 2014). With La blocking the Li pathways, the domain boundaries were found to impede ionic transport. Beyond this, structural features that cannot be easily detected by diffraction methods may also be visualized. As mentioned above, the Li transport within LLTO relies on the La-poor layers. However, none of the previous diffraction studies detected such crucial features in the most conductive polymorph, the 1350°C-quenched $La_{0.56}Li_{0.33}TiO_3$ (Stramare et al., 2003). As a result, its ionic transport mechanism remained unclear for years. Recently, an atomic resolution STEM study directly visualized the previously overlooked short-range-ordered Li pathways in this material (Ma et al., 2016). The coherence length of the ordering was found to be at the mesoscopic scale (below 10 nm), which prevented it from being detected by most diffraction methods. In combination with molecular dynamics (MD) simulations, this observation indicated that such an elusive mesoscopic framework can most effectively maximize the number of Li transport pathways, leading to a high conductivity. The discovery not only reconciled the long-existing structure–property inconsistency but also pointed out a new angle on improving ionic conductivity.

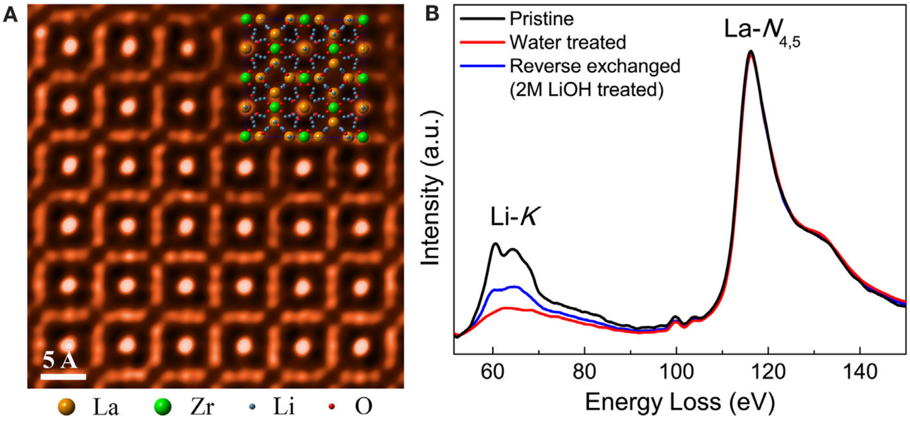

FIGURE 1 | **(A)** The atomic structure of the electron beam-sensitive solid electrolyte LLZO successfully visualized by high-angle annular dark-field (HAADF) STEM imaging. **(B)** EELS data of LLZO after the Li^+/H^+ exchange with different aqueous solutions. The Li content can be precisely monitored. Reproduced with permission from (Ma et al., 2015).

Although atomic resolution (S)TEM greatly benefited the fundamental understanding of ionic transport, current studies are limited to oxides. In comparison, sulfide solid electrolytes, regardless of their higher conductivity (Takada, 2013), are rarely investigated. Microscopy studies on these materials are extremely challenging because of (1) the vulnerability of weak Li–S bonds to electrons and (2) their sensitivity to ambient atmosphere. If these issues can be mitigated, (S)TEM will play an even more critical role in the research of solid electrolytes.

IMPACTS OF GRAIN BOUNDARIES

Although the research on solid electrolytes primarily focuses on the grain interior, grain boundaries are frequently the actual bottleneck. While the bulk conductivity of many solid electrolytes is already comparable to those of conventional liquid electrolytes, their large grain boundary resistance typically lowers the total conductivity by orders of magnitude (Takada, 2013). Due to the absence of a proper understanding on the grain boundary Li conduction mechanism, a targeted optimization is not yet possible.

Grain boundaries in solids are often confined to a very small length scale with widths of only a few unit cells. Therefore, STEM, with its sub-angstrom resolution, appears to be an ideal tool to study them. Ma et al. (2014) successfully utilized atomic resolution STEM/EELS to unravel the atomic-scale origin of the large grain boundary resistance in LLTO. Most grain boundaries were observed to show darker *Z*-contrast than the adjacent grains, suggesting that the average atomic number at the grain boundary is lower. Further atomic-scale analysis showed that the grain boundary atomic configuration significantly deviated from that of the grain interior (**Figures 2A,B**). Instead of the ABO_3 perovskite structure, such reconstructed grain boundaries are essentially a binary Ti–O layer, forbidding the abundance of the charge carrier Li^+. Therefore, they act as internal barriers for Li transport. This topic has also been investigated by HRTEM and EDS. In addition, Gellert et al. (2012) studied the grain boundaries in lithium aluminum titanium phosphate (LATP). Depending on the relative orientation between the neighboring grains, two types of grain boundaries were observed. If the orientations are similar, a thick crystalline grain boundary will be present. Its high degree of crystallinity was believed to allow for a relatively facile ionic transport. If the orientations differ greatly, a thinner but amorphous layer forms, which was believed to be highly resistive.

Unlike the two materials discussed above, LLZO exhibits a grain boundary resistance comparable to that of the grain interior (Murugan et al., 2007). However, the origin of this benign behavior remains unknown. Several research groups have attempted to study LLZO grain boundaries using electron microscopy, but the results are inconsistent. Kumazaki et al. (2011) observed amorphous Li–Al–Si–O and nanocrystalline $LiAlSiO_4$ at the LLZO grain boundaries. In contrast, clean grain boundaries, which are free of any second phase or compositional variations, were reported by Wolfenstine et al. (2012). Systematic investigations with higher spatial resolution are necessary to reach a conclusive explanation.

These studies demonstrate that the grain boundaries, despite their highly localized nature, can be effectively investigated using (S)TEM combined with local analytical methods, such as EELS and EDS. However, current efforts in this area are very limited. Before a systematic understanding and a rational optimization of Li transport at grain boundaries can be realized, further in-depth investigations are needed.

BEHAVIOR OF ELECTROLYTE–ELECTRODE INTERFACES

The stable and conductive electrode/electrolyte interface is a prerequisite for the long-term operation of solid electrolyte-based batteries (Zhu et al., 2015 & 2016; Richards et al., 2016). Nevertheless, due to the absence of a mechanistic understanding to guide the rational improvement, it is still very difficult to form such interfaces. As the first step toward this goal, a direct experimental observation of the interfaces is essential.

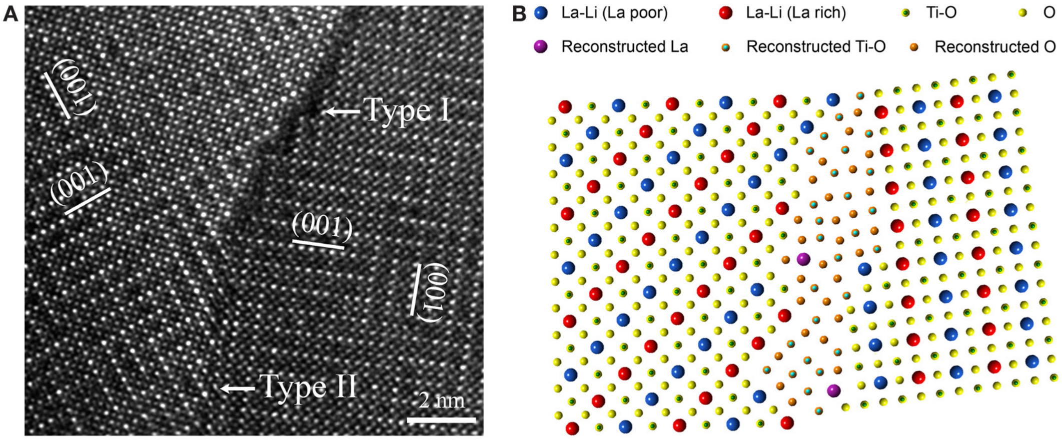

FIGURE 2 | **(A)** Atomic resolution HAADF-STEM image of a grain boundary in LLTO. **(B)** Atomic model of the Li-deficient LLTO grain boundary based on a comprehensive STEM/EELS study. Reproduced with permission from (Ma et al., 2014).

Although no atomic resolution electron microscopy studies have been reported to date, interfaces between cathode materials and several solid electrolytes have been examined *via* nano-electron diffraction (NED), STEM, and EDS. Kim et al. (2011) investigated the interfacial stability between LLZO and $LiCoO_2$ (LCO). An LCO thin film was grown on the polished surface of the LLZO ceramic through pulsed laser deposition at 937 K. TEM observations revealed the existence of an interface reaction layer of ~50 nm thick. EDS line profile measurements and NED acquired in the vicinity of the interface suggested that this reaction layer consisted of La_2CoO_4, which is believed to hinder Li diffusion. In addition, the interface between LCO and $Li_2S–P_2S_5$, a prototypical sulfide electrolyte, was studied by Sakuda et al. (2009). The interface was simply formed by mechanical grinding. After charging, an interfacial layer associated with the mutual diffusion of Co, P, and S emerged, and this layer gave rise to a large resistance. A similar behavior was observed between $LiMn_2O_4$ and $Li_2S–P_2S_5$ (Kitaura et al., 2010). An interfacial layer resulting from the diffusion of Mn into the solid electrolyte was observed and believed to yield large resistance. These electron microscopy studies suggest that a reaction layer may frequently form between the solid electrolyte and cathode due to inter-diffusion. Unlike the solid electrolyte interface (SEI) in conventional LIBs, reaction layers at solid electrolyte/electrode interfaces are usually detrimental rather than beneficial, as they typically impede the ionic transport (Qian et al., 2015).

Beyond these experimentally observed reaction layers, highly localized interfacial decomposition at the solid electrolyte and electrode interfaces was frequently speculated, although they show a certain degree of stability in electrochemical measurements (Zhu et al., 2015 & 2016; Richards et al., 2016). However, most of such speculations are proposed based on theoretical calculations. The experimental verification is quite challenging due to the extremely small length scale of the speculated thickness and the high volatility/instability of Li metal (Wenzel et al., 2015, 2016). (S)TEM, which can probe local features at an extremely high spatial resolution down to sub-angstrom level, presents excellent opportunities to interrogate these intriguing interfacial behaviors.

SUMMARY AND PROSPECTS

In this mini-review, we discussed recent progress of (S)TEM studies on solid electrolytes for Li batteries. With the success in alleviating the challenges caused by electron beam irradiation damage, more and more investigations that could not be performed previously are reported. These studies clarified several long-standing confusions regarding the structure–property relationship, provided first experimental insights into the large grain boundary resistance, and contributed insights regarding the reaction layer at cathode/SEIs.

Regardless, further challenges remain. For the ionic transport within the grain, sulfide electrolytes, which often exhibit a higher conductivity than oxides, demand a thorough study at atomic scale. Their vulnerary to electron beam, due to the weak bonds of Li with S in the structure and limited electron conductivity, significantly limit reliable measurements of their atomic and electronic structures in TEMs. In order to understand the role of grain boundaries in solid electrolytes, a wide range of materials need to be investigated in order to establish the systematic understanding. In particular, the materials with benign grain boundaries deserve special attention, as they may inspire the design of materials with conductive grain boundaries. For the solid electrolyte/electrode interface, one of the most pressing tasks is to verify the highly localized interfacial reaction layers that are proposed recently by theoretical works. Furthermore, the variation of these interfaces with composition, processing conditions, and cycling also remained to be investigated. It must be emphasized that recently developed *in situ* TEM techniques, such as *in situ* heating, and *in situ* electrochemical cycling with a desirable spatial resolution, will greatly facilitate these studies (Gu et al., 2013; Chi et al., 2015; Zeng et al., 2015). Their capability of real-time, high-resolution structural/chemical analysis will provide unique insights that cannot be acquired otherwise. With the recent remarkable developments in microscopy instrumentations, such as fast cameras and detectors, low voltage TEMs, and multi-functional specimen stages, these challenges should be overcome in the near future, and electron microscopy is expected to play an increasingly significant role in the research of Li-ion-conducting solid electrolytes.

AUTHOR CONTRIBUTIONS

All authors listed have made substantial, direct, and intellectual contribution to the work and approved it for publication.

FUNDING

This work was sponsored by the U.S. Department of Energy (DOE), Office of Science, Office of Basic Energy Sciences, Materials Sciences and Engineering Division. Materials characterization was performed as part of a user proposal at the Center for Nanophase Materials Sciences, which is a U.S. DOE Office of Science User Facility.

REFERENCES

Bruce, P. G., Freunberger, S. A., Hardwick, L. J., and Tarascon, J.-M. (2012). Li-O_2 and Li-S batteries with high energy storage. *Nat. Mater.* 11, 19–29. doi:10.1038/nmat3191

Buschmann, H., Dolle, J., Berendts, S., Kuhn, A., Bottke, P., Wilkening, M., et al. (2011). Structure and dynamics of the fast lithium ion conductor "$Li_7La_3Zr_2O_{12}$". *Phys. Chem. Chem. Phys.* 13, 19378–19392. doi:10.1039/c1cp22108f

Chi, M. F., Mizoguchi, T., Martin, L. W., Bradley, J. P., Ikeno, H., Ramesh, R., et al. (2011). Atomic and electronic structures of the $SrVO_3$-$LaAlO_3$ interface. *J. Appl. Phys.* 110, 046104. doi:10.1063/1.3601870

Chi, M. F., Wang, C., Lei, Y. K., Wang, G. F., Li, D. G., More, K. L., et al. (2015). Surface faceting and elemental diffusion behaviour at atomic scale for alloy nanoparticles during *in situ* annealing. *Nat. Commun.* 6, 8925. doi:10.1038/ncomms9925

Cussen, E. J. (2010). Structure and ionic conductivity in lithium garnets. *J. Mater. Chem.* 20, 5167–5173. doi:10.1039/b925553b

Egerton, R. F., Li, P., and Malac, M. (2004). Radiation damage in the TEM and SEM. *Micron* 35, 399–409. doi:10.1016/j.micron.2004.02.003

Gao, X., Fisher, C. A. J., Kimura, T., Ikuhara, Y. H., Kuwabara, A., Moriwake, H., et al. (2014). Domain boundary structures in lanthanum lithium titanates. *J. Mater. Chem. A* 2, 843–852. doi:10.1039/C3TA13726K

Gao, X., Fisher, C. A. J., Kimura, T., Ikuhara, Y. H., Moriwake, H., Kuwabara, A., et al. (2013). Lithium atom and A-site vacancy distributions in lanthanum lithium titanate. *Chem. Mater.* 25, 1607–1614. doi:10.1021/cm3041357

Gellert, M., Gries, K. I., Yada, C., Rosciano, F., Volz, K., and Roling, B. (2012). Grain boundaries in a lithium aluminum titanium phosphate-type fast lithium ion conducting glass ceramic: microstructure and nonlinear ion transport properties. *J. Phys. Chem. C* 116, 22675–22678. doi:10.1021/jp305309r

Gu, M., Parent, L. R., Mehdi, B. L., Unocic, R. R., McDowell, M. T., Sacci, R. L., et al. (2013). Demonstration of an electrochemical liquid cell for operando transmission electron microscopy observation of the lithiation/delithiation behavior of Si nanowire battery anodes. *Nano Lett.* 13, 6106–6112. doi:10.1021/nl403402q

Kim, K. H., Iriyama, Y., Yamamoto, K., Kumazaki, S., Asaka, T., Tanabe, K., et al. (2011). Characterization of the interface between $LiCoO_2$ and $Li_7La_3Zr_2O_{12}$ in an all-solid-state rechargeable lithium battery. *J. Power Sources* 196, 764–767. doi:10.1016/j.jpowsour.2010.07.073

Kitaura, H., Hayashi, A., Tadanaga, K., and Tatsumisago, M. (2010). All-solid-state lithium secondary batteries using $LiMn_2O_4$ electrode and Li_2S-P_2S_5 solid electrolyte. *J. Electrochem. Soc.* 157, A407–A411. doi:10.1149/1.3298441

Kumazaki, S., Iriyama, Y., Kim, K.-H., Murugan, R., Tanabe, K., Yamamoto, K., et al. (2011). High lithium ion conductive $Li_7La_3Zr_2O_{12}$ by inclusion of both Al and Si. *Electrochem. Commun.* 13, 509–512. doi:10.1016/j.elecom.2011.02.035

Ma, C., Chen, K., Liang, C. D., Nan, C. W., Ishikawa, R., More, K., et al. (2014). Atomic-scale origin of the large grain-boundary resistance in perovskite Li-ion-conducting solid electrolytes. *Energy Environ. Sci.* 7, 1638–1642. doi:10.1039/c4ee00382a

Ma, C., Cheng, Y., Chen, K., Li, J., Sumpter, B., Nan, C.-W., et al. (2016). Mesoscopic framework enables facile ionic transport in solid electrolytes for Li batteries. *Adv. Energy Mater.* doi:10.1002/aenm.201600053

Ma, C., Rangasamy, E., Liang, C. D., Sakamoto, J., More, K. L., and Chi, M. F. (2015). Excellent stability of a lithium-ion-conducting solid electrolyte upon reversible Li^+/H^+ exchange in aqueous solutions. *Angew. Chem. Int. Ed.* 54, 129–133. doi:10.1002/anie.201410930

Muller, D. A., Kourkoutis, L. F., Murfitt, M., Song, J. H., Hwang, H. Y., Silcox, J., et al. (2008). Atomic-scale chemical imaging of composition and bonding by aberration-corrected microscopy. *Science* 319, 1073–1076. doi:10.1126/science.1148820

Murugan, R., Thangadurai, V., and Weppner, W. (2007). Fast lithium ion conduction in garnet-type $Li_7La_3Zr_2O_{12}$. *Angew. Chem. Int. Ed.* 46, 7778–7781. doi:10.1002/anie.200701144

Pennycook, S. J. (1992). Z-contrast transmission electron microscopy – direct atomic imaging of materials. *Ann. Rev. Mater. Sci.* 22, 171–195. doi:10.1146/annurev.ms.22.080192.001131

Qian, D., Ma, C., More, K. L., Meng, Y. S., and Chi, M. (2015). Advanced analytical electron microscopy for lithium-ion batteries. *NPG Asia Mater.* 7, e193. doi:10.1038/am.2015.50

Quartarone, E., and Mustarelli, P. (2011). Electrolytes for solid-state lithium rechargeable batteries: recent advances and perspectives. *Chem. Soc. Rev.* 40, 2525–2540. doi:10.1039/c0cs00081g

Richards, W. D., Miara, L. J., Wang, Y., Kim, J. C., and Ceder, G. (2016). Interface stability in solid-state batteries. *Chem. Mater.* 28, 266–273. doi:10.1021/acs.chemmater.5b04082

Sakuda, A., Hayashi, A., and Tatsumisago, M. (2009). Interfacial observation between $LiCoO_2$ electrode and Li_2S-P_2S_5 solid electrolytes of all-solid-state lithium secondary batteries using transmission electron microscopy. *Chem. Mater.* 22, 949–956. doi:10.1021/cm901819c

Stramare, S., Thangadurai, V., and Weppner, W. (2003). Lithium lanthanum titanates: a review. *Chem. Mater.* 15, 3974–3990. doi:10.1021/cm0300516

Takada, K. (2013). Progress and prospective of solid-state lithium batteries. *Acta Mater.* 61, 759–770. doi:10.1016/j.actamat.2012.10.034

Wang, Y., Richards, W. D., Ong, S. P., Miara, L. J., Kim, J. C., Mo, Y., et al. (2015). Design principles for solid-state lithium superionic conductors. *Nat. Mater.* 14, 1026–1031. doi:10.1038/nmat4369

Wenzel, S., Leichtweiss, T., Krüger, D., Sann, J., and Janek, J. (2015). Interphase formation on lithium solid electrolytes – an *in situ* approach to study interfacial reactions by photoelectron spectroscopy. *Solid State Ionics* 278, 98–105. doi:10.1016/j.ssi.2015.06.001

Wenzel, S., Weber, D. A., Leichtweiss, T., Busche, M. R., Sann, J., and Janek, J. (2016). Interphase formation and degradation of charge transfer kinetics between a lithium metal anode and highly crystalline $Li_7P_3S_{11}$ solid electrolyte. *Solid State Ionics* 286, 24–33. doi:10.1016/j.ssi.2015.11.034

Wolfenstine, J., Sakamoto, J., and Allen, J. L. (2012). Electron microscopy characterization of hot-pressed Al substituted $Li_7La_3Zr_2O_{12}$. *J. Sci. Mater.* 47, 4428–4431. doi:10.1007/s10853-012-6300-y

Wu, Y., Ma, C., Yang, J. H., Li, Z. C., Allard, L. F., Liang, C. D., et al. (2015). Probing the initiation of voltage decay in Li-rich layered cathode materials at the atomic scale. *J. Mater. Chem. A* 3, 5385–5391. doi:10.1039/C4TA06856D

Yabuuchi, N., Yoshii, K., Myung, S. T., Nakai, I., and Komaba, S. (2011). Detailed studies of a high-capacity electrode material for rechargeable batteries, Li_2MnO_3-$LiCo_1/3Ni_1/3Mn_1/3O_2$. *J. Am. Chem. Soc.* 133, 4404–4419. doi:10.1021/ja108588y

Zeng, Z. Y., Zhang, X. W., Bustillo, K., Niu, K. Y., Gammer, C., Xu, J., et al. (2015). *In situ* study of lithiation and delithiation of MoS_2 nanosheets using electrochemical liquid cell transmission electron microscopy. *Nano Lett.* 15, 5214–5220. doi:10.1021/acs.nanolett.5b02483

Zhu, Y., He, X., and Mo, Y. (2015). Origin of outstanding stability in the lithium solid electrolyte materials: insights from thermodynamic analyses based on first-principles calculations. *ACS Appl. Mater. Interfaces* 7, 23685–23693. doi:10.1021/acsami.5b07517

Zhu, Y., He, X., and Mo, Y. (2016). First principles study on electrochemical and chemical stability of the solid electrolyte-electrode interfaces in all-solid-state Li-ion batteries. *J. Mater. Chem. A*. 4, 3253–3266. doi:10.1039/C5TA08574H

Conflict of Interest Statement: The authors declare that the research was conducted in the absence of any commercial or financial relationships that could be construed as a potential conflict of interest.

frontiers
in Energy Research

ORIGINAL RESEARCH
published: 02 June 2016
doi: 10.3389/fenrg.2016.00022

Structure and Ionic Conductivity of Li_2S–P_2S_5 Glass Electrolytes Simulated with First-Principles Molecular Dynamics

*Takeshi Baba and Yoshiumi Kawamura**

Toyota Motor Corporation, Shizuoka, Japan

Lithium thiophosphate-based materials are attractive as solid electrolytes in all-solid-state lithium batteries because glass or glass-ceramic structures of these materials are associated with very high conductivity. In this work, we modeled lithium thiophosphates with amorphous structures and investigated Li^+ mobilities by using molecular dynamics calculations based on density functional theory (DFT-MD). The structures of $x$$Li_2S$–$(100 - x)$$P_2S_5$ ($x = 67$, 70, 75, and 80) were created by randomly identifying appropriate compositions of Li^+, PS_4^{3-}, $P_2S_7^{4-}$, and S^{2-} and then annealing them with DFT-MD calculations. Calculated relative stabilities of the amorphous structures with $x = 67, 70,$ and 75 to crystals with the same compositions were 0.04, 0.12, and 0.16 kJ/g, respectively. The implication is that these amorphous structures are metastable. There was good agreement between calculated and experimental structure factors determined from X-ray scattering. The differences between the structure factors of amorphous structures were small, except for the first sharp diffraction peak, which was affected by the environment between Li and S atoms. Li^+ diffusion coefficients obtained from DFT-MD calculations at various temperatures for picosecond simulation times were on the order of 10^{-3}–10^{-5} Å^2/ps. Ionic conductivities evaluated by the Nernst–Einstein relationship at 298.15 K were on the order of 10^{-5} S/cm. The ionic conductivity of the amorphous structure with $x = 75$ was the highest among the amorphous structures because there was a balance between the number density and diffusibility of Li^+. The simulations also suggested that isolated S atoms suppress Li^+ migration.

Keywords: lithium sulfide glass, solid electrolyte, first-principles molecular dynamics, structure factor, ionic conductivity

Edited by:
Shyue Ping Ong,
University of California San Diego, USA

Reviewed by:
Jijeesh Ravi Nair,
Politecnico di Torino, Italy
Yifei Mo,
University of Maryland, USA

Correspondence:
Yoshiumi Kawamura
yoshiumi_kawamura@mail.toyota.co.jp

Specialty section:
This article was submitted to Energy Storage, a section of the journal Frontiers in Energy Research

Received: *01 February 2016*
Accepted: *19 May 2016*
Published: *02 June 2016*

Citation:
Baba T and Kawamura Y (2016) Structure and Ionic Conductivity of Li_2S–P_2S_5 Glass Electrolytes Simulated with First-Principles Molecular Dynamics.
Front. Energy Res. 4:22.
doi: 10.3389/fenrg.2016.00022

INTRODUCTION

The possibility of producing all-solid-state lithium-ion batteries (LIBs) has attracted much attention because the replacement of an organic liquid electrolyte with an inorganic solid electrolyte (SE) would simplify battery design, increase energy density, and make batteries safer and more durable. Realization of such batteries is critical for practical applications such as electric vehicles and plug-in hybrid electric vehicles. A major obstacle to the development of all-solid-state LIBs is that the ionic conductivity of SEs at room temperature (RT) is too low to achieve high-rate charging and discharging. In recent years, inorganic ceramics with high ionic conductivity have been widely studied (Knauth, 2009; Fergus, 2010; Takada, 2013; Ren et al., 2015). Sulfide SEs with the same level of conductivity as conventional liquid electrolytes have been discovered. For example, crystalline thiophosphate with thio-LIthium Super Ionic CONductor (thio-LISICON) have high ionic conductivity. The ionic conductivity of a $Li_{10}GeP_2S_{12}$ crystal, in particular, is 1.2×10^{-2} S/cm (Kamaya et al., 2011). Argyrodite-type crystals with the stoichiometry Li_6PS_5X (X = Cl, Br, or I) also have high ionic conductivity ($>10^{-3}$ S/cm) (Deiseroth et al., 2008; Rao and Adams, 2011; Boulineau et al., 2012). In addition, the conductivities of some glasses, including $30Li_2S–26B_2S_3–44LiI$ (Wada et al., 1983), $50Li_2S–17P_2S_5–33LiBH_4$ (Yamauchi et al., 2013), and $63Li_2S–36SiS_2–1Li_3PO_4$ (Aotani et al., 1994), have been reported to be as high as $1.5–1.7 \times 10^{-3}$ S/cm.

The focus of this study was on the binary $Li_2S–P_2S_5$ system. An additional advantage of the $Li_2S–P_2S_5$ system is that no metallic elements, such as Ge and Si, are needed. The electrochemical stability of an electrolyte with no metallic element might be relatively high because metals might easily be reduced or oxidized during electrochemical reactions. Sulfide SEs are classified into three categories based on their structural characteristics: crystalline, amorphous (glass), and partially crystalline (glass-ceramic), all of which are known to be fast ionic conductors. Among the crystalline SEs, metastable $Li_7P_3S_{11}$ (Yamane et al., 2007; Minami et al., 2010) and nanoporous β-Li_3PS_4 (Liu et al., 2013) have high conductivities, 3×10^{-3} and 1.6×10^{-4} S/cm, respectively. Much research has been conducted since the first report that the glass and glass-ceramic phases are fast ionic conductors (Zhang and Kennedy, 1990). At present, the maximum conductivity occurs at 70–80 mol% Li_2S (i.e., 30–20 mol% P_2S_5), depending on the conditions during preparation (Minami et al., 2006; Mizuno et al., 2006). In general, it is difficult to prepare sulfide glasses with higher Li concentrations because crystallization occurs easily during the cooling process. The glasses are therefore prepared by mechanical milling technique or by twin-roller rapid-quenching technique. Glass ceramics are prepared by heating mechanically milled glass to a moderately high temperature. Crystals are prepared using solid-state reactions or with the same approach used to prepare glass ceramics. Crystallization of glasses usually results in a lowering of conductivities because the conductivities of the crystals that precipitate out are low. However, the ionic conductivity of $Li_2S–P_2S_5$ glass ceramics is enhanced by the precipitation of metastable phases with high conductivities. These metastable phases are analogous to crystalline $Li_7P_3S_{11}$ and Li_3PS_4. However, the role of metastable crystalline phases in glass ceramics is still unclear. In order to understand the mechanism responsible for the high conductivities of the binary $Li_2S–P_2S_5$ system experimentally, several groups have studied the Li^+ diffusion profiles using $^{6/7}$Li solid-state nuclear magnetic resonance spectroscopy (NMR) measurements (Graf et al., 2013; Hayamizu and Aihara, 2013; Hayamizu et al., 2014; Murakami et al., 2015). NMR is a powerful tool and provides many findings such as the rate of ionic motion. However, because the obtained signals are limited to the space-averaged information, it is difficult to clarify the origin of the Li^+ diffusion only by the NMR study.

Since computational studies facilitate analysis of the Li diffusion process at the atomic scale, several researches based on the density functional theory (DFT) calculation have recently been reported. Holzwarth and co-workers have performed the DFT calculations on several crystal structures of the $Li_2S–P_2S_5$ system, including $Li_7P_3S_{11}$ and γ- and β-Li_3PS_4. They used the nudged elastic band method to estimate the activation energy for Li^+ migration in the crystal and obtained results in good agreement with experiments (Holzwarth et al., 2011; Lepley and Holzwarth, 2012; Lepley et al., 2013). Holzwarth and co-workers suggested that the process of vacancy-interstitial pair formation contributes to superionic conductivities. Yang and Tse (2015) used DFT-based molecular dynamics (DFT-MD) calculations to investigate the mechanisms of Li^+ transport in both the nanoporous and the crystalline phases of β-Li_3PS_4. One of the advantages of DFT-MD studies is that Li^+ diffusivity can be simulated directly without use of a parametric force field. Mori et al. (2013) used the reverse Monte Carlo method with X-ray and neutron diffraction data to model the structures of $Li_2S–P_2S_5$ glasses as well as $Li_7P_3S_{11}$ crystals. Mori et al. used bond valence sum (BVS) analysis (Adams and Swenson, 2004, 2005; Hall et al., 2004) to analyze Li^+ migration pathways. Mori et al. classified the pathways to the Li^+ stable and metastable regions and found that the size of latter region was an indicator of Li^+ diffusivity. However, they also stated that the quantitative relationship between the BVS results and the activation energy of ion migration still remained to be ascertained. Because static analysis is limited in terms of quantification, dynamical considerations must be taken into account to understand the high conductivities of glass SEs.

In the present work, we used DFT-MD calculations to investigate both the structure and the ionic conductivity of the binary $Li_2S–P_2S_5$ glass. The glass structures were modeled in an *ab initio* fashion, that is, without adjustments to take into account experimental information. To investigate ionic conductivity, we adopted an approach similar to that of the DFT-MD study of Yang and Tse (2015). Section "Computational Methods" briefly describes the simulation frameworks. Section "Results and Discussion" presents the simulated structures of the SEs and then compares the corresponding mass density and experimental diffraction data. The dynamical properties, such as the diffusion coefficients and ionic conductivities, are then presented. The relationship between the compositions of glasses and the dynamical properties are also discussed. Section "Conclusion" consists of a summary and some conclusions.

COMPUTATIONAL METHODS

In this work, the amorphous phases of lithium sulfide with compositions of $xLi_2S–(100 - x)P_2S_5$, where $x = 67$, 70, 75, or 80, were studied. In order to obtain a realistic model of amorphous structures, we used a melt-and-quench MD method, which is the common computational method for disordered materials (Massobrio et al., 2015). In the melt-and-quench technique, the choice of an initial coordinate is categorized into two types: a structure of the known crystal and a fully random coordinate of component atoms. We could not use the former because crystal structures with the same composition of the amorphous structure with $x = 67$ and 80 are unknown. Whereas the latter is applicable to any compound, a major issue is that the generated structures are far from the reasonable structures. Specifically, covalent bonding between P and S are missing. Indeed, in our preliminary examination, the convergences of the wavefunction optimization, which is the first part of DFT-MD simulations, were slow and sometimes failed. To circumvent this issue, the ionic units, such as Li^+, tetrahedral PS_4^{3-}, di-tetrahedral $P_2S_7^{4-}$, and S^{2-}, are located randomly. In order to pack bulky units in a cell efficiently, we used the Amorphous Cell module in the BIOVIA Materials Studio program (by Dassault Systèmes, BIOVIA Corp.). During the model construction, close contacts between atoms were minimized while ensuring realistic distributions (Allen and Tildesley, 1989) using the COMPASS II force field (Sun, 1998). Stoichiometric compositions were maintained for $x = 67$, 70, and 75, i.e., $4 \times Li^+$ and $P_2S_7^{4-}$; $7 \times Li^+$, PS_4^{3-}, and $P_2S_7^{4-}$; and $3 \times Li^+$ and PS_4^{3-}, respectively. The amorphous structures with $x = 80$ were composed of eight Li^+, two PS_4^{3-}, and one S^{2-}. For each amorphous structure, ~130 atoms were placed in a cubic box. The initial volume sizes were defined by setting the volumetric mass density to 2 g/cm^3, which corresponds to the experimental density for Li_3PS_4 and $Li_7P_3S_{11}$ crystals.

Starting from the initial coordinates, the amorphous structures were annealing by the melt-and-quench procedure in a framework of DFT-MD simulations. All the systems were heated to 1000 K and then cooled to 667, 500, 400, and 300 K in a stepwise manner. The structures were kept at each temperature for ca. 2.8 ps before going to the next temperature. The cooling rate was ca. 48 K/ps, which is a typical value of the DFT-MD study (Massobrio et al., 2015). In all case, variable-cell, Car–Parrinello dynamics (Car and Parrinello, 1985; Laasonen et al., 1993; Bernasconi et al., 1995) were performed by using the CP module in the Quantum ESPRESSO program package (Giannozzi et al., 2009). A fictitious electronic mass of 400 a.u. and a time step of 6 a.u. (ca. 0.14 fs) were applied. The electronic and ionic motions were propagated by a standard Verlet algorithm (Verlet, 1967). Cell dynamics were simulated by use of a damped Parrinello–Rahman method (Parrinello and Rahman, 1981). The ionic and cell temperatures were controlled by a Nosé thermostat (Nosé, 1984; Hoover, 1985; Martyna et al., 1992). Periodic boundary conditions were applied, and only the axis length was allowed to change (i.e., the angles were kept constant). DFT calculations were performed using the Perdew–Burke–Ernzerhof exchange-correlation functional for solids (PBEsol) (Perdew et al., 2008) with Vanderbilt-type ultrasoft pseudopotentials (Vanderbilt, 1990). The energy cutoff of the plane wave basis set was set to 30 Ry (408 eV). Only one k-point of $1 \times 1 \times 1$ was sampled.

After equilibration, DFT-MD calculations at each temperature were accumulated for at least 10 ps for a so-called production step. The computational settings of the DFT and MD components were the same as those described in the previous paragraph. In order to reduce the statistical inaccuracy, at least three simulations of this sequence were performed independently for each amorphous structure. Averaged data were used for the analysis. Furthermore, to validate the duration of equilibration (ca. 2.8 ps) and production (ca. 10 ps) steps, additional 30–40 ps of DFT-MD calculations were performed for some amorphous structures at 500 and 300 K.

RESULTS AND DISCUSSION

Amorphous Structures

Figure 1 shows geometrical snapshots of DFT-MD simulations in the final production steps at 300 K for $x\mathrm{Li_2S}$–$(100 - x)\mathrm{P_2S_5}$ amorphous structures with $x = 67$, 70, 75, and 80. In almost all amorphous structures, unit structures, such as tetrahedral PS_4^{3-}, and di-tetrahedral $P_2S_7^{4-}$, were maintained and were distributed randomly. It is noteworthy that no decomposition or segregation of the units was observed in almost all trajectories, whereas rearrangement of the units, such as $2P_2S_7 \rightarrow PS_4 + P_3S_{10}$, occurred for only one amorphous structure model with $x = 67$.

In order to examine the effect of the simulation duration, the energy, the cell volume, and the atomic orientation with respect to the time evolution were investigated. **Figure 2A** shows the time evolution of the relative stability and the volumetric mass density for amorphous structure with $x = 75$ at 300 K simulation. The relative stability was defined as the energy difference between the amorphous structure and the crystal with the same composition (γ-Li_3PS_4) and normalized by the molecular weight. The relative stabilities averaged over first 10 ps and total 40 ps were 0.159 and 0.144 kJ/g, respectively. The mass densities averaged over the first and total duration were 1.789 and 1.788 g/cm^3, respectively. In both cases, the difference was relatively small. We investigated the pair correlation function (PCF) between Li and S and that between S and S belongs to the other PS_4^{3-} units. To clarify the duration effect, the PCF averaged over each ca. 10 ps are shown in **Figure 2B**. There were no significant differences in the sampling period for both PCFs. Therefore, the procedure that consists of equilibration (ca. 2.8 ps) and production (10 ps) steps is enough to discuss the amorphous structures.

Figure 3A shows the volumetric mass densities simulated by the DFT-MD at each temperature. As temperature decreased, the densities increased monotonically. Regardless of composition, the difference of the density between high (1000 K) and low (300 K) temperatures was ca. 0.15 g/cm^3, which corresponds to approximately a 1.5% variation of each lattice length. Thus, our calculation simulated a trend of lattice expansion with increasing temperature, which is considered to be an important factor for Li^+ migration.

The calculated density of the amorphous structures decreased in the order $x = 70$, 67, 80, and 75, which is not the same as the order of the molecular ratios. Experimental densities for amorphous structures have not been measured, to the best of our knowledge. Thus, **Figure 3B** provides a comparison of the calculated densities of amorphous structures and the experimental densities of the crystals (Yamane et al., 2007; Onodera et al., 2010; Homma et al., 2011). In addition, **Figure 3B** shows comparisons with the density of crystal obtained by geometrical optimization of the usual DFT calculation. Crystals with $x = 80$, for which the stoichiometric composition is $Li_8P_2S_9$, are also unknown, to our knowledge. To assess the accuracy of the calculation, we added the known Li_7PS_6 (corresponding to $87.5Li_2S$–$12.5P_2S_5$) crystal (Kong et al., 2010). For the crystals, the calculated densities were in good agreement with the experimental ones. In general, the densities of the amorphous structure were lower than those of the corresponding crystals. This pattern is common in silica and

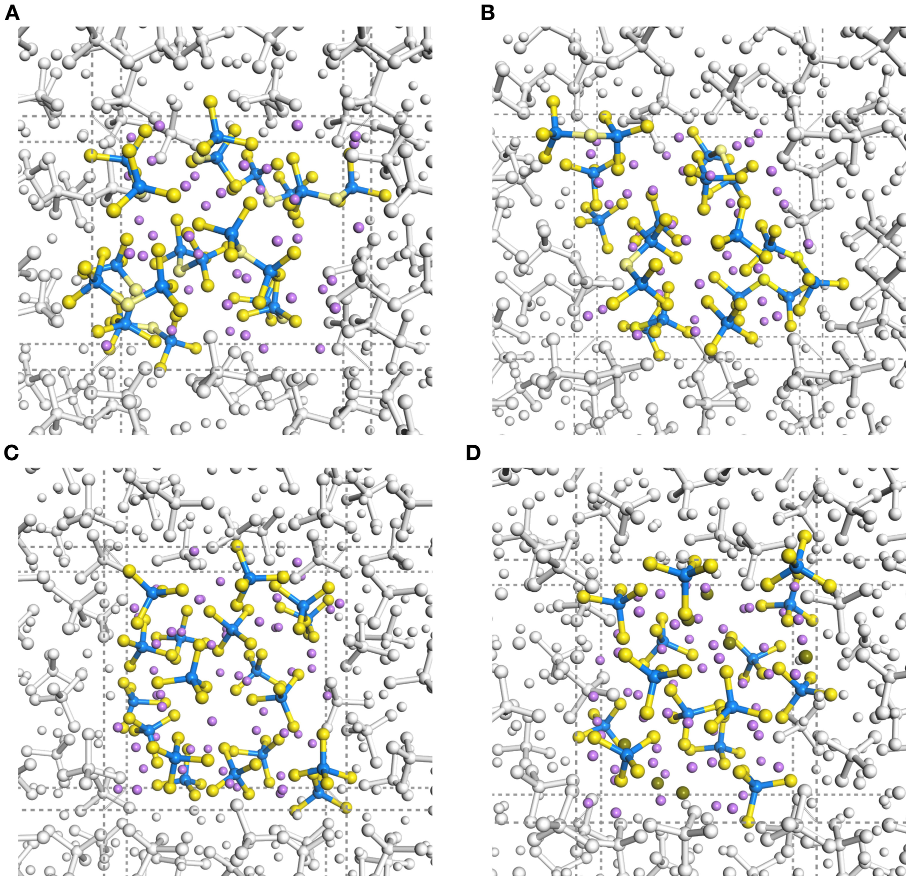

FIGURE 1 | Trajectory snapshots in DFT-MD simulations at 300 K of (A) $67Li_2S–33P_2S_5$, (B) $70Li_2S–30P_2S_5$, (C) $75Li_2S–25P_2S_5$, and (D) $80Li_2S–20P_2S_5$ amorphous structures. Purple, blue, and yellow spheres indicate Li, P, and S atoms, respectively. Sticks with standard bond distances represent P–S bonds.

alumina glasses (Benoit et al., 2000). The pattern with respect to molecular ratios, as mentioned above, is also similar between amorphous and crystalline structures.

To investigate stability of the amorphous structure, we compared the relative stabilities as defined above. The stability for $x = 80$ was not examined because there is no reference crystal, as mentioned in the previous paragraph. The averaged relative stabilities of amorphous structures with $x = 67$, 70, and 75 were 0.035, 0.121, and 0.155 kJ/g, respectively. A positive value means that the amorphous structure is less stable than the corresponding crystal. Our analysis thus indicates that the amorphous structures were metastable.

The simulated amorphous structures can be compared directly to experimental results by calculating the static structure factor, $S(Q)$, obtained from X-ray and neutron diffraction studies. **Figure 4** shows the X-ray structure factor $S_X(Q)$ for each amorphous structure. The neutron diffraction results $S_N(Q)$ are shown in Supplementary Material. The calculated results were analyzed for trajectories by a DFT-MD simulation at 300 K using the ISAACS program (Le Roux and Petkov, 2010). We determined the experimental data based on the previous work of Ohara et al. (2016). Whereas the calculated results show the fluctuations due to our limited sampling, the agreement between our results and the experimental data is good for large values of Q, and the agreement is still good for small values of Q with respect to the positions of maxima and minima. In both the DFT-MD-simulated and experimental results, the first sharp diffraction peaks (FSDP) were observed at ca. 1.3 1/Å. The appearance of FSDP is a fundamental characteristic of amorphous structures. There was little difference between the structure factors of the amorphous structures, except for the FSDP. Although there was no sharp peak at 1.3 1/Å for the amorphous structure with $x = 67$, the peak heights of the FSDPs of the amorphous structures with $x = 70$ and 75 were in good agreement with the experimental ones. This peak is thought to mainly reflect the environment between Li and S, and it was enhanced as the Li concentration increased for $x = 67$, 70, and 75. However, the amorphous structure with $x = 80$ resulted in a smaller peak than the other amorphous structures. The implication is that the environment between Li and S is not uniform. The amplitudes of the second peaks (SSDPs) at ca. 2.1 1/Å were smaller than the experimental amplitudes. Further refinement of the spectrum will require a system at least 10 times as large as the system used in the previous study of Mori et al. (2013).

Diffusion Properties

As is usual in a MD study, we used the production steps of trajectories to investigate the diffusion profile. The diffusion coefficient was calculated from the slope of the average mean square

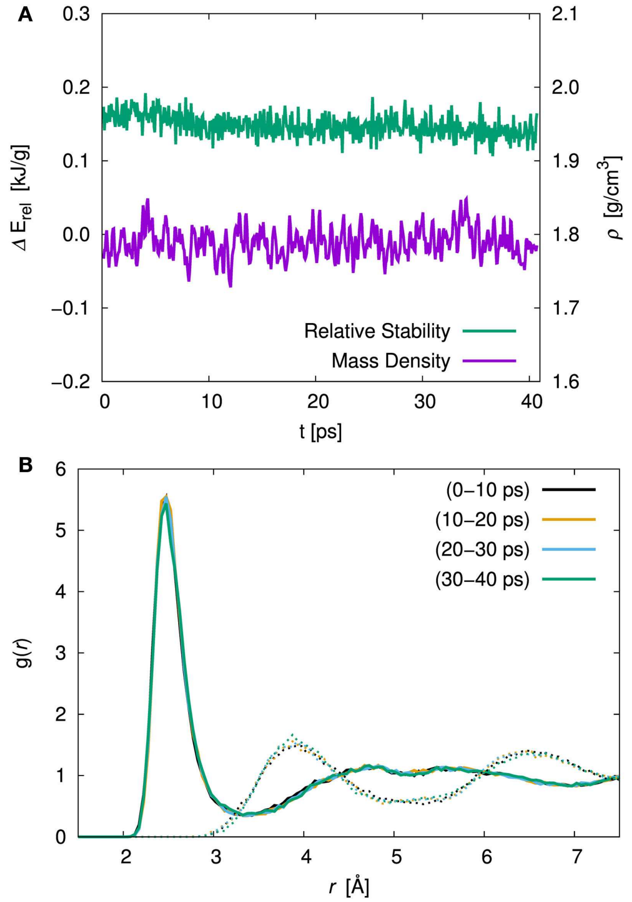

FIGURE 2 | (A) Time evolution of the relative stability, ΔE_{rel}, and the volumetric mass density, ρ, and **(B)** pair correlation function (PCF), $g(r)$ of Li–S (solid line) and inter-thiophosphate S–S (dotted line) for the $75Li_2S–25P_2S_5$ amorphous structure at 300 K simulation. The averaged PCF were sampled every 10 ps.

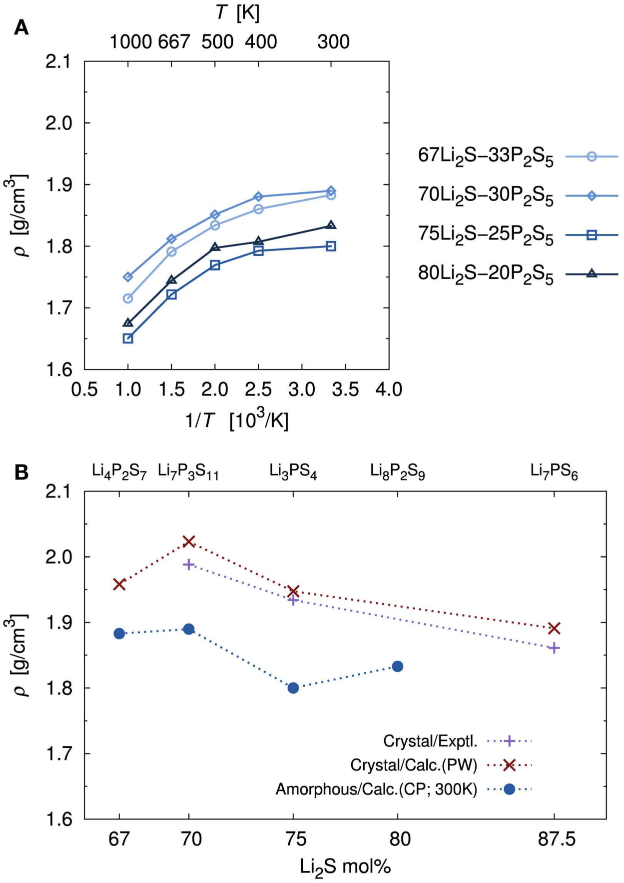

FIGURE 3 | (A) Temperature dependence of mass densities, ρ, of amorphous structures determined by DFT-MD simulations and **(B)** comparisons with experimental and calculated crystal mass densities. Crystal calculations were performed with the PW module in the Quantum ESPRESSO package using the same functional and pseudopotential as the CP module. The major difference was the number of k-point meshes. Note that because the $Li_4P_2S_7$ crystal structure is unknown, the known $Li_4P_2O_7$ crystal structure ($P\bar{1}$) was used as an initial geometry. This approach is the same one used in a previous computational study (Holzwarth et al., 2011). The Li_7PS_6 (corresponding to $87.5Li_2S–12.5P_2S_5$) crystal structure, which has been reported, was added to address the accuracy of the calculation.

displacement (MSD) of Li atoms over time. Before evaluating the diffusion coefficient, we examine the effect of the simulation duration as the previous section. **Figure 5** shows the MSD as a function of lag-time among short (ca. 10 ps) and long (ca. 50 ps) duration for the amorphous structure with $x = 75$ and 80 at 500 K. The plots obtained from short duration coincide with those obtained from the long duration. To assess the individual Li mobilities, the root-MSD (RMSD) were evaluated. **Figure 6** shows the relative frequency distributions of RMSD after 10 ps for amorphous structures with $x = 75$ at 1000, 667, 500, 400, and 300 K temperature, respectively. The time evolutions of RMSD for all Li in one model are shown in Supplemental Material. At 300 K, almost all (99.1%) of Li moved within 2.5 Å. It means most of Li were unable to reach the nearest neighbor Li sites in the amorphous structures. At 400 K, 11.9% of Li moved over 2.5 Å from the initial coordinate after 10 ps. A few (1.6%) Li also migrated over 4.5 Å, which corresponds to the distance to the second nearest neighbor site. More Li migrated at higher temperature (9.5, 36.5, and 85.2% of Li migrated over 4.5 Å at 500, 667, and 1000 K, respectively). Certainly our simulation time was much shorter than typical setting in the classical MD method, but the electronic environment around Li, which was obtained by the DFT method accurately, was important to define the flexibility of Li as discussed later. Thus, we used the sampling over 10-ps duration to analyze the diffusion property for each amorphous structure, although the results for 300 K were removed from the consideration. **Figure 7** shows the Arrhenius plot of the calculated diffusion coefficients for the amorphous structures with temperatures from 400 to 1000 K. The relationship for each amorphous structure was linear in this region. Whereas the diffusion coefficients for amorphous structures with $x = 67$, 70, and 75 were similar, the diffusion coefficient for $x = 80$ was slightly lower than the others. The implication is that the diffusivity of only the amorphous structure with $x = 80$ was low. It would be confirmed by the comparison of the distribution of RMSD between amorphous structures with $x = 75$ and 80 (shown in the inset figure in **Figure 6**). This difference will be discussed later.

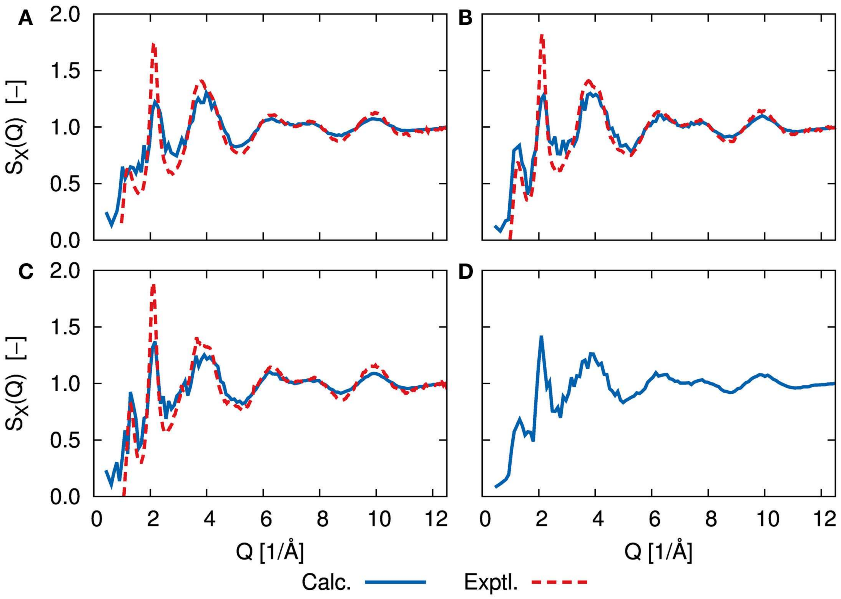

FIGURE 4 | X-ray structure factor, $S_X(Q)$, determined by DFT-MD simulations (solid blue line) and scattering experiments (dashed red line) of (A) $67Li_2S–33P_2S_5$, (B) $70Li_2S–30P_2S_5$, (C) $75Li_2S–25P_2S_5$, and (D) $80Li_2S–20P_2S_5$ amorphous structure. Experimental measurements are lacking for $80Li_2S–20P_2S_5$. Neutron scattering results, $S_N(Q)$, are shown in Supplementary Material.

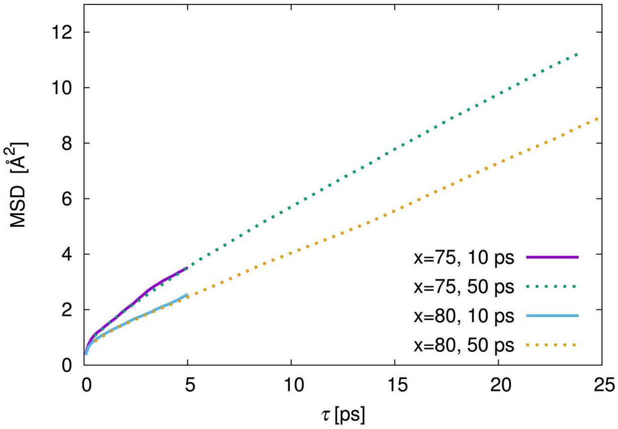

FIGURE 5 | Mean square displacement (MSD) against lag time, τ, among 10 ps (solid line) and 50 ps (dotted line) of production steps for the amorphous structures with $75Li_2S–25P_2S_5$ ($x = 75$) and $80Li_2S–20P_2S_5$ ($x = 80$) amorphous structures at 500 K simulation. The MSD of 10 and 50 ps were derived from the independent trajectories.

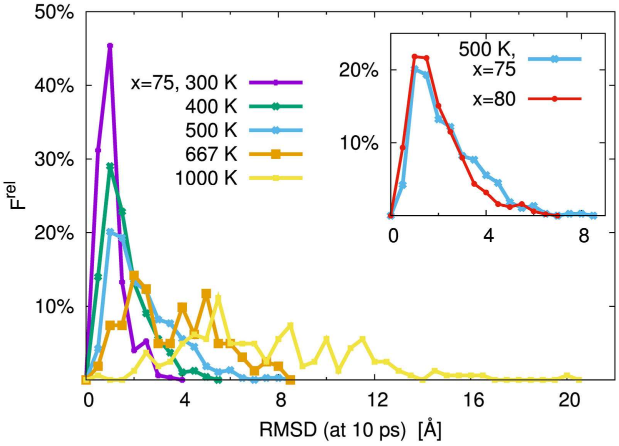

FIGURE 6 | Relative frequency distribution, F^{rel}, of root mean square displacement (RMSD) after 10 ps for Li. The main figure was the distributions for the $75Li_2S–25P_2S_5$ amorphous structure at $T = 300$, 400, 500, 667, and 1000 K, respectively. The inset figure was comparison of $75Li_2S–25P_2S_5$ ($x = 75$) and $80Li_2S–20P_2S_5$ ($x = 80$) amorphous structures at 500 K distribution. The bin width was 0.5 Å.

To estimate the ionic conductivity, σ, we used the Nernst–Einstein relationship:

$$\sigma = \frac{N(Ze)^2}{k_B T} D$$

where N, Z, e, k_B, T, and D are the number density of transported species, the charge of the transported species, the elementary charge, the Boltzmann constant, the target temperature, and the diffusion coefficient of the transported species, respectively. The target temperature is set to the RT (298.15 K) to compare the computational results with experimental ones. Because the transported species was the Li^+ in this study, N is the concentration of Li atoms in each amorphous structure calculated by using the number of Li atoms in a unit cell and the average simulated volume at 300 K, which is close to the target temperature. For Li^+, $Z = 1$. D is the diffusion coefficient of Li^+ at the target temperature. Because the diffusion coefficients obtained from 300 K trajectories were less accurate for small movements in our simulations, we used values of D extrapolated from the diffusion coefficients between 1000 and 400 to 298.15 K.

Table 1 summarizes the estimated σ values as well as the N and D values. The calculated and experimental (Mizuno et al., 2005)

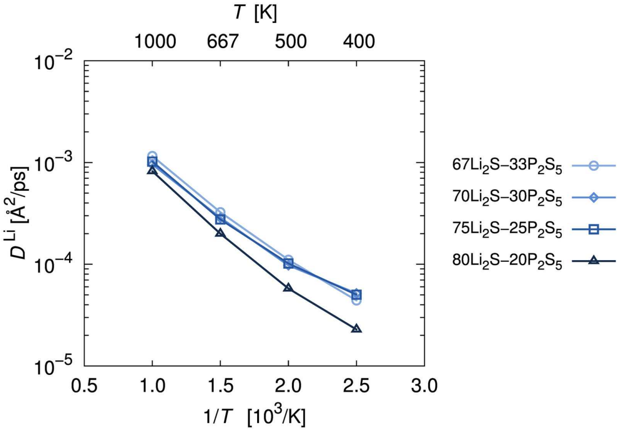

FIGURE 7 | Arrhenius plot of lithium diffusion coefficients, D^{Li}. Diffusion coefficients were estimated by averaging the mean square displacement of Li atoms at each trajectory.

TABLE 1 | Number densities, diffusion coefficients, and ionic conductivities of lithium at the RT for xLi_2S–$(100 - x)P_2S_5$ amorphous structures.

	Number density (1/cm^3)	Diffusion coefficient (cm^2/s)	Ionic conductivity (S/cm)
$67Li_2S$–$33P_2S_5$	1.44×10^{22}	6.30×10^{-10}	5.68×10^{-5}
$70Li_2S$–$30P_2S_5$	1.59×10^{22}	8.22×10^{-10}	8.16×10^{-5}
$75Li_2S$–$25P_2S_5$	1.81×10^{22}	7.80×10^{-10}	8.78×10^{-5}
$80Li_2S$–$20P_2S_5$	2.18×10^{22}	2.59×10^{-10}	3.51×10^{-5}

Number densities were evaluated for the number of lithium atoms in the simulation box and the time-averaged volume at 300 K trajectory. Diffusion coefficients at 298.15 K were derived by linear extrapolation from results at 400–1000 K. Ionic conductivities were estimated with the Nernst–Einstein relationship using these values and assuming that all lithium atoms were transported.

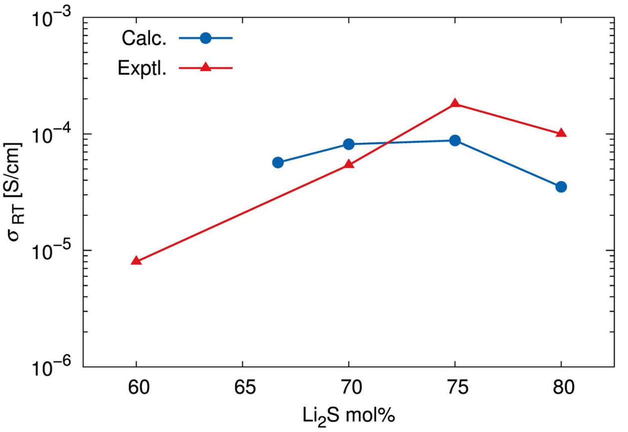

FIGURE 8 | Ionic conductivity σ at room temperature (298.15 K). Calculated results were estimated by using the Nernst–Einstein relationship, an extrapolated diffusion coefficient, and the number density of Li determined by DFT-MD simulations. Experimental data are adapted from Mizuno et al. (2005).

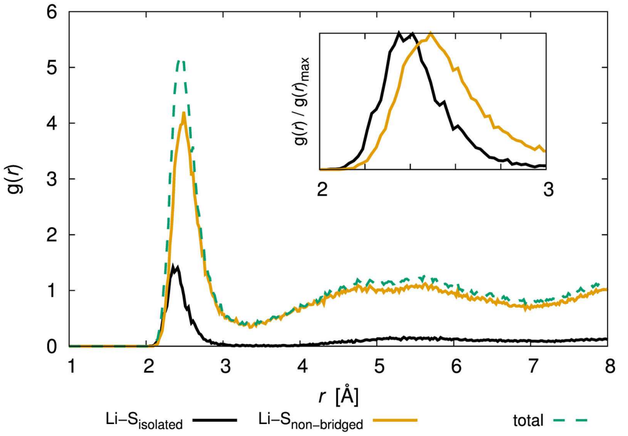

FIGURE 9 | Pair correlation function, g(r), of Li–S for the $80Li_2S$–$20P_2S_5$ amorphous structure determined by DFT-MD simulation. The inset figure shows an enlarged view of 2–3 Å and normalized maximum values. The results for the other amorphous structures are shown in Supplementary Material.

σ versus the composition of the amorphous structures are shown in **Figure 8**. The fact that the highest calculated ionic conductivity of an amorphous structure corresponded to $x = 75$ is consistent with experimental results. Whereas the calculated diffusion coefficient of the amorphous structure was lower for $x = 75$ than for $x = 70$, the ionic conductivity of the amorphous structure was higher for $x = 75$ than for $x = 70$. These results explain why the percentage difference was larger for number densities than for diffusion coefficients. The ionic conductivity of the amorphous structure was lower for $x = 67$ than for $x = 70$ and 75 because both the number density and the diffusion coefficient were lower for $x = 67$. However, the number density of the amorphous structure with $x = 80$ was the highest, but the calculated ionic conductivity was the lowest. The explanation is that the diffusion coefficient was significantly lower for the $x = 80$ structure than for the other structures. These results suggest that a relatively high number density of conductive species enhances conductivity, but only up to a certain density. In other words, the balance between the number density and diffusion coefficient is important.

It might seem that the agreement between the calculated and experimental conductivity was only semiquantitative. Indeed, we averaged sampling results among only a few independent models for each amorphous structure. We would have to increase the number of samples and/or cell size to achieve higher accuracy, as was apparent in the discussion of structure factors. It is noteworthy that Mo et al. (2012) argued for the limitation of the DFT-MD study due to the statistical uncertainty associated with fitting a curve to the MSD versus time data. Therefore, it seems reasonable to conclude that our simulations correctly determined the order of magnitude of the ionic conductivity and represented the diffusion properties of amorphous structures as a function of their composition.

Let us now turn to the argument that only the diffusivity of the amorphous structure with $x = 80$ was low. To reveal the environment around Li^+, we examined the PCF of Li and S. **Figure 9** shows the PCF for the amorphous structure with $x = 80$ over production steps at 300 K (the results for the other amorphous structures are shown in Supplementary Material). Note that we

TABLE 2 | Average atomic charge distributions for xLi$_2$S–(100 − x)P$_2$S$_5$ amorphous structures determined by Bader analyses.

	Li	P	$S_{isolated}$	$S_{non-bridged}$	$S_{bridged}$
$67Li_2S$–$33P_2S_5$	0.886 (0.010)	1.255 (0.113)		−0.910 (0.058)	−0.593 (0.051)
$70Li_2S$–$30P_2S_5$	0.884 (0.008)	1.239 (0.085)		−0.927 (0.067)	−0.608 (0.065)
$75Li_2S$–$25P_2S_5$	0.884 (0.008)	1.273 (0.119)		−0.981 (0.055)	
$80Li_2S$–$20P_2S_5$	0.878 (0.008)	1.275 (0.114)	−1.698 (0.020)	−0.985 (0.056)	

The values in parenthesis are the standard deviations. S atoms were typed on the basis of bond numbers. The Bader charge analysis was performed by using the MedeA-VASP package (by Materials Design, Inc.), and the PBEsol functional with projector augmented wave potentials (Blöchl, 1994; Kresse and Joubert, 1999) at the final snapshot structure in the 300 K simulation.

distinguished the bond type of S atoms, i.e., isolated S atoms for which the formal bond number is zero, and that of S atoms in a PS_4 unit, for which the bond number is one. We denoted the latter as "non-bridged S." The total PCFs were divided between PCFs involving Li and isolated S and the PCF of Li and non-bridged S. Interestingly, the position of the first peak was slightly different; the statistically stable distances between Li and S atoms of the former and latter were 2.36 and 2.45 Å, respectively. The results mean that isolated S attracts Li atoms more than non-bridged S does.

Further evidence relevant to the Li–S attraction comes from the difference of atomic charges. **Table 2** summarizes the average atomic populations based on a Bader charge analysis (Bader, 1990; Tang et al., 2009). Because bond numbers of S atom are distinguished in a way similar to the method discussed in the previous paragraph to characterize bond types, we have denoted the S atoms for which the bond number is two, namely, the S atoms in the P_2S_7 unit (i.e., S of –P–S–P–) in our models, as "bridged S." The atomic charge distributions of Li, 0.88–0.89, were very similar among the amorphous structures (**Table 2**). The deviations were very small. The atomic charge distributions of P atom were also similar among the amorphous structures and fell within the range of 1.24–1.28, but the deviations were an order of magnitude larger for P than for Li atom. The atomic charge distribution of isolated S was −1.70, those of non-bridged S varied from −0.99 to −0.91, and those of bridged S ranged from −0.61 to −0.59. The deviations were relatively modest. It is clear that the bond type defines the charge distributions of S. In the case of the amorphous structure with $x = 80$, the isolated S had approximately twice the negative charge of the non-bridged S. In other words, an isolated S with a relatively large negative charge may more strongly attract positive Li^+ electrostatically. This conclusion is consistent with the above discussion of PCF. The implication with respect to diffusibility is that the attraction of Li to isolated S suppresses the migration of Li^+, and this suppression accounts for the fact that the amorphous structure with $x = 80$ has the lowest diffusion coefficient among the amorphous structures.

To briefly summarize these results, the ionic conductivities of amorphous structures based on lithium sulfide depend on both the number density and the diffusibility of Li^+. A higher number density enhances conductivity. However, when the ratio of S to P atom is above the stoichiometric ratio (S/P > 4), the residual S atoms interfere with the migration of Li^+. Because isolated S is derived from Li_2S, the conditions under which the amorphous structure is synthesized are quite important. What is needed is an environment in which all the S atoms from Li_2S react. Such an environment is characterized not only by the most appropriate relative amounts of Li_2S and P_2S_5 but also by the process conditions, such as the mechanical milling techniques. Although our modeling involves several assumptions and limitations, including ideal compositions, a single phase of amorphous structures, model size, and sampling steps, the DFT-MD simulations provided important insights that were based on accurate descriptions of the electronic states and atomic interactions.

CONCLUSION

In this study, we used DFT-MD calculations to investigate the structural and dynamical properties of glass sulfide SEs. We initiated the study by modeling the glass structures in *ab initio* fashion. The structures of xLi$_2$S–(100 − x)P$_2$S$_5$ ($x = 67$, 70, 75, and 80) were created by randomly identifying appropriate compositions of Li^+, PS_4^{3-}, $P_2S_7^{4-}$, and S^{2-} and then annealing them with DFT-MD calculations. Because the calculated mass densities as a function of composition corresponded to the mass densities of crystals and because the calculated structure factors were also in good agreement with experimental structures, the model seemed appropriate for simulating the characteristics of sulfide glass.

Second, Li^+ diffusion coefficients were obtained from the DFT-MD calculations at various temperatures for picosecond simulation times. Ionic conductivities evaluated by the Nernst–Einstein relationship at 298.15 K were in the order of 10^{-5} S/cm. The ionic conductivity of the amorphous structure with $x = 75$ was the highest because there was a balance between the number density and the diffusibility of Li^+. The simulations also suggested that isolated sulfur suppresses Li^+ migration.

Our computational methodology is clearly applicable to not only sulfide glasses but also to crystalline phases. In other words, although the size of the model was limited, the study established the efficacy of the method for evaluating the properties of various SEs. Further computational studies may lead to better understanding of the so-called lithium superionic conductors.

AUTHOR CONTRIBUTIONS

All calculations were performed by TB. Analysis and discussion were performed by TB and YK. Manuscript was written by TB and revised by YK.

ACKNOWLEDGMENTS

We thank Akio Mitsui for helpful discussions about structure factors.

SUPPLEMENTARY MATERIAL

The Supplementary Material for this article can be found online at http://journal.frontiersin.org/article/10.3389/fenrg.2016.00022

REFERENCES

Adams, S., and Swenson, J. (2004). Structure conductivity correlation in reverse Monte Carlo models of single and mixed alkali glasses. *Solid State Ionics* 175, 665–669. doi:10.1016/j.ssi.2004.08.038

Adams, S., and Swenson, J. (2005). Bond valence analysis of reverse Monte Carlo produced structural models; a way to understand ion conduction in glasses. *J. Phys. Condens. Matter* 17, S87. doi:10.1088/0953-8984/17/5/010

Allen, M. P., and Tildesley, D. J. (1989). *Computer Simulation of Liquids*. New York: Oxford University Press.

Aotani, N., Iwamoto, K., Takada, K., and Kondo, S. (1994). Synthesis and electrochemical properties of lithium ion conductive glass, Li_3PO_4-Li_2S-SiS_2. *Solid State Ionics* 68, 35–39. doi:10.1016/0167-2738(94)90232-1

Bader, R. F. W. (1990). *Atoms in Molecules: a Quantum Theory*. New York: Oxford University Press.

Benoit, M., Ispas, S., Jund, P., and Jullien, R. (2000). Model of silica glass from combined classical and ab initio molecular-dynamics simulations. *Eur. Phys. J. B* 13, 631–636. doi:10.1007/s100510050079

Bernasconi, M., Chiarotti, G., Focher, P., Scandolo, S., Tosatti, E., and Parrinello, M. (1995). First-principle-constant pressure molecular dynamics. *J. Phys. Chem. Solids* 56, 501–505. doi:10.1016/0022-3697(94)00228-2

Blöchl, P. E. (1994). Projector augmented-wave method. *Phys. Rev. B* 50, 17953–17979. doi:10.1103/PhysRevB.50.17953

Boulineau, S., Courty, M., Tarascon, J.-M., and Viallet, V. (2012). Mechanochemical synthesis of Li-argyrodite Li_6PS_5X (X = Cl, Br, I) as sulfur-based solid electrolytes for all solid state batteries application. *Solid State Ionics* 221, 1–5. doi:10.1016/j.ssi.2012.06.008

Car, R., and Parrinello, M. (1985). Unified approach for molecular dynamics and density-functional theory. *Phys. Rev. Lett.* 55, 2471–2474. doi:10.1103/PhysRevLett.55.2471

Deiseroth, H.-J., Kong, S.-T., Eckert, H., Vannahme, J., Reiner, C., Torsten, Z., et al. (2008). Li_6PS_5X: a class of crystalline Li-rich solids with an unusually high Li^+ mobility. *Angew. Chem. Int. Ed.* 47, 755–758. doi:10.1002/anie.200703900

Fergus, J. (2010). Ceramic and polymeric solid electrolytes for lithium-ion batteries. *J. Power Sources* 195, 4554–4569. doi:10.1016/j.jpowsour.2010.01.076

Giannozzi, P., Baroni, S., Bonini, N., Calandra, M., Car, R., Cavazzoni, C., et al. (2009). QUANTUM ESPRESSO: a modular and open-source software project for quantum simulations of materials. *J. Phys. Condens. Matter* 21, 395502. doi:10.1088/0953-8984/21/39/395502

Graf, M., Kresse, B., Privalov, A. F., and Vogel, M. (2013). Combining ^{7}Li field-cycling relaxometry and stimulated-echo experiments: a powerful approach to lithium ion dynamics in solid-state electrolytes. *Solid State Nucl. Magn. Reson.* 5, 25–30. doi:10.1016/j.ssnmr.2013.01.001

Hall, A., Adams, S., and Swenson, J. (2004). The nature of conduction pathways in mixed alkali phosphate glasses. *Ionics* 10, 396–404. doi:10.1007/BF02378000

Hayamizu, K., and Aihara, Y. (2013). Lithium ion diffusion in solid electrolyte $(Li_2S)_7(P_2S_5)_3$ measured by pulsed-gradient spin-echo 7Li NMR spectroscopy. *Solid State Ionics* 238, 7–14. doi:10.1016/j.ssi.2013.02.014

Hayamizu, K., Aihara, Y., and Machida, N. (2014). Anomalous lithium ion migration in the solid electrolyte $(Li_2S)_7(P_2S_5)_3$; fast ion transfer at short time intervals studied by PGSE NMR spectroscopy. *Solid State Ionics* 259, 59–64. doi:10.1016/j.ssi.2014.02.016

Holzwarth, N., Lepley, N., and Du, Y. A. (2011). Computer modeling of lithium phosphate and thiophosphate electrolyte materials. *J. Power Sources* 196, 6870–6876. doi:10.1016/j.jpowsour.2010.08.042

Homma, K., Yonemura, M., Kobayashi, T., Nagao, M., Hirayama, M., and Kanno, R. (2011). Crystal structure and phase transitions of the lithium ionic conductor Li_3PS_4. *Solid State Ionics* 182, 53–58. doi:10.1016/j.ssi.2010.10.001

Hoover, W. G. (1985). Canonical dynamics: equilibrium phase-space distributions. *Phys. Rev. A* 31, 1695–1697. doi:10.1103/PhysRevA.31.1695

Kamaya, N., Homma, K., Yamakawa, Y., Hirayama, M., Kanno, R., Yonemura, M., et al. (2011). A lithium superionic conductor. *Nat. Mater.* 10, 682–686. doi:10.1038/nmat3066

Knauth, P. (2009). Inorganic solid Li ion conductors: an overview. *Solid State Ionics* 180, 911–916. doi:10.1016/j.ssi.2009.03.022

Kong, S. T., Gun, O., Koch, B., Deiseroth, H. J., Eckert, H., and Reiner, C. (2010). Structural characterisation of the Li argyrodites Li_7PS_6 and Li_7PSe_6 and their solid solutions: quantification of site preferences by MAS-NMR spectroscopy. *Chem. Eur. J.* 16, 5138–5147. doi:10.1002/chem.200903023

Kresse, G., and Joubert, D. (1999). From ultrasoft pseudopotentials to the projector augmented-wave method. *Phys. Rev. B* 59, 1758–1775. doi:10.1103/PhysRevB.59.1758

Laasonen, K., Pasquarello, A., Car, R., Lee, C., and Vanderbilt, D. (1993). Car-Parrinello molecular dynamics with Vanderbilt ultrasoft pseudopotentials. *Phys. Rev. B* 47, 10142–10153. doi:10.1103/PhysRevB.47.10142

Le Roux, S. É., and Petkov, V. (2010). ISAACS – interactive structure analysis of amorphous and crystalline systems. *J. Appl. Crystallogr.* 43, 181–185. doi:10.1107/S0021889809051929

Lepley, N. D., and Holzwarth, N. A. W. (2012). Computer modeling of crystalline electrolytes: lithium thiophosphates and phosphates. *J. Electrochem. Soc.* 159, A538–A547. doi:10.1149/2.jes113225

Lepley, N. D., Holzwarth, N. A. W., and Du, Y. A. (2013). Structures, Li^+ mobilities, and interfacial properties of solid electrolytes Li_3PS_4 and Li_3PO_4 from first principles. *Phys. Rev. B* 88, 104103. doi:10.1103/PhysRevB.88.104103

Liu, Z., Fu, W., Payzant, E. A., Yu, X., Wu, Z., Dudney, N. J., et al. (2013). Anomalous high ionic conductivity of nanoporous β-Li3PS4. *J. Am. Chem. Soc.* 135, 975–978. doi:10.1021/ja3110895

Martyna, G. J., Klein, M. L., and Tuckerman, M. (1992). Nose-Hoover chains: the canonical ensemble via continuous dynamics. *J. Chem. Phys.* 97, 2635–2643. doi:10.1063/1.463940

Massobrio, C., Du, J., Bernasconi, M., and Salmon, P. S. (2015). *Molecular Dynamics Simulations of Disordered Materials*. Switzerland: Springer International Publishing.

Minami, K., Hayashi, A., and Tatsumisago, M. (2010). Preparation and characterization of superionic conducting $Li_7P_3S_{11}$ crystal from glassy liquids. *J. Ceram. Soc. Jpn.* 118, 305–308. doi:10.2109/jcersj2.118.305

Minami, T., Hayashi, A., and Tatsumisago, M. (2006). Recent progress of glass and glass-ceramics as solid electrolytes for lithium secondary batteries. *Solid State Ionics* 177, 2715–2720. doi:10.1016/j.ssi.2006.07.017

Mizuno, F., Hayashi, A., Tadanaga, K., and Tatsumisago, M. (2005). New, highly ion-conductive crystals precipitated from Li_2S-P_2S_5 glasses. *Adv. Mater.* 17, 918–921. doi:10.1002/adma.200401286

Mizuno, F., Hayashi, A., Tadanaga, K., and Tatsumisago, M. (2006). High lithium ion conducting glass-ceramics in the system Li_2S-P_2S_5. *Solid State Ionics* 177, 2721–2725. doi:10.1016/j.ssi.2006.04.017

Mo, Y., Ong, S. P., and Ceder, G. (2012). First principles study of the $Li_{10}GeP_2S_{12}$ lithium super ionic conductor material. *Chem. Mater.* 24, 15–17. doi:10.1021/cm203303y

Mori, K., Ichida, T., Iwase, K., Otomo, T., Kohara, S., Arai, H., et al. (2013). Visualization of conduction pathways in lithium superionic conductors: Li_2S-P_2S_5 glasses and $Li_7P_3S_{11}$ glass-ceramic. *Chem. Phys. Lett.* 584, 113–118. doi:10.1016/j.cplett.2013.08.016

Murakami, M., Shimoda, K., Shiotani, S., Mitsui, A., Ohara, K., Onodera, Y., et al. (2015). Dynamical origin of ionic conductivity for $Li_7P_3S_{11}$ metastable crystal as studied by $^{6/7}$Li and ^{31}P solid-state NMR. *J. Phys. Chem. C* 119, 24248–24254. doi:10.1021/acs.jpcc.5b06308

Nosé, S. (1984). A unified formulation of the constant temperature molecular dynamics methods. *J. Chem. Phys.* 81, 511–519. doi:10.1063/1.447334

Ohara, K., Mitsui, A., Mori, M., Onodera, Y., Shiotani, S., Koyama, Y., et al. (2016). Strucutral and electronic features of binary Li_2S-P_2S_5 glasses. *Sci. Rep.* 6, 21302. doi:10.1038/srep21302

Onodera, Y., Mori, K., Otomo, T., Hannon, A. C., Kohara, S., Itoh, K., et al. (2010). Crystal structure of $Li_7P_3S_{11}$ studied by neutron and synchrotron X-ray powder diffraction. *J. Phys. Soc. Jpn.* 79SA, 87–89. doi:10.1143/JPSJS.79SA.87

Parrinello, M., and Rahman, A. (1981). Polymorphic transitions in single crystals: a new molecular dynamics method. *J. Appl. Phys.* 52, 7182–7190. doi:10.1063/1.328693

Perdew, J. P., Ruzsinszky, A., Csonka, G. I., Vydrov, O. A., Scuseria, G. E., Constantin, L. A., et al. (2008). Restoring the density-gradient expansion for exchange in solids and surfaces. *Phys. Rev. Lett.* 100, 136406. doi:10.1103/PhysRevLett.100.136406

Rao, R. P., and Adams, S. (2011). Studies of lithium argyrodite solid electrolytes for all-solid-state batteries. *Phys. Status Solidi A* 208, 1804–1807. doi:10.1002/pssa.201001117

Ren, Y., Chen, K., Chen, R., Liu, T., Zhang, Y., and Nan, C.-W. (2015). Oxide electrolytes for lithium batteries. *J. Am. Ceram. Soc.* 98, 3603–3623. doi:10.1111/jace.13844

Sun, H. (1998). COMPASS: an ab initio force-field optimized for condensed-phase applications – overview with details on alkane and benzene compounds. *J. Phys. Chem. B* 102, 7338–7364. doi:10.1021/jp980939v

Takada, K. (2013). Progress and prospective of solid-state lithium batteries. *Acta Mater.* 61, 759–770. doi:10.1016/j.actamat.2012.10.034

Tang, W., Sanville, E., and Henkelman, G. (2009). A grid-based Bader analysis algorithm without lattice bias. *J. Phys. Condens. Matter* 21, 084204. doi:10.1088/0953-8984/21/8/084204

Vanderbilt, D. (1990). Soft self-consistent pseudopotentials in a generalized eigenvalue formalism. *Phys. Rev. B* 41, 7892–7895. doi:10.1103/PhysRevB.41.7892

Verlet, L. (1967). Computer "Experiments" on classical fluids. I. Thermodynamical properties of Lennard-Jones molecules. *Phys. Rev.* 159, 98–103. doi:10.1103/PhysRev.159.98

Wada, H., Menetrier, M., Levasseur, A., and Hagenmuller, P. (1983). Preparation and ionic conductivity of new B_2S_3-Li_2S-LiI glasses. *Mater. Res. Bull.* 18, 189–193. doi:10.1016/0025-5408(83)90080-6

Yamane, H., Shibata, M., Shimane, Y., Junke, T., Seino, Y., Adams, S., et al. (2007). Crystal structure of a superionic conductor, $Li_7P_3S_{11}$. *Solid State Ionics* 178, 1163–1167. doi:10.1016/j.ssi.2007.05.020

Yamauchi, A., Sakuda, A., Hayashi, A., and Tatsumisago, M. (2013). Preparation and ionic conductivities of $(100 - x)(0.75Li_2S{\cdot}0.25P_2S_5){\cdot}xLiBH_4$ glass electrolytes. *J. Power Sources* 244, 707–710. doi:10.1016/j.jpowsour.2012.12.001

Yang, J., and Tse, J. S. (2015). First-principles molecular simulations of Li diffusion in solid electrolytes Li_3PS_4. *Comput. Mater. Sci.* 107, 134–138. doi:10.1016/j.commatsci.2015.05.022

Zhang, Z., and Kennedy, J. H. (1990). Synthesis and characterization of the B_2S_3-Li_2S, the P_2S_5-Li_2S and the B_2S_3-P_2S_5-Li_2S glass systems. *Solid State Ionics* 38, 217–224. doi:10.1016/0167-2738(90)90424-P

Conflict of Interest Statement: The authors declare that the research was conducted in the absence of any commercial or financial relationships that could be construed as a potential conflict of interest.

frontiers in Energy Research

ORIGINAL RESEARCH
published: 20 May 2016
doi: 10.3389/fenrg.2016.00020

Electrochemical Stability of $Li_{6.5}La_3Zr_{1.5}M_{0.5}O_{12}$ (M = Nb or Ta) against Metallic Lithium

Yunsung Kim*[1]*, Aeri Yoo*[2]*, Robert Schmidt*[1]*, Asma Sharafi*[1]*, Heechul Lee*[2]*, Jeff Wolfenstine*[3] *and Jeff Sakamoto*[1]*

[1] Department of Mechanical Engineering, University of Michigan, Ann Arbor, MI, USA, [2] Department of Advanced Materials Engineering, Korea Polytechnic University, Siheung, South Korea, [3] Army Research Laboratory, RDRL-SED-C, Adelphi, MD, USA

The electrochemical stability of $Li_{6.5}La_3Zr_{1.5}Nb_{0.5}O_{12}$ (LLZNO) and $Li_{6.5}La_3Zr_{1.5}Ta_{0.5}O_{12}$ (LLZTO) against metallic Li was studied using direct current (DC) and electrochemical impedance spectroscopy (EIS). Dense polycrystalline LLZNO (ρ = 97%) and LLZTO (ρ = 92%) were made using sol–gel synthesis and rapid induction hot-pressing at 1100°C and 15.8 MPa. During DC cycling tests at room temperature (± 0.01 mA/cm^2 for 36 cycles), LLZNO exhibited an increase in Li–LLZNO interface resistance and eventually short-circuiting while the LLZTO was stable. After DC cycling, LLZNO appeared severely discolored while the LLZTO did not change in appearance. We believe the increase in Li–LLZNO interfacial resistance and discoloration are due to reduction of Nb^{5+} to Nb^{4+}. The negligible change in interfacial resistance and no color change in LLZTO suggest that Ta^{5+} may be more stable against reduction than Nb^{5+} in cubic garnet versus Li during cycling.

Keywords: garnet stability, LLZO, electrochemical stability, ceramic electrolyte, interfacial resistance

OPEN ACCESS

Edited by:
Xueliang Andy Sun,
Western University, Canada

Reviewed by:
Hao Liu,
Chinese Academy of Engineering Physics, China
Deyu Qu,
Wuhan University of Technology, China

****Correspondence:***
Jeff Sakamoto
jeffsaka@umich.edu

Specialty section:
This article was submitted to Energy Storage, a section of the journal Frontiers in Energy Research

Received: *29 February 2016*
Accepted: *03 May 2016*
Published: *20 May 2016*

Citation:
Kim Y, Yoo A, Schmidt R, Sharafi A, Lee H, Wolfenstine J and Sakamoto J (2016) Electrochemical Stability of $Li_{6.5}La_3Zr_{1.5}M_{0.5}O_{12}$ (M = Nb or Ta) against Metallic Lithium. Front. Energy Res. 4:20. doi: 10.3389/fenrg.2016.00020

INTRODUCTION

Improving the performance and safety of batteries may be achieved through the development and integration of solid-state ceramic electrolytes into solid-state batteries (Salam et al., 1999; Dudney et al., 2015). While numerous solid-electrolytes exhibit high conductivity, few examples of viable bulk-scale solid-state batteries have been reported (Knauth, 2009; Dudney et al., 2015). One of the challenges in developing solid-state batteries stems from the lack of understanding of solid electrode-solid electrolyte interface stability, specifically of the Li metal–solid electrolyte interface. Owing to the electropositive nature of Li, there are few examples of bulk oxide solid-electrolytes that are stable at 0 V versus Li/Li$^+$. The Perovskite-type Li-ion conductor, lithium lanthanum titanate (LLTO), exhibits one of the highest bulk ionic conductivities (~1 mS/cm) at room temperature (RT) (Inaguma et al., 1993). Similarly, Aono et al. (1990) reported NASICON (Na superionic conductor) type $Li_{1.3}M_{0.3}Ti_{1.7}(PO_4)_3$ (M = Al or Sc, LATP) also exhibits high bulk ionic conductivity (0.7 mS/cm) at RT. However, LLTO and LATP contain Ti^{4+}, which spontaneously reduces to Ti^{3+} upon contact with metallic Li. In addition, despite its known stable cycling behavior, Schwöbel et al. (2015) found LIPON decomposed into Li_3PO_4, Li_3P, Li_3N, and Li_2O when paired with a metallic Li anode. Thus, cells using LIPON to enable Li anodes likely form a kinetically limited passivation layer. Recent reports of garnet type electrolyte suggest that the formulation consisting of lithia, lanthania, and zirconia is stable against metallic Li (Murugan et al., 2007). However, it is known that stoichiometric $Li_7La_3Zr_2O_{12}$ (LLZO) results in the tetragonal polymorph with Li-ion conductivities in the 10^{-5} S/cm range at 25°C (Awaka et al., 2009; Wolfenstine et al., 2012; Thompson et al., 2014). We and others have demonstrated that ~0.4–0.5 mol of Li vacancies are required to stabilize the higher conductivity (~10^{-4} to 10^{-3} S/cm at 25°C) cubic garnet type polymorph (Geiger et al., 2011; Rangasamy et al., 2012; Thompson et al., 2014, 2015). For example, when approximately >0.2 mol of Al^{3+} or Ga^{3+} substitute for Li, >0.4 mol of Li vacancies are created in the LLZO lattice, thus stabilizing the cubic garnet type polymorph (Geiger et al., 2011; Rangasamy et al., 2012). Similarly, when approximately 0.25–0.5 mol of Nb or Ta substitute for Zr, 0.25–0.5 mol of Li vacancies are created, respectively, thus stabilizing the cubic garnet type polymorph (Ohta et al., 2011; Adams and Rao, 2012; Miara et al., 2013). It has been shown that the latter doping scheme (doping on the Zr site) is the approach that results in the highest bulk ionic conductivities approaching 1 mS/cm at 25°C (Ohta et al., 2011; Miara et al., 2013; Thompson et al., 2015). Overall, correlating LLZO formulations with conductivity is reasonably well understood, but understanding the effect of cubic garnet type stabilizing dopants on stability against Li metal is not. Thus, the purpose of this work was to study the electrochemical stability against Li metal for the highest known conductivity garnet type formulations; $Li_{6.5}La_3Zr_{1.5}Nb_{0.5}O_{12}$ (LLZNO) and $Li_{6.5}La_3Zr_{1.5}Ta_{0.5}O_{12}$ (LLZTO).

In this study, cubic garnet type LLZNO and LLZTO powders were synthesized using a sol–gel method taking care to prevent Al contamination. The powders were densified using rapid induction hot-pressing (RIHP) to produce >92% relative density. To achieve high phase purity (e.g., limit the commonly observed pyrochlore $La_2Zr_2O_7$ phase) excess Li_2CO_3 was added after calcination and before hot-pressing. The resulting pellets were characterized in Li–garnet–Li cells for electrochemical stability. Electrochemical impedance spectroscopy (EIS) and direct current (DC) electrochemical techniques were used to characterize interfacial stability. It will be shown that of these two high conductivity garnet type formulations, the Ta dopant is more electrochemically stable against Li metal than Nb.

MATERIALS AND METHODS

Powder Preparation

Cubic Al-free LLZTO and LLZNO with the nominal composition $Li_{6.5}La_3Zr_{1.5}Ta_{0.5}O_{12}$ and $Li_{6.5}La_3Zr_{1.5}Nb_{0.5}O_{12}$ were prepared using a sol–gel synthesis method, respectively (Sakamoto et al., 2013). $LiNO_3{\cdot}x6H_2O$ ($x = 0.5$, 99.999%, Alfa Aesar), $La(NO_3)_3{\cdot}6H_2O$ (99.9% Sigma Aldrich), $Zr(OH_7C_3)$ (70 wt.% in 1-propanol, Sigma Aldrich), and $Nb(OCH_2CH_3)_5$ (99.95%, Sigma Aldrich) and/or $Ta(CH_3C_2H_2O)_5$ (99.98%, Sigma Aldrich) were used as the sol–gel precursors. 1-propanol (anhydrous 99.7%, Sigma Aldrich) and $CH_3OCH_2CH_2OH$ (2-MOE, anhydrous 99.8%, Sigma Aldrich) were used as a solvent, and acetic acid (AC, 1.0M CH_3COOH, Fluka) was used as a chelating agent. The sol–gel process flow chart is shown in **Figure 1**. The Li and La precursors were dissolved in 1-propanol, and Zr and Nb (or Ta) precursors were dissolved in 2-MOE. After the precursors were dissolved, the solutions were combined and stirred until gelation occurred (approximately 45 min) followed by 12 h of aging to assure the reaction was complete. The gels were dried at room temperature for 9 h followed by drying at 450°C for 4 h under air to eliminate organics. The dried powder was cold-pressed into pellets at 10 MPa in a 2 cm diameter stainless steel die. The cold-pressed pellets were then calcined at 900°C for 4 h in an MgO crucible under air. The heating rate was 5°C/min. After calcination, the pellets were manually crushed with an agate mortar and pestle followed by ball-milling for 15 min at 350 rpm using a planetary mill (PM 100; Retsch, Haan, Germany). 80 mL agate vial and 6 agate balls of 10 mm diameter were used 6 and 11 wt.% excess Li_2CO_3 (99.9% Alfa Aesar) were added to LLZNO and LLZTO, respectively, to compensate for Li loss during calcination and densification.

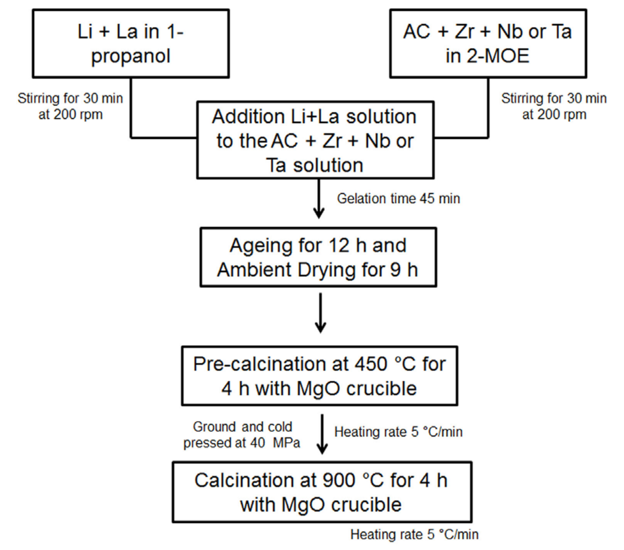

FIGURE 1 | Process flow chart of sol–gel synthesis for $Li_{6.2}La_3Zr_{1.5}Ta_{0.5}O_{12}$ and $Li_{6.2}La_3Zr_{1.5}Nb_{0.5}O_{12}$ powder.

Densification

Al-free LLZNO and LLZTO powders were hot-pressed at 1100°C using a RIHP. A 1.27 cm bore graphite die was used as the susceptor in flowing argon (Rangasamy et al., 2012; David et al., 2015). Since LLZNO and LLZTO powders included excess Li_2CO_3, which melts at ~725°C, a two-step heating profile was used. First, the powder was heated at 1100°C for 15 min without pressure to prevent expulsion of molten Li_2CO_3, followed by the application of 15.8 MPa pressure for 45 min. The cooling rate was 6°C/min. After hot-pressing, each pellet was mounted in Crystalbond® wax and cut into two discs using a diamond saw. To ensure parallel surfaces, the discs were ground with sand paper (400 grit Black ice dry/wet sand paper, Norton Corporation, USA) using a lapping fixture (Model 900; Southbay Technologies, San Clemente, CA, USA) (Kim et al., 2016). The discs were stored in an argon-filled glove box (<1 ppm O_2, <1 ppm H_2O) to minimize surface contamination (Jin and McGinn, 2013; Larraz et al., 2015).

Characterization

The relative densities were defined by dividing the geometric by the theoretical density. The theoretical density was determined by dividing the mass of the atoms in a unit cell by the volume of unit cell determined using X-ray diffraction refinement (XRD, Rigaku Miniflex 600 system, 40 kV and 25 mA).

The phase purity was determined using XRD and Raman spectroscopy (inVia confocal Raman microscope, UK) on of LLZNO and LLZTO before and after cycling test. Raman spectroscopy was performed using a 532 nm green laser and an 1800 line per millimeter holographic grating.

To characterize the stability of the hot-pressed LLZTO and LLZNO samples against Li metal, Li–LLZNO (or LLZTO)–Li symmetric cells were assembled in an argon-filled glove box. To remove the Li_2CO_3 and LiOH surface contamination layers (Jin and McGinn, 2013; Larraz et al., 2015), the hot-pressed LLZNO and LLZTO discs were dry polished with sand paper on a glass plate in the argon-filled glove box. Li foil (Alfa Aesar) was scraped using a spatula to remove the oxide surface layer. A 465 N uniaxial force was applied to the cells and measured using a compression load cell (Omega, LC304-1k, New England, USA).

Direct current cycling was conducted using a potentiostat (VMP300, Bio-Logic, Knoxville) at 23.5 ± 1°C in the argon-filled glove box. Prior to cycling tests, preconditioning cycles were conducted to lower the cell impedance between the LLZNO (or LLZTO) and the Li electrodes. The preconditioning cycles were carried out using ± 0.01 mA/cm^2 at 70°C for 10 cycles (each cycle for 2 h). After preconditioning, DC cycling tests were performed at 23.5 ± 1°C for 36 cycles using ± 0.01 mA/cm^2. The cell impedance was characterized using EIS between 1 Hz to 7 MHz using the 100 mV perturbation amplitude.

The microstructure of the hot-pressed LLZNO and LLZTO pellets was examined using an optical microscope (Meiji EMZ-13TR, Japan) in the argon-filled glove box.

RESULTS AND DISCUSSION

Materials Characterization

The XRD patterns after hot-pressing for LLZNO and LLZTO with/without 6 and 11 wt.% Li_2CO_3 and the reference pattern for cubic garnet LLZO are shown in **Figure 2**. All the hot-pressed samples consisted of the cubic garnet phase, however some secondary phases were observed in the hot-pressed LLZNO and LLZTO without excess Li_2CO_3. The predominant secondary phase was pyrochlore ($La_2Zr_2O_7$) and was present at ~6.2 and 17.7 wt.% estimated from XRD in LLZNO and LLZTO, respectively. Based on the wt.% fraction of pyrochlore present, the excess Li_2CO_3 required to compensate for Li loss was empirically determined to be 6 and 11 wt.% for LLZNO and LLZTO, respectively. Consequently, the hot-pressed cubic LLZNO and LLZTO with no observable secondary phases were obtained except for a small amount of an unknown phase that was present in the hot-pressed LLZNO with 6 wt.% excess Li_2CO_3 (**Figure 2**). The relative densities of the hot-pressed samples were 97% for LLZNO and 92% for LLZTO.

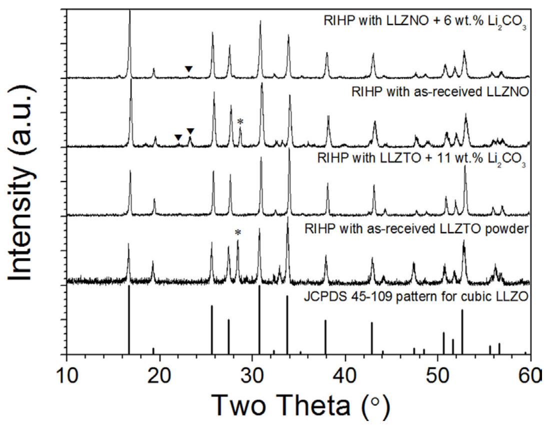

FIGURE 2 | X-ray diffraction patterns of hot-pressed $Li_{6.5}La_3Zr_{1.5}Ta_{0.5}O_{12}$ with 0 and 11 wt.% excess Li_2CO_3, and $Li_{6.5}La_3Zr_{1.5}Nb_{0.5}O_{12}$ with 0 and 6 wt.% excess Li_2CO_3, respectively. *Pyrochlore ($La_2Zr_2O_7$) and ▼ (unknown phase).

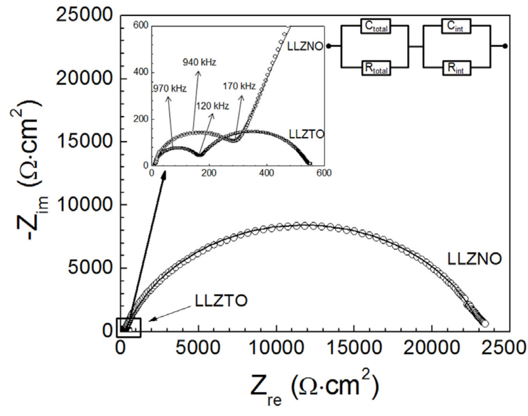

FIGURE 3 | The impedance spectrum with fitted line for as-fabricated Li–LLZNO (or LLZTO)-Li symmetric cells at 23.5 ± 1°C. The solid line corresponds to the fitted the result of the equivalent circuit (○: $Li_{6.5}La_3Zr_{1.5}Nb_{0.5}O_{12}$ and □: $Li_{6.5}La_3Zr_{1.5}Ta_{0.5}O_{12}$).

Initial and after Preconditioning Electrochemical Impedance

Dramatically different cell impedance was observed when comparing LLZNO and LLZTO (**Figure 3**). The impedance spectra are composed of a small semicircle in the high frequency range from 120 kHz to 7 MHz, which is attributed to the total resistance (R_{total}) of the bulk and grain boundaries for the hot-pressed LLZNO (or LLZTO). The relatively large semicircle in the low frequency range between 1 Hz and 120 kHz is attributed to the interfacial resistance (R_{int}) between the hot-pressed LLZNO (or LLZTO) and the Li electrode (**Figure 3**). To determine each impedance and capacitance component, equivalent circuit modeling was conducted. The refined capacitance values for the total resistance of LLZNO (or LLZTO) fall within the range between 10^{-12} and 10^{-8} F/cm^2. In addition, the refined capacitance values for the interfacial resistance between LLZNO (or LLZTO) and the Li electrodes fall within the range of 10^{-7}–10^{-5} F/cm^2. These values are in agreement with the expected capacitance values of the respective charge transport phenomena (Irvine et al., 1990; Thompson et al., 2014; Sharafi et al., 2016). In addition, the total ionic conductivities were 0.48 and 0.66 mS/cm for the hot-pressed LLZTO and LLZNO calculated from the resistance values ($R_{LLZTO} = 156.1\ \Omega\ cm^2$ and $R_{LLZNO} = 280.9\ \Omega\ cm^2$), respectively. These values are in agreement with the reported values in the literature (Ohta et al., 2011; Liu et al., 2014). From **Figure 3**, it is observed that interfacial resistances ($R_{int,LLZTO} = 373.6\ \Omega\ cm^2$ and $R_{int,LLZNO} = 22{,}924\ \Omega\ cm^2$) are relatively large compared to the total cell resistances. The large difference in Li electrode interfacial resistance between the Li–LLZTO and Li–LLZNO could be affected by the difference in relative density (ρ_{LLZTO} = 92% and ρ_{LLZNO} = 97%) of the hot-pressed samples, which would enhance wettability and increase surface area. However, it cannot fully explain the ~61 times higher interfacial resistance of Li–LLZNO compared to that of Li–LLZTO. The cause of this difference will be discussed later. It is known that the Li–garnet interfacial resistance can be reduced by simultaneously heating and cycling (Sharafi et al., 2016). It was suggested that the heat and cycling increased wetting and physical contact between LLZTO (or LLZNO) and the Li electrodes. To emulate previous work, preconditioning was performed at low current density (±0.01 mA/cm^2) for 10 cycles at 70°C. The EIS results after preconditioning are shown in **Figures 4A,B**. A comparison of **Figures 3** and **4** reveals that preconditioning reduced the interfacial resistances by ~39% for the hot-pressed LLZTO (**Figure 4A**) and by ~7% for the hot-pressed LLZNO (**Figure 4B**).

Cycling and Electrochemical Impedance

The results of DC cycling and EIS of the LLZNO and LLZTO cells are shown in **Figure 4**. The EIS spectra were measured after preconditioning (0 cycle), 4, 8, 12, 20, 28, and 36 cycles. From **Figure 4A**, it can be observed that the interfacial resistance of the LLZTO cells remained nearly constant during cycling. It can also be observed that the LLZTO sample exhibited stable DC cycling behavior up to 36 cycles (**Figure 4C**). This suggests that LLZTO is stable against Li during cycling. In contrast, the impedance of the LLZNO cell was dramatically reduced, compared to before preconditioning, after four DC cycles (**Figure 4B**). We believe that the decrease in interfacial resistance during the first four

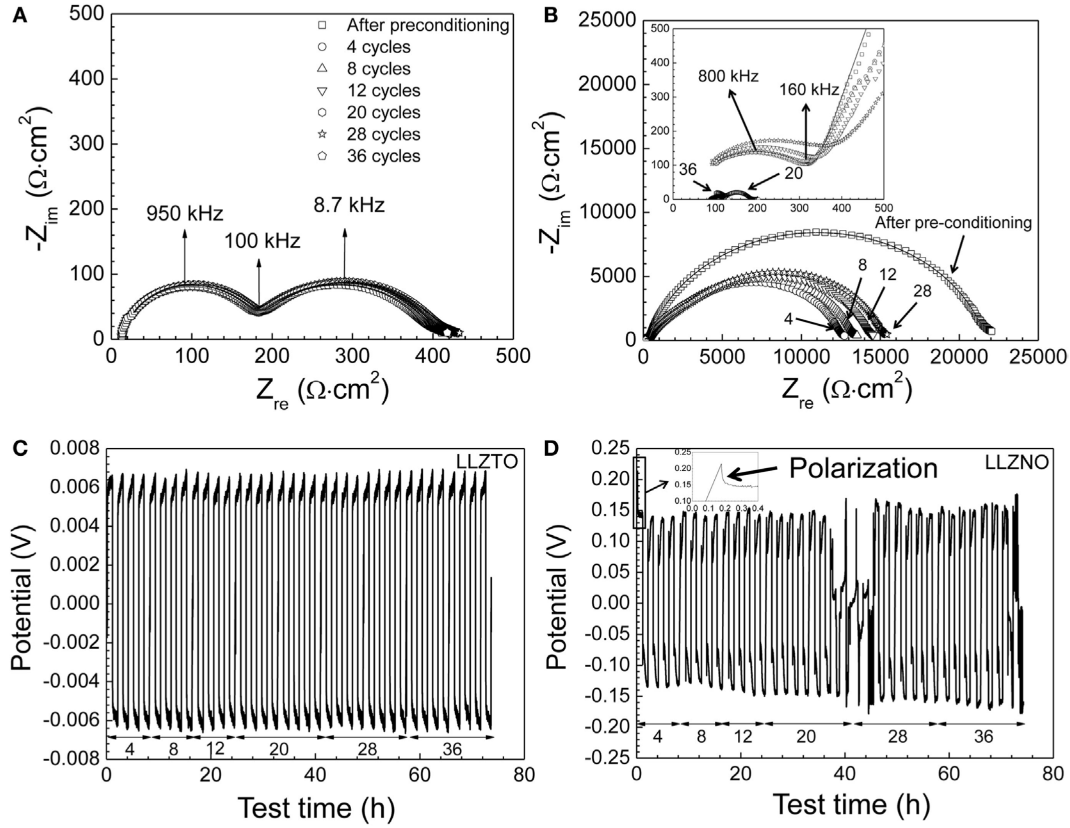

FIGURE 4 | The impedance spectra with fitted line of (A) the Li–$Li_{6.5}La_3Zr_{1.5}Ta_{0.5}O_{12}$–Li cell and (B) the Li–$Li_{6.5}La_3Zr_{1.5}Nb_{0.5}O_{12}$–Li cell as a function of the DC cycling (0, 4, 8, 12, 28, and 36 cycles) at 23.5 ± 1°C, respectively. Since the complexity of the modeling with the $Li_{6.5}La_3Zr_{1.5}Nb_{0.5}O_{12}$ after 4 DC cycles, the modeling with LLZNO was not performed during the cycling tests. The results of the DC cycling for Li–$Li_{6.5}La_3Zr_{1.5}Ta_{0.5}O_{12}$–Li **(C)** and for Li–$Li_{6.5}La_3Zr_{1.5}Nb_{0.5}O_{12}$–Li **(D)** with the 0.01 mA/cm^2 at 23.5 ± 1°C were plotted, respectively. The number of DC cycles was noted below the DC cycling plot.

cycles was due to the plating of Li at the Li–LLZTO interface, which improved contact and reduced interfacial impedance as suggested by Gibson (1976). Gibson (1976) observed a reduction in interfacial impedance after the first few cycles of Na-beta alumina. The increase in impedance with continued cycling suggests that some reaction between LLZNO and Li electrodes had occurred. It is known that Nb^{5+} can be reduced to Nb^{4+} at relatively low potentials (Kodama et al., 2006; Wang et al., 2011). Therefore, the reduction of Nb^{5+} may adversely affect charge transport in LLZNO and/or the formation of a passivating layer. Previous work observed similar behavior in $Li_{6.25}La_3Zr_{1.25}$ $Nb_{0.75}O_{12}$ compared to $Li_{6.25}La_3Zr_{1.25}Ta_{0.75}O_{12}$ (Nemori et al., 2015). Further proof of some interaction between LLZNO and the Li electrodes can observed in **Figure 4D** where short-circuiting of the Li–LLZNO–Li cell occurred during cycling. The potential of the Li–LLZNO–Li cell dramatically decreased after 18 cycles. The occurrence of short-circuiting during DC cycling was in agreement with the EIS measurements (inset in **Figure 4B**) after 20 cycles, where a significant reduction in LLZNO impedance was observed. We believe the short-circuiting was due to the propagation of a Li dendrite through LLZNO (Ishiguro et al., 2013). After 20 cycles, the LLZNO DC cycling behavior was erratic and likely due to Li dendrite forming and breaking-up during continued cycles as observed by Buqa et al. (2005). At cycle 36, a stable Li dendrite likely formed, thus resulting in a short-circuiting.

Characterization after Cycling

The optical images of the hot-pressed LLZTO and LLZNO after 36 cycles of DC cycling are shown in **Figure 5**. Aside from the shiny metallic spots (Li metal) embedded in pores (~8% porosity), there was no evidence of severe discoloration on the surface of the hot-pressed LLZTO before and after DC cycling (**Figure 5A**). Conversely, severe macroscopic discoloration was observed on the surface of the hot-pressed LLZNO (**Figure 5B**). The optical analysis is consistent with the result previously reported by Nemori et al. (2015) and observance of a significant change in the Li–LLZNO impedance spectra (**Figure 4**). The color change in the DC cycled hot-pressed LLZNO confirms that the LLZNO is unstable in contact with Li (**Figure 5B**). Similar discoloration phenomena has been observed in Li_3NbO_4 where darkening, such as the formation of yellow and black regions, resulted from the reduction of Nb^{5+} to Nb^{4+} (Zverev et al., 1972; DeLeo et al., 1988; Nyman et al., 2010). The color change of the hot-pressed LLZNO may be similar to what is observed in the reduction of Nb^{5+} in Li_3NbO_4, which resulted in the loss of Li and/or O. The reduction of Nb^{5+} can affect transport properties (Ishiguro et al., 2013; Nemori et al., 2015), thus a similar phenomenon may occur in the LLZNO causing the interfacial resistance to increase. Conversely, the reduction of Ta^{5+} is less likely compared to Nb^{5+}, which is consistent with the observation that no apparent change in LLZTO was noted in this work (Zverev et al., 1972).

The short-circuiting phenomenon observed during electrochemical characterization (**Figures 4B,D**) also appears to correspond with the optical image of the fracture surface (**Figure 5B**). Macroscopic discoloration was observed on the face and fracture surfaces the hot-pressed LLZNO (**Figure 5B**). Thus, the discoloration through the entire LLZNO pellet could indicate the Li dendrite grew through the hot-pressed LLZNO during cycling test. On the contrary, no color change and/or an evidence of Li dendrite growth were observed on the fracture surface of the hot-pressed LLZTO (**Figure 5A**). These results are in good agreement with the stable DC cycling and EIS behavior up to 36 cycles (**Figures 4A,C**).

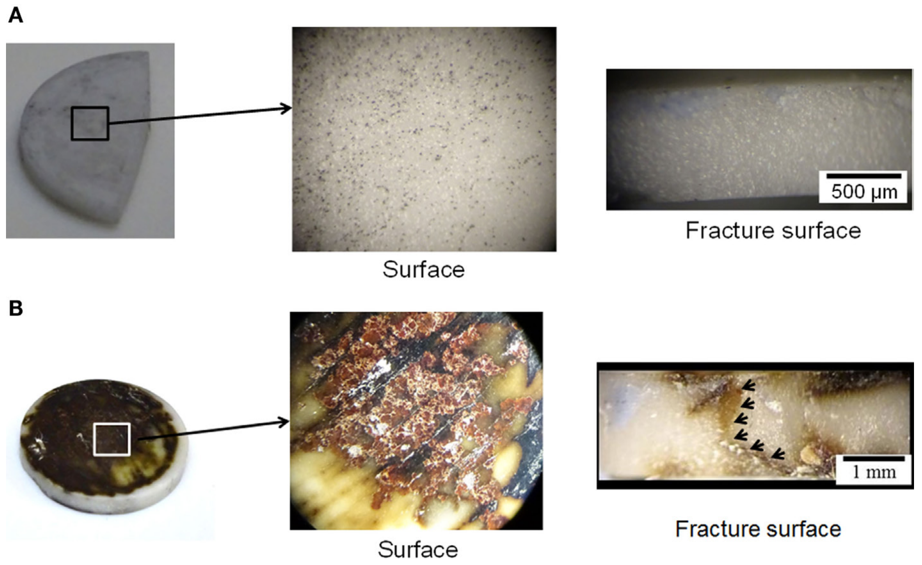

FIGURE 5 | The optical images of the pellet faces and fracture surfaces for the DC cycled hot-pressed (A) $Li_{6.5}La_3Zr_{1.5}Ta_{0.5}O_{12}$ and (B) $Li_{6.5}La_3Zr_{1.5}Nb_{0.5}O_{12}$ after 36 cycles at 23.5 ± 1°C. The arrows indicate the extended dark region across the hot-pressed $Li_{6.5}La_3Zr_{1.5}Nb_{0.5}O_{12}$.

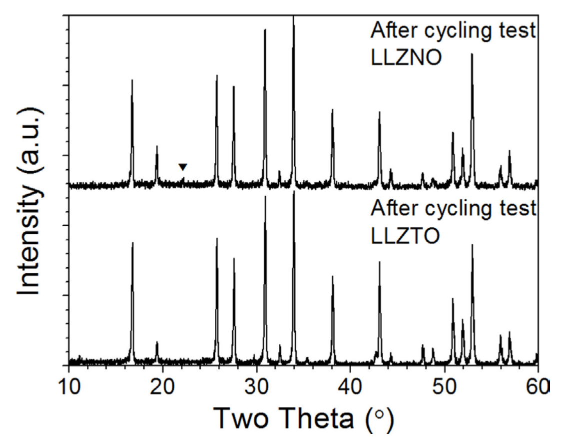

FIGURE 6 | X-ray diffraction patterns of hot-pressed $Li_{6.5}La_3Zr_{1.5}Ta_{0.5}O_{12}$ and $Li_{6.5}La_3Zr_{1.5}Nb_{0.5}O_{12}$ after DC cycling at 23.5 ± 1°C, respectively. ▼ (unknown phase).

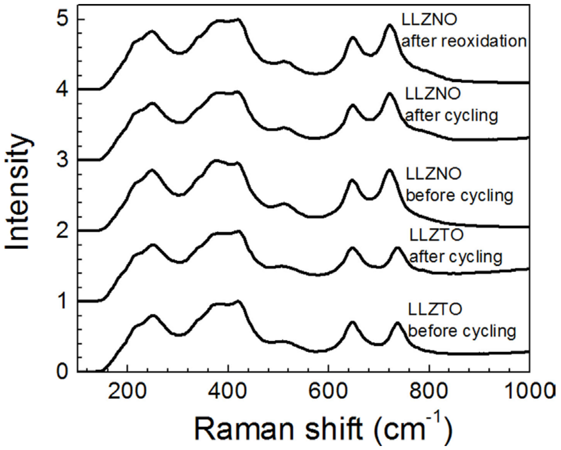

FIGURE 7 | Raman spectra of $Li_{6.5}La_3Zr_{1.5}Ta_{0.5}O_{12}$ and $Li_{6.5}La_3Zr_{1.5}Nb_{0.5}O_{12}$ before and after DC cycling at 23.5 ± 1°C; (top spectrum) LLZNO after DC cycling and after heat treatment at 600°C in air for 2 h.

X-ray diffraction refinement patterns after the 36th cycle for LLZNO and LLZTO are shown in **Figure 6**. No impurity peaks were detected even though the appearance of the hot-pressed LLZNO had undergone significant discoloration after cycling test.

Raman spectroscopy was also conducted to determine if the surface chemistry of LLZNO and LLZTO changed before and after DC cycling (**Figure 7**). The Raman spectra were in good agreement with the results of XRD, which determined that only the cubic garnet phase was present on the surface. In addition, the Raman spectra were consistent with the spectra of cubic LLZTO reported by Thompson et al. (2014). The LLZTO band at ~640 and ~740 cm^{-1} are related with Zr–O bond stretching (Tietz et al., 2013; Larraz et al., 2013) and Ta–O bond stretching (Thompson et al., 2014), respectively. Therefore, the LLZNO band at ~640 and ~720 cm^{-1} of LLZNO can be assigned to the stretching of ZrO_6 and NbO_6 octahedron, respectively. In addition, no peak separation, which could have resulted from the lower symmetry found in the tetragonal phase, was observed in low frequency region (<350 cm^{-1}) after DC cycling. The results of the Raman analysis indicate that the cubic garnet phase was present despite the color change. However, it was possible that the fraction of impurity phases present were too low for detection using conventional benchtop XRD and Raman spectroscopy.

To determine if the LLZNO discoloration after DC cycling was associated with the reduction of Nb^{5+} to Nb^{4+}, the sample was heated in ambient air at 600°C for 2 h. After heating in air, the dark discoloration was converted back to the original white color. In addition, Raman showed no change in the structure after cycling and re-oxidation (**Figure 7**). This suggests that the color change could be associated with a change in valence from Nb^{5+} to Nb^{4+}.

CONCLUSION

The electrochemical stability of the LLZTO and LLZNO against Li was investigated. The LLZTO and LLZNO powders, which were synthesized using sol–gel, were hot-pressed for 1 h at 1100°C, resulting in 92 and 97% relative densities, respectively. The cubic garnet type phase for both LLZTO and LLZNO were obtained by adding excess Li_2CO_3 (6 wt.% for LLZNO and 11 wt.% for LLZTO).

Direct current and EIS were conducted on Li–LLZNO (or LLZTO)–Li cells. Several observations were made from these tests. First, preconditioning at 70°C reduced cell impedance likely due to improved physical contact and wettability between the LLZNO (or LLZTO) and the Li electrode. Second, the resistance of the Li–LLZNO interface significantly decreased after four DC cycles. We believe that electrochemical Li deposition onto the surface resulted in enhanced physical contact between Li and LLZNO compared to the as-assembled cell impedance. Subsequently, the resistance of Li–LLZNO increased with continued DC cycling while that of Li–LLZTO interface remained constant up to 36 DC cycles at 23.5 ± 1°C. Third, LLZNO severely discolored while LLZTO did not change after DC cycling. We believe that the increase in interfacial resistance and discoloration in LLZNO are a result of the reduction of Nb^{5+} to Nb^{4+}. The color change of DC cycled LLZNO from dark to original white after heat treatment at 600°C for 2 h supports the reduction of Nb^{5+} to Nb^{4+} during DC cycling. In contrast, there was no evidence of Ta^{5+} instability in LLZTO after DC cycling. Overall, the results of this study indicate while numerous supervalent dopants can stabilize the high Li-ion conducting garnet phase, not all are stable against reduction in contact with metallic Li.

AUTHOR CONTRIBUTIONS

YK conducted the majority of experiments and wrote the majority of the manuscript. AY synthesized the LLZNO and LLZTO garnet powder by sol–gel. RS performed the part of densification experiments. AS coordinated the electrochemical test conditions and analysis work. HL designed the sol–gel synthesis process and made intellectual contribution to this work. JW made intellectual contribution and provided background and data analysis of the manuscript. JS designed this work concept and made intellectual contribution and edited the manuscript.

REFERENCES

Adams, S., and Rao, R. P. (2012). Ion transport and phase transition in $Li_{7-x}La_3(Zr_{2-x}M_x)O_{12}$ (M=Ta^{5+}, Nb^{5+}, x=0, 0.25). *J. Mater. Chem.* 22, 1426–1434. doi:10.1039/C1JM14588F

Aono, H., Sugimoto, E., Sadaoka, Y., Imanaka, N., and Adachi, G. (1990). Ionic conductivity of solid electrolytes based on lithium titanium phosphate. *J. Electrochem. Soc.* 137, 1023–1027. doi:10.1149/1.2086597

Awaka, J., Kijima, N., Hayakawa, H., and Akimoto, J. (2009). Synthesis and structure analysis of tetragonal $Li_7La_3Zr_2O_{12}$ with the garnet-related type structure. *J. Solid State Chem.* 182, 2046–2052. doi:10.1016/j.jssc.2009.05.020

Buqa, H., Goers, D., Holzapfel, M., Spahr, M. E., and Novak, P. (2005). High rate capability of graphite negative electrodes for lithium-ion batteries. *J. Electrochem. Soc.* 152, A474–A481. doi:10.1149/1.1851055

David, N. I., Thompson, T., Wolfenstine, J., Allen, J. L., and Sakamoto, J. (2015). Microstructure and Li-ion conductivity of hot-pressed cubic $Li_7La_3Zr_2O_{12}$. *J. Am. Ceram. Soc.* 98, 1209–1214. doi:10.1111/jace.13455

DeLeo, G. G., Dobson, J. L., Masters, M. F., and Bonjack, L. H. (1988). Electronic structure of an oxygen vacancy in lithium niobate. *Phys. Rev. B* 37, 8394–8400. doi:10.1103/PhysRevB.37.8394

Dudney, N. J., West, W. C., and Nanda, J. (2015). *Handbook of Solid State Batteries*. Singapore: World Scientific.

Geiger, C. A., Alekseev, E., Lazic, B., Fisch, M., Armbruster, T., Langner, R., et al. (2011). Crystal chemistry and stability of "$Li_7La_3Zr_2O_{12}$" garnet: a fast lithium-ion conductor. *Inorg. Chem.* 50, 1089–1097. doi:10.1021/ic101914e

Gibson A. (1976). "A study of the electrode interface formed between sodium metal and beta alumina solid electrolyte," in *Proc. of the 10th Int. Power Sources Sym*, Brighton, England.

Inaguma, Y., Liquan, C., Itoh, M., Nakamura, T., Uchida, T., Ikuta, H., et al. (1993). High ionic conductivity in lithium lanthanum titanate. *Solid State Ionics.* 86, 689–693. doi:10.1016/0038-1098(93)90841-A

Irvine, J. T. S., Sinclair, D. C., and West, A. R. (1990). Electroceramics: characterization by impedance spectroscopy. *Adv. Mater.* 2, 132–138. doi:10.1002/adma.19900020304

Ishiguro, K., Nakata, Y., Matsui, M., Uehi, I., Takeda, Y., Yamamoto, O., et al. (2013). Stability of Nb-doped cubic $Li_7La_3Zr_2O_{12}$ with lithium metal. *J. Electrochem. Soc.* 160, A1690–A1693. doi:10.1149/2.036310jes

Jin, Y., and McGinn, P. J. (2013). $Li_7La_3Zr_2O_{12}$ electrolyte stability in air and fabrication of a Li/$Li_7La_3Zr_2O_{12}$/Cu0.1V2O5 solid-state battery. *J. Power Sources* 239, 326–331. doi:10.1016/j.jpowsour.2013.03.155

Kim, Y., Jo, H., Allen, J. L., Choe, H., Wolfenstine, J., and Sakamoto, J. (2016). The effect of relative density on the mechanical properties of hot-pressed cubic $Li_7La_3Zr_2O_{12}$. *J. Am. Ceram. Soc.* 99, 1367–1374. doi:10.1111/jace.14084

Knauth, P. (2009). Inorganic solid Li ion conductors: an overview. *Solid State Ionics.* 180, 911–916. doi:10.1016/j.ssi.2009.03.022

Kodama, R., Terada, Y., Nakai, I., Komaba, I., Komaba, S., and Kumagai, N. (2006). Electrochemical and in situ XAFS-XRD investigation of Nb_2O_5 for rechargeable lithium batteries. *J. Electrochem. Soc.* 153, A583–A588. doi:10.1149/1.2163788

Larraz, G., Orera, A., and Sanjuan, M. L. (2013). Cubic phases of garnet-type $Li_7La_3Zr_2O_{12}$: the role of hydration. *J. Mater. Chem.* A1, 11419–11428. doi:10.1039/C3TA11996C

Larraz, G., Orera, A., Sanz, J., Sobrados, I., Diez-Gomez, V., and Sanjuan, M. L. (2015). NMR study of Li distribution in $Li_{7-x}H_xLa_3Zr_2O_{12}$ garnets. *J. Mater. Chem. A* 3, 5683–5691. doi:10.1039/C4TA04570J

Liu, K., Ma, J. T., and Wang, C. A. (2014). Excess lithium salt functions more than compensating for lithium loss when synthesizing $Li_{6.5}La_3Ta_{0.5}Zr_{1.5}O_{12}$ in alumina crucible. *J. Power Sources* 260, 109–114. doi:10.1016/j.jpowsour.2014.02.065

Miara, L. J., Ong, S. P., Mo, Y., Richards, D. R., Park, Y., Lee, J. M., et al. (2013). Effect of Rb and Ta doping on the ionic conductivity and stability of the garnet $Li_{7+2x-y}(La_{3-x}Rb_x)(Zr_{2-y}Ta_y)O_{12}$ ($0 \leq x \leq 0.375$, $0 \leq y \leq 1$) superionic conductor: a first principles investigation. *Chem. Mater.* 25, 3048–3055. doi:10.1021/cm401232r

FUNDING

YK, RS, AS, JW, and JS would like to acknowledge support from the Advanced Research Projects Agency-Energy (DE-AR0000399) and from Department of Energy (DE-EE-00006821).

Murugan, R., Thangadurai, V., and Weppner, W. (2007). Fast lithium ion conduction in garnet-type $Li_7La_3Zr_2O_{12}$. *Angew. Chem. Int. Ed.* 46, 7778–7781. doi:10.1002/anie.200701144

Nemori, H., Matsuda, Y., Mitsuoka, S., Matsui, M., Yamamoto, O., Takeda, Y., et al. (2015). Stability of garnet-type solid electrolyte $Li_xLa_3A_{2-y}B_yO_{12}$ (A=Nb or Ta, B=Sc or Zr). *Solid State Ionics.* 282, 7–12. doi:10.1016/j.ssi.2015.09.015

Nyman, M., Alam, T. M., McIntyre, S. K., Bleier, G. C., and Ingersoll, D. (2010). Alternative approach to increasing Li mobility in Li-LaNb/Ta garnet electrolytes. *Chem. Mater.* 22, 5401–5410. doi:10.1021/cm101438x

Ohta, S., Kobayashi, T., and Asaoka, T. (2011). High lithium ionic conductivity in the garnet-type oxide $Li_{7-x}La_3(Zr_{2-x}, Nb_x)O_{12}$ (X=0-2). *J. Power Sources* 196, 3342–3345. doi:10.1016/j.jpowsour.2010.11.089

Rangasamy, E., Wolfenstine, J., and Sakamoto, J. (2012). The role of Al and Li concentration on the formation of cubic garnet solid electrolyte of nominal composition $Li_7La_3Zr_2O_{12}$. *Solid State Ionics.* 206, 28–32. doi:10.1016/j.ssi.2011.10.022

Sakamoto, J., Rangasamy, E., Kim, H., Kim, Y., and Wolfenstine, J. (2013). Synthesis of nano-scale fast ion conducting cubic $Li_7La_3Zr_2O_{12}$. *Nanotechnology* 24, 424005. doi:10.1088/0957-4484/24/42/424005

Salam, F., Brike, P., and Weppner, W. (1999). Solid-state CO_2 sensor with Li_2CO_3-MgO electrolyte and $LiMn_2O_4$ as solid reference electrode. *Electrochem. Solid State Lett.* 2, 201–204. doi:10.1149/1.1390783

Schwöbel, A., Hausbrabd, R., and Jaegermann, W. (2015). Interface reaction between LIPON and lithium studied by in-situ X-ray photoemission. *Solid State Ionics.* 273, 51–54. doi:10.1016/j.ssi.2014.10.017

Sharafi, A., Meyer, H. M., Nanda, J., Wolfenstine, J., and Sakamoto, J. (2016). Characterizing the Li-$Li_7La_3Zr_2O_{12}$ interface stability and kinetics as a function of temperature and current density. *J. Power Sources* 302, 135–139. doi:10.1016/j.jpowsour.2015.10.053

Thompson, T., Sharafi, A., Johannes, M. D., Huq, A., Allen, J. L., Wolfenstine, J., et al. (2015). A tale of two sites: on defining the carrier concentration in garnet-based ionic conductors for advanced Li batteries. *Adv. Energy Mater.* 1500096, 1–9. doi:10.1002/aenm.201500096

Thompson, T., Wolfenstine, J., Allen, J. L., Johannes, M., Huq, A., David, I. N., et al. (2014). Tetragonal vs. cubic phase stability in Al-free Ta doped $Li_7La_3Zr_2O_{12}$. *J. Mater. Chem. A* 2, 13431–13436. doi:10.1039/C4TA02099E

Tietz, F., Wegener, T., Gerhards, M. T., Giarola, M., and Mariotto, G. (2013). Synthesis and Raman micro-spectroscopy investigation of $Li_7La_3Zr_2O_{12}$. *Solid State Ionics* 230, 77–82. doi:10.1016/j.ssi.2012.10.021

Wang, X. J., Krumeich, F., Worle, M., Nesper, R., Jantsky, L., and Fiellvag, H. (2011). Niobium(V) oxynitride: synthesis, characterization, and feasibility as anode material for rechargeable lithium-ion batteries. *Chem. Eur. J.* 18, 5970–5978. doi:10.1002/chem.201102653

Wolfenstine, J., Rangasamy, E., Allen, J. L., and Sakamoto, J. (2012). High conductivity of dense tetragonal $Li_7La_3Zr_2O_{12}$. *J. Power Sources* 208, 193–196. doi:10.1016/j.jpowsour.2012.02.031

Zverev, G. M., Levchuk, E. A., Pashkov, V. A., and Poryadin, Y. D. (1972). Laser-radiation-induced damage to the surface of lithium niobate and tantalite single crystals. *Sov. J. Quantum Electron.* 2, 167–169. doi:10.1070/QE1972v002n02ABEH004409

frontiers
in Energy Research

ORIGINAL RESEARCH
published: 13 May 2016
doi: 10.3389/fenrg.2016.00018

The Electrochemical Characteristics and Applicability of an Amorphous Sulfide-Based Solid Ion Conductor for the Next-Generation Solid-State Lithium Secondary Batteries

***Yuichi Aihara*[1]*, *Seitaro Ito*[1], *Ryo Omoda*[1], *Takanobu Yamada*[1], *Satoshi Fujiki*[1], *Taku Watanabe*[1], *Youngsin Park*[2] *and Seokgwang Doo*[2]**

[1] Samsung R&D Institute Japan, Minoo-shi, Japan, [2] Samsung Advanced Institute of Technology, Samsung Electronics Co., Ltd, Suwon-si, South Korea

Sulfide-based solid electrolytes (SEs) are of considerable practical interest for all solid-state batteries due to their high ionic conductivity and pliability at room temperature. In particular, iodine containing lithium thiophosphate is known to exhibit high ionic conductivity, but its applicability in solid-state battery remains to be examined. To demonstrate the possibility of the iodine-doped SE, LiI–Li_3PS_4, was used to construct two different types of test cells: Li/SE/S and Li/SE/$LiNi_{0.80}Co_{0.15}Al_{0.05}$ cells. The SE, LiI–Li_3PS_4, showed a high ionic conductivity approximately 1.2 mS cm^{-1} at 25°C. Within 100 cycles, the capacity retention was better in the Li/SE/S cell, and no redox shuttle was observed due to physical blockage of SE layer. The capacity fade after 100 cycles in Li/SE/S cell was approximately 4% from the maximum capacity observed at 10th cycle. In contrast, the capacity fade was much larger in Li/SE/$LiNi_{0.80}Co_{0.15}Al_{0.05}$ cell, probably due to the decomposition of the electrolyte at the operating potential range. Nevertheless, both the Li/SE/$LiNi_{0.80}Co_{0.15}Al_{0.05}$ and Li/SE/S cells exhibited high coulombic efficiencies above 99.6 and 99.9% during charge–discharge cycle test, respectively. This indicates that a high energy density can be achieved without an excess lithium metal anode. In addition, it was particularly interesting that the SE showed a reversible capacity about 260 mAh g^{-1}_{SE} (the value calculated using the net solid electrolyte weight). This electrolyte may behave not only as an ionic conductor but also as a catholyte.

Keywords: solid-state battery, solid electrolyte, lithium–sulfur batteries, lithium secondary batteries, sulfide electrolyte, catholyte

OPEN ACCESS

Edited by:
Fuminori Mizuno,
Toyota Research Institute of North America, USA

Reviewed by:
Yongguang Zhang,
Hebei University of Technology, China
Xiao-Liang Wang,
Seeo Inc., USA

****Correspondence:***
Yuichi Aihara
yuichi.aihara@samsung.com

Specialty section:
This article was submitted to Energy Storage, a section of the journal Frontiers in Energy Research

Received: *01 February 2016*
Accepted: *18 April 2016*
Published: *13 May 2016*

Citation:
Aihara Y, Ito S, Omoda R, Yamada T, Fujiki S, Watanabe T, Park Y and Doo S (2016) The Electrochemical Characteristics and Applicability of an Amorphous Sulfide-Based Solid Ion Conductor for the Next-Generation Solid-State Lithium Secondary Batteries. Front. Energy Res. 4:18. doi: 10.3389/fenrg.2016.00018

INTRODUCTION

Nowadays, requirements for batteries have been increasingly stringent in terms of energy density and safety because of the diversity of functions of electronic devices and their usage as a power source especially in transportation. Lithium ion batteries (LIBs) have been in the market over two decades because of their high energy density, but even better batteries have been sought to meet ever stricter requirements (Scrosati and Garche, 2010). Solid-state lithium batteries have received considerable attention since the inception of primary and secondary lithium batteries (Weppner, 1981). From viewpoints of (1) theoretical capability and (2) physical properties, solid-state lithium batteries have been believed to be next-generation power sources. Unfortunately, the commercial applications of all solid-state batteries are limited to a few cases, such as the Li–I primary battery, and thin film type solid-state batteries because of serious technical challenges (Bates et al., 1993).

Recently, fast lithium ion conductors have been found in sulfide compounds (Kamaya et al., 2011). A large difference between typical oxide- and sulfide-based solid electrolytes (SEs) is in their physicomechanical properties, especially on their deformability. In particular, a large grain boundary resistance, observed in oxide SEs, does not unambiguously exist in many sulfide SEs because of the pliable nature of the sulfide compounds; seamless reaction interfaces can be easily formed by a cold press without high temperature sintering (Tatsumisago et al., 2002). Recently, excellent cell characteristics have been reported using a small pellet cell (Ogawa et al., 2012). Unfortunately, most of these studies adopted a Li–In alloy, because of its stable cycle due to the solid solution, unlike a dissolution–deposition reaction. As well as a conventional LIB, a rocking chair type all-solid-state battery (Ogawa et al., 2012) and Li–S battery (Nagata and Chikusa, 2014) have also been proposed. We have shown the possibility of a practical 2-Ah class all-solid LIB using a sulfide electrolyte (Ito et al., 2014). We also have investigated the anode kinetics using Li_3PS_4, i.e., Li_2S:P_2S_5 = 75:25 (Yamada et al., 2015). Use of the solid-state electrolyte greatly facilitates the design of a highly save battery unlike the ones using flammable organic liquid solvents.

Among many sulfide compounds, lithium thiophosphates containing halogens exhibit relatively high ionic conductivities. Mercier et al. (1981) reported a structure and property relation of Li_2S–P_2S_5–LiI systems. They reported that the addition of LiI to Li_2S–P_2S_5 lowered the glass transition temperature, and the material had a high ionic conductivity of approximately 10^{-3} S cm^{-1} at 25°C when the molar ratio of LiI:$0.66Li_2S$–$0.33P_2S_5$ is 0.45. Ohtomo et al. (2013) investigated the electrochemical stability and ionic conductivity of LiI–Li_2O–Li_2S–P_2S_5 glass. They found that 30LiI–70 ($0.07Li_2O$–$0.68Li_2S$–$0.25P_2S_5$) is stable over 0–10 V and exhibited a high ionic conductivity of 1.3×10^{-3} S cm^{-1}. The stability and ionic conductivity of Li7P2S8I was reported by Rangasamy et al. (2015). They observed that the addition of iodine to the β-Li_3PS_4-based structure resulted in good electrochemical stability against an Li metal anode while maintaining a conductivity of 6.3×10^{-4} S cm^{-1} at room temperature. These literatures indicate that iodine-containing lithium thiophosphates have great potential and that there is considerable practical interest in investigating the applicability of this class of materials as SE in all solid-state batteries.

In this paper, we report the cell cycle characteristics longer than 100 cycles with the theoretical sulfur redox capacity plus the electrolyte redox capacity, using an amorphous LiI–Li_3PS_4 electrolyte, referring with $LiNi_{0.80}Co_{0.15}Al_{0.05}$ (NCA) cathode. To clarify the origin of the excess cell capacity from a net sulfur specific capacity, the electrolyte was also tested as a cathode. It was found that amorphous LiI–Li_3PS_4 had a reversible capacity of about 260 mAh g^{-1} within the potential range of 1.3–2.7 V versus Li/Li$^+$. The possibility of using a sulfide-based solid electrolyte in solid-state lithium secondary batteries using was also discussed.

EXPERIMENTAL

Materials

The solid-state electrolyte (SE), LiI–Li_3PS_4, was prepared by the mechanical milling method in an Ar-gas-filled vessel was used for above preparation to prevent degradation of the sample. Specifically, 35 mol% of LiI (Aldrich, 99.999%) and 65mol% of $0.75Li_2S$ (Alfa, 99.9%)–$0.25P_2S_5$ (Aldrich, 99%) were mixed at 380 rpm for 35 h (70 cycles of 20 min of operation and 10 min of interval) by using Fritsch (Idar-Oberstein) P-5 grinding bowl fasteners. The synthesized electrolyte was characterized using Raman spectroscopy (JASCO, NRS-3100, Tokyo) and X-ray diffraction (XRD, CuKα, 45 kV, 40 mA, Panalytical, Empyrean XRD, Almelo).

$LiNi_{0.80}Co_{0.15}Al_{0.05}$ (NCA) was coated with Li_2O–ZrO_2 (LZO) and was used for the reference cathode material. The preparation of LZO–NCA was given in our previous report (Ito et al., 2014). An NCA cathode composite was prepared by mixing the LZO–NCA, LiI–Li_3PS_4 and a vapor grown carbon fiber (VF, the fiber diameter: approximately 200–500 nm, the length: approximately 5–10 μm) in the weight ratio of 0.60:0.35:0.05 using a mortar (hand mixing) in an Argon box (MBraun, LABmaster dp, $H_2O < 0.1$ ppm, $O_2 < 0.1$ ppm).

For preparing the lithium-sulfur (Li–S) cell, the carbon-sulfur (C–S) composite was first prepared using the ball milling method. Dried sulfur powder (Alfa Aesar) was mixed with an activated carbon (MAXSORB® MSC-30, Kansai Coke and Chemicals Co., Ltd.) in the weight ratio of 26:74 wt% in an argon-filled 45-mL zirconia vessel by using high-energy ball milling at 370 rpm for 10 h (20 cycles of 20 min operation and 10 min interval). Then, the C–S composite was further mixed with LiI–Li_3PS_4 (SE) in the weight ratio 0.5:0.5 to make a carbon-sulfur-solid electrolyte (C–S–SE) composite, using the same high energy ball milling method. The mixing procedure is the same as for the C–S preparation. The weight fraction of the prepared sulfur cathode composite was 0.37:0.13:0.50 for sulfur:carbon:LiI–Li_3PS_4. The C–SE composite (0.21:0.79) was similarly prepared using the ball milling method. Lithium foil (t = 30 μm, Honjo Metal, Osaka) was used for the anode.

Differential scanning calorimetry (DSC) was performed on a SII X-DSC7000 calorimeter (Seiko SII, Tokyo) using an Ar-filled closed pan for the prepared LiI, Li_3PS_4, LiI–Li_3PS_4, C–S–SE, and C–SE composites. The measurements were performed between room temperature and 400°C with scanning rate of 2°min^{-1}.

For the evaluation of the applicability of cathode materials, the in-house electrochemical cell (two electrodes cell, φ 13 mm) was adopted. The cell preparation method and the schematic structure are also described in our previous paper (Ito et al., 2014). The details of the prepared cells are listed in **Table 1**.

Electrochemical Measurements

The ionic conductivity of the SE was determined from the cell constant and bulk resistance observed in electrochemical

TABLE 1 | Specification of the test cells.

	S-cell	NCA-cell
Cathode active material weight fraction (wt%)	37	60
Cathode composite loading (mg · cm^{-2})	2.7	11.3
Active material loading (mg · cm^{-2})	1.0	6.8
Active material/carbon ratio (w/w)	2.9	(12.0)
Cell capacity (mAh)	2.1	1.2
Cathode area specific capacity (mAh · cm^{-2})	1.6	0.9
Anode area specific capacity (mAh · cm^{-2})	23.2	23.2
Anode/cathode capacity ratio	14.5	25.8
Utilization of anode at DOD = 100% (%)	6.9	4.0

DOD, depth of discharge.

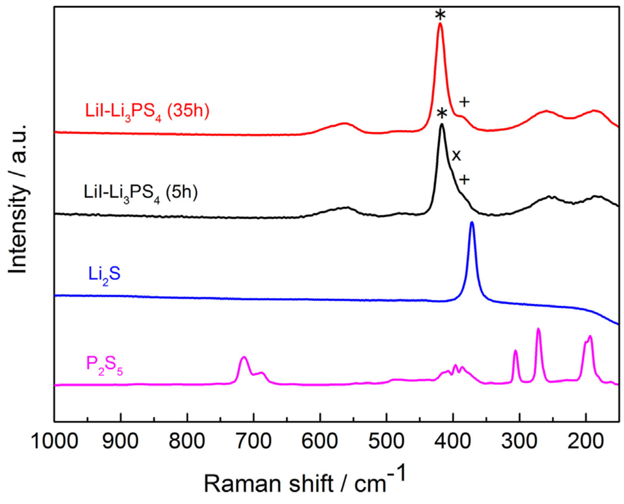

FIGURE 1 | Raman spectra of the starting materials and the solid-state electrolyte, LiI–Li$_3$PS$_4$ after ball milling for 5 h (black) and 35 h (red). *420 cm^{-1}: stretching of PS$_4$ anion; x405 cm^{-1}: stretching of P$_2$S$_7$ anion; +387 cm^{-1}: stretching of P$_2$S$_6$ anion.

impedance spectroscopy (EIS). The EIS was performed using an AUTOLAB PGSTAT30 with an frequency response analysis FRA module (Metrohm Autolab, Utrecht) controlled by a personal computer. Linear sweep voltammetry (LSV) was performed using the same equipment. An asymmetric two electrodes cell with a Pt working electrode and a lithium counter (reference) electrode was prepared for LSV. The galvanostatic charge/discharge profiles were obtained using a battery test station, TOSCAT3100 (Toyo system, Iwaki) at 25°C position in a temperature chamber.

RESULTS

Characterization of LiI–Li$_3$PS$_4$

The crystallinity and anion structure of the SE, LiI–Li$_3$PS$_4$, was characterized by Raman spectroscopy (**Figure 1**) and XRD (**Figure 2**). It is clear from the Raman spectra that the reaction proceeded because of the high-energy ball milling within the first 5 h. After 35 h of ball milling, the intensities of the P$_2$S$_7$ dimer diminished in the spectrum. However, even after 35 h, the P$_2$S$_6$ peak was not completely suppressed. Furthermore, some reaction residue of LiI was found in the XRD pattern. The XRD pattern and Raman spectrum did not show any obvious change after 35 h, and so synthesis was discontinued at this point. From the above results, the synthesized electrolyte was mostly amorphous containing a small fraction of P$_2$S$_6$ dimer and crystalline LiI. The main anion frame structure was ortho-PS_4^- (and I$^-$).

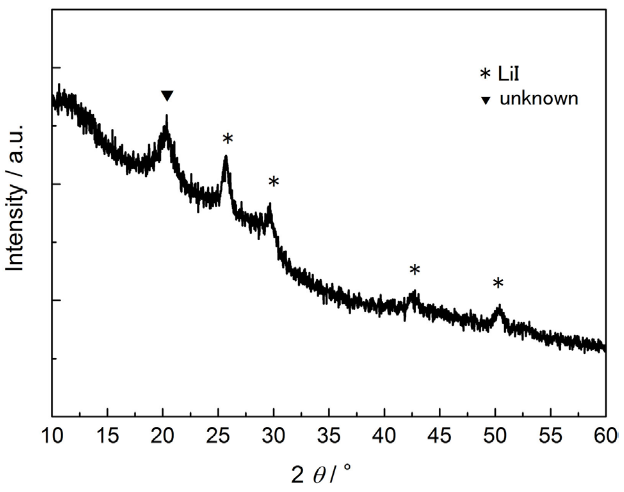

FIGURE 2 | X-ray diffraction of LiI-Li$_3$PS$_4$. *Peaks assigned in the reaction residue of LiI crystalline. Li$_2$S was completely consumed by the reaction.

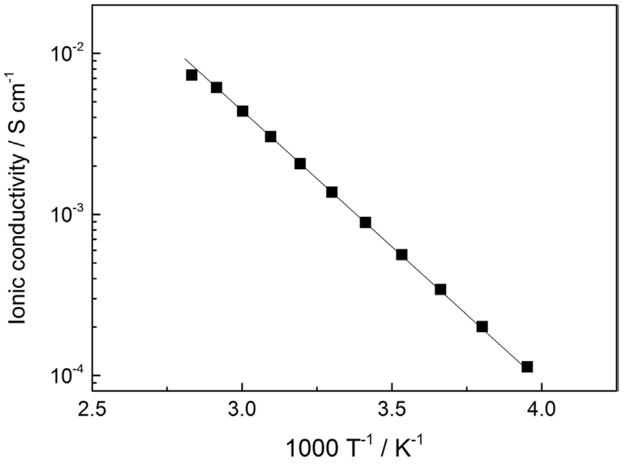

FIGURE 3 | Arrhenius plot of the ionic conductivity of LiI–Li$_3$PS$_4$.

The temperature dependence of the ionic conductivity for LiI–Li$_3$PS$_4$ is plotted in **Figure 3**. The temperature dependence was a typical Arrhenius type, and the activation energy of the ionic conductivity was 29.1 ± 1.1 kJ mol^{-1}. The ionic conductivity was 1.2 mS cm^{-1} at 25°C, and it is approximately 10 times than that of amorphous Li$_3$PS$_4$ SE (Yamada et al., 2015).

The electrochemical stability of the electrolyte was determined using LSV (**Figure 4**). The potential was scanned from the open circuit potential to 5.0 V versus co-counter/reference electrodes of Li/Li$^+$. At 2.8 V, a small spike peak was observed for LiI–Li$_3$PS$_4$.

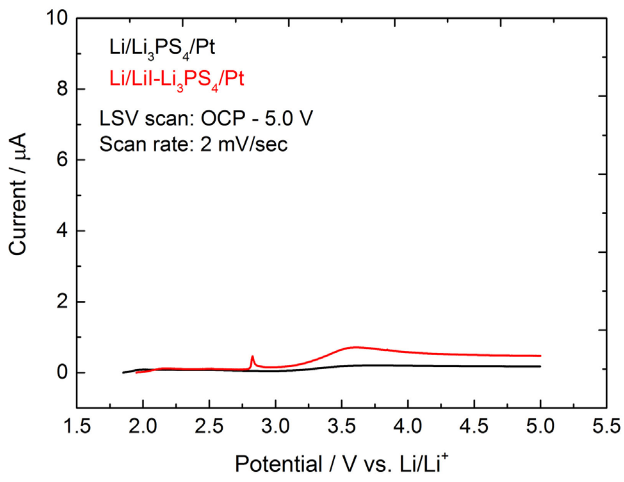

FIGURE 4 | Linear sweep voltammogram of Li_3PS_4 and LiI–Li_3PS_4 at 25°C. WE: Pt, CE-RE: Li, scan rate: 2 mV s^{-1}.

This peak might originate from isolated lithium iodide and its anodic oxidation. Although the anodic decomposition current was not significant, the current profile indicated a small anodic oxidation above 3.1 V for LiI–Li_3PS_4. On the contrary, no anodic current was observed in Li_3PS_4 cell.

Li/LiI–Li_3PS_4/LZO–NCA Cell (NCA Cell)

The discharge profiles and capacity attenuation during 100 cycles for Li/LiI–Li_3PS_4/LZO–NCA cell (NCA cell) is shown in **Figures 5A,B**. The cell showed initial discharge capacities of approximately 134 and 94 mAh g^{-1} at 0.05 and 0.5°C, respectively. These cathode specific capacities were larger than in our previous study (Ito et al., 2014). However, the specific capacity decreased from 95 to 70 mAh g^{-1} after 100 cycles with the charge/discharge condition of 0.1 C CC–CV/0.5 C CC. The capacity fade was much faster than that in Graphite/Li_2S–P_2S_5 (80:20 mol%)/LZO–NCA (Ito et al., 2014). The initial coulombic efficiency was 69.4% and gradually increased to 99.0% by the sixth cycle. The average coulombic efficiency during the last 50 cycles was 99.6%. After 100 cycles, the average cell closed potential decreased due to the increase of *i*R drop up in the first 2 s right after the galvanostatic charge/discharge started. These performance characteristics indicate that the cell-specific capacity gradually decreased due to the increase of cell resistance with the same cutoff potential.

Li/LiI–Li_3PS_4/C–S Cell (S Cell)

The discharge profiles and capacity attenuation during 100 cycles for the Li/LiI–Li_3PS_4/S (S cell) is shown in **Figures 6A,B**. On account of the expected poor rate capability of the S cell, the discharge rate was fixed at 0.15 C (0.25 mA cm^{-2}) with the charge/discharge cut off potentials between 3.1 and 1.3 V (constant current charge/discharge). In **Figure 6A**, the discharge profiles including 1st, 10th, and 100th are shown at the same discharge rate. The initial cell capacity was only about 1300 mAh g_{-s}^{-1} (the value calculated using the net sulfur weight), lower than what is expected for a Li–S cell of this type. The specific capacity increased with the cycle and achieved a maximum value of 1688 mAh g_{-s}^{-1} (calculated using the net sulfur weight) at the 10th cycle.

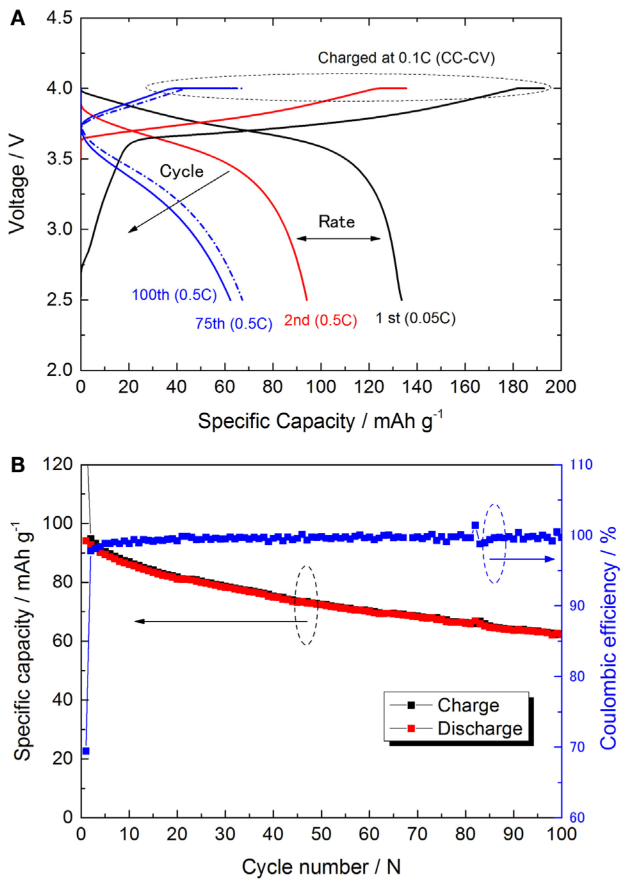

FIGURE 5 | (A) Charge/discharge curves of NCA-cell for 1st, 10th, and 100th cycle at 25°C. The 0.1 C constant current–4.0 V constant voltage (CC–CV) mode was adopted for all the charge sequences. First discharge was done at 0.05 C to check the full capacity. **(B)** Charge/discharge capacities and the coulombic efficiency are plotted versus the cycle (within the 2nd cycle to 100th cycle).

After the 10th cycle, the specific capacity gradually decreased to 1622 mAh g_{-s}^{-1} by 100th cycle. The coulombic efficiency reached beyond 99.9% after the 30th cycle. From the maximum capacity obtained at the 10th cycle, the specific capacity decreased only 4% in the last 90 cycles. Also, it is clear that no redox shuttle was observed. This result is consistent with our previous report on the all-solid-state Li–S cell (Yamada et al., 2015). Unfortunately, the cycle performance was lower than the expectation. Nevertheless, in this paper, we changed the SE and the carbon support used in the cathode. Both the material change positively influenced the cell performance. The results are summarized and compared with the former NCA cell in **Table 2**.

Li/LiI–Li_3PS_4/C–LiI–Li_3PS_4 (E Cell)

Because of the strange charge plateau above 2.5 V, the possibility of a reversible redox reaction of the electrolyte was investigated.

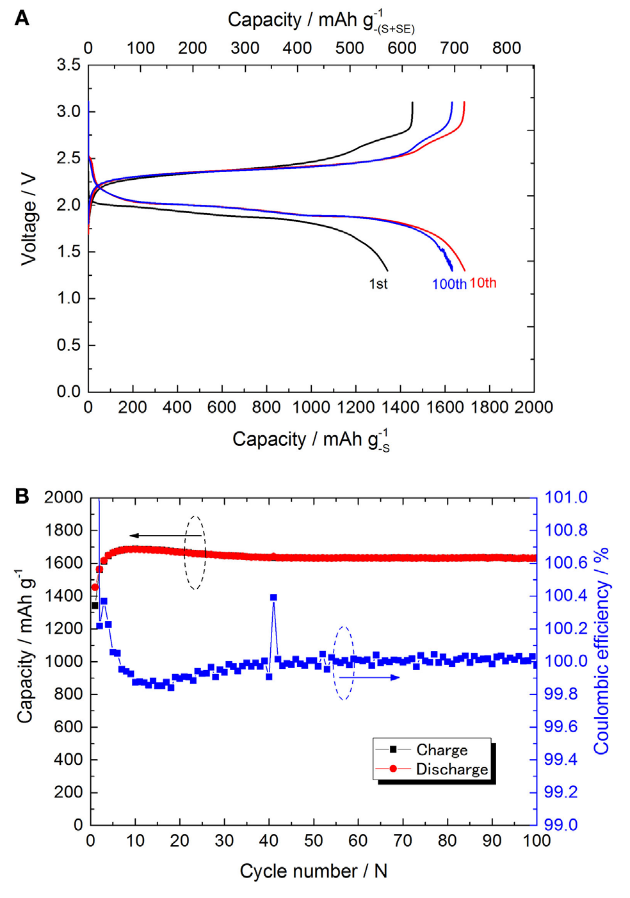

FIGURE 6 | (A) Charge/discharge curves of S-cell for 1st, 10th, and 100th cycle at 25°C. All the charge/discharge was done at 0.15 C (0.25 mA cm^{-2}) constant current with the cutoff potential of 3.1 and 1.3 V. **(B)** Charge/discharge capacities and the coulombic efficiency are plotted versus the cycle.

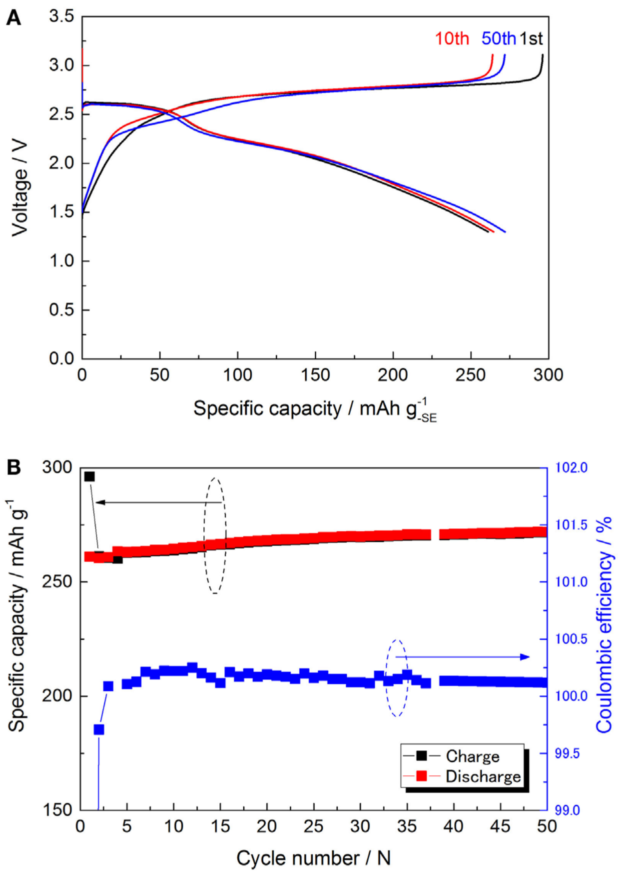

FIGURE 7 | (A) Charge/discharge curves of E-cell for 1st, 10th, and 50th cycle at 25°C. All the charge/discharge was operated by the same condition of S-cell. **(B)** Charge/discharge capacities and the coulombic efficiency are plotted versus the cycle.

TABLE 2 | Summary of the cell characteristics.

	S-cell	NCA-cell
Cell capacity (mAh)[a]	2.1	1.2
$V_{1/2Q}$ at 1st cycle (V)[b]	1.9	3.7
Cathode active material energy density (Wh/kg)	3000	493
Cathode composite energy density (Wh/kg)	1111	259
Average coulombic efficiency within last 50 cycles (%)	100.0	99.6
Capacity retention at 100th cycle (%)[c]	96	74

[a] *Maximum capacities are adopted (S-cell: the discharge capacity at 10th cycle and NCA-cell: the discharge capacity at 1st cycle).*

[b] *The average discharge voltage was determined at the half capacity.*

[c] *The capacity retention was determined from 1st/100th capacity (S-cell) and 2nd/100th capacity (NCA-cell) to be fixed as the discharge rate.*

Recently, the reversible reaction of Li_3PS_4 and "sulfur-rich lithium polysulfidophosphates" has been suggested (Lin et al., 2013; Hakari et al., 2015). Reactivity of the carbon–electrolyte (C–SE) composite was investigated using a similar cell configuration to the S-cell, but it did not contain sulfur in the cathode composite. The galvanostatic charge/discharge profile and the capacity attenuation are plotted in **Figures 7A,B**. The redox capacity calculated using the weight of the electrolyte in the cathode composite was 261 mAh g^{-1}_{-SE} at 10th cycle. The charge/discharge capacities were quite stable during the cycle (the coulombic efficiency was always nearly equal to 100%). Although the actual reaction scheme is unclear, two potential plateaus were clearly observed in the discharge profile.

To examine the condition of the electrolyte in the C–SE composite, we measured Raman spectroscopy of our sample. However, after the ball milling, the Raman shift related to the electrolyte (420 cm^{-1}, PS_4^{3-} anion structure) was not observable. Other observed peaks were assigned to D/G bands of graphite (1570–1360 cm^{-1}). DSC was performed (**Figure 8**) and the results are summarized in **Table 3**. There was a significant difference between the profiles of Li_3PS_4 and LiI–Li_3PS_4. LiI–Li_3PS_4 exhibited a large peak at 160.9°C. This exothermic peak might be related to the reorientation and crystallization of LiI. In the scan, the glass transition appeared just before the crystallization of LiI. The heat flow decreases slightly in the SE and C–SE samples. Furthermore, the other peaks related to Li_3PS_4 (crystallizing and transformation to the thio-LISICON phase) showed high temperature shifts.

The peak pattern of the C–SE composite was unchanged after ball milling with activated carbon. However, the sharp peak shifted to high temperature in comparison with LiI–Li_3PS_4. The reason for this high temperature shift is obscure. In the C–S–SE sample, the peak pattern was completely changed by the ball milling. The sulfur (S_8) generally does not show any exothermic peak, and only endothermic melting peaks were observed before 300°C. However, the C–S–SE composite showed only a small endothermic peak around 107°C and two exothermic peaks. The presence of excess sulfur certainly changes the chemical environment and must be promoting alternate chemical reactions. Unfortunately, it was still not clear whether the materials were changed by the heating during the DSC or by the mechanical milling.

DISCUSSION

Characteristic of LiI–Li_3PS_4

In this paper, we have demonstrated two types of lithium metal secondary cells using a solid-state electrolyte based on an amorphous LiI–Li_3PS_4. This electrolyte consists of 48 mol% ortho-Li_3PS_4, and the 52 mol% of LiI. Although LiI is an ionic conductive material (3.2 µS cm^{-1}) (Rao et al., 1978), it is impossible to explain the improvement of ionic conductivity by the addition of LiI to Li_3PS_4, because of the poorer conductivity of LiI than that of Li_3PS_4. We assumed that the carrier number did not significantly change upon 52 mol% substitution by LiI compared to amorphous Li_3PS_4. The PS_4 anion actually has a symmetrical tetrahedron structure, and substitution with LiI replaces this highly symmetric spherical anion in the framework. This substitution influences the probability of the ion exchange between anions and Li^+ in the mixed electrolytes and increases the total ionic conductivity. However, the details of the phenomenon are still unclear, requiring further investigation. The LiI–Li_3PS_4 showed a high ionic conductivity, and this improved the cell performance, especially for the S-cell in comparison with our previous study (Ito et al., 2014). Unfortunately, LiI–Li_3PS_4 is unstable at high potentials (>2.7 V) probably due to oxidation of I^-. In the NCA cell, the capacity fade in the cycle test is much larger compared to previous results although the anode is different. On the other hand, the S cell showed very stable cycles (even though the utilization of the anode is deeper in the S cell); the electrolyte is at least as stable against the Li/Li^+ redox reaction. Although LiI–Li_3PS_4 may not be applicable to a 4 V system, it could be used for a metal lithium secondary battery with a high coulombic efficiency.

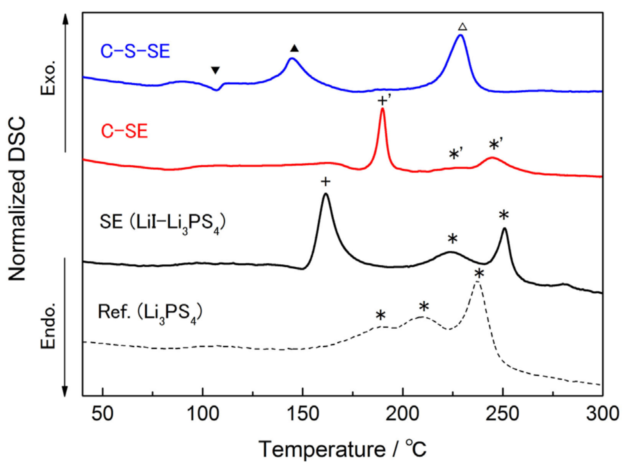

FIGURE 8 | DSC chart for the electrolytes and composites at the first heating. The heat flow was normalized by the sample weight. DSC scan rate was 2°C min^{-1}.

At this point, one may wonder whether the electrolyte material in the separate layer plays any role on the charge–discharge capacities. Hakari et al. (2015) have already demonstrated that the cathode composite without sufficient electronic conductivity does not allow any observable redox reactions. In our system, the electrical conductivity is given to the cathode composite by ball milling the SE with carbon to form complexes. Therefore, the SE in the separator region has no contribution in the capacity of the battery.

Exact Reactions in S Cell

The charge/discharge curves nearly emulated the theoretical redox capacity of sulfur. However, as described above, the charge/discharge capacities must be based on the summation of redox capacities of sulfur and SE, because the electrolyte shows reversible redox capacity in the same potential range 3.1–1.3 V versus Li/Li^+. The cathode composite consists of 50 wt% (SE) and 37 wt% (sulfur). Considering the reversible capacity of the electrolyte,

TABLE 3 | Summary of the DSC analysis of the samples.

Sample	Peak top/°C [heat capacity (J/g)]			
	Sulfur related	LiI related	Li_3PS_4 related	Unknown
Ref. (Li_3PS_4)			*188.8 (–17.1)^x *208.3 (–17.8)^x *237.3 (–28.6)^x	
SE (Li_3PS_4–LiI)		+160.9 (–18.5)	*224.2 (–9.1)^x *250.6 (–9.1)^x	
C–SE (SE = 80%)		+190.0 (–7.2)	*′226.8 (–1.2)^x *′244.5 (–4.8)^x	
C–S–SE (S = 37%, SE = 50%)	▼107 (1.0)			▲145 (–7.1) Δ 229 (–15.7)

^{x}Vertical partitioning.
*The symbols before the values correspond to the symbols in **Figure 8**.*

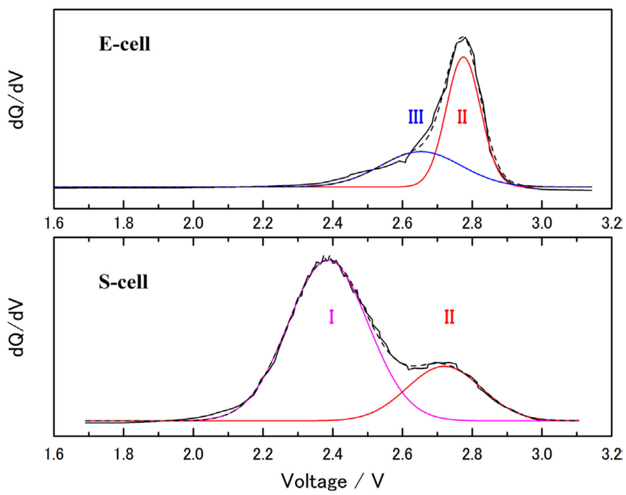

FIGURE 9 | dQ/dV plot of the charge process for S-cell (bottom) and E-cell (upper). Gaussian peak fitting was performed onto the dQ/dV data with $R^2 > 0.998$. Each peak consists of I: main red-ox reaction of sulfur, II: red-ox capacity with poly-condensation of Li3PS4, and III: red-ox capacity of LiI.

the net capacity of sulfur was estimated. For estimating the each value, dQ/dV profiles of S- and E-cell were examined and are presented in **Figure 9**. The main peak in region I (around 2.37 V) including a shoulder peak around 2.19 V represents the majority of the reaction in S-cell. Region II (around 2.75 V) is not generally observed in a typical Li–S cell. In the dQ/dV of the S-cell, the areas assigned in regions I and II were separated by Gaussian peak fitting ($R^2 > 0.998$). The peak area of region II in the S-cell was about 25% of the total integrated area between 1.8 and 3.0 V. If it is assumed that the extra capacity originated from the reaction of the electrolyte at 2.75 V, the net sulfur redox capacity was about 75% of the apparent sulfur specific capacity (1600 mAh $\mathrm{g}_{\text{-S}}^{-1}$) and was equal to 1200 mAh $\mathrm{g}_{\text{-S}}^{-1}$. For the E-cell, the peak could be separated in two peaks. One of them gives the same potential with region II. The second peak (region III) appeared at 2.65 V. The ratio of the peak areas for region II:III is 61:39. We have calculated and estimated the reaction based on the electrolyte composition. There was only one possibility that the summation of the redox capacity of LiI and Li_3PS_4 (higher than two electrons reaction) can provide the capacity of 250 mA g^{-1} for the SE.

$$\mathrm{LiI} \rightarrow \mathrm{Li}^{+} + \mathrm{I} + \mathrm{e}^{-}\left(200\ \mathrm{mAhg}^{-1}\right)$$

$$\mathrm{Li_3PS_4} \rightarrow \mathrm{xLi}^{+} + \mathrm{Li}_{(3-x)}\mathrm{PS_4}\left(\mathrm{condensation}\right) + \mathrm{xe}^{-}\left(\mathrm{x} = 1:149,\ 2:298,\ 3:449\ \mathrm{mAhg}^{-1}\right)$$

$$\mathrm{Total}: 0.52\mathrm{LiI} - 0.48\mathrm{Li_3PS_4} \rightarrow \mathrm{xLi}^{+} + \mathrm{I} + \mathrm{Li}_{(3-x)}\mathrm{PS_4}\left(\mathrm{condensation}\right) + \left(\mathrm{x}+1\right)\mathrm{e}^{-}\left(\mathrm{x} = 1:176,\ 2:247,\ 3:319\ \mathrm{mAhg}^{-1}\right)$$

Although there are some unclear points (e.g., the exact formation of the anions in the cathode composite), LiI and two electron redox of Li_3PS_4 ($3 \geqq x \geqq 2$) were suitable for considering the reversible capacity of the LiI–Li_3PS_4, which was used in this study. Because of the unusual DSC peaks observed in the C–S–SE composite, carbon and sulfur might also contribute to the highly complicated active material. Although further investigation is required to clarify this redox system, it is clear that the solid-state electrolyte, LiI–Li_3PS_4, has scope for use in real cell reactions.

CONCLUSION

A sulfide-based SE, amorphous LiI–Li_3PS_4, was prepared by mechanical milling. The ionic conductivity was determined to be 1.2 mS cm^{-1} at 25°C with an activation energy of 29.1 kJ mol^{-1}. We have demonstrated the successful fabrication of two types of lithium secondary cells using LiI–Li_3PS_4. In the NCA-cell, the cell performance improved in comparison to the Li_3PS_4 adopted cell in our previous study, except for the cycle ability. Due to its poor electrochemical stability of LiI–Li_3PS_4, the cycle performance was unsatisfactory in the 4-V system. On the contrary, the cycle performance was significantly improved in the S-cell using the same electrolyte compared to our previous study. The high coulombic efficiency above 99.9% during charge–discharge cycle test was verified in the S-cell. This indicates that the cell can basically operate 1000 cycles without reserve lithium capacity in terms of the figure of merit.

Interestingly, the C–SE composite electrochemically reacted and clearly showed a reversible capacity in the potential range of 3.1–1.3 V versus Li/Li^+. Although the exact reaction needs to be clarified, the stable capacity was about 260 mAh g^{-1}. Also, a cooperative reaction between sulfur, LiI, and Li_3PS_4 was observed in the C–S–SE composite. The coulombic efficiency was extremely high, even though some complex reaction was expected. Also, no evidence for a polysulfide redox shuttle was observed within 100 cycles. These facts indicate that the solid-state electrolyte and its adopted system is one of the most promising approaches for producing high-capacity lithium secondary batteries.

AUTHOR CONTRIBUTIONS

YA and SI proposed the idea and strategy for the experimental work. SI, SF, RO, and TY designed the experiments and performed the synthesis and characterization of the samples in addition to the electrochemical measurements. The experimental data were analyzed and the manuscript was written by YA and TW. The entire project was coordinated by YP and SD.

ACKNOWLEDGMENTS

This work is financially supported by Samsung Electronics. The authors acknowledge Prof. Machida (Konan University) for valuable discussion on the solid electrolyte and also express their sincere gratitude to Prof. Price (Western Sydney University) for improving the manuscript.

REFERENCES

Bates, J. B., Dudney, N. J., Gruzalski, G. R., Zuhr, R. A., Choudhury, A., Luck, C. F., et al. (1993). This volume contains the Proceedings of the 6th International Meeting on Lithium Batteries Fabrication and characterization of amorphous lithium electrolyte thin films and rechargeable thin-film batteries. *J. Power Sources* 43, 103–110. doi:10.1016/0378-7753(93)80106-Y

Hakari, T., Nagao, M., Hayashi, A., and Tatsumisago, M. (2015). All-solid-state lithium batteries with Li_3PS_4 glass as active material. *J. Power Sources* 293, 721–725. doi:10.1016/j.jpowsour.2015.05.073

Ito, S., Fujiki, S., Yamada, T., Aihara, Y., Park, Y., Kim, T. Y., et al. (2014). A rocking chair type all-solid-state lithium ion battery adopting Li_2O-ZrO_2 coated $LiNi_{0.8}Co_{0.15}Al_{0.05}O_2$ and a sulfide based electrolyte. *J. Power Sources* 248, 943–950. doi:10.1016/j.jpowsour.2013.10.005

Kamaya, N., Homma, K., Yamakawa, Y., Hirayama, M., Kanno, R., Yonemura, M., et al. (2011). A lithium superionic conductor. *Nat. Mater.* 10, 682–686. doi:10.1038/nmat3066

Lin, Z., Liu, Z., Fu, W., Dudney, N. J., and Liang, C. (2013). Lithium polysulfidophosphates: a family of lithium-conducting sulfur-rich compounds for lithium-sulfur batteries. *Angew. Chem. Int. Ed.* 52, 7460–7463. doi:10.1002/anie.201300680

Mercier, R., Malugani, J.-P., Fahys, B., and Robert, G. (1981). Proceedings of the International Conference on Fast Ionic Transport in Solids Superionic conduction in Li_2S-P_2S_5-LiI glasses. *Solid State Ionics* 5, 663–666. doi:10.1016/0167-2738(81)90341-6

Nagata, H., and Chikusa, Y. (2014). A lithium sulfur battery with high power density. *J. Power Sources* 264, 206–210. doi:10.1016/j.jpowsour.2014.04.106

Ogawa, M., Kanda, R., Yoshida, K., Uemura, T., and Harada, K. (2012). High-capacity thin film lithium batteries with sulfide solid electrolytes. *J. Power Sources* 205, 487–490. doi:10.1016/j.jpowsour.2012.01.086

Ohtomo, T., Hayashi, A., Tatsumisago, M., and Kawamoto, K. (2013). All-solid-state batteries with Li_2O-Li_2S-P_2S_5 glass electrolytes synthesized by two-step mechanical milling. *J. Sol. St. Electrochem.* 17, 2551–2557. doi:10.1007/s10008-013-2149-5

Rangasamy, E., Liu, Z., Gobet, M., Pilar, K., Sahu, G., Zhou, W., et al. (2015). An iodide-based $Li_7P_2S_8I$ superionic conductor. *J. Am. Chem. Soc.* 137, 1384–1387. doi:10.1021/ja508723m

Rao, B. M. L., Silbernagel, B. G., and Jacobson, A. J. (1978). Evaluation of solid electrolytes for high temperature lithium batteries: a preliminary study. *J. Power Sources* 3, 59–66. doi:10.1016/0378-7753(78)80005-6

Scrosati, B., and Garche, J. (2010). Lithium batteries: status, prospects and future. *J. Power Sources* 195, 2419–2430. doi:10.1016/j.jpowsour.2009.11.048

Tatsumisago, M., Hama, S., Hayashi, A., Morimoto, H., and Minami, T. (2002). New lithium ion conducting glass-ceramics prepared from mechanochemical Li_2S-P_2S_5 glasses. *Solid State Ionics* 15, 635–640. doi:10.1016/S0167-2738(02)00509-X

Weppner, W. (1981). Proceedings of the International Conference on Fast Ionic Transport in Solids Trends in new materials for solid electrolytes and electrodes. *Solid State Ionics* 5, 3–8. doi:10.1016/0167-2738(81)90186-7

Yamada, T., Ito, S., Omoda, R., Watanabe, T., Aihara, Y., Agostini, M., et al. (2015). All solid-state lithium-sulfur battery using a glass-type P_2S_5-Li_2S electrolyte: benefits on anode kinetics. *J. Electrochem. Soc.* 162, A646–A651. doi:10.1149/2.0441504jes

Conflict of Interest Statement: The authors declare that the research was conducted in the absence of any commercial or financial relationships that could be construed as a potential conflict of interest.

frontiers
in Energy Research

ORIGINAL RESEARCH
published: 10 May 2016
doi: 10.3389/fenrg.2016.00019

High Reversibility of “Soft” Electrode Materials in All-Solid-State Batteries

Atsushi Sakuda, Tomonari Takeuchi*, Masahiro Shikano, Hikari Sakaebe and Hironori Kobayashi*

Department of Energy and Environment, Research Institute for Electrochemical Energy, National Institute of Advanced Industrial Science and Technology (AIST), Ikeda, Japan

All-solid-state batteries using inorganic solid electrolytes (SEs) are considered to be ideal batteries for electric vehicles and plug-in hybrid electric vehicles because they are potentially safer than conventional lithium-ion batteries (LIBs). In addition, all-solid-state batteries are expected to have long battery life owing to the inhibition of chemical side reactions because only lithium ions move through the typically used inorganic SEs. The development of high-energy density (more than 300 Wh kg^{-1}) secondary batteries has been eagerly anticipated for years. The application of high-capacity electrode active materials is essential for fabricating such batteries. Recently, we proposed metal polysulfides as new electrode materials. These materials show higher conductivity and density than sulfur, which is advantageous for fabricating batteries with relatively higher energy density. Lithium niobium sulfides, such as Li_3NbS_4, have relatively high density, conductivity, and rate capability among metal polysulfide materials, and batteries with these materials have capacities high enough to potentially exceed the gravimetric-energy density of conventional LIBs. Favorable solid–solid contact between the electrode and electrolyte particles is a key factor for fabricating high performance all-solid-state batteries. Conventional oxide-based positive electrode materials tend to give rise to cracks during fabrication and/or charge–discharge processes. Here, we report all-solid-state cells using lithium niobium sulfide as a positive electrode material, where favorable solid–solid contact was established by using lithium sulfide electrode materials because of their high processability. Cracks were barely observed in the electrode particles in the all-solid-state cells before or after charging and discharging with a high capacity of approximately 400 mAh g^{-1} suggesting that the lithium niobium sulfide electrode charged and discharged without experiencing substantial mechanical damage. As a result, the all-solid-state cells retained more than 90% of their initial capacity after 200 cycles of charging and discharging at 0.5 mA cm^{-2}.

Keywords: all-solid-state battery, lithium niobium sulfide, electrode morphology, sulfide solid electrolyte, long cycle life

Edited by:
Jeff Sakamoto,
University of Michigan, USA

Reviewed by:
Francois Aguey-Zinsou,
The University of New South Wales,
Australia
Jeff B. Wolfenstine,
Army Research Laboratory, USA

****Correspondence:***
Atsushi Sakuda
a.sakuda@aist.go.jp;
Tomonari Takeuchi
takeuchi.tomonari@aist.go.jp

Specialty section:
This article was submitted to
Energy Storage,
a section of the journal
Frontiers in Energy Research

Received: *01 February 2016*
Accepted: *25 April 2016*
Published: *10 May 2016*

Citation:
Sakuda A, Takeuchi T, Shikano M,
Sakaebe H and Kobayashi H (2016)
High Reversibility of “Soft” Electrode
Materials in All-Solid-State Batteries.
Front. Energy Res. 4:19.
doi: 10.3389/fenrg.2016.00019

INTRODUCTION

Secondary batteries are one of the most important components of electric vehicles (EVs) and plug-in hybrid electric vehicles (PHEVs). Among many types of secondary batteries, lithium-ion batteries (LIBs) are typically used in current EVs and PHEVs because of their high-energy density and long life (Armand and Tarascon, 2008; Dunn et al., 2011; Etacheri et al., 2011). To achieve a long driving range, the batteries must be densely packed in the battery pack because of the limited space for batteries in EVs and PHEVs. However, this dense packing usually increases the operating temperature of batteries. Thus, the safety and cyclability of these batteries at high temperature must be improved for use in EVs and PHEVs; otherwise, large-volume cooling units will be required.

Conventional LIBs employ liquid electrolytes with organic solvents (Armand and Tarascon, 2008; Dunn et al., 2011). These batteries are associated with some safety risks and exhibit accelerated degradation when they are operated at high temperatures. All-solid-state batteries that use inorganic solid electrolytes (SEs) are considered to be ideal batteries for EVs and PHEVs because they are potentially safer than conventional LIBs (Minami et al., 2006; Kamaya et al., 2011; Sakuda et al., 2013a). In addition, these batteries are expected to have long battery life because of the inhibition of chemical side reactions as only the lithium ions move in the typically used inorganic SEs.

The development of high-energy density (more than 300 Wh kg^{-1}) secondary batteries has been eagerly anticipated for years. The application of high-capacity electrode-active materials is essential for the fabrication of such batteries. Lithium/sulfur batteries have attracted attention because of their high theoretical energy densities based on the high capacities of sulfur in positive electrode materials (Yamin and Peled, 1983; Ji et al., 2009; Bruce et al., 2012; Schuster et al., 2012). However, the use of sulfur–carbon composites is required to activate insulating sulfur, and the composites require large amounts of carbon to achieve high performance, which decreases their energy density. Recently, we proposed metal polysulfides as new electrode materials (Hayashi et al., 2012a; Matsuyama et al., 2012; Sakuda et al., 2013b, 2014a,b,c,d). These materials show higher conductivity and density than sulfur. Thus, they are expected to exhibit improved volumetric-energy densities because of their relatively low conductive carbon ratios and relatively high material densities.

Understanding and exploiting the materials' mechanical properties are important in all-solid-state batteries (Hayashi et al., 2012b; Sakuda et al., 2013a). The all-solid-state batteries with sulfide SEs can be fabricated through high-pressure pressing at room temperature because of the sulfide SEs unique mechanical properties. The sulfide SE powder becomes highly densified as the grain boundaries decrease during pressing at room temperature. We term this densification "room-temperature pressure sintering" (Sakuda et al., 2013a). This phenomenon enables the creation of intimate contact between the electrode and SE materials, which is an essential requirement for all-solid-state operation, *via* room-temperature processing. The mechanical properties of electrode materials are also important. When brittle materials are used as the active material, the fragmentation of the electrode particles may occur during the high-pressure pressing used for cell construction. This fragmentation is especially serious at the interfaces between brittle materials as a result of stress concentration during high-pressure pressing (Sakuda et al., 2016). When electrode materials with some plastic character are used, the morphology of the electrode layer differs from that when brittle materials are used. For instance, the fragmentation during high-pressure pressing is expected to be suppressed. Furthermore, a dense electrode layer with a favorable electrode–electrolyte interface can likely be constructed. Electrode materials with large capacities usually show large volume changes during charging and discharging. The maintenance of intimate solid–solid contact is an essential requirement for long cycle life. The plasticity of the electrode materials is believed to affect the maintenance of this contact. Lithium-containing metal sulfides with three-dimensional (3D) structures are attractive model materials with some degree of plastic character based on an intermediate bond character between ionic and covalent. Lithium niobium sulfides, such as rock-salt Li_3NbS_4, have relatively high density, conductivity, and rate capability among metal polysulfide materials (Sakuda et al., 2014c,d). Additionally, the batteries that use these materials have capacities that are high enough to potentially exceed the gravimetric-energy density of conventional LIBs. Furthermore, Li_3NbS_4 is considered to have relatively soft mechanical nature. Its application in all-solid-state batteries is expected to enhance these batteries' cyclability.

Here, we report high reversibility of soft electrode materials in all-solid-state batteries. The Li_3NbS_4 is used as a model material of soft electrode materials. This material shows unique mechanical properties that it can be densified by pressing at room temperature, and charged and discharged without the fragmentation. As a result, a dense electrode layer with a favorable conducting pathway and electrode–electrolyte interface is constructed. Furthermore, the dense electrode layer is maintained during charging and discharging, and the all-solid-state cell created here has a long cycle performance.

MATERIALS AND METHODS

Li_3NbS_4 was mechanochemically synthesized using a planetary ball mill apparatus (P-5, Fritsch GmbH). In an argon-filled glove box, a mixture of lithium sulfide (Li_2S, 99.9%, Mitsuwa Pure Chemicals), niobium disulfide (NbS_2, 99%, High Purity Chemicals), and sulfur (S_8, 99.9%, Wako Pure Chemical Industries) was placed into a zirconia pot (500 mL) along with zirconia balls (4 mm in diameter, 1,000 g). The total weight of the mixture of the starting materials was 10 g. The rotation speed and time of ball milling were fixed at 250 rpm and 120 h (60 min × 120 times), respectively. The $75Li_2S \cdot 25P_2S_5$ (mol%) glassy SE (Hayashi et al., 2001) was used, because it is the most typical sulfide-based SE. The SE was mechanochemically prepared from Li_2S and phosphorus pentasulfide (P_2S_5, 99%, Sigma-Aldrich) *via* planetary ball milling. Heptane was used as the ball-milling solvent. Zirconia pots (500 mL) and zirconia balls (4 mm in diameter, 1,000 g) were used. The starting materials were weighed in an argon-filled glove box and milled in air-sealing pots for 20 h. The lithium-ion conductivity of the powder-compressed pellet of the as-prepared SE and smaller-sized SE particles exhibited almost the same value (approximately 4×10^{-4} S cm^{-1}) at 25°C. All-solid-state cells were constructed as follows. The Li_3NbS_4 and the SE were mixed at a weight ratio of 75:25 for 3 min using a vortex mixer (IKA® Lab Dancer test tube shakers) *via* a dry process to prepare the positive composite electrode. The conductive additive was not included in this study because electronic conductivity of the Li_3NbS_4 is sufficiently high ($>2 \times 10^{-3}$ S cm^{-1}) relative to the lithium-ion conductivity in the composite electrode (Sakuda et al., 2014c,d). The resistance component attributable to electronic resistance in the composite electrode was hardly observed by AC impedance measurements. A lithium–indium alloy was used as the counter/reference electrode for the two-electrode cell. The lithium–indium alloy has been reported to show a voltage plateau at 0.62 V vs. Li^+/Li, over a wide range of compositions (Takada et al., 1996). Bilayer pellets (φ = 10 mm) consisting of the positive composite electrodes (10 mg) and the SE (80 mg) were obtained by pressing under 330 MPa at room temperature; indium foil (*t* = 0.3 mm, φ = 9 mm) and lithium foil (*t* = 0.2 mm, φ = 8 mm) were then attached to the bilayer pellets by pressing under 100 MPa. The pellets were pressed using two stainless steel rods, which were used as current collectors for both the positive and negative electrodes. All the processes involved in preparing the all-solid-state cells were performed in an argon-filled glove box [(H_2O) < 1 ppm].

Powder XRD measurements were performed at room temperature over the 2θ angle range $10° \leq 2\theta \leq 80°$ with a step size of 0.1° using a D8 ADVANCE (Bruker AXS) diffractometer with CuKα radiation. The particle size distribution was measured using a particle size analyzer (SALD-7500nano, Shimadzu) with heptane/dibutyl ether as a solvent. Cross sections of the all-solid-state cells were prepared for scanning electron microscopy (SEM) observation using an argon-ion beam cross-section polisher (CP; IB-9020CP, JEOL) with an air-sealing holder. The samples were placed in the argon-filled glove box, transferred to the CP using the air-sealing holder, and milled for approximately 2 h. The acceleration voltage and argon gas pressure used were 6 kV and 3×10^{-3} Pa, respectively. During argon-ion milling, the stage was rocked ±30° to prevent beam striations and ensure uniform etching of the composite materials. Then, the obtained cross-section samples were transferred to the glove box and placed in the transfer vessel for SEM (JSM-6510A, JEOL) observation. The charge–discharge performances were evaluated at 50°C.

RESULTS

Figure 1 shows the XRD patterns of the Li_3NbS_4 prepared by mechanical milling (MM) with some reference materials. The peaks attributable to rock-salt type Li_3NbS_4 (Sakuda et al., 2014c,d) were confirmed after MM for 120 h, according to the preparation conditions used in this study. The average crystalline diameter of the Li_3NbS_4 estimated from the XRD peak widths was <10 nm, indicating that the sample obtained here included an amorphous phase.

Figure 2 shows the SEM images of the (**Figure 2A**) Li_3NbS_4 and (**Figure 2B**) $75Li_2S{\cdot}25P_2S_5$ glassy SE particles. The average particle sizes of the Li_3NbS_4 and $75Li_2S{\cdot}25P_2S_5$ glassy particles measured by the particle size analyzer were 5.7 and 15 μm, respectively. The Li_3NbS_4 particles are smaller than the SE particles in this study.

Figure 3 shows the cross-sectional SEM image of the positive electrode layer. The light- and dark-gray particles are Li_3NbS_4 and the SE, respectively. The dense pellet was obtained by pressing at room temperature. It should be noted that the grain boundaries are hardly visible at some interfaces between Li_3NbS_4 particles. No cracking or fragmentation can be seen in the Li_3NbS_4.

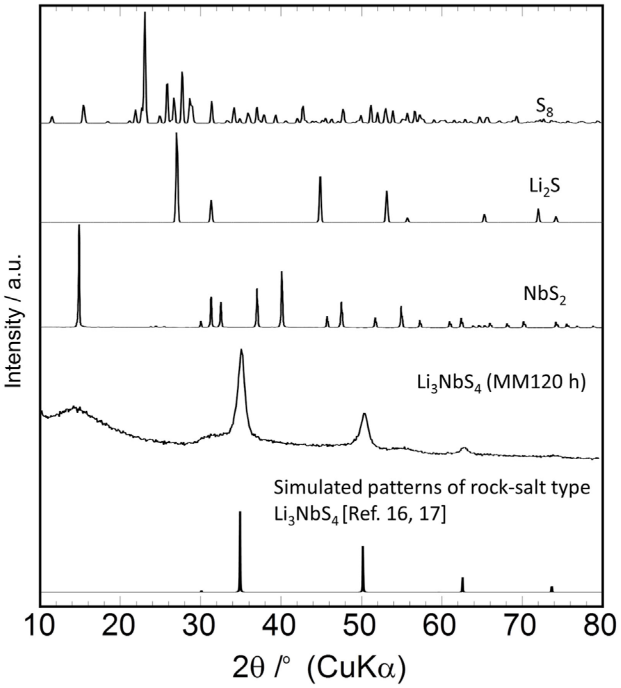

FIGURE 1 | XRD patterns of samples of Li_3NbS_4 prepared by MM for 120 h. The XRD patterns of the starting materials and rock-salt Li_3NbS_4 are also shown.

Figure 4 shows the dependence of the density of the Li_3NbS_4 pellet on the molding pressure. In this measurement, the Li_3NbS_4 was uniaxially compressed in a 10-mm-diameter mold. The relative densities were defined by the ratios between the pellets' densities and the powder true density, which was determined using a gas pycnometer (AccuPyc II 1340, Shimadzu), and the relative density was 2.92 g cm^{-3} for Li_3NbS_4. The relative density increases as the applied pressure increases and exceeds 90% when the Li_3NbS_4 powder is compressed by a pressure of over 500 MPa. Compressed Li_3NbS_4 with a remarkably high relative density can be obtained by pressing without heat treatment. Thus, Li_3NbS_4 is amenable to room-temperature pressure sintering.

Figure 5A shows the charge–discharge curves of the all-solid-state Li–In/Li_3NbS_4 cells. The current density used was 0.25 mA cm^{-2}. Cutoff voltages of 2.4 and 0.9 V (vs. Li–In) were used in this study and correspond to 3.0 and 1.5 V (vs. Li^+/Li). **Figure 5B** presents the charge–discharge curves, with the number of lithium atoms per formula unit shown on the *x*-axis. The initial charge and discharge capacities were 263 and 370 mAh g^{-1}, respectively. After the first cycle, a capacity of *ca.* 370 mAh g^{-1} was maintained for the charge and discharge process; however, a small increase in the capacity believed to be attributable to some sort of electrode activation was observed. This capacity corresponds to structures ranging from $Li_{0.6}NbS_4$ to $Li_{4.0}NbS_4$. The reversible capacity per unit area was 3.54 mAh cm^{-2}. Rock-salt Li_3NbS_4 has been reported to exhibit reversible charging and discharging for compositions ranging between $Li_{0.4}NbS_4$ and $Li_{3.9}NbS_4$ when charged and discharged with cutoff voltages of 3.0 and 1.5 V

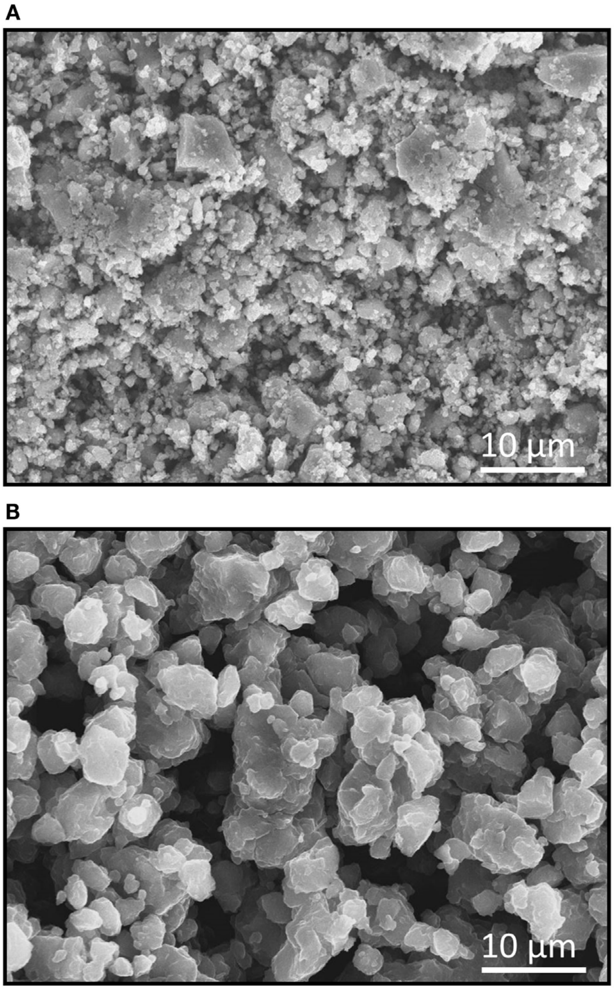

FIGURE 2 | SEM images of (A) Li_3NbS_4 prepared by MM for 120 h and (B) $75Li_2S·25P_2S_5$ glassy SE particles.

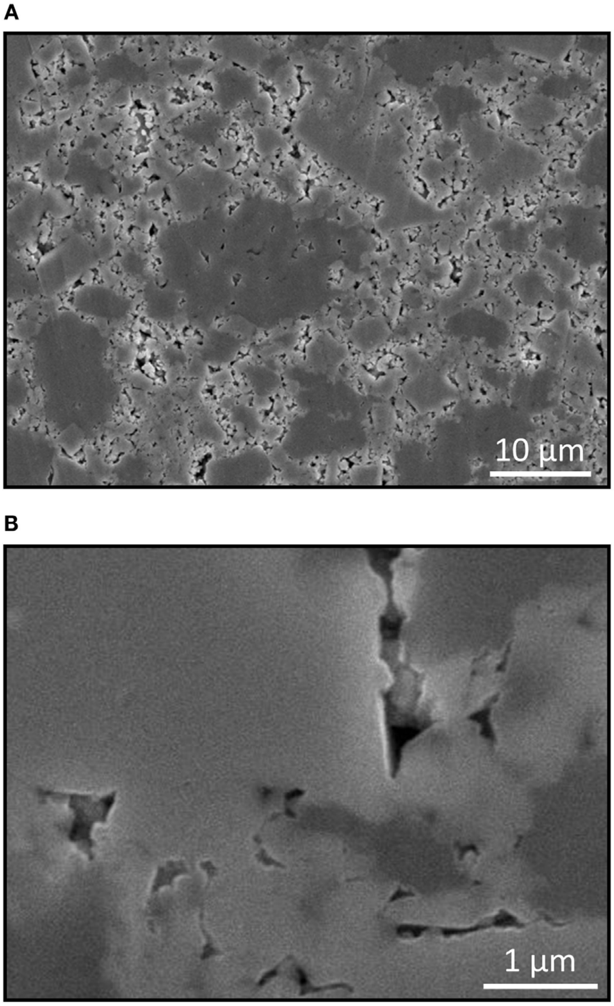

FIGURE 3 | Cross-sectional SEM images of the composite electrode of the all-solid-state cell with Li_3NbS_4. (A) Low- and **(B)** high-magnification images.

(vs. Li^+/Li), respectively (Sakuda et al., 2014c). Thus, Li_3NbS_4 can be used in all-solid-state cells as well as in the cells with carbonate-based liquid electrolytes. The potentials for charging and discharging were almost the same as those in cells with carbonate-based liquid electrolytes.

Figure 6 shows the cross-sectional SEM image of the positive composite electrode layer after the first charging (**Figure 6A**) and discharging (**Figure 6B**). The respective EDX mappings for Nb, P, and S are also shown in **Figures 6C,D**. The figures show that the electrode layers are free of cracks. The EDX mappings show that the light- and dark-gray particles are Li_3NbS_4 and the SE, respectively. The void volume increases after charging, and it decreases after discharging. It is noted that the Li_3NbS_4 particles are well connected in the composite electrode after discharging process. The fragmentation of Li_3NbS_4 is hardly observed.

Figure 7 shows the cycle performance of the all-solid-state cell. The current densities used for the cycle test were 0.25 mA cm^{-2} for the first through fifth cycles and 0.5 mA cm^{-2} after the sixth cycle. The capacity decreased only slightly when the current

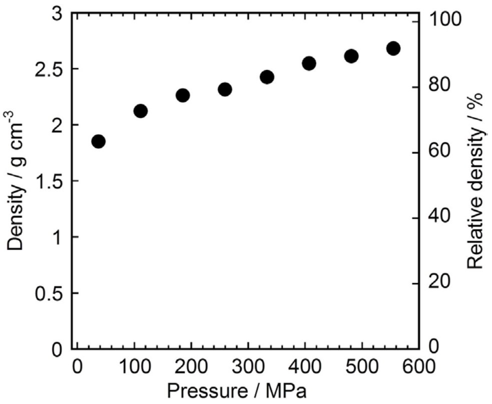

FIGURE 4 | Molding pressure dependence of the relative density of Li_3NbS_4.

density changed from 0.25 to 0.5 mA cm^{-2}. The all-solid-state cell exhibited high cyclability, retaining 92.3% of its capacity from the 7th to 200th cycle. The average cycle efficiency was 99.96% per cycle, and the average coulombic efficiency was 99.998%.

DISCUSSION

The experimental results show that dense electrode layer can be prepared solely by pressing the composite electrode with Li_3NbS_4 electrode and $75Li_2S{\cdot}25P_2S_5$ SE particles. The grain boundaries are hardly visible in the some interfaces between Li_3NbS_4 particles, indicating that this material sinters during pressing at room temperature. The Li_3NbS_4 particles are effectively deformed, make intimate contact, and create chemical bonds between the contacting particles. The cracking and fragmentation of electrode particles occur at the stress concentration point when typical lithium metal oxide electrodes, which are rather brittle materials, are used (Sakuda et al., 2016).

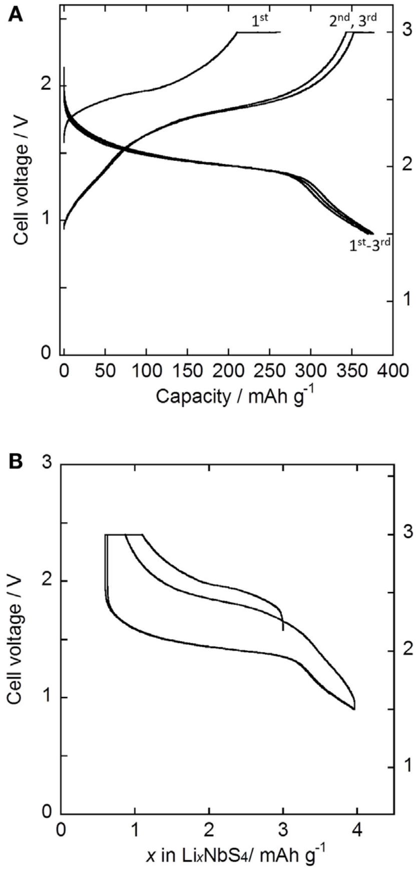

FIGURE 5 | (A) Charge–discharge curves of the all-solid-state Li–In/Li_3NbS_4 cells measured at 50°C. **(B)** Charge–discharge curves with the number of lithium atoms per formula unit shown on the *x*-axis. The current density was 0.25 mA cm^{-2}, and the cutoff voltage was 0.9–2.4 V vs. Li–In electrode.

After charging and discharging, the electrode layer was still free of cracks (**Figures 6A,B**), despite the strong possibility of the electrode experiencing a large volume change during the charging and discharging cycle. The charge–discharge of Li_3NbS_4 involves large crystal structure changes, including amorphization. Therefore, it is difficult to determine the degree of volume change of the material by XRD measurements in charged and discharged electrodes. Thus, we estimated the volume change by measuring the molar volume of the mechanochemically prepared lithium niobium sulfides with the composition of Li_xNbS_4 ($x = 0, 1, 2,$ and 3) (Sakuda et al., 2014d) by measuring the powder true density using a gas pycnometer. **Table 1** summarizes the results of the powder true density measurements. These materials potentially include amorphous phase because of the preparation process. The powder true densities and molar volumes gradually changed as the lithium contents changed. The changes in the molar volume relative to Li_3NbS_4 range from 79% for $x = 0$ to 106% for $x = 4$. Thus, the molar volume of Li_3NbS_4 changes from *ca.* 82% ($x = 0.6$) to 106% ($x = 4$) during charging and discharging. In fact, the density of the electrode was largely changed during charging and discharging process (**Figures 6A,B**). Although an electrode that undergoes large volume changes usually exhibit fragmentation of the electrode particles, loss of interfacial contact between the electrode and electrolyte, and decreased packing density, these effects were not observed here. Instead, the electrode's density decreased by charging and increased by discharging relative to the as-prepared composite electrode layer (**Figure 3**). This result suggests that the room-temperature pressure sintering of the electrode particles occurred during discharging process, increasing the contact area of both electrode–electrolyte interface and electrode–electrode interface. The Nb–S bond in the Li_xNbS_4 structure has a relatively covalent bond character and is relatively strong. The Li–S bond in the Li_xNbS_4 structure has an intermediate bond character between ionic and covalent. The bond-dissociation energy of the Li–S bond in Li_3NbS_4 is relatively small compared to that of a typical ionic bond, such as Li–F, and a typical covalent bond, such as Si–O. This intermediate bond character and relatively small bond energy make these particles

TABLE 1 | Powder true density, molar mass, molar volume, mean atomic volume, and change in molar volume (vs. Li_3NbS_4) of lithium niobium sulfides (Li_xNbS_4) prepared by MM.

x in Li_xNbS_4	Composition	Observed crystalline phase	Powder true density (g cm^{-3})	Molar mass (g mol^{-1})	Molar volume (cm^3 mol^{-1})	Mean atomic volume (cm^3 mol^{-1})	Change in molar volume (%)
0	NbS_4	Amorphous	3.38	221.17	65.5	13.1	79.0
1	$LiNbS_4$	Amorphous	3.24	228.11	70.4	11.7	84.9
2	Li_2NbS_4	Rock salt	3.12	235.05	75.3	10.8	90.8
3	Li_3NbS_4	Rock salt	2.92	241.99	82.9	10.4	100.0
4	Li_4NbS_4	Antifluorite	2.82	248.93	88.1	9.8	106.3

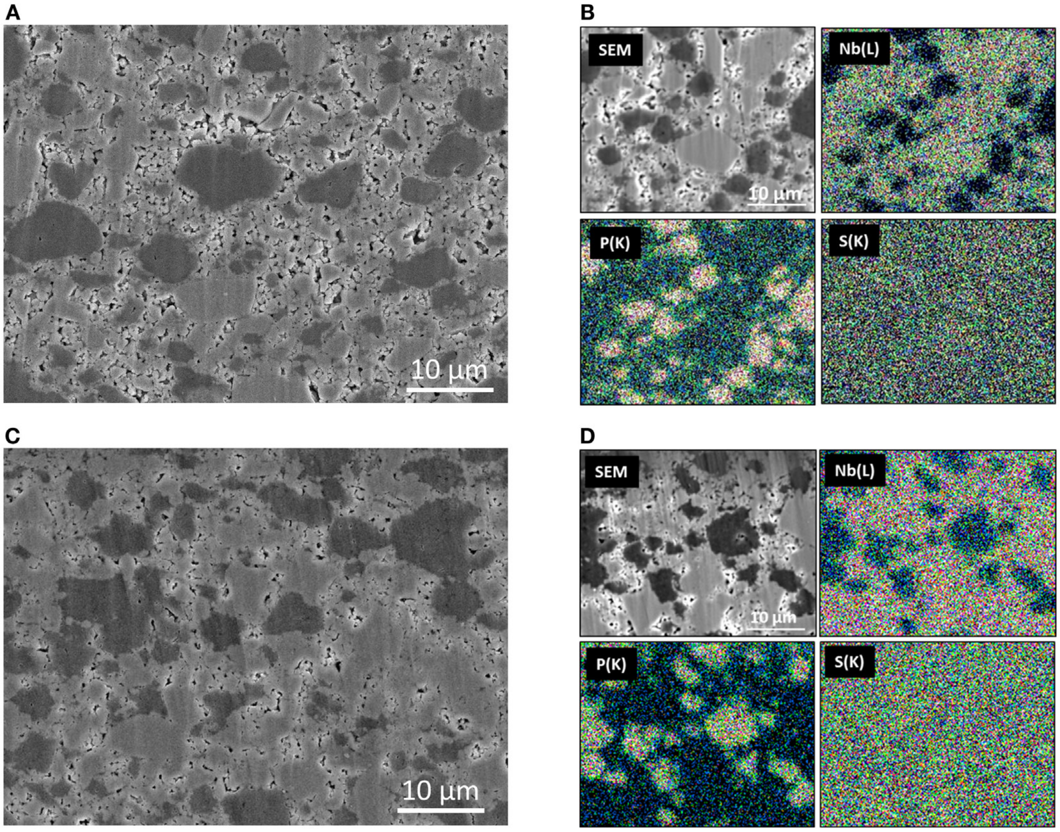

FIGURE 6 | Cross-sectional SEM images of the composite electrode of the all-solid-state cell after the first charging (A) and discharging (B). The EDX mappings for Nb–L, P–K, and S–K of the cross-sections of the composite electrode after first charging **(C)** and discharging **(D)** are also shown.

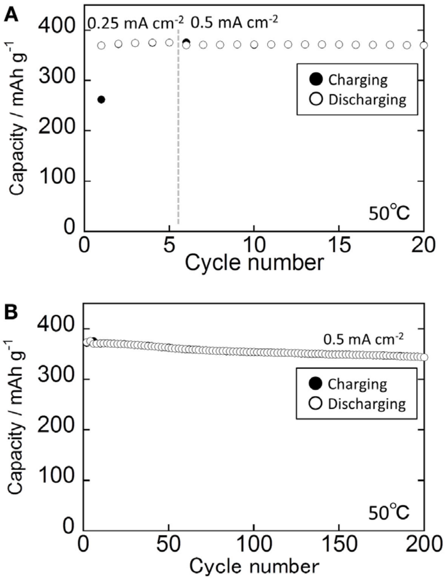

FIGURE 7 | Cycle performance of the all-solid-state Li–In/Li_3NbS_4 cell. **(A)** 1st to 20th cycle and **(B)** 1st to 200th cycles.

amenable to room-temperature pressure sintering by quasi-plastic deformation. Quasi-plastic deformation involves the breaking and reformation of chemical bonds, such as the Li–S bond. Furthermore, niobium's coordination structure is flexible in sulfide materials. Thus, the stress magnification factor of Li_xNbS_4 should be small, and the material should exhibit quasi-plastic deformation. The crystalline size of the Li_3NbS_4 in this study was very small; the crystalline diameter estimated based on the XRD pattern was <10 nm. The Li_3NbS_4 crystal domains are believed to be connected by an amorphous Li–Nb–S matrix. This structure is favorable for quasi-plastic deformation because amorphous phases usually have larger free volumes and smaller cohesive energies than crystal phases. Clearly, the application of some degree of pressure to the all-solid-state cells during operation is important for these cells' high performance. Under the applied pressure, the interfacial contact between the Li_3NbS_4 electrode and SE can be maintained despite relatively large volume changes.

The high cyclability of the all-solid-state batteries as shown in **Figure 7** is attributable to the unique mechanical properties of the Li_3NbS_4 particles, which are believed to deform effectively without fragmentation during charging and discharging. The composite electrode layer rather becomes dense during discharging process, although the electrode becomes less dense during charging. This densification is also likely related to the small capacity increase during the initial several cycles.

In this study, we presented a new, qualitative perspective concerning the usefulness of deformable electrode materials in all-solid-state batteries. The effective electrode–electrode intimate contacts can be maintained even if the electrode shows volume changes during charging and discharging by using the deformable soft electrode materials. The transition metal sulfides with sulfur-rich composition are model materials as the soft electrode materials with high capacity. In addition to the deformability of electrode materials, many other factors, such as elastic modulus and morphology of the electrode particles, and the pore volume of the composite electrode, also affect battery performance. Therefore, additional quantitative studies are required to better understand the requirements to achieve "ideal" all-solid-state batteries.

AUTHOR CONTRIBUTIONS

AS wrote the manuscript and TT, MS, HS, and HK revised the manuscript. AS, TT, and HK designed the work. AS conducted the experiments and AS, TT, MS, HS, and HK characterized the materials.

FUNDING

This work was partially supported by JSPS KAKENHI (Grant Number 15K17920).

REFERENCES

Armand, M., and Tarascon, J.-M. (2008). Building better batteries. *Nature* 451, 652–657. doi:10.1038/451652a

Bruce, P. G., Freunberger, S. A., Hardwick, L. J., and Tarascon, J.-M. (2012). Li-O$_2$ and Li-S batteries with high energy storage. *Nat. Mater.* 11, 19–29. doi:10.1038/nmat3191

Dunn, B., Kamath, H., and Tarascon, J.-M. (2011). Electrical energy storage for the grid: a battery of choices. *Science* 334, 928–935. doi:10.1126/science.1212741

Etacheri, V., Marom, R., Elazari, R., Salitra, G., and Aurbach, D. (2011). Challenges in the development of advanced Li-ion batteries: a review. *Energy Environ. Sci.* 4, 3243–3262. doi:10.1039/C1EE01598B

Hayashi, A., Hama, S., Morimoto, H., Tatsumisago, M., and Minami, T. (2001). Preparation of Li$_2$S-P$_2$S$_5$ amorphous solid electrolytes by mechanical milling. *J. Am. Ceram. Soc.* 84, 477–479. doi:10.1111/j.1151-2916.2001.tb00685.x

Hayashi, A., Matsuyama, T., Sakuda, A., and Tatsumisago, M. (2012a). Amorphous titanium sulfide electrode for all-solid-state rechargeable lithium batteries with high capacity. *Chem. Lett.* 41, 886–889. doi:10.1246/cl.2012.886

Hayashi, A., Noi, K., Sakuda, A., and Tatsumisago, M. (2012b). Superionic glass-ceramic electrolytes for room-temperature rechargeable sodium batteries. *Nat. Commun.* 3, 856–860. doi:10.1038/ncomms1843

Ji, X., Lee, K. T., and Nazar, L. F. (2009). A highly ordered nanostructured carbon-sulphur cathode for lithium-sulphur batteries. *Nat. Mater.* 8, 500–506. doi:10.1038/NMAT2460

Kamaya, N., Homma, K., Yamakawa, Y., Hirayama, M., Kanno, R. M., Yonemura, R., et al. (2011). A lithium superionic conductor. *Nat. Mater.* 10, 682–686. doi:10.1038/NMAT3066

Matsuyama, T., Sakuda, A., Hayashi, A., Togawa, Y., Mori, S., and Tatsumisago, M. (2012). Preparation of amorphous TiS$_x$ thin film electrodes by the PLD method and their application to all-solid-state lithium secondary batteries. *J. Mater. Sci.* 47, 6601–6606. doi:10.1007/s10853-012-6594-9

Minami, T., Hayashi, A., and Tatsumisago, M. (2006). Recent progress of glass and glass-ceramics as solid electrolytes for lithium secondary batteries. *Solid State Ionics.* 177, 2715–2720. doi:10.1016/j.ssi.2006.07.017

Sakuda, A., Hayashi, A., and Tatsumisago, M. (2013a). Sulfide solid electrolyte with favorable mechanical property for all-solid-state lithium battery. *Sci. Rep.* 3, 2261. doi:10.1038/srep02261

Sakuda, A., Taguchi, N., Takeuchi, T., Kobayashi, H., Sakaebe, H., Tatsumi, K., et al. (2013b). Amorphous TiS$_4$ positive electrode for lithium-sulfur secondary batteries. *Electrochem. commun.* 31, 71–75. doi:10.1016/j.elecom.2013.03.004

Sakuda, A., Taguchi, N., Takeuchi, T., Kobayashi, H., Sakaebe, H., Tatsumi, K., et al. (2014a). Composite positive electrode based on amorphous titanium polysulfide for application in all-solid-state lithium secondary batteries. *Solid State Ionics.* 31, 143–146. doi:10.1016/j.ssi.2013.09.044

Sakuda, A., Taguchi, N., Takeuchi, T., Kobayashi, H., Sakaebe, H., Tatsumi, K., et al. (2014b). Amorphous niobium sulfides as novel positive-electrode materials. *ECS Electrochem. Lett.* 3, A79–A81. doi:10.1149/2.0091407eel

Sakuda, A., Takeuchi, T., Okamura, K., Kobayashi, H., Sakaebe, H., Tatsumi, K., et al. (2014c). Rock-salt-type lithium metal sulphides as novel positive-electrode materials. *Sci. Rep.* 4, 4883. doi:10.1038/srep04883

Sakuda, A., Takeuchi, T., Kobayashi, H., Sakaebe, H., Tatsumi, K., and Ogumi, Z. (2014d). Preparation of novel electrode materials based on lithium niobium sulfides. *Electrochemistry* 82, 880–883. doi:10.5796/electrochemistry.82.880

Sakuda, A., Takeuchi, T., and Kobayashi, H. (2016). Electrode morphology in all-solid-state lithium secondary batteries consisting of LiNi$_{1/3}$Co$_{1/3}$Mn$_{1/3}$O$_2$ and Li$_2$S-P$_2$S$_5$ solid electrolytes. *Solid State Ionics.* 285, 112–117. doi:10.1016/j.ssi.2015.09.010

Schuster, J., He, G., Mandlmeier, B., Yim, T., Lee, K. T., Bein, T., et al. (2012). Spherical ordered mesoporous carbon nanoparticles with high porosity for lithium-sulfur batteries. *Angew. Chem. Int. Ed.* 51, 3591. doi:10.1002/anie.201107817

Takada, K., Aotani, N., Iwamoto, K., and Kondo, S. (1996). Solid state lithium battery with oxysulfide glass. *Solid State Ionics.* 86-88, 877–882. doi:10.1016/0167-2738(96)00199-3

Yamin, H., and Peled, E. (1983). Electrochemistry of a non-aqueous lithium sulfur cell. *J. Power Sources* 9, 281–287. doi:10.1016/0378-7753(83)87029-3

Conflict of Interest Statement: The authors declare that the research was conducted in the absence of any commercial or financial relationships that could be construed as a potential conflict of interest.

frontiers
in Energy Research

ORIGINAL RESEARCH
published: 21 April 2016
doi: 10.3389/fenrg.2016.00016

Aqueous Stability of Alkali Superionic Conductors from First-Principles Calculations

Balachandran Radhakrishnan and Shyue Ping Ong*

Department of NanoEngineering, University of California San Diego, La Jolla, CA, USA

Ceramic alkali superionic conductor solid electrolytes (SICEs) play a prominent role in the development of rechargeable alkali-ion batteries, ranging from replacement of organic electrolytes to being used as separators in aqueous batteries. The aqueous stability of SICEs is an important property in determining their applicability in various roles. In this work, we analyze the aqueous stability of twelve well-known Li-ion and Na-ion SICEs using Pourbaix diagrams constructed from first-principles calculations. We also introduce a quantitative free-energy measure to compare the aqueous stability of SICEs under different environments. Our results show that though oxides are, in general, more stable in aqueous environments than sulfides and halide-containing chemistries, the cations present play a crucial role in determining whether solid phases are formed within the voltage and pH ranges of interest.

Keywords: superionic conductors, Pourbaix diagrams, aqueous stability, passivation, corrosion

Edited by:
Guoxiu Wang,
University of Technology Sydney, Australia

Reviewed by:
Li Wang,
Tsinghua University, China
Branimir Nikola Grgur,
University of Belgrade, Serbia

****Correspondence:***
Shyue Ping Ong
ongsp@eng.ucsd.edu

Specialty section:
This article was submitted to Energy Storage, a section of the journal Frontiers in Energy Research

Received: *01 February 2016*
Accepted: *04 April 2016*
Published: *21 April 2016*

Citation:
Radhakrishnan B and Ong SP (2016) Aqueous Stability of Alkali Superionic Conductors from First-Principles Calculations.
Front. Energy Res. 4:16.
doi: 10.3389/fenrg.2016.00016

1. INTRODUCTION

Ceramic alkali superionic conductor solid electrolytes (SICEs) are key enablers to new rechargeable alkali-ion battery architectures that can significantly outperform today's Li-ion batteries (Goodenough et al., 1976; Aono et al., 1990; Kanno et al., 2000; Mizuno et al., 2005; Murugan et al., 2007; Kamaya et al., 2011; Rao and Adams, 2011; Rangasamy et al., 2012). SICEs are non-flammable and may potentially support wider electrochemical windows, leading to enhanced safety and higher energy densities compared to traditional liquid organic solvent electrolytes (Xu, 2014). A good SICE must satisfy many properties, namely, excellent alkali ionic conductivity, a wide electrochemical window and interfacial stability, mechanical compatibility with the electrodes, and phase and aqueous stability. Though properties other than ionic conductivity have not received as much attention in the past, there have been several recent efforts aimed at addressing other properties such as elastic properties (Deng et al., 2016) and electrochemical stability (Zhu et al., 2015; Richards et al., 2016) that have arguably become a more critical bottleneck in SICE design than ionic conductivity.

The aqueous stability of SICEs is also important in all-solid state batteries. In the event of mechanical abuse (Doughty and Pesaran, 2012), the SICE is exposed to environmental elements. On such exposures, the SICEs can react with moisture in the air to either form passivating layers that could alter their ionic conductivity or form hazardous materials. SICEs can also be used as separators between electrodes and electrolytes in aqueous batteries (Luo et al., 2010; Ma et al., 2015). In particular, separators are necessary when Li metal is used as an anode, for example, in Li-air systems (Visco and Chu, 2000; Liu et al., 2015), as Li reduces most electrolytes on contact. Separators in such applications must be stable against Li metal as well as aqueous electrolytes of varying pH values. In particular, the NAtrium SuperIonic CONductor (NASICON), such as $Li_{1.4}Al_{0.4}Ti_{1.4}Ge_{0.2}(PO_4)_3$ and garnet-type SICEs, have shown great promise in such roles (Zhang et al., 2008; Imanishi et al., 2014).

Determination of the aqueous stability of solid electrolytes has thus far been predominantly based on experimental observations. Such experiments take anywhere between a week to a month (Fuentes et al., 2001), where the electrolyte is immersed in an aqueous solution, sometimes with LiOH, LiCl, etc. (Hasegawa et al., 2009; Imanishi et al., 2014), and tested for changes in surface morphology, chemistry, and ionic conductivity. These experiments are time-consuming as well as limited in the set of environmental elements that can be tested. Also, typical experiments are performed at 0 V vs. the standard hydrogen electrode (SHE) and do not reflect the environment that the electrolyte is exposed during battery operation.

In this work, we apply and extend the Pourbaix diagram formalism developed by Persson et al. (2012) to develop a quantitative measure of the aqueous stability of solid electrolytes based on the free-energy change and the phase of the products formed. We then apply this methodology to twelve well-known SICEs that are of current interest. Unsurprisingly, we find that oxide SICEs are significantly more stable than sulfide and halide-containing SICEs. However, we also find wide variations in aqueous stability even within the same anion chemistry. We will discuss these findings in context of the various potential applications of SICEs in energy storage.

2. MATERIALS AND METHODS

To keep the discussion self-contained, we provide a brief description of the equations used in plotting the aqueous stability plots here, and interested readers are referred to the previous work of Persson et al. (2012) for more details. For a given material, operating under an externally applied potential, V_{ext}, the chemical reaction with an aqueous medium can be represented by the following equation:

$$[\mathrm{Mat}] + \mathrm{H_2O} \overset{V_{ext}}{\Leftrightarrow} [\mathrm{Prod}] + \mathrm{mH^+} + \mathrm{ze^-} \tag{1}$$

From the Nernst equation, we can then derive the free-energy change as follows:

$$\Delta G_{rxn} = \Delta G^{o}_{rxn} + 2.303 \times RT \times \log\frac{[Prod]}{[Mat]} \\ -2.303 \times RT \times m \times pH - zV_{ext}, \tag{2}$$

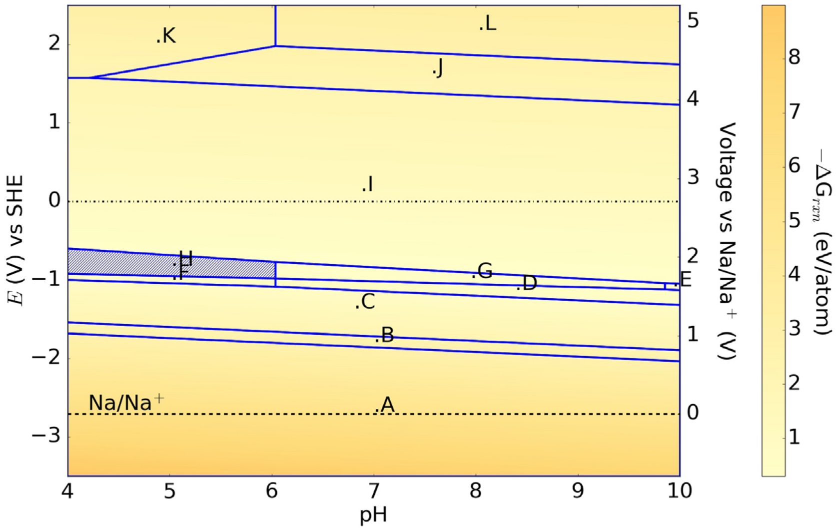

Label	Phase equilibra
A	Zr_5Si_4(s) , NaSi(s) , PH_3(aq)
B	Zr_5Si_4(s) , $Na_2ZrSi_4O_{11}$(s) , PH_3(aq)
C	$Na_2ZrSi_4O_{11}$(s) , PH_3(aq)
D	ZrO_2(s) , $Na_2ZrSi_4O_{11}$(s) , PH_3(aq)
E	ZrO_2(s) , Na^+ , $HSi(OH)^{6-}$, PH_3(aq)
F	$Na_2ZrSi_4O_{11}$(s) , ZrO^{2+} , PH_3(aq)
G	ZrO_2(s) , Na^+ , H_4SiO_4(aq) , PH_3(aq)
H	ZrO^{2+} , Na^+ , H_4SiO_4(aq) , PH_3(aq)
I	$ZrSiO_4$(s) , $NaZr_2(PO_4)_3$(s)
J	$Na_2ZrSi_4O_{11}$(s) , $Zr_2P_2O_9$(s) , $Si_5P_6O_{25}$(s)
K	$Na_2Si_2O_5$(s) , SiP_2O_7(s) , ZrO^{2+}
L	Na_3P_7(s) , ZrO_2(s) , SiP_2O_7(s)

FIGURE 1 | Pourbaix diagram of $Na_3Zr_2Si_2PO_{12}$. Shaded region indicates absence of any solid phase products.

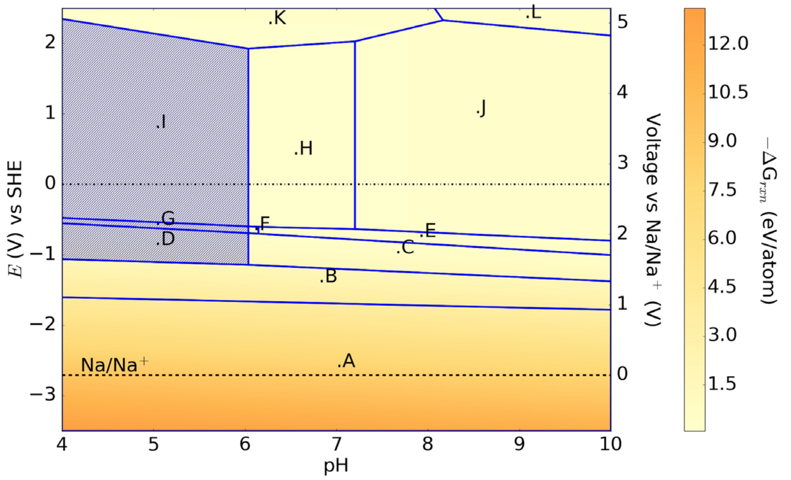

Label	Phase equilibra
A	$ZrH_2(s)$, $NaH(s)$, $PH_3(aq)$
B	$ZrH_2(s)$, Na^+ , $PH_3(aq)$
C	$ZrO_2(s)$, Na^+ , $PH_3(aq)$
D	ZrO^{2+} , Na^+ , $PH_3(aq)$
E	$ZrO_2(s)$, Na^+ , $HPO_3{}^{2-}$
F	$ZrO_2(s)$, Na^+ , $H_2PO_3{}^-$
G	ZrO^{2+} , Na^+ , $H_2PO_3{}^-$
H	$ZrO_2(s)$, Na^+ , $H_2PO_4{}^-$
I	ZrO^{2+} , Na^+ , $H_2PO_4{}^-$
J	$ZrO_2(s)$, Na^+ , $HPO_4{}^{2-}$
K	$Na_2P_3HO_9(s)$, $Zr_2P_2O_9(s)$
L	$ZrO_2(s)$, $Na_2O_2(s)$, $HPO_4{}^{2-}$

FIGURE 2 | **Pourbaix diagram of $NaZr_2(PO_4)_3$.** Shaded region indicates absence of any solid phase products.

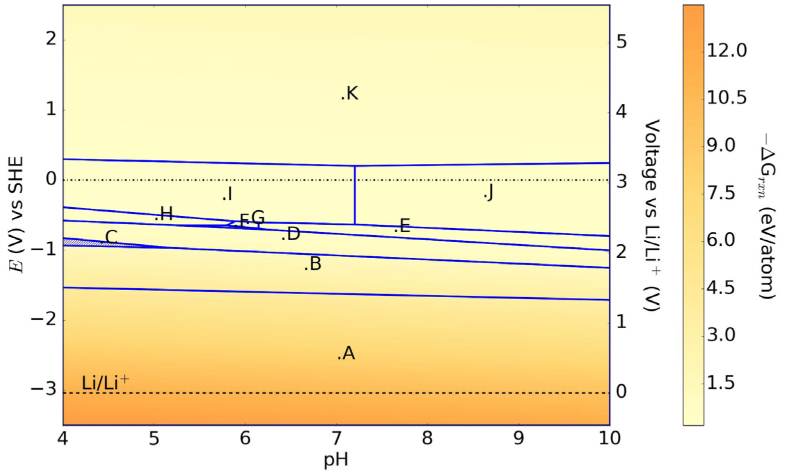

Label	Phase equilibra
A	$TiH_2(s)$, $LiH(s)$, $PH_3(aq)$
B	$TiH_2(s)$, Li^+ , $PH_3(aq)$
C	Li^+ , Ti^{2+} , $PH_3(aq)$
D	$TiO_2(s)$, Li^+ , $PH_3(aq)$
E	$TiO_2(s)$, Li^+ , $HPO_3{}^{2-}$
F	$TiO_2(s)$, $Li_3PO_4(s)$
G	$TiO_2(s)$, Li^+ , $H_2PO_3{}^-$
H	$Ti_5(PO_5)_4(s)$, Li^+
I	$TiO_2(s)$, Li^+ , $H_2PO_4{}^-$
J	$TiO_2(s)$, Li^+ , $HPO_4{}^{2-}$
K	$TiP_2O_7(s)$, $LiOH(s)$

FIGURE 3 | **Pourbaix diagram of $LiTi_2(PO_4)_3$.** Shaded region indicates absence of any solid phase products.

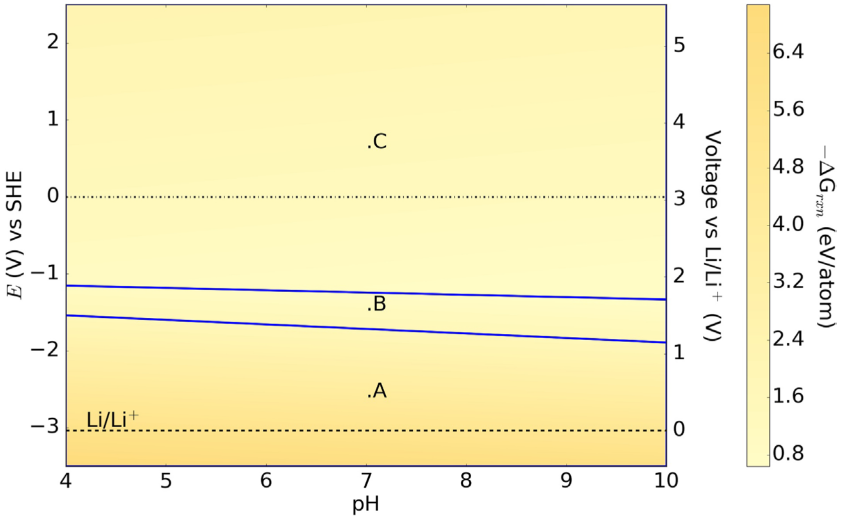

Label	Phase equilibra
A	LaH_3(s) , LiH(s) , ZrH_2(s)
B	LaH_3(s) , Li_2ZrO_3(s)
C	Li_2ZrO_3(s) , La^{3+}

FIGURE 4 | **Pourbaix diagram of $Li_7La_3Zr_2O_{12}$.**

where, $\Delta G^o_{rxn} = G^o_{Prod} - G^o_{Mat}$ is the free-energy change in the reaction under ideal environments (1 molar concentrations and $V_{ext} = 0$ V), R is the Universal gas constant, T is the temperature(=298 K), pH (=−log[H^+]) is the measure of acidity of the aqueous medium, and [Mat] and [Prod] represent the concentration of the chemical species involved in the reaction. The activity of H_2O is assumed to be 1. In our analysis, we use $-\Delta G_{rxn}$ as a quantitative measure of aqueous stability of the material. The larger the value of this free-energy change, the greater is the thermodynamic driving force for the reaction to occur.

All first principles calculated energies are obtained with the Vienna *Ab initio* Simulation Package (VASP) (Kresse and Furthmüller, 1996) implementation of density functional theory (DFT), using the Perdew–Burke–Ernzerhof (PBE) generalized gradient approximation (Perdew et al., 1996) description of the exchange-correlation energy. The calculation parameters are similar to those used in the Materials Project (Jain et al., 2013), and all analyses were performed using the Python Materials Genomics package (Ong et al., 2013).

As per the formalism proposed by Persson et al. (2012), the reference energies for O_2 gas and H_2O are fitted to experimental values (Kubaschewski et al., 1993), and the H_2 energy is fixed to reproduce the H_2O formation energy. The free energies of aqueous ions were calculated from the dissolution energy of solids as given in Johnson et al. (1992) and Pourbaix (1966). The Pourbaix diagrams of SICEs are constructed by fixing the relative ratios of all chemical species except H and O. For example, to generate the Pourbaix diagram of the $Na_3Zr_2Si_2PO_{12}$ NASICON, the Na:Zr:Si:P ratio is fixed at 3:2:2:1, and the Pourbaix diagram at that composition is plotted as a function of pH and the applied voltage.

3. CHEMISTRIES INVESTIGATED

Twelve well-known Li-ion and Na-ion SICEs in a wide range of cation and anion chemistries are studied in this work. For each chemistry, we selected the most stable polymorph for analysis. While many metastable polymorphs are of greater interest due to their higher ionic conductivities, we argue that our analysis provides an upper limit to the free energy of decomposition in aqueous media, i.e., the metastable polymorph will be less stable (in a thermodynamic sense) than the specific phases investigated in this work. Furthermore, the relative energy differences between different polymorphs are on the order of ~10 meV, about 2–3 orders magnitude smaller than the free-energy change of solvation. Our analysis is also limited to the undoped structures as we do not expect small dopant concentrations to alter the aqueous stability significantly. The SICEs studied in this work are as follows:

1. *Oxides*: The NAtrium SuperIonic CONductor (NASICON) and garnet families are two of the most widely explored oxide SICEs. In this work, we have studied the $Na_3Zr_2Si_2PO_{12}$ (Goodenough et al., 1976), $NaZr_2(PO_4)_3$, and $LiTi_2(PO_4)_3$ (Subramanian et al., 1986) members of the NASICON family, which allows us to study the effect of alkali ion and cation chemistry on aqueous stability. We have also selected the tetragonal $Li_7La_3Zr_2O_{12}$ (LLZO) (Murugan et al., 2007) garnet, which is the stable polymorph of the cubic garnet phase that is of interest because of its good ionic conductivity of 0.4 mS/cm and excellent stability against Li metal anodes.
2. *Sulfides*: Sulfide SICEs have received wide attention recently due to their significantly higher ionic conductivities compared

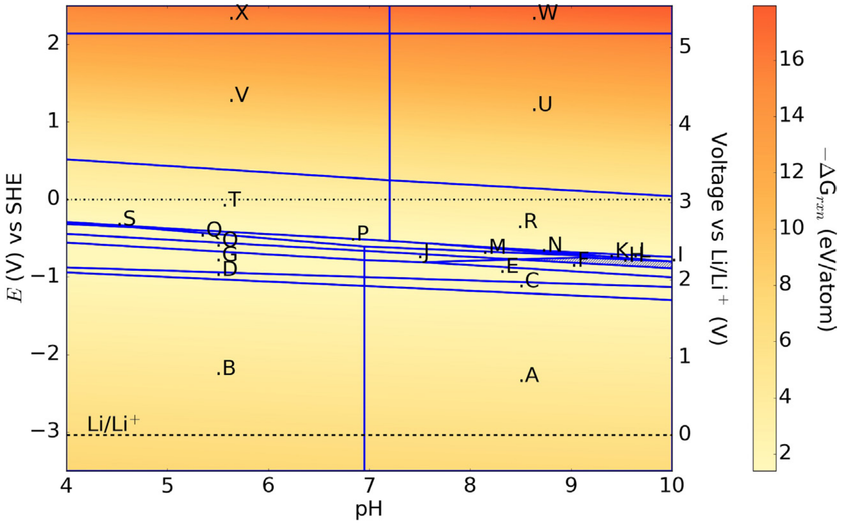

Label	Phase equilibra
A	LiGe(s) , HS^- , PH_3(aq)
B	LiGe(s) , H_2S(aq) , PH_3(aq)
C	$Li_2Ge_7O_{15}$(s) , HS^- , PH_3(aq)
D	$Li_2Ge_7O_{15}$(s) , H_2S(aq) , PH_3(aq)
E	Ge(s) , HS^- , Li^+ , PH_3(aq)
F	Ge(s) , HS^- , Li^+ , HPO_3^{2-}
G	Ge(s) , H_2S(aq) , Li^+ , PH_3(aq)
H	$HGeO_3^-$, HS^- , Li^+ , HPO_3^{2-}
I	$Li_2Ge_7O_{15}$(s) , HS^- , HPO_3^{2-}
J	$Li_7P_3S_{11}$(s) , Ge(s) , HS^- , Li^+
K	$HGeO_3^-$, HS^- , Li^+ , HPO_4^{2-}
L	$Li_2Ge_7O_{15}$(s) , HS^- , HPO_4^{2-}
M	$Li_7P_3S_{11}$(s) , $HGeO_3^-$, HS^- , Li^+
N	$Li_7P_3S_{11}$(s) , $HGeO_3^-$, HPO_4^{2-}
O	$Li_7P_3S_{11}$(s) , Ge(s) , H_2S(aq) , Li^+
P	$Li_7P_3S_{11}$(s) , $HGeO_3^-$, Li^+
Q	$Li_7P_3S_{11}$(s) , $HGeO_3^-$, H_2S(aq) , Li^+
R	Li_2GeS_3(s) , HPO_4^{2-}
S	GeS(s) , Li_3PO_4(s)
T	Li_2GeS_3(s) , $H_2PO_4^-$
U	$Li_2Ge_7O_{15}$(s) , SO_4^{2-} , HPO_4^{2-}
V	$Li_2Ge_7O_{15}$(s) , SO_4^{2-} , $H_2PO_4^-$
W	$Li_2Ge_7O_{15}$(s) , $S_2O_8^{2-}$, $H_2PO_4^-$
X	$Li_2Ge_7O_{15}$(s) , $S_2O_8^{2-}$, HPO_4^{2-}

FIGURE 5 | **Pourbaix diagram of $Li_{10}GeP_2S_{12}$.** Shaded region indicates absence of any solid phase products.

to oxides. Among these sulfides, two of the most promising candidates are $Li_{10}GeP_2S_{12}$ (LGPS), which was reported by Kamaya et al. (2011) to have an ionic conductivity of 12 mS/cm, and $Li_7P_3S_{11}$ (Minami et al., 2007), which has the highest reported conductivity of 17 mS/cm thus far. We also included γ-Li_3PS_4 (Liu et al., 2013), which is one of the parent structures of the widely used LiPON solid electrolyte, and tetragonal Na_3PS_4 (t-Na_3PS_4), which is the stable polymorph of the cubic Na_3PS_4 SICE (Hayashi et al., 2012).

3. *Halide-containing chemistries*: Several halide-containing compounds have recently emerged as potential SICEs. The lithium-rich anti-perovskites (LRAP) (Zhao and Daemen, 2012) are a recently discovered class of SICEs, and we have included the Li_3OCl and Li_3OBr compounds in our analysis. We have also included both the oxide Li_6PO_5Cl and sulfide Li_6PS_5Cl members of the argyrodite family (Kong et al., 2010).

4. RESULTS

Using the above methodology, we have analyzed the aqueous stability of twelve well-known SICEs in a pH range of 4.0–10.0, i.e., from acidic to basic environments. The externally applied voltage is varied between −3.5 V and 2.5 V (versus SHE), which encompasses an equivalent voltage range of −0.46 to 5.54 V versus Li/Li^+ (−3.04 V vs SHE) and −0.79 to 5.21 V versus Na/Na^+ (−2.71 V vs SHE) (Vanysek, 2011). In all Pourbaix diagrams, the corresponding alkali anode half-cell voltage is indicated for reference, and all aqueous ions other than H^+ are fixed at a molality of 10^{-6} mol/L.

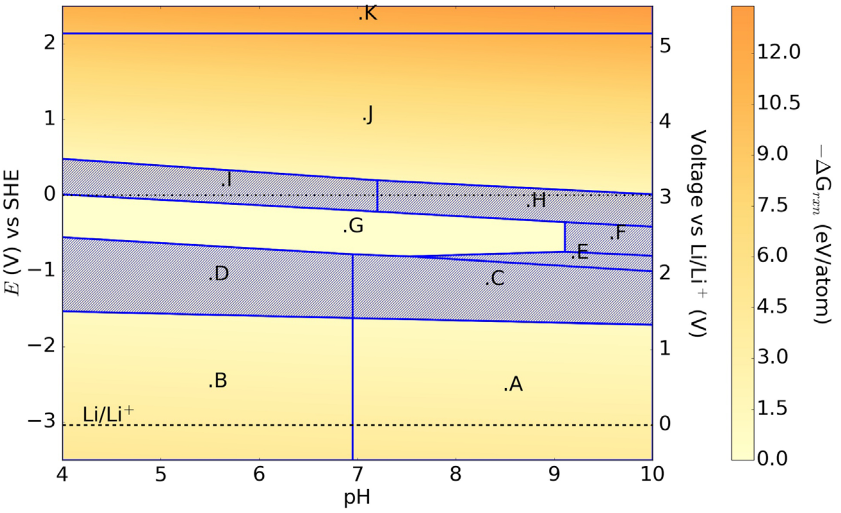

Label	Phase equilibra
A	$LiH(s)$, HS^- , $PH_3(aq)$
B	$LiH(s)$, $H_2S(aq)$, $PH_3(aq)$
C	HS^- , Li^+ , $PH_3(aq)$
D	$H_2S(aq)$, Li^+ , $PH_3(aq)$
E	HS^- , Li^+ , $HPO_3{}^{2-}$
F	HS^- , Li^+ , $HPO_4{}^{2-}$
G	$Li_7P_3S_{11}(s)$
H	$SO_4{}^{2-}$, Li^+ , $HPO_4{}^{2-}$
I	$SO_4{}^{2-}$, Li^+ , $H_2PO_4{}^-$
J	$LiPO_3(s)$, $SO_4{}^{2-}$
K	$LiPO_3(s)$, $S_2O_8{}^{2-}$

FIGURE 6 | **Pourbaix diagram of $Li_7P_3S_{11}$.** Shaded region indicates absence of any solid phase products.

4.1. Oxides

4.1.1. NASICON $Na_3Zr_2Si_2PO_{12}$, $NaZr_2(PO_4)_3$, and $LiTi_2(PO_4)_3$

The Pourbaix diagram of the $Na_3Zr_2Si_2PO_{12}$ NASICON is shown in **Figure 1**. On exposure to neutral environments, the non-silicon version of NASICON:$NaZr_2(PO_4)_3$ is formed along with $ZrSiO_4$ at 0 V, materials known to be less ionically conductive compared to NASICON. This is qualitatively in good agreement with the experiments explaining the change in the surface morphology as well as the conductivity (Ahmad et al., 1987; Mauvy et al., 1999; Fuentes et al., 2001). Fuentes et al. (2001) attributes the change in surface morphology to the formation of hydronium NASICON, but positive identification has been found lacking. In the voltage range −3.5 to −1 V (SHE), exposure to aqueous environments leads to formation of phosphine, which in gaseous form is known to be toxic and highly flammable. Otherwise, the Pourbaix diagram predicts that the NASICON forms solid insulating phases at high voltages. At low voltages, however, ZrH_2, a metallic alloy (Bickel and Berlincourt, 1970), is predicted to be the only solid product formed, which may not protect the SICE against further reaction.

The free-energy change shows that NASICON is more stable at reducing environments than oxidizing environments, especially at neutral environments with $-\Delta G_{rxn} \leq 1$ eV/atom. In comparison, we observe that $NaZr_2(PO_4)_3$ (**Figure 2**) is more stable at neutral environments than $Na_3Zr_2Si_2PO_{12}$ (lower free-energy change), but corrodes in acidic environments.

$LiTi_2(PO_4)_3$ (LTP), which also crystallizes in the NASICON structure, is one of the most stable electrolytes at 0 V across the pH range with a $-\Delta G_{rxn} \leq 0.2$ eV/atom, as shown in **Figure 3**. When exposed to aqueous environments at anodic voltages, it forms LiH, TiH_2, and phosphine gas. At voltages >0 V (SHE), the solid products formed, such as TiO_2 and Li_2O_2, can potentially provide a stable passivating layer. Acidity of the aqueous medium does not alter the composition of the passivating layers. The passivity predicted in the Pourbaix diagram explains the experimental observations that LTP is generally quite stable in aqueous environments (Zhang et al., 2008; Hasegawa et al., 2009). The same experiments also reported that exposure to LiCl and LiOH, which are used in aqueous batteries, alters only the surface chemistry while the electrolyte material itself was stable. At anodic voltages, the tendency for Ti^{4+} to be reduced to Ti^{2+}-forming TiH_2 may account for the larger driving force toward decomposition. It should be noted that TiH_2 (Ito et al., 2006) is metallic.

4.1.2. Garnet $Li_7La_3Zr_2O_{12}$

The Pourbaix diagram of garnet $Li_7La_3Zr_2O_{12}$ (**Figure 4**) shows that it is relatively stable in aqueous environments, with solid phases formed throughout the voltage range of interest. Li_2ZrO_3, formed at 0 V and oxidizing environments, is known to be a stable solid with low ionic conductivity. At anodic voltages <−1 V (SHE), hydrides of Li, Zr, and La are formed.

Like LTAP, garnet SICEs have been explored for the role of a separator in aqueous electrolytes with Li metal anodes (Imanishi et al., 2014). Similar to the NASICONs, we find that the acidity of the aqueous medium does not significantly alter the products formed. Also, the low free-energy change (≤1 eV/atom at 0 V) throughout the pH range shows that the garnet is relatively stable in aqueous environments, consistent with previous experimental observations (Murugan et al., 2007; Shimonishi et al., 2011).

4.2. Sulfides

4.2.1. $Li_{10}GeP_2S_{12}$ (LGPS)

From **Figure 5**, we may observe that the $Li_{10}GeP_2S_{12}$ (LGPS) (Kamaya et al., 2011) superionic conductor is predicted to form solid phases throughout the entire voltage range. At 0 V (SHE) and oxidizing environments, $Li_2Ge_7O_{15}$ is one of the products formed, which can potentially form a good passivation layer even though it has much lower ionic conductivity compared to LGPS. However, either LiGe or Ge are formed at voltages ≤−1 V (SHE), which being poor electronic insulators, may not passivate the SICE against further reaction. Between voltages ±0.5 V (SHE), Li_2GeS_3 is formed which has a reasonable ionic conductivity of 0.1 mS/cm (Seo and Martin, 2011). As with other phosphorous containing compounds, phosphine gas is one of the predicted products at voltages ≤0 V (SHE).

Though solid phases are generally formed for LGPS throughout the pH and voltage range of interest, we find that the driving force for the formation of these products is generally higher than for the oxide phases. Unlike the NASICON and garnet, LGPS shows greater driving force toward oxidation rather than reduction.

4.2.2. $Li_7P_3S_{11}$

In contrast to $Li_{10}GeP_2S_{12}$, the $Li_7P_3S_{11}$ (Minami et al., 2007) glass–ceramic is predicted to be significantly less stable in aqueous environments. There are large E–pH regions where no solid phases are stable (shaded regions in **Figure 6**). The potentially passivating $LiPO_3$ phase is formed at cathodic voltages of 5 V (vs SHE), while hydrides and phosphine are formed at anodic voltages ≤−1.5 V (SHE), similar to other SICEs.

4.2.3. t-Na_3PS_4 and γ-Li_3PS_4

M_3PS_4 (M = Na and Li) also belongs to the $M_2S–P_2S_5$ glass–ceramic system. The qualitative features of their Pourbaix diagrams (**Figures 7** and **8**) are very similar to that of $Li_7P_3S_{11}$, with large E–pH regions where no solid phases are stable. Phosphates and

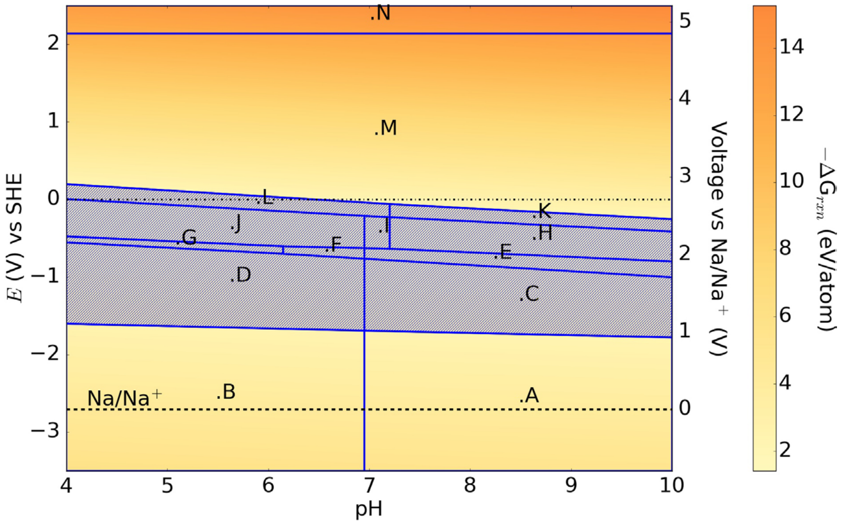

Label	Phase equilibra
A	NaH(s) , HS^- , PH_3(aq)
B	NaH(s) , H_2S(aq) , PH_3(aq)
C	HS^- , Na^+ , PH_3(aq)
D	H_2S(aq) , Na^+ , PH_3(aq)
E	HS^- , Na^+ , HPO_3^{2-}
F	H_2S(aq) , Na^+ , HPO_3^{2-}
G	H_2S(aq) , Na^+ , $H_2PO_3^-$
H	HS^- , Na^+ , HPO_4^{2-}
I	HS^- , Na^+ , $H_2PO_4^-$
J	H_2S(aq) , Na^+ , $H_2PO_4^-$
K	SO_4^{2-} , Na^+ , HPO_4^{2-}
L	SO_4^{2-} , Na^+ , $H_2PO_4^-$
M	$Na_2P_3HO_9$(s) , SO_4^{2-}
N	$Na_2P_3HO_9$(s) , $S_2O_8^{2-}$

FIGURE 7 | Pourbaix diagram of t-Na_3PS_4. Shaded region indicates absence of any solid phase products.

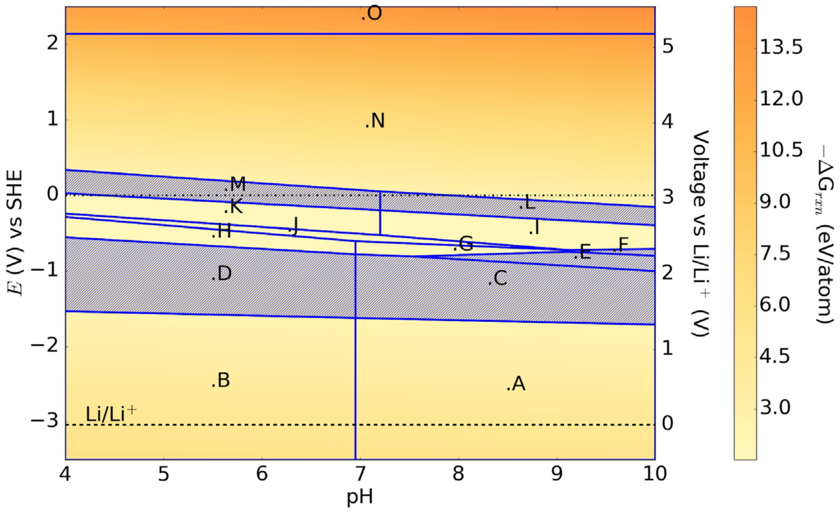

Label	Phase equilibra
A	LiH(s) , HS^- , PH_3(aq)
B	LiH(s) , H_2S(aq) , PH_3(aq)
C	HS^- , Li^+ , PH_3(aq)
D	H_2S(aq) , Li^+ , PH_3(aq)
E	HS^- , Li^+ , HPO_3^{2-}
F	HS^- , Li^+ , HPO_4^{2-}
G	$Li_7P_3S_{11}$(s) , HS^- , Li^+
H	$Li_7P_3S_{11}$(s) , H_2S(aq) , Li^+
I	$Li_7P_3S_{11}$(s) , HPO_4^{2-}
J	$Li_7P_3S_{11}$(s) , Li^+
K	$Li_7P_3S_{11}$(s) , $H_2PO_4^-$
L	SO_4^{2-} , Li^+ , HPO_4^{2-}
M	SO_4^{2-} , Li^+ , $H_2PO_4^-$
N	$LiPO_3$(s) , SO_4^{2-}
O	$LiPO_3$(s) , $S_2O_8^{2-}$

FIGURE 8 | **Pourbaix diagram of γ-Li_3PS_4.** Shaded region indicates absence of any solid phase products.

hydrated phosphates are generally formed at cathodic voltages, while hydrides are formed at anodic voltages.

4.3. Halide-Containing Chemistries

4.3.1. Lithium-Rich Anti-Perovskites (LRAP) Li_3OCl and Li_3OBr

Figures 9 and **10** show the Pourbaix diagrams of the Li_3OCl and Li_3OBr anti-perovskites, respectively. In general, the anti-perovskites are predicted to be unstable in aqueous environments with large regions where no solid phases are formed. Lithium peroxide Li_2O_2 is predicted to form at voltages ≥1 V (SHE), while LiH is predicted to form at voltages ≤−1.5 V (SHE). Between the two anion chemistries, the key difference is in the free-energy change of reaction. The chloride is predicted to have a higher free-energy change, i.e., larger driving force for decomposition, compared to the bromide. Nevertheless, these free-energy changes are much smaller in magnitude compared to the sulfides, which suggest that the LRAPs are less reactive compared to the sulfides in aqueous media.

4.3.2. Argyrodites Li_6PO_5Cl and Li_6PS_5Cl

The Pourbaix diagram of the oxide-argyrodite Li_6PO_5Cl (**Figure 11**) has generally similar features as that of the LRAPs, with large E–pH regions containing no stable solid phases. Somewhat surprisingly, we find that the sulfur-argyrodite Li_6PS_5Cl may form a passivating layer of $Li_7P_3S_{11}$ at 0 V (SHE) as shown in **Figure 12**. A computational study on the sulfur-argyrodites (Li_6PS_5X) by Chen et al. (2015) hypothesized the formation of LiX, LiOH, H_2S, and Li_3PO_4 on hydrolysis with predicted decomposition energies of the order of 0.3 eV/atom. Our results predict decomposition energies ranging 1.5–12 eV/atom with a range of both solid and aqueous products formed across the E–pH range.

5. DISCUSSION

In this work, we investigated the aqueous stability of twelve well-known SICE chemistries using a Pourbaix diagram formalism. None of the SICEs investigated are found to be completely non-reactive on exposure to moisture. However, the decomposition of an electrolyte itself is not necessarily fatal to the electrochemical performance. After all, the organic solvents, such as ethylene carbonate and dimethylcarbonate, are unstable with respect to reduction by Li metal. The key is whether a good passivation layer can be formed that will protect the SICE against further

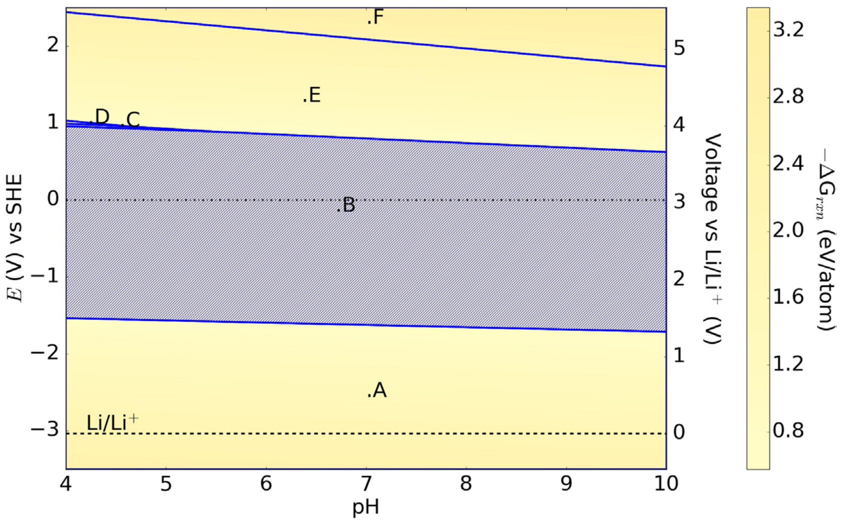

Label	Phase equilibra
A	LiH(s) , Cl^-
B	Cl^- , Li^+
C	ClO_2(s) , Li^+
D	ClO_3(s) , Li^+
E	$LiClO_4$(s) , Li^+
F	Li_2O_2(s) , $LiClO_4$(s)

FIGURE 9 | **Pourbaix diagram of Li_3OCl**. Shaded region indicates absence of any solid phase products.

reaction and still provide a reasonable pathway for alkali-ion transport.

Our broad findings are in general agreement with previous experimental studies and expected behavior of chemistries, i.e., that sulfide and halide-containing SICEs are less stable under aqueous media than oxide SICEs, with larger driving forces to oxidize at cathodic (high) voltages vs SHE. However, we find that there are significant variations in stability even within the same anion chemistry. For instance, comparing the $Na_3Zr_2Si_2PO_{12}$ and $NaZr_2(PO_4)_3$ NASICONs, we find that the former is more stable, particularly under acidic environments at high voltages, due to the presence of Si which promotes formation of solid silicate phases. Indeed, this observation suggests that the choice of cation (other than the alkali ion) may be a possible means to tune the phases formed at various E–pH. Another example can be seen by comparing the Pourbaix diagrams of LGPS, $Li_7P_3S_{11}$, and γ-Li_3PS_4. Although all the three materials are thiophosphates, the presence of Ge in LGPS results in the formation of stable solid phases across most of the investigated E–pH range.

In rechargeable alkali batteries, an ultimate goal is the use of a metal anode, which would yield significant increases in energy density over traditional carbon-based (graphitic for Li and hard carbons for Na) anodes. However, the inherent reactivity of the alkali metal, as well as the potential for dendrite formation during plating (for Li), has thus far pose a great challenge in the real-world applications. One potential strategy of addressing both issues is to use a separator to protect the alkali metal, as well as act as a barrier against dendrite formation. Indeed, the two common SICEs explored for this purpose, $LiTi_2(PO_4)_3$ and garnet LLZO (Zhang et al., 2008; Imanishi et al., 2014), are predicted to have relatively good stability in aqueous media. The garnet LLZO, in particular, is remarkable for its relative lack of reactivity across wide voltage and pH ranges, and low driving forces for decomposition.

It should be noted that the analysis presented is a purely thermodynamic one, and no kinetic factors are taken into account. Furthermore, while the lack of any stable solid phase would certainly preclude the possibility of passivation in a particular E–pH region, the existence of stable solid phases does not necessarily mean that a stable passivation layer will be formed. Ultimately, whether a solid phase can form a useful passivation layer depends on its morphology upon formation, its electronic conductivity, and its ionic conductivity. Nevertheless, we believe this work provides useful predictions of the phase equilibria at various E–pH and a quantification of the thermodynamic driving forces for reaction. These predictions can, and hopefully would be, validated against comprehensive experimental studies of SICEs in aqueous media.

6. CONCLUSION

To conclude, we have analyzed and compared the aqueous stability of twelve SICEs using a Pourbaix diagram formalism. In general, the predicted relative stabilities of the SICEs are in line with previous experimental results, where available, and expected behavior of chemistries. We find that the anion chemistry is a primary determinant of aqueous stability, though

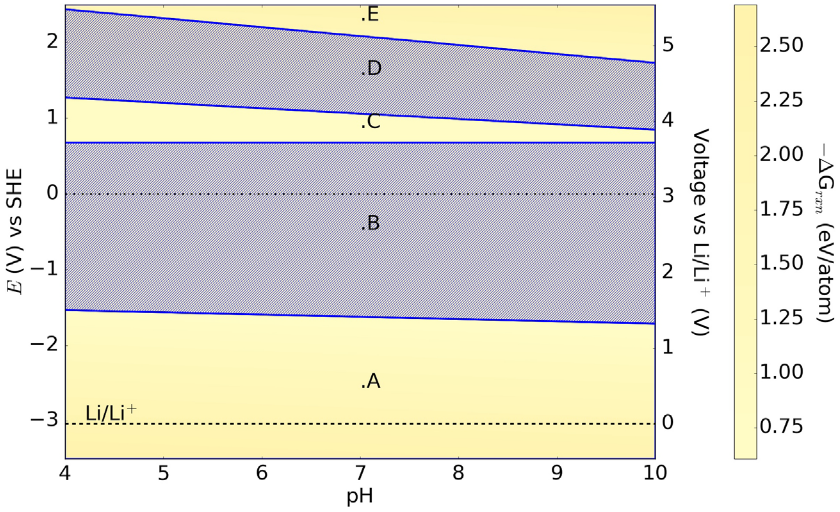

Label	Phase equilibra
A	LiH(s) , Br^-
B	Li^+ , Br^-
C	Br(s) , Li^+
D	Li^+ , BrO_3^-
E	Li_2O_2(s) , BrO_3^-

FIGURE 10 | **Pourbaix diagram of Li_3OBr**. Shaded region indicates absence of any solid phase products.

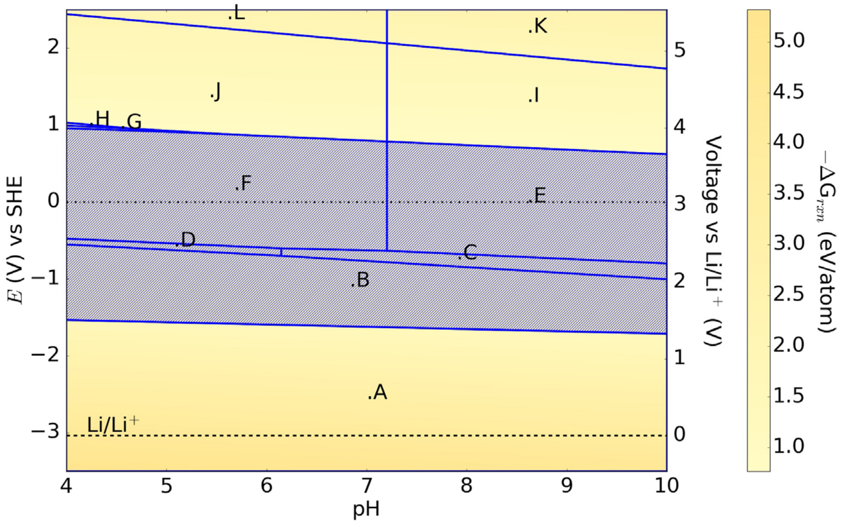

Label	Phase equilibra
A	LiH(s) , Cl^- , PH_3(aq)
B	Cl^- , Li^+ , PH_3(aq)
C	Cl^- , Li^+ , HPO_3^{2-}
D	Cl^- , Li^+ , $H_2PO_3^-$
E	Cl^- , Li^+ , HPO_4^{2-}
F	Cl^- , Li^+ , $H_2PO_4^-$
G	ClO_2(s) , Li^+ , $H_2PO_4^-$
H	ClO_3(s) , Li^+ , $H_2PO_4^-$
I	$LiClO_4$(s) , Li^+ , HPO_4^{2-}
J	$LiClO_4$(s) , Li^+ , $H_2PO_4^-$
K	Li_2O_2(s) , $LiClO_4$(s) , HPO_4^{2-}
L	Li_2O_2(s) , $LiClO_4$(s) , $H_2PO_4^-$

FIGURE 11 | **Pourbaix diagram of Li_6PO_5Cl**. Shaded region indicates absence of any solid phase products.

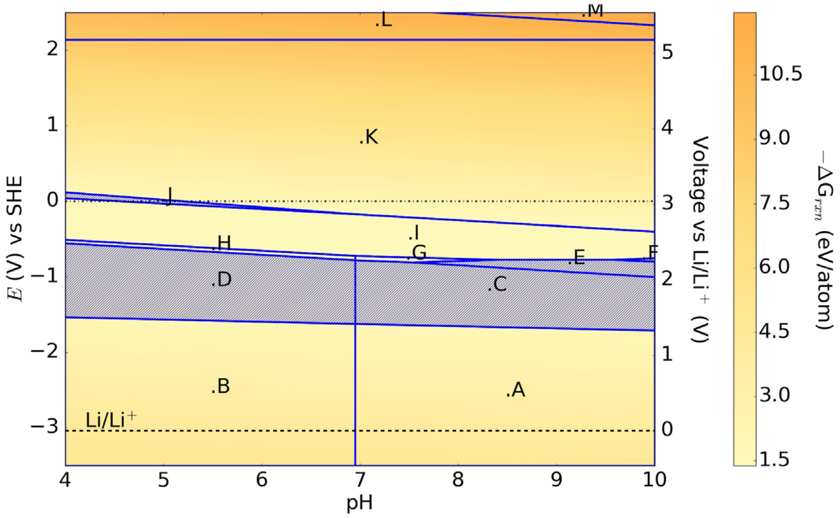

Label	Phase equilibra
A	$LiH(s)$, HS^-, Cl^-, $PH_3(aq)$
B	$LiH(s)$, $H_2S(aq)$, Cl^-, $PH_3(aq)$
C	HS^-, Cl^-, Li^+, $PH_3(aq)$
D	$H_2S(aq)$, Cl^-, Li^+, $PH_3(aq)$
E	HS^-, Cl^-, Li^+, HPO_3^{2-}
F	HS^-, Cl^-, Li^+, HPO_4^{2-}
G	$Li_7P_3S_{11}(s)$, HS^-, Cl^-, Li^+
H	$Li_7P_3S_{11}(s)$, $H_2S(aq)$, Cl^-, Li^+
I	$Li_7P_3S_{11}(s)$, Cl^-, Li^+
J	SO_4^{2-}, Cl^-, Li^+, $H_2PO_4^-$
K	$Li_3PO_4(s)$, $Li_4H_3ClO_3(s)$, SO_4^{2-}
L	$Li_3PO_4(s)$, $Li_4H_3ClO_3(s)$, $S_2O_8^{2-}$
M	$LiClO_4(s)$, $Li_2O_2(s)$, $S_2O_8^{2-}$, HPO_4^{2-}

FIGURE 12 | **Pourbaix diagram of Li_6PS_5Cl**. Shaded region indicates absence of any solid phase products.

careful tuning of the cation chemistry can alter the solid phases formed and is a potential means of tuning SICEs for specific applications. Beyond SICEs, the first-principles approach presented here can be similarly applied to other technological applications, where aqueous stability of a material is a design concern.

AUTHOR CONTRIBUTIONS

BR designed and implemented the study on aqueous stability of alkali superionic conductors. SO is the principal investigator of this project and supervised the conceptualization and implementation. Both authors made equal contribution toward analysis of results and drafting the manuscript.

FUNDING

This work was supported by the National Science Foundation's Designing Materials to Revolutionize and Engineer our Future (DMREF) program under Grant No. 1436976. Some of the computations in this work were performed using the Extreme Science and Engineering Discovery Environment (XSEDE), which is supported by National Science Foundation grant number ACI-1053575.

REFERENCES

Ahmad, A., Wheat, T., Kuriakose, A., Canaday, J., and McDonald, A. (1987). Dependence of the properties of NASICONS on their composition and processing. *Solid State Ionics* 24, 89–97. doi:10.1016/0167-2738(87)90070-1

Aono, H., Sugimoto, E., Sadaoka, Y., Manaka, N., and Adachi, G. (1990). Ionic conductivity of solid electrolytes based on lithium titanium phosphate. *J. Electrochem. Soc.* 137, 1023–1027. doi:10.1149/1.2086597

Bickel, P. W., and Berlincourt, T. G. (1970). Electrical properties of hydrides and deuterides of zirconium. *Phys. Rev. B* 2, 4807–4813. doi:10.1103/PhysRevB.2.4807

Chen, H. M., Maohua, C., and Adams, S. (2015). Stability and ionic mobility in argyrodite-related lithium-ion solid electrolytes. *Phys. Chem. Chem. Phys.* 17, 16494–16506. doi:10.1039/c5cp01841b

Deng, Z., Wang, Z., Chu, I.-H., Luo, J., and Ong, S. P. (2016). Elastic properties of alkali superionic conductor electrolytes from first principles calculations. *J. Electrochem. Soc.* 163, A67–A74. doi:10.1149/2.0061602jes

Doughty, D. H., and Pesaran, A. A. (2012). *Vehicle Battery Safety Roadmap Guidance*. Golden: National Renewable Energy Laboratory.

Fuentes, R. O., Figueiredo, F., Marques, F. M. B., and Franco, J. I. (2001). Reaction of NASICON with water. *Solid State Ionics.* 139, 309–314. doi:10.1016/S0167-2738(01)00683-X

Goodenough, J. B., Hong, H. Y.-P., and Kafalas, J. A. (1976). Fast Na/+/-ion transport in skeleton structures. *Mater. Res. Bull.* 11, 203–220. doi:10.1016/0025-5408(76)90077-5

Hasegawa, S., Imanishi, N., Zhang, T., Xie, J., Hirano, A., Takeda, Y., et al. (2009). Study on lithium/air secondary batteries-stability of NASICON-type lithium ion conducting glass-ceramics with water. *J. Power Sources* 189, 371–377. doi:10.1016/j.jpowsour.2008.08.009

Hayashi, A., Noi, K., Sakuda, A., and Tatsumisago, M. (2012). Superionic glass-ceramic electrolytes for room-temperature rechargeable sodium batteries. *Nat. Commun.* 3, 856. doi:10.1038/ncomms1843

Imanishi, N., Matsui, M., Takeda, Y., and Yamamoto, O. (2014). Lithium ion conducting solid electrolytes for aqueous lithium-air batteries. *Electrochemistry* 82, 938–945. doi:10.5796/electrochemistry.82.938

Ito, M., Setoyama, D., Matsunaga, J., Muta, H., Kurosaki, K., Uno, M., et al. (2006). Electrical and thermal properties of titanium hydrides. *J. Alloys Comp.* 420, 25–28. doi:10.1016/j.jallcom.2005.10.032

Jain, A., Ong, S. P., Hautier, G., Chen, W., Richards, W. D., Dacek, S., et al. (2013). Commentary: the materials project: a materials genome approach to accelerating materials innovation. *APL Mater.* 1, 011002. doi:10.1063/1.4812323

Johnson, W. J., Oelkers, H. E., and Helgeson, C. H. (1992). SUPCRT92: a software package for calculating the standard molal thermodynamic properties of minerals, gases, aqueous species, and reactions from 1 to 5000 bar and 0 to 1000C. *Comput. Geosci.* 18, 899–947. doi:10.1016/0098-3004(92)90029-Q

Kamaya, N., Homma, K., Yamakawa, Y., Hirayama, M., Kanno, R., Yonemura, M., et al. (2011). A lithium superionic conductor. *Nat. Mater.* 10, 682–686. doi:10.1038/nmat3066

Kanno, R., Hata, T., Kawamoto, Y., and Irie, M. (2000). Synthesis of a new lithium ionic conductor, thio-LISICON – lithium germanium sulfide system. *Solid State Ionics.* 130, 97–104. doi:10.1016/S0167-2738(00)00277-0

Kong, S. T., Deiseroth, H. J., Maier, J., Nickel, V., Weichert, K., and Reiner, C. (2010). Li_6PO_5Br and Li_6PO_5Cl: the first lithium-oxide-argyrodites. *Z. Anorg. Allg. Chem.* 636, 1920–1924. doi:10.1002/zaac.201000121

Kresse, G., and Furthmüller, J. (1996). Efficient iterative schemes for ab initio total-energy calculations using a plane-wave basis set. *Phys. Rev. B Condens. Matter* 54, 11169–11186. doi:10.1103/PhysRevB.54.11169

Kubaschewski, O., Alcock, C. B., and Spencer, P. J. (1993). *Materials Thermochemistry*. New York: Pergamon Press.

Liu, T., Leskes, M., Yu, W., Moore, A. J., Zhou, L., Bayley, P. M., et al. (2015). Cycling $Li-O_2$ batteries via LiOH formation and decomposition. *Science* 350, 530–533. doi:10.1126/science.aac7730

Liu, Z., Fu, W., Payzant, E. A., Yu, X., Wu, Z., Dudney, N. J., et al. (2013). Anomalous high ionic conductivity of nanoporous beta-Li_3PS_4. *J. Am. Chem. Soc.* 135, 975–978. doi:10.1021/ja3110895

Luo, J.-Y., Cui, W.-J., He, P., and Xia, Y.-Y. (2010). Raising the cycling stability of aqueous lithium-ion batteries by eliminating oxygen in the electrolyte. *Nat. Chem.* 2, 760–765. doi:10.1038/nchem.763

Ma, C., Rangasamy, E., Liang, C., Sakamoto, J., More, K. L., and Chi, M. (2015). Excellent stability of a lithium-ion-conducting solid electrolyte upon reversible Li+/H+ exchange in aqueous solutions. *Angew. Chem. Int. Ed. Engl.* 127, 131–135. doi:10.1002/ange.201500056

Mauvy, F., Siebert, E., and Fabry, P. (1999). Reactivity of NASICON with water and interpretation of the detection limit of a NASICON based Na+ ion selective electrode. *Talanta* 48, 293–303. doi:10.1016/S0039-9140(98)00234-3

Minami, K., Mizuno, F., Hayashi, A., and Tatsumisago, M. (2007). Lithium ion conductivity of the $Li_2SP_2S_5$ glass-based electrolytes prepared by the melt quenching method. *Solid State Ionics* 178, 837–841. doi:10.1016/j.ssi.2007.03.001

Mizuno, F., Hayashi, A., Tadanaga, K., and Tatsumisago, M. (2005). New, highly ion-conductive crystals precipitated from Li_2S-P_2S_5 glasses. *Adv. Mater. Weinheim* 17, 918–921. doi:10.1002/adma.200401286

Murugan, R., Thangadurai, V., and Weppner, W. (2007). Fast lithium ion conduction in garnet-type Li(7)La(3)Zr(2)O(12). *Angew. Chem. Int. Ed. Engl.* 46, 7778–7781. doi:10.1002/anie.200701144

Ong, S. P., Richards, W. D., Jain, A., Hautier, G., Kocher, M., Cholia, S., et al. (2013). Python Materials Genomics (pymatgen): a robust, open-source python library for materials analysis. *Comput. Mater. Sci.* 68, 314–319. doi:10.1016/j.commatsci.2012.10.028

Perdew, J., Burke, K., and Ernzerhof, M. (1996). Generalized gradient approximation made simple. *Phys. Rev. Lett.* 77, 3865–3868. doi:10.1103/PhysRevLett.77.3865

Persson, K. A., Waldwick, B., Lazic, P., and Ceder, G. (2012). Prediction of solid-aqueous equilibria: scheme to combine first-principles calculations of solids with experimental aqueous states. *Phys. Rev. B* 85, 235438. doi:10.1103/PhysRevB.85.235438

Pourbaix, M. (1966). *Atlas of Electrochemical Equilibria in Aqueous Solutions*. Oxford: Pergamon Press.

Rangasamy, E., Wolfenstine, J., and Sakamoto, J. (2012). The role of Al and Li concentration on the formation of cubic garnet solid electrolyte of nominal composition $Li_7La_3Zr_2O_{12}$. *Solid State Ionics* 206, 28–32. doi:10.1016/j.ssi.2011.10.022

Rao, R. P., and Adams, S. (2011). Studies of lithium argyrodite solid electrolytes for all-solid-state batteries. *Phys Status Solidi A Appl. Mater.* 208, 1804–1807. doi:10.1002/pssa.201001117

Richards, W. D., Miara, L. J., Wang, Y., Kim, J. C., and Ceder, G. (2016). Interface stability in solid-state batteries. *Chem. Mater.* 28, 266–273. doi:10.1021/acs.chemmater.5b04082

Seo, I., and Martin, S. W. (2011). Preparation and characterization of fast ion conducting lithium thio-germanate thin films grown by RF magnetron sputtering. *J. Electrochem. Soc.* 158, A465. doi:10.1149/1.3552927

Shimonishi, Y., Toda, A., Zhang, T., Hirano, A., Imanishi, N., Yamamoto, O., et al. (2011). Synthesis of garnet-type $Li_{7-x}La_3Zr_2O_{12-1/2x}$ and its stability in aqueous solutions. *Solid State Ionics* 183, 48–53. doi:10.1016/j.ssi.2010.12.010

Subramanian, M., Subramanian, R., and Clearfield, A. (1986). Lithium ion conductors in the system AB(IV)2(PO4)3 (B = Ti, Zr and Hf). *Solid State Ionics* 18-19, 562–569. doi:10.1016/0167-2738(86)90179-7

Vanysek, P. (2011). "Electrochemical series," in *Handbook of Chemistry and Physics*, ed. W. M. Haynes, 92nd Edn (London: CRC Press), 5-80–5-89.

Visco, S. J., and Chu, M.-Y. (2000). *Protective Coatings for Negative Electrodes*. Patent No: US 6025094 A

Xu, K. (2014). Electrolytes and interphases in Li-ion batteries and beyond. *Chem. Rev.* 114, 11503–11618. doi:10.1021/cr500003w

Zhang, T., Imanishi, N., Hasegawa, S., Hirano, A., Xie, J., Takeda, Y., et al. (2008). Li polymer electrolyte water stable lithium-conducting glass ceramics composite for lithium-air secondary batteries with an aqueous electrolyte. *J. Electrochem. Soc.* 155, A965. doi:10.1149/1.2990717

Zhao, Y., and Daemen, L. L. (2012). Superionic conductivity in lithium-rich anti-perovskites. *J. Am. Chem. Soc.* 134, 15042–15047. doi:10.1021/ja305709z

Zhu, Y., He, X., and Mo, Y. (2016). First principles study on electrochemical and chemical stability of the solid electrolyte-electrode interfaces in all-solid-state Li-ion batteries. *J. Mater. Chem. A* 4, 3253–3266. doi:10.1039/C5TA08574H

Conflict of Interest Statement: The authors declare that the research was conducted in the absence of any commercial or financial relationships that could be construed as a potential conflict of interest.

frontiers in Energy Research

ORIGINAL RESEARCH
published: 07 April 2016
doi: 10.3389/fenrg.2016.00012

High Lithium-Ion-Conducting NASICON-Type $Li_{1+x}Al_xGe_yTi_{2-x-y}(PO_4)_3$ Solid Electrolyte

Shang Xuefu[1,2], *Hiroyoshi Nemori*[3], *Shigehi Mitsuoka*[3], *Peng Xu*[4], *Masaki Matsui*[1], *Yasuo Takeda*[1], *Osamu Yamamoto*[1] *and Nobuyuki Imanishi*[1]*

[1] Graduate School of Engineering, Mie University, Tsu, Japan, [2] Department of Physics, Faculty of Engineering, Jiangsu University, Zhenjiang, China, [3] Group 4, Component Engineering Development Department, Suzuki Motor Corporation, Hamamatsu, Japan, [4] Department of Physics, Zhejiang University, Hangzhou, China

A water-stable solid electrolyte is a key material without which aqueous lithium–air batteries could not be operated. In this study, we have examined the electrical conductivity and mechanical properties of a water-stable lithium-ion-conducting solid electrolyte, $Li_{1+x}Al_xGe_yTi_{2-x-y}(PO_4)_3$ with the NASICON-type structure, as a function of the Al and Ge content. $Li_{1+x}Al_xGe_yTi_{2-x-y}(PO_4)_3$ was synthesized by the conventional solid-state reaction method. The highest lithium-ion conductivity of 1.0×10^{-3} S cm^{-1} at 25°C and the highest three-point bending strength of 90 N mm^{-2} at room temperature were observed for a pellet of $Li_{1.45}Al_{0.45}Ge_{0.2}Ti_{1.35}(PO_4)_3$ sintered at 900°C.

Keywords: electrical conductivity, lithium–air battery, lithium conductor, NASICON-type, solid electrolyte

OPEN ACCESS

Edited by:
Fuminori Mizuno,
Toyota Research Institute of North America, USA

Reviewed by:
Hailei Zhao,
University of Science and Technology Beijing, China
Wenping Sun,
University of Wollongong, Australia

****Correspondence:***
Nobuyuki Imanishi
imanishi@chem.mie-u.ac.jp

Specialty section:
This article was submitted to Energy Storage, a section of the journal Frontiers in Energy Research

Received: *01 February 2016*
Accepted: *21 March 2016*
Published: *07 April 2016*

Citation:
Xuefu S, Nemori H, Mitsuoka S, Xu P, Matsui M, Takeda Y, Yamamoto O and Imanishi N (2016) High Lithium-Ion-Conducting NASICON-Type $Li_{1+x}Al_xGe_yTi_{2-x-y}(PO_4)_3$ Solid Electrolyte.
Front. Energy Res. 4:12.
doi: 10.3389/fenrg.2016.00012

INTRODUCTION

In the last half century, many types of lithium-ion-conducting solid electrolytes have been reported, such as Li_3N (Alpen et al., 1977), B_2S_3–Li_2S–LiI glass (Wada et al., 1983), NASICON-type $Li_{1+x}A_xTi_{2-x}(PO_4)_4$ (Aono et al., 1990), perovskite-type $La_{2/3-x}Li_xTiO_3$ (Inaguma et al., 1993), garnet-type $Li_7La_3Zr_2O_{12}$ (Murugan et al., 2007), and thio-LISICON-type $Li_{10}GeP_2S_{12}$ (Kamaya et al., 2011). At present, the highest lithium-ion conductivity of 1.2×10^{-2} S cm^{-1} at room temperature is reported in $Li_{10}GeP_2S_{12}$, which is higher than that of conventional liquid electrolytes, because its lithium-ion transport number is unity. Lithium-ion-conducting solid electrolytes are generally hygroscopic and so are difficult to handle in the open atmosphere, especially the high conductivity sulfide-based solid electrolytes. NASICON-type $Li_{1+x}A_xTi_{2-x}(PO_4)_3$ lithium-conducting solid electrolytes are less sensitive to moisture and can be prepared in the open air, and are also stable in contact with LiCl-saturated aqueous solution (Shimonishi et al., 2011). Aono et al. (1990) has reported the electrical conductivity of the $Li_{1+x}A_xTi_{2-x}(PO_4)_3$ (A = Al, Cr, Ga, Fe, In, La, Sc, and Y) system and found the highest electrical conductivity of 7×10^{-4} S cm^{-1} at 25°C for $Li_{1.3}Al_{0.3}Ti_{1.7}(PO_4)_3$.

Since the report by Aono et al., the NASICON-type lithium-ion-conducting solid electrolytes have been extensively examined. The highest electrical conductivity of 4.62×10^{-3} S cm^{-1} at 27°C was reported for the $Li_{1.5}Al_{0.5}Ge_{1.5}(PO_4)_3$ glass–ceramic by Thokchom and Kumar (2010). However, Fu (1997) studied the $Li_{1-x}Al_xGe_{2-x}(PO_4)_3$ glass–ceramics and found the electrical conductivity of $Li_{1.5}Al_{0.5}Ge_{1.5}(PO_4)_3$ was 4.0×10^{-4} S cm^{-1} at 25°C, and also Xu et al. (2007) found an electrical conductivity of 7.25×10^{-4} S cm^{-1} at room temperature for the $Li_{1.5}Al_{0.5}Ge_{1.5}(PO_4)_3$–0.05 Li_2O glass–ceramic. The preparation of glass–ceramics is somewhat complex, and the effect of aging on the electrical conductivity is questionable. The $Li_{1+x+y}Al_x(Ge, Ti)_{2-x}Si_yP_{4-y}O_{12}$ glass–ceramics have been commercialized by Ohara, Ltd., Japan. The glass–ceramic is water-permeation free, and the electrical conductivity is 10^{-4} S cm^{-1} at room temperature. Recently, Zhang et al. (2013) reported that the electrical conductivity of $Li_{1.4}Al_{0.4}Ti_{1.6}(PO_4)_3$ was enhanced by a partial substitution of Ge for Ti. The highest electrical conductivity of 1.3×10^{-3} S cm^{-1} at 25°C was observed in $Li_{1.4}Al_{0.4}Ge_{0.2}Ti_{1.4}(PO_4)_3$, where the content of Al was fixed to 0.4, and the $Li_{1.4}Al_{0.4}Ge_xTi_{1.6-x}(PO_4)_3$ powders were prepared by a sol–gel method using expensive Ti and Ge alkoxides. In this study, we have examined the electrical conductivity and mechanical properties of the $Li_{1+x}Al_xGe_yTi_{2-x-y}(PO_4)_3$ system in the range of $x = 0.30$–0.55 and $y = 0.1$–0.3 using less expensive starting materials. Water-stable high lithium-ion-conducting solid electrolytes have potential applications for aqueous lithium–air batteries (Zhang et al., 2010; Bruce et al., 2012) and aqueous lithium batteries with aqueous cathodes (Lu et al., 2011; Zhao et al., 2013). These electrolytes have been used as a protective layer for the lithium metal electrode to avoid direct contact with the aqueous solution, because lithium metal reacts vigorously with water.

MATERIALS AND METHODS

The NASICON-type $Li_{1+x}Al_xGe_yTi_{2-x-y}(PO_4)_3$ lithium-ion-conducting solid electrolytes were prepared by conventional solid-state reaction. Corresponding amounts of chemical reagent grade Li_2CO_3, TiO_2, GeO_2, Al_2O_3, and $NH_4H_2PO_4$ were ball milled with zirconia balls in a zirconia vessel for 2 h at 400 rpm using high energy mechanical milling (HEMM) with a planetary micro mill (Fritsch Pulverisette 7), and the mixed powders were then pressed into pellets at 150 MPa and calcined at 600°C for 4 h. The calcined pellets were reground and again ball milled using HEMM. The obtained powders were isostatically pressed into pellets at 150 MPa and sintered at various temperatures (850–1,000°C) for 7 h. Tape-cast $Li_{1.45}Al_{0.45}Ge_{0.2}Ti_{1.35}(PO_4)_3$ films were prepared using a previously reported method (Zhang et al., 2015). Briefly, fine $Li_{1.45}Al_{0.45}Ge_{0.2}Ti_{1.35}(PO_4)_3$ powders prepared by the solid-state reaction were dispersed in a mixed solution of ethanol and toluene (1:1 v/v) using menhaden fish oil [2 wt% to $Li_{1.45}Al_{0.45}Ge_{0.2}Ti_{1.35}(PO_4)_3$] as a dispersant. The mixed slurry was ball milled for 10 h using HEMM. Polyvinyl alcohol [8 wt% to $Li_{1.45}Al_{0.45}Ge_{0.2}Ti_{1.35}(PO_4)_3$] was then added to the mixed slurry as a plasticizer and ball milled for another 12 h. After tape casting, the green sheets were kept in a sealed box with a small amount of ethanol in a refrigerator to slow the drying process at 5°C for 24 h. Several green sheets were hot pressed at 90°C for 10 min and then sintered at 900°C for 7 h.

The crystal structures of sintered samples were analyzed by X-ray diffraction (XRD) analysis using a Rigaku RINT 2500 diffractometer with Cu-Kα radiation in the 2θ range from 10° to 90° at a scanning step rate of 0.02°s^{-1}. The relative density of the sintered samples was estimated from the ratio of the density calculated from the lattice constants and that calculated from the volume and weight of the sintered body. The electrical conductivity of the sintered pellets (ca. 12 mm diameter and 1 mm thick) with gold sputtered electrodes were measured using an impedance phase analyzer (Solartron 1260) in the frequency range of 0.1 Hz–1 MHz with the bias voltage at 10 mV. Bulk and grain boundary conductivities of the sintered samples were estimated from complex impedance plots using Zview 2. Three-point bending strength of the sintered pellets (ca. 0.24 mm thick and ca. 15 mm wide) was measured at room temperature using a materials tester (Shimadzu EZ-SX 500N).

RESULTS AND DISCUSSION

Figure 1 shows XRD patterns of the $Li_{1.5}Al_{0.5}Ge_{0.2}Ti_{1.3}(PO_4)_3$ samples sintered at various temperatures for 7 h with a silicon internal standard to measure the lattice constant. An impurity phase of $AlPO_4$ was observed for the sample sintered at 850°C. At sintering temperatures as low as 850°C, the reaction was not completed. All diffraction lines of the samples sintered at 900, 950, and 1,000°C could be indexed as the NASICON-type structure (Perez-Estebanez et al., 2014). **Figure 2** shows the relative density of $Li_{1.5}Al_{0.5}Ge_{0.2}Ti_{1.3}(PO_4)_3$ pellets sintered at various temperatures. The sample with the impurity phase that was sintered at 850°C showed a low relative density of 87%. The highest relative density of 95.5% was observed for the sample sintered at 900°C, and the relative density decreased with further increase of the sintering temperature. The decreasing of the relative density may be due to the evaporation of lithium compounds at these higher temperatures. **Figure 3** shows impedance profiles of $Li_{1.5}Al_{0.5}Ge_{0.2}Ti_{1.3}(PO_4)_3$ samples (ca. 1 mm thick) sintered at various temperatures and measured at 25°C. The impedance profiles showed a large semicircle followed by a straight line. The semicircle may be attributed to the grain boundary resistance (Bruce and West, 1983). The intercept of the semicircle on the real axis at high frequency represents the bulk resistance, and the diameter of the semicircle indicates the grain boundary resistance. The semicircle due to the bulk resistance was out of the frequency range for the impedance analyzer used. The samples sintered at 900, 950, and 1,000°C showed almost the same bulk conductivity of ca. 2×10^{-3} S cm^{-1}, while the sample sintered at 850°C showed a low bulk conductivity of ca. 10^{-3} S cm^{-1}. The low bulk conductivity may be due to the non-equilibrium phase of $Li_{1.5}Al_{0.5}Ge_{0.2}Ti_{1.3}(PO_4)_3$ prepared at the lower sintering temperature. The grain boundary resistance was dependent on the sintering temperature, and the sample sintered at 900°C with the highest relative density exhibited the lowest grain boundary resistance.

The electrical conductivity, relative density, and three-point bending strength for the $Li_{1+x}Al_xGe_{0.2}Ti_{1.8-x}(PO_4)_3$ system sintered at 900°C for 7 h were examined as a function of x. **Figure 4** shows the XRD patterns of $Li_{1+x}Al_xGe_{0.2}Ti_{1.8-x}(PO_4)_3$. Almost all the diffraction lines for $Li_{1+x}Al_xGe_{0.2}Ti_{1.8-x}(PO_4)_3$ were indexed with the NASICON-type structure. However, $Li_{1+x}Al_xGe_{0.2}Ti_{1.8-x}(PO_4)_3$ with $x = 0.45$, 0.5, and 0.55 also showed diffraction lines due to $AlPO_4$. The changes in the lattice parameter with x in $Li_{1+x}Al_xGe_{0.2}Ti_{1.8-x}(PO_4)_3$ are shown in **Figure 5**. The a lattice parameter of 0.812 at $x = 0.30$ increased to 0.882 nm at $x = 0.40$, and the c lattice parameter of 2.171 nm decreased to 2.043 nm at $x = 0.4$. Cretin and Fabry (1999) reported that the a parameter decreases and the c parameter increases with increasing x in

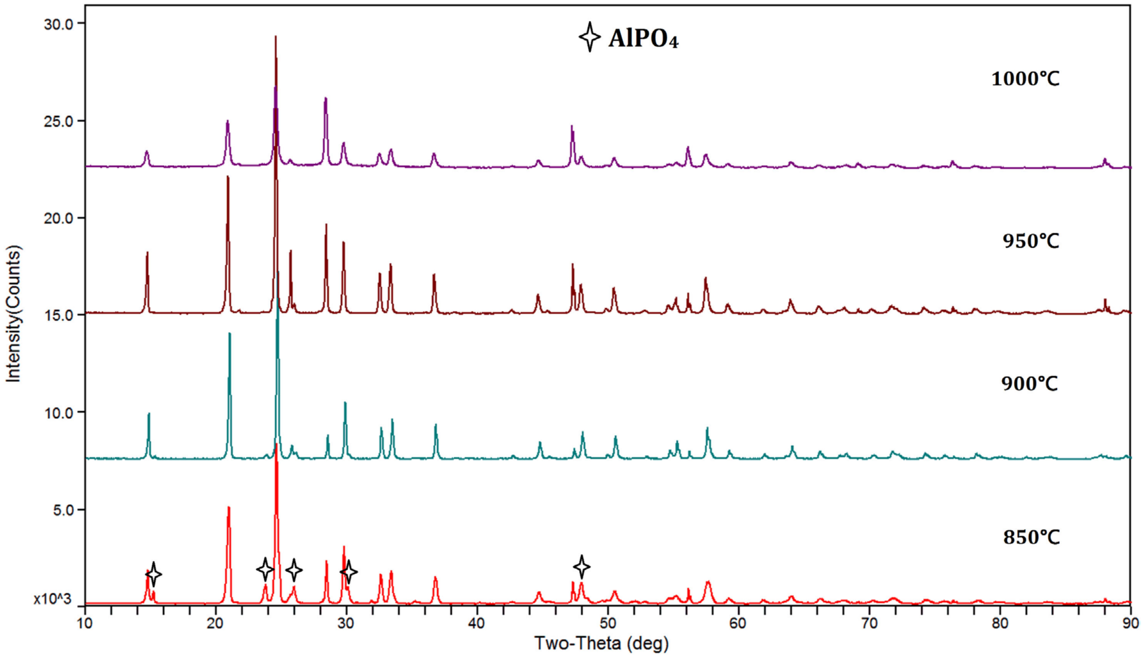

FIGURE 1 | XRD patterns of $Li_{1.5}Al_{0.5}Ge_{0.2}Ti_{1.3}(PO_4)_3$ sintered at various temperatures.

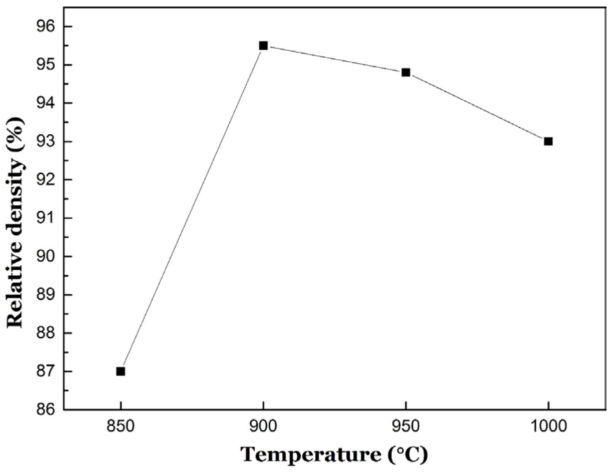

FIGURE 2 | Relative density of $Li_{1.5}Al_{0.5}Ge_{0.2}Ti_{1.3}(PO_4)_3$ sintered at various temperatures.

$Li_{1+x}Al_xTi_{2-x}(PO_4)_3$, while Aono et al. (1990) found both the *a* and *c* parameters decreased with increasing *x*. The decrease of the *c* parameter can be attributed to the substitution of Al^{3+} with a small ionic radius (0.53 nm) for Ti^{4+} with a large ionic radius (0.605 nm) in the octahedral sites. Several factors play a determinant role in the inference of the cation substitution on the structure (Delmas et al., 1981). Additional Li^+ ions are located in the unoccupied Li sites by the substitution of Al^{3+} for Ti^{4+} and Ge^{4+} sites, as observed in $Na_{1+x}Al_xTi_{2-x}(PO_4)_3$ (Maldonado-Manso et al., 2005), to maintain charge neutrality. The additional lithium ions in these sites lead to repulsion along the *a* axis. The reason for the smaller *c* and larger *a* parameters for $Li_{1.55}Al_{0.55}Ge_{0.2}Ti_{1.25}(PO_4)_3$ compared to those for $Li_{1.5}Al_{0.5}Ge_{0.2}Ti_{1.3}(PO_4)_3$ is not clear but may be due to the formation of $AlPO_4$ impurity phases. These results suggest that the solubility limit of Al in $Li_{1+x}Al_xGe_{0.2}Ti_{1.8-x}(PO_4)_3$ is $x = 0.4$, as observed by Aono et al. (1990) for $Li_{1+x}Al_xTi_{2-x}(PO_4)_3$. **Figure 6** shows impedance profiles for $Li_{1+x}Al_xGe_{0.2}Ti_{1.8-x}(PO_4)_3$ measured at 25°C as a function of *x*. The lowest grain boundary resistance was observed for $Li_{1.45}Al_{0.45}Ge_{0.2}Ti_{1.35}(PO_4)_3$. The equivalent circuit in **Figure 6** assumes a general model comprising grains and uniform grain boundaries that are parallel or perpendicular to the current flow. This results in the one with two parallel resistance–capacitance elements, one for the perpendicular grain boundary (R_{p1} and CPE_1) and one from the parallel grain boundary (R_{p2} and CPE_2) connected in parallel. In microcrystalline ceramics, where the effective grain boundary width is negligible compared to the grain size, the contribution of the parallel grain boundary can be neglected. However, parallel grain boundary contribution must be taken into account if the parallel grain boundary conductivity becomes significantly larger than that of the grain and/or if the effective grain boundary width is no longer negligible with respect to the grain size (Bouchet et al., 2003). The change in the grain boundary resistance with *x* could be explained by the change of the relative density as shown in **Figure 7**. $Li_{1.55}Al_{0.55}Ge_{0.2}Ti_{1.25}(PO_4)_3$ with the $AlPO_4$ impurity phase had similar impedance profiles to those of $Li_{1.50}Al_{0.5}Ge_{0.2}Ti_{1.3}(PO_4)_3$ with the $AlPO_4$ impurity phase sintered at 850°C, which revealed a high grain boundary resistance and low bulk conductivity. **Figure 7** shows the electrical conductivities of total, grain bulk, grain boundary, and the relative density of $Li_{1+x}Al_xGe_{0.2}Ti_{1.8-x}(PO_4)_3$ measured at 25°C that are plotted as a function of *x*. The highest total conductivity of

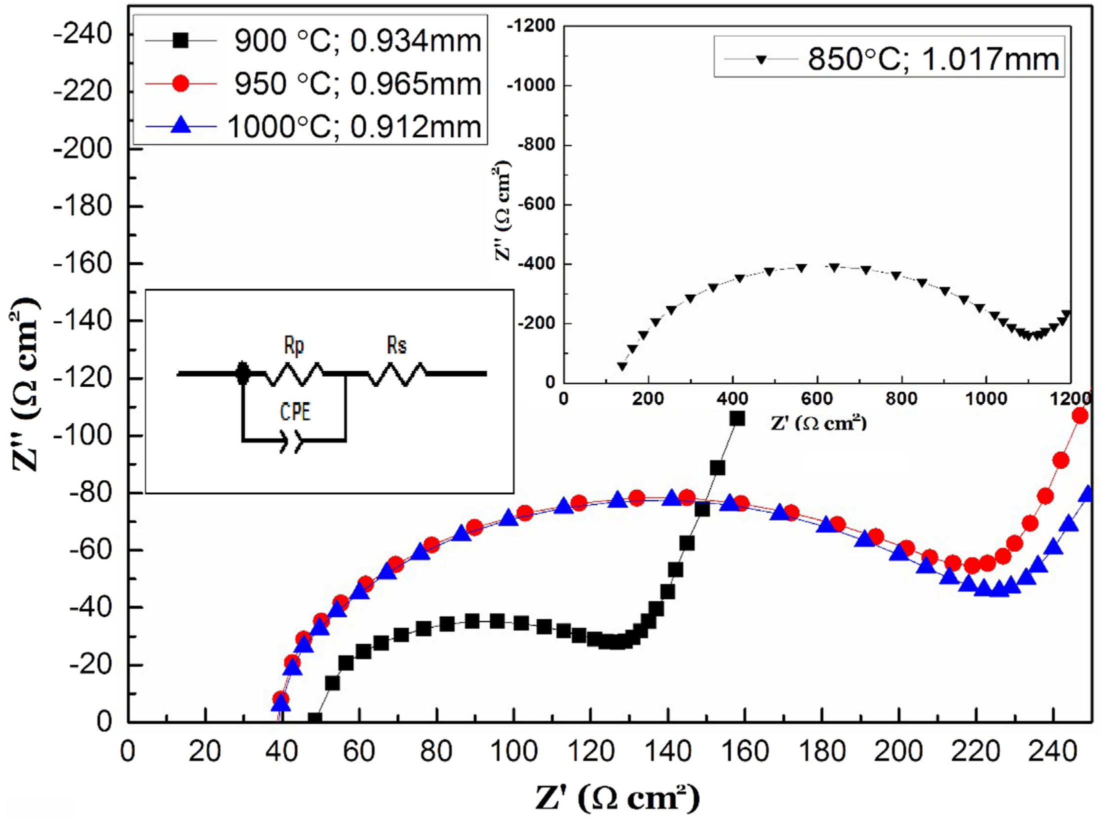

FIGURE 3 | **Impedance profiles of Au/$Li_{1.5}Al_{0.5}Ge_{0.2}Ti_{1.3}(PO_4)_3$/Au as a function of the sintering temperature.**

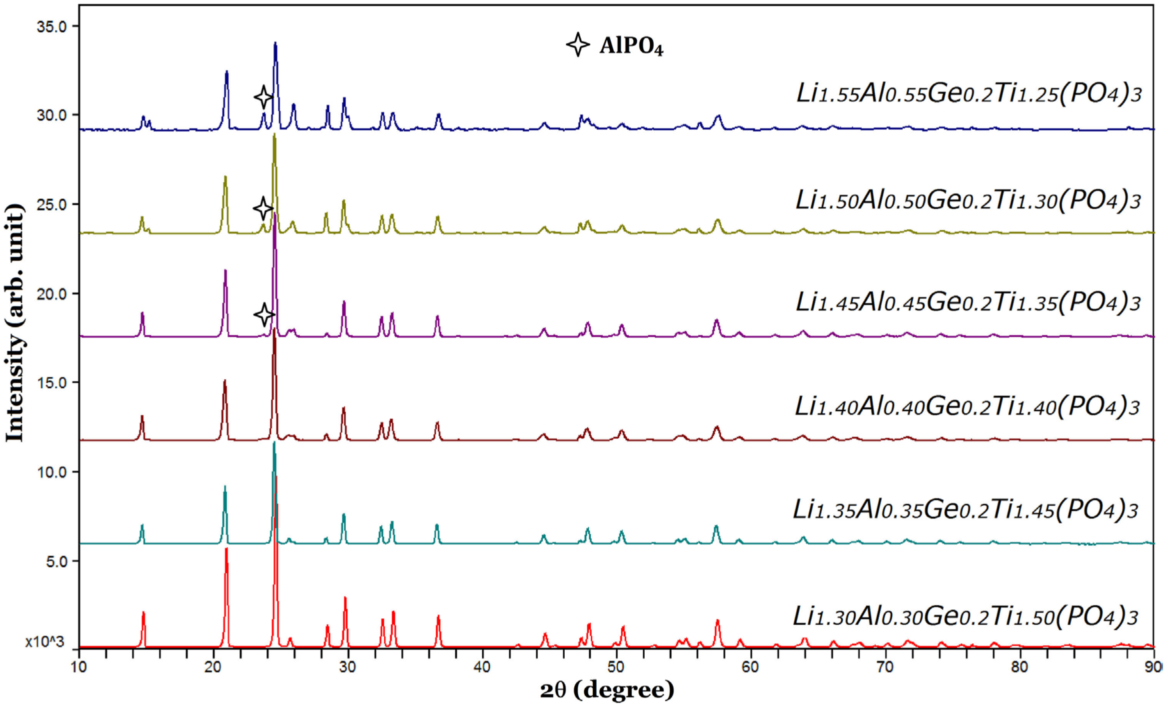

FIGURE 4 | **XRD patterns of $Li_{1+x}Al_xGe_{0.2}Ti_{1.8-x}(PO_4)_3$ sintered at 900°C as a function of *x*.**

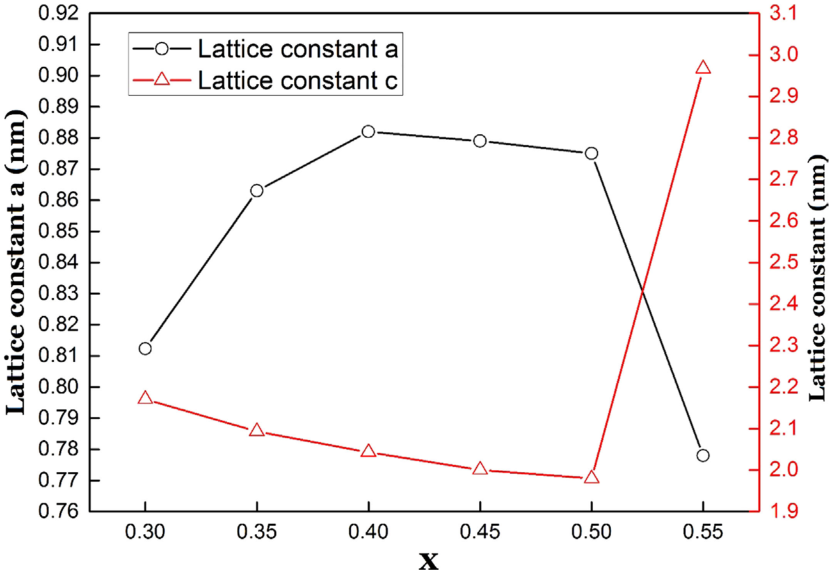

FIGURE 5 | Lattice parameter for $Li_{1+x}Al_xGe_{0.2}Ti_{1.8-x}(PO_4)_3$ sintered at 900°C as a function of *x*.

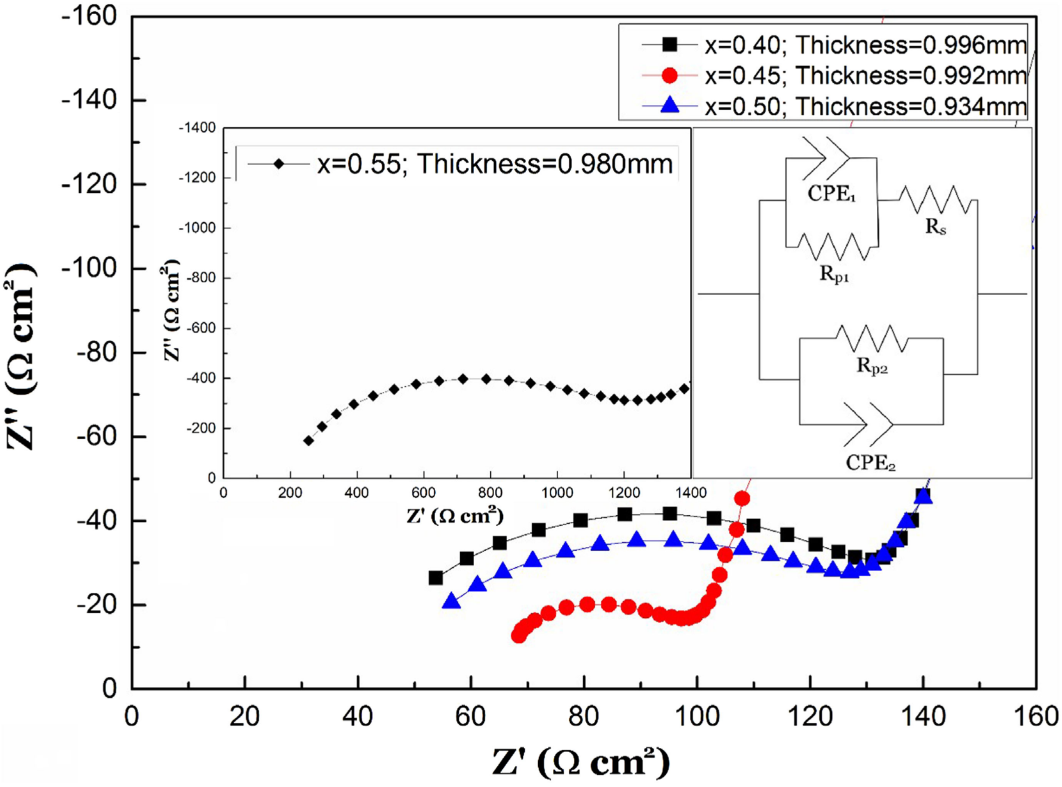

FIGURE 6 | Impedance profiles for $Li_{1+x}Al_xGe_{0.2}Ti_{1.8-x}(PO_4)_3$ measured at 25°C as a function of *x*.

1.0×10^{-3} S cm^{-1} and the highest relative density of 95.8% were observed for $Li_{1.45}Al_{0.45}Ge_{0.2}Ti_{1.35}(PO_4)_3$ at $x = 0.45$. The grain bulk conductivities at $x = 0.40$ and 0.50 are higher than that at $x = 0.45$. The reason for this tendency is not yet clarified. Aluminum composition in the grain bulk may slightly deviate from the nominal one by its accumulation at the grain boundary region.

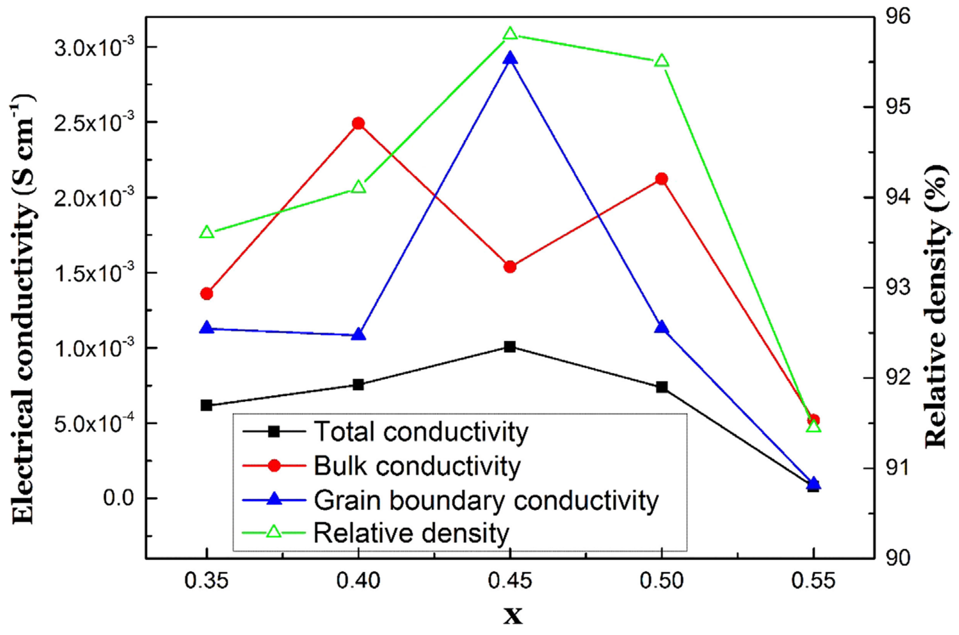

FIGURE 7 | Total, bulk, and grain boundary electrical conductivity at 25°C, and relative density of $Li_{1+x}Al_xGe_{0.2}Ti_{1.8-x}(PO_4)_3$ as a function of *x*.

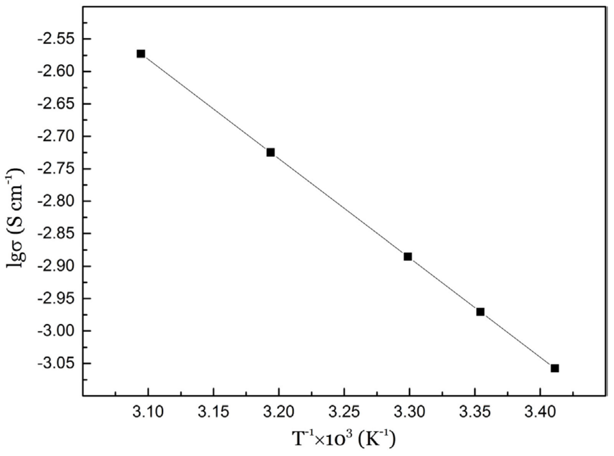

FIGURE 8 | Temperature dependence of the electrical conductivity of $Li_{1.45}Al_{0.45}Ge_{0.2}Ti_{1.35}(PO_4)_3$.

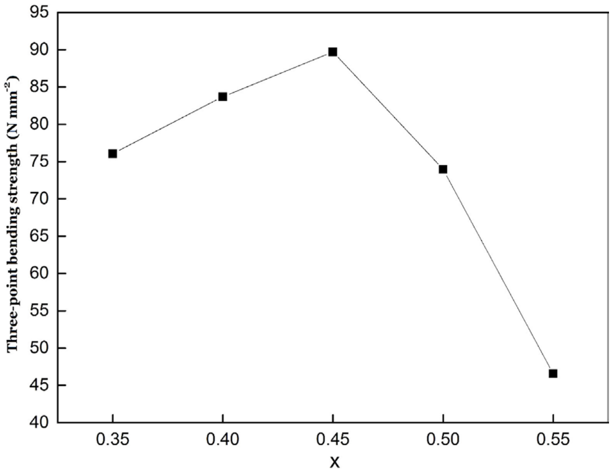

FIGURE 9 | Three-point bending strength of $Li_{1+x}Al_xGe_{0.2}Ti_{1.8-x}(PO_4)_3$ as a function of *x*.

As another thought, the estimation of the bulk conductivity could be influenced by a parallel grain boundary conduction path as illustrated in the equivalent circuit in **Figure 6**, although the grain boundary conductivities of $Li_{1+x}Al_xGe_{0.2}Ti_{1.8-x}(PO_4)_3$ at $x = 0.40$ and 0.50 were lower than that for $Li_{1.45}Al_{0.45}Ge_{0.2}Ti_{1.35}(PO_4)_3$. As a rough tendency, it is possible to state that conductivity becomes maximum around $x = 0.45$, and as leaving from the composition, the bulk and the grain boundary conductivity decreases. **Figure 8** shows the temperature dependence of the total electrical conductivity for $Li_{1.45}Al_{0.45}Ge_{0.2}Ti_{1.35}(PO_4)_3$. The activation energy for the electrical conduction was calculated to be 31 kJ mole^{-1}, which is comparable to that for $Li_{1.4}Al_{0.4}Ge_{0.2}Ti_{1.4}(PO_4)_3$, as reported previously (Zhang et al., 2013). **Figure 9** shows the dependence of the three-point bending strength on the Al content for $Li_{1+x}Al_xGe_{0.2}Ti_{1.8-x}(PO_4)_3$ sintered at 900°C for 7 h. The maximum bending strength of 90 N mm^{-2} was observed for $Li_{1.45}Al_{0.45}Ge_{0.2}Ti_{1.35}(PO_4)_3$ with a relative density of 95.8%. The bending strength is higher than that of 65 N mm^{-2} for

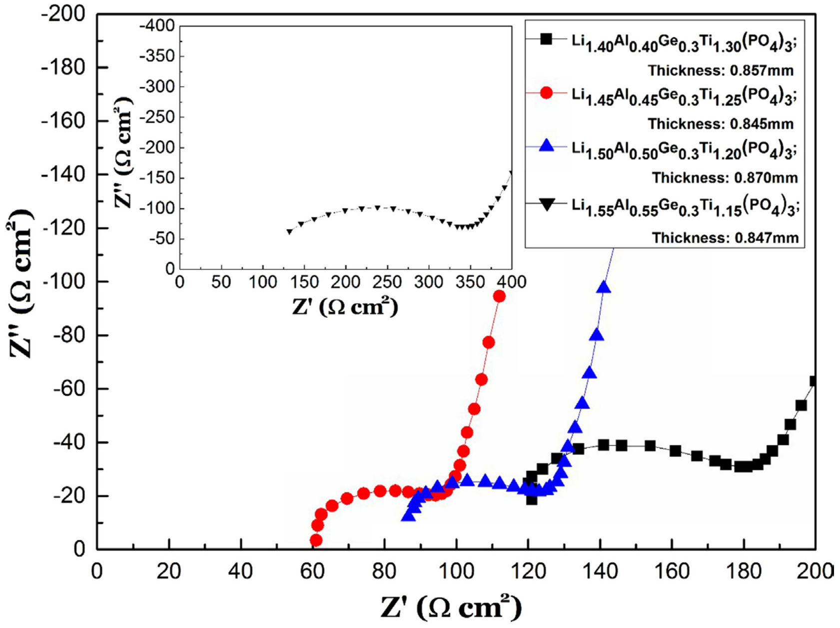

FIGURE 10 | **Impedance profiles measured at 25°C of $Li_{1+x}Al_xGe_{0.3}Ti_{1.7-x}(PO_4)_3$ as a function of *x*.**

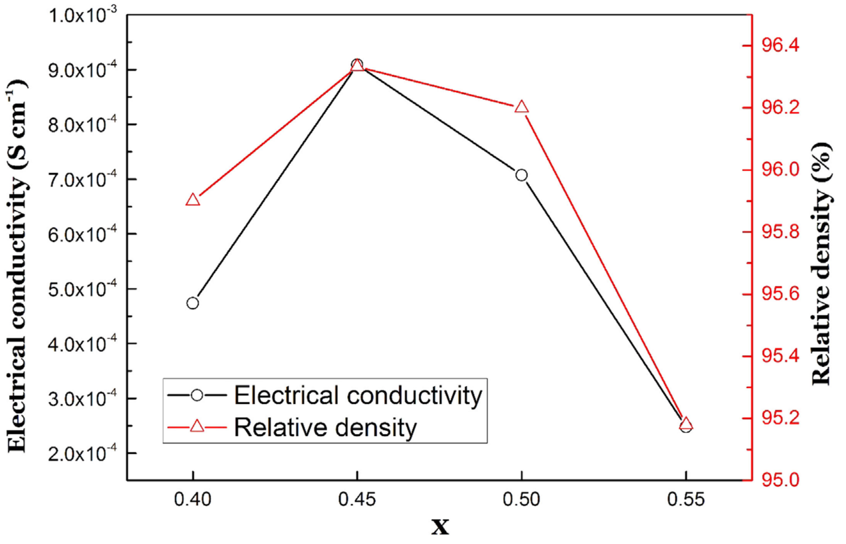

FIGURE 11 | **Total electrical conductivity at 25°C and relative density of $Li_{1+x}Al_xGe_{0.3}Ti_{1.8-x}(PO_4)_3$ as a function of *x*.**

$Li_{1.4}Al_{0.4}Ge_{0.2}Ti_{1.4}(PO_4)_3$ prepared by tape casting using powder prepared by the sol–gel method (Zhang et al., 2015) and lower than that of 140 N mm^{-2} for a polished Ohara plate of $Li_{1+x+y}Al_x(Ti,Ge)Si_yP_{3-y}O_{12}$ glass–ceramics, the conductivity of which is as low as 1×10^{-4} S cm^{-1} at room temperature. The high bending strength of $Li_{1.45}Al_{0.45}Ge_{0.2}Ti_{1.35}(PO_4)_3$ prepared by the conventional solid-state reaction is quite attractive for applications, such as the water-stable protective layer in aqueous lithium batteries.

Zhang et al. (2013) examined the electrical conductivity dependence on the Ge content in $Li_{1.4}Al_{0.4}Ge_xTi_{1.6-x}(PO_4)_3$, and the highest conductivity was observed for $Li_{1.4}Al_{0.4}Ge_{0.2}Ti_{1.4}(PO_4)_3$ prepared by the sol–gel method. We also examined the effect of the Ge content in $Li_{1+x}Al_xGe_yTi_{2-x-y}(PO_4)_3$. **Figure 10** shows impedance profiles measured at 25°C of $Li_{1+x}Al_xGe_{0.3}Ti_{1.7-x}(PO_4)_3$ as a function of *x*. The highest bulk conductivity of 1.39×10^{-3} S cm^{-1} and total conductivity of 8.95×10^{-4} S cm^{-2} were observed for

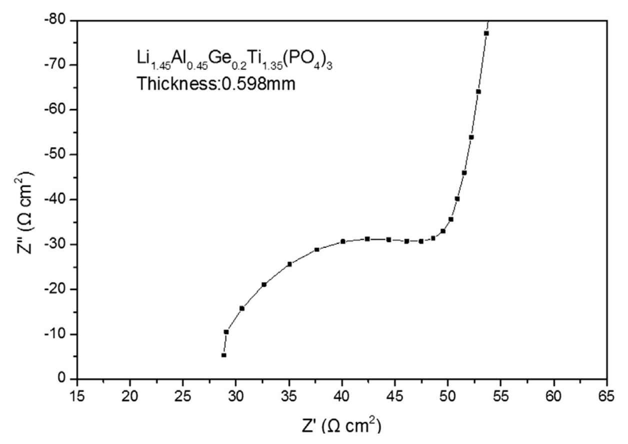

FIGURE 12 | Impedance profile of the tape cast $Li_{1.45}Al_{0.45}Ge_{0.2}Ti_{1.35}(PO_4)_3$ film measured at 25°C.

$Li_{1.45}Al_{0.45}Ge_{0.3}Ti_{1.25}(PO_4)_3$. The total conductivity and relative density of $Li_{1+x}Al_xGe_{0.3}Ti_{1.7-x}(PO_4)_3$ are shown as a function of x in **Figure 11**. The bulk conductivities of $Li_{1.5}Al_{0.5}Ge_{0.3}Ti_{1.2}(PO_4)_3$ and $Li_{1.4}Al_{0.4}Ge_{0.3}Ti_{1.3}(PO_4)_3$ are considerably lower than those of $Li_{1.5}Al_{0.5}Ge_{0.2}Ti_{1.3}(PO_4)_3$ and $Li_{1.4}Al_{0.4}Ge_{0.2}Ti_{1.4}(PO_4)_3$, respectively. The highest relative density of 96.3% was observed for $Li_{1.45}Al_{0.45}Ge_{0.3}Ti_{1.25}(PO_4)_3$. The $Li_{1.5}Al_{0.5}Ge_{0.1}Ti_{1.4}(PO_4)_3$ sample with a low Ge content had a low total conductivity of 2.7×10^{-4} S cm^{-1} and a low grain boundary conductivity of 3.3×10^{-4} S cm^{-1} at 25°C.

The tape casting method is suitable to prepare solid electrolytes for the large size batteries in electric vehicles and stationary electricity storage systems. Takahashi et al. (2012) reported the electrical conductivity for a tape-cast $Li_{1.4}Al_{0.4}Ti_{1.6}(PO_4)_3$–3 wt% TiO_2 film as 7.6×10^{-4} S cm^{-1} at 25°C. Zhang et al. (2015) also reported an electrical conductivity of 1.22×10^{-3} S cm^{-1} at 25°C for a tape-cast film of $Li_{1.4}Al_{0.4}Ge_{0.2}Ti_{1.4}(PO_4)_3$. The powders for these tape casting films were prepared by the sol–gel method using expensive Ti and Ge alkoxides. Here, we prepared $Li_{1.45}Al_{0.45}Ge_{0.2}Ti_{1.35}(PO_4)_3$ films by the tape casting method using powders prepared by the conventional solid-state reaction using TiO_2 and GeO_2. The impedance profile of the film measured at 25°C is shown in **Figure 12**. Zhang et al. (2015) reported an aging effect on the electrical conductivity of a tape-cast film stored in an air atmosphere. Therefore, the impedance was measured for a film stored for 1 week in an Ar glove box. The total and bulk conductivities at 25°C were estimated to be 1.01×10^{-3} and 2.21×10^{-3} S cm^{-1}, respectively, which are comparable to those of a sintered plate prepared from a pressed green body.

CONCLUSION

The NASICON-type water-stable lithium-ion-conducting solid electrolyte of $Li_{1+x}Al_xGe_yTi_{2-x-y}(PO_4)_3$ was prepared using conventional solid-state reaction at 900°C for 7 h. The highest lithium-ion conductivity of 10^{-3} S cm^{-1} at 25°C was found for the $Li_{1+x}Al_xGe_yTi_{2-x-y}(PO_4)_3$ composition with $x = 0.45$ and $y = 0.2$. The relative density of the sintered pellets was as high as 95.8%, and the three-point bending strength was 90 N mm^{-2}. Tape cast films of $Li_{1.45}Al_{0.45}Ge_{0.2}Ti_{1.35}(PO_4)_3$ were prepared using powder prepared by solid-state reaction. The total and bulk electrical conductivities of the film were comparable with those of a sintered plate prepared from a pressed green body. This water-stable high lithium-ion-conducting solid electrolyte has potential application as the protective layer of lithium metal electrodes in aqueous lithium–air batteries and lithium batteries with aqueous liquid cathodes.

AUTHOR CONTRIBUTIONS

SX, HN, and PX did preparation of NASICON-type oxide, characterization, and conductivity measurements. SX also did the tape casting of the ceramics. SM, MM, YT, and OY supported and gave an advice on each experimental work. NI managed the research direction and provided necessary instructions and opportunities for discussions among all authors.

REFERENCES

Aono, H., Sugimoto, E., Sadaoka, Y., Imanaka, S., and Adachi, G. (1990). Ionic conductivity of solid electrolyte based on lithium titanium phosphate. *J. Electrochem. Soc.* 137, 1023–1027. doi:10.1149/1.2086597

Alpen, U. V., Rubenau, A., and Talt, G. H. (1977). Ionic conducting in Li_3N single crystal. *Appl. Phys. Lett.* 30, 621–623. doi:10.1063/1.89283

Bouchet, R., Knauth, P., and Laugler, J. M. (2003). Theoretical analysis of IS of polycrystalline materials with blocking or conducting grain boundary: from microcrystals to nanocrystals. *J. Electrochem. Soc.* 150, E348–E354. doi:10.149/1.1580151

Bruce, P. G., Feunberger, S. A., Hardwick, L. J., and Tarascon, J. M. (2012). Li-O_2 and Li-S batteries with high energy storage. *Nat. Mater.* 11, 19–29. doi:10.1038/nmat3191

Bruce, P. G., and West, A. R. (1983). The A-C conductivity of polycrystalline LISICON $Li_{2+2x}Zn_{1+x}GeO_4$ and a model for the intergranular construction resistance. *J. Electrochem. Soc.* 130, 662–669. doi:10.1149/1.2119778

Cretin, M., and Fabry, P. (1999). Comparative study of lithium ion conductors in the system $Li_{1+x}Al_xA_{2-x}^{IV}(PO_4)_3$ with A^{IV}=Ti or Ge and $0 \leq x \leq 0.7$ for use as Li^+ sensitive membranes. *J. Eur. Ceram. Soc.* 19, 2931–2940. doi:10.1016/s0955-2219(99)00055-2

Delmas, C., Viala, J. C., Olazcuage, R., Le Flem, G., Hagnemuller, P., and Chrkaoui, F. (1981). Conductivite ionique dnas les systmes $Na_{1+x}Zr_{2+x}L_x(PO_4)_3$(L=Cr, Yb). *Mater. Res. Bull.* 16, 83–90. doi:10.1016/0025-5408(81)90182-3

Fu, J. (1997). Fast Li^+ ion conducting glass-ceramics in the system Li_2O-Al_2O_3-GeO_2-P_2O_5. *Solid State Ionics.* 104, 191–194. doi:10.1016/s0167-2738(99)00434-7

Inaguma, N., Chen, L., Itoh, M., Nakamura, T., Uchida, T., Ikuta, H., et al. (1993). High ionic conductivity in lithium lanthanum titanate. *Solid State Commun.* 86, 689–693. doi:10.1016/0038-1098(93)90841-A

Kamaya, N., Honma, K., Yamakawa, Y., Nakamura, T., Hirayama, M., Kanno, R., et al. (2011). A lithium super ionic conductor. *Nat. Mater.* 10, 682–686. doi:10.1038/nmat.3066

Lu, Y., Goodenough, J. R., and Kim, Y. (2011). Aqueous cathode for next-generation alkali-ion batteries. *J. Am. Chem. Soc.* 133, 5756–5759. doi:10.1021/ja.201118f

Maldonado-Manso, P., Aranda, M. A. G., Bruque, J. S., and Losilla, E. R. (2005). Nominal vs. actual stoichiometries in Al-doped NASICONs; a study of the $Na_{1.4}Al_{0.4}M_{1.6}(PO_4)_3$ (M=Ge, Sn, Ti, Hf, Zr) family. *Solid State Ionics* 176, 1613–1625. doi:10.1016/jss.2005.04.009

Murugan, R., Thangadurai, V., and Weppner, W. (2007). Fast lithium ion conduction in garnet-type $Li_7La_3Zr_2O_{12}$. *Angew. Chem. Int. Ed.* 46, 7778–7781. doi:10.1002/anie.200701144

Perez-Estebanez, M., Lasai-Marin, J., Tobbens, D. M., Rivera-Calzada, A., and Leon, C. (2014). A systematic study on NASICON-type $Li_{1+x}M_xTi_{2-x}(PO_4)_3$ (M=Cr, Al, Fe,) by neutron diffraction and impedance spectroscopy. *Solid State Ionics* 266, 1–8. doi:10.1016/j.ssi.2014.07.018

Shimonishi, Y., Zhang, T., Imanishi, N., Im, D., Lee, D. I., Hirano, A., et al. (2011). A study on lithium/air second batteries – stability of the NASICON-type lithium ion conducting solid electrolyte in alkaline aqueous solution. *J. Power Sources* 196, 5128–4133. doi:10.1016/jpowersouce.2011.02.023

Takahashi, K., Johnson, P., Imanishi, N., Sammes, N., Takeda, Y., and Yamamoto, O. (2012). A water-stable high lithium ion conducting $Li_{1.4}Ti_{1.6}Al_{0.4}(PO4)_3$-epoxy resin hybrid sheet. *J. Electrochem. Soc.* 159, A1065–A1069. doi:10.1149/2.072207jes

Thokchom, J. S., and Kumar, B. (2010). The effects of crystallization parameters on the ionic conductivity of a lithium aluminum germanium phosphate glass ceramics. *J. Power Sources* 195, 2870–2879. doi:10.1018/j.powersouces.2009.11.037

Wada, H., Menetrierm, A., Lavasseurs, A., and Hagenmuller, P. (1983). Preparation and ionic conductivity of new B_2S_3-Li_2S-LiI glass. *Mater. Res. Bull.* 18, 189–192. doi:10.1018/0025-5408(83)90080-6

Xu, X., Wen, Z., Wu, X., Yang, X., and Gu, Z. (2007). Lithium ion-conducting glass-ceramics of $Li_{1.5}Al_{0.5}Ge_{1.5}(PO_4)_3$-$xLi_2O$ (x=0.0-0.20) with good electrical and electrochemical properties. *J. Am. Ceram. Soc.* 90, 2802–2806. doi:10.1111/j.1511-2916.207.01827.x

Zhang, P., Matsui, M., Hirano, A., Takeda, Y., Yamamoto, O., and Imanishi, N. (2013). Water-stable lithium ion conducting solid electrolyte of the $Li_{1.4}Al_{0.4}Ti_{1.6-x}Ge_x(PO_4)_3$ system (A=x=0-1.0) with NASICON-type structure. *Solid State Ionics* 253, 175–180. doi:10.1016/j.ssi.2013.09.022

Zhang, P., Wang, H., Lee, Y.-G., Matsui, M., Takeda, Y., Yamamoto, O., et al. (2015). Tape-cast water-stable NASICON-type high lithium ion conducting solid electrolyte films for aqueous lithium-air batteries. *J. Electrochem. Soc.* 162, A1265–A1271. doi:10.1149/2.0711507jes

Zhang, T., Imanishi, N., Shimonishi, Y., Hirano, A., Takeda, Y., Yamamoto, O., et al. (2010). A novel high energy rechargeable lithium/air battery. *Chem. Commun.* 46, 1661–1663. doi:10.1039/b926012f

Zhao, Y., Wang, L., and Byon, H. R. (2013). High-performance rechargeable lithium-iodine batteries using triiodide/iodide redox couples in an aqueous cathode. *Nat. Commun.* 4, 1896. doi:10.1038/ncomms2907

Conflict of Interest Statement: The authors declare that the research was conducted in the absence of any commercial or financial relationships that could be construed as a potential conflict of interest.

frontiers
in Energy Research

ORIGINAL RESEARCH
published: 31 March 2016
doi: 10.3389/fenrg.2016.00014

Intermittent Contact Alternating Current Scanning Electrochemical Microscopy: A Method for Mapping Conductivities in Solid Li Ion Conducting Electrolyte Samples

*Samantha Raisa Catarelli[1], Daniel Lonsdale[1], Lei Cheng[2,3], Jaroslaw Syzdek[4] and Marca Doeff[2]**

[1] Uniscan Instruments Ltd., Macclesfield, UK, [2] Energy Storage and Distribution Resources Division, Lawrence Berkeley National Laboratory, Berkeley, CA, USA, [3] Materials Sciences and Engineering Department, University of California Berkeley, Berkeley, CA, USA, [4] Bio-Logic USA LLC, Knoxville, TN, USA

Edited by:
Jeff Sakamoto,
University of Michigan, USA

Reviewed by:
Venkataraman Thangadurai,
University of Calgary, Canada
Charles A. Geiger,
Salzburg University, Austria

Correspondence:
Marca Doeff
mmdoeff@lbl.gov

Specialty section:
This article was submitted to Energy Storage, a section of the journal Frontiers in Energy Research

Received: *09 January 2016*
Accepted: *21 March 2016*
Published: *31 March 2016*

Citation:
Catarelli SR, Lonsdale D, Cheng L, Syzdek J and Doeff M (2016) Intermittent Contact Alternating Current Scanning Electrochemical Microscopy: A Method for Mapping Conductivities in Solid Li Ion Conducting Electrolyte Samples. Front. Energy Res. 4:14. doi: 10.3389/fenrg.2016.00014

Intermittent contact alternating current scanning electrochemical microscopy (ic-ac-SECM) has been used to determine the electrochemical response to an ac signal of several types of materials. A conductive gold foil and insulating Teflon sheet were first used to demonstrate that the intermittent contact function allows the topography and conductivity to be mapped simultaneously and independently in a single experiment. Then, a dense pellet of an electronically insulating but Li ion conducting garnet phase, Al-substituted $Li_7La_3Zr_2O_{12}$ (LLZO), was characterized using the same technique. The polycrystalline pellet was prepared by classical ceramic sintering techniques and was comprised of large (~150 μm) grains. Critical information regarding the contributions of grain and grain boundary resistances to the total conductivity of the garnet phase was lacking due to ambiguities in the impedance data. In contrast, the use of the ic-ac-SECM technique allowed spatially resolved information regarding local conductivities to be measured directly. Impedance mapping of the pellet showed that the grain boundary resistance, while generally higher than that of grains, varied considerably, revealing the complex nature of the LLZO sample.

Keywords: intermittent contact alternating current scanning electrochemical microscopy, solid electrolyte, lithium lanthanum zirconium oxide, garnet, grain boundaries

INTRODUCTION

Solid electrolytes have been proposed for use in a number of battery configurations such as all solid-state lithium metal batteries (Jones and Akridge, 1993; Bates et al., 2000; Kamaya et al., 2011; Nagao et al., 2013), hybrid systems with aqueous electrolytes in which the metallic lithium electrode is protected by a solid electrolyte (Chu et al., 2002), and hybrid flow batteries with aqueous cathodes and metallic lithium anodes (Lu and Goodenough, 2011). The use of a solid electrolyte in optimized devices suppresses dendrite formation and allows reliable cycling of the lithium electrode, thereby potentially enabling higher energy densities than currently available with conventional lithium-ion battery designs.

Several classes of inorganic materials show high Li ion conductivities (Knauth, 2009) including glasses, composites, and crystalline oxides or sulfides. Some of the most promising of these, based both on good transport properties and apparent resistance to reduction by lithium metal, are garnet-structured phases related to the compound $Li_7La_3Zr_2O_{12}$ (LLZO) (Murugan et al., 2007; Cussen, 2010; Thangadurai et al., 2014; Rettenwander et al., 2015). To stabilize the cubic polymorph, which is several orders of magnitude more conductive than the tetragonal one, a small amount of Al is usually substituted for some of the lithium in LLZO compositions (Geiger et al., 2011).

To maximize ionic conductivity and ensure that shorting does not occur, very thin but dense layers of the solid electrolyte are required in electrochemical devices. The electrochemical characteristics of polycrystalline electrolytes are intimately related to details of their microstructures, including grain size, grain orientation, and the nature of the grain boundaries (Verkerk et al., 1982; Buechele et al., 1983; Ban and Choi, 2001) and profoundly affect how devices containing them function. For example, we have recently discovered that symmetrical Li/LLZO/Li cells containing small-grained samples (~20 μm) of LLZO failed later than those with larger-grained ones (~150 μm) and could sustain higher critical current densities during cycling (Cheng et al., 2015a). The effect was attributed to the presence of more low-resistance grain boundaries that could effectively dissipate currents in the small-grained samples. In contrast, current focusing at the grain boundaries in the large-grained samples resulted in rapid shorting of the symmetrical cells. While impedance measurements on the LLZO samples appeared to be consistent with this interpretation, quantitative values for grain boundary resistances could not be extracted from the data. Methods allowing direct measurements of local conductivities and correlations with topographical features would be extremely helpful in determining which microstructures exhibit the most robust behavior during electrochemical cycling in order to design more reliable high energy density batteries utilizing solid electrolytes.

Herein, we describe a technique, intermittent contact alternating current scanning electrochemical microscopy (ic-ac-SECM), which combines two previously developed methods [ic-SECM (McKelvey et al., 2010; Lazenby et al., 2013) and ac-SECM (Diakowski and Ding, 2007; Eckhard and Schuhmann, 2008; Gebala et al., 2011; Trinh et al., 2011)] that allows this correlation and demonstrate its effectiveness using several types of samples, including a large-grained LLZO pellet. This extends the growing trend of using SECM techniques to answer questions pertaining to battery materials and to energy applications at micron or greater length scales (Bertoncello, 2010; Lai et al., 2012; Bülter et al., 2014; Zampardi et al., 2015a,b). Furthermore, two recent papers describe the use of SECM to characterize solid electrolyte interfaces in batteries (Bülter et al., 2015; Ventosa et al., 2015).

MATERIALS AND METHODS

Sample Preparation and Characterization

$Li_7La_3Zr_2O_{12}$ powders used for preparing dense pellets were synthesized from stoichiometric amounts of Li_2CO_3, $La(OH)_3$, ZrO_2, and Al_2O_3, as described in Cheng et al. (2014). Powders were attrition-milled to an average size of about 1 μm and then compacted into pellets. These were fired at 1100°C in a fresh LLZO powder bed for 12 h to densify them, and then dry-polished to remove a 50-μm thick layer from each side. The densified and polished pellets were approximately 1.5 mm thick and 8.0 mm in diameter.

The image of the pellet surface was obtained by SEM using a Hitachi TM-1000 tabletop microscope. Impedance measurements were obtained on dense LLZO pellets between blocking electrodes using a VMP3 multichannel potentiostat/galvanostat (Bio-Logic Science Instruments). For these experiments, a gold layer was sputtered on both sides of the pellet and Pt meshes and wires were attached and used as current collectors. Measurements were made at frequencies from 1 MHz to 0.1 Hz, and conductivities were determined from the intercepts of the arcs with the real axes in the Nyquist plots, using the equation $\sigma = \frac{1}{Z} \times \frac{L}{A}$, where Z is the impedance, L is the pellet thickness, and A is the pellet area.

Scanning Electrochemical Microscopy Experiments

A model ic-SECM470 scanning probe microscope [Bio-Logic Science Instruments (http://www.bio-logic.info/scanning-systems-scan-lab/instruments/)] was used to make measurements on LLZO samples immersed in 0.1M tetrabutylammonium perchlorate (TBA-ClO_4) in propylene carbonate (PC) solutions. A 10-μm diameter Pt ultramicroelectrode (glass sheath, ratio of glass to Pt at the apex, R/G = 10) was used as the probe, with the gold layer on the back of the LLZO sample used as the counter-electrode, and a Pt sheet electrode as a pseudo-reference. For the control experiments using an insulating polytetrafluoroethylene (PTFE) blank, a Pt wire was used as the counter-electrode instead. For control experiments with the electronically conducting gold disk, which was embedded in an insulating plastic resin, experiments were performed in tap water using the Pt probe described above with a Pt counter-electrode and a standard calomel electrode (SCE) as reference, because PC dissolves the resin. These results are provided in Supplementary Material. All experiments were carried out at room temperature.

The concept of ic-SECM is similar to tapping-mode AFM. The probe vibration spectrum is recorded, a frequency slightly lower than the resonant frequency is selected, then the tip amplitude and set point are selected. The approach to the surface is executed until the tip oscillation amplitude reaches the predefined set point by probe interaction (damping of vibration) with the surface. Throughout the mapping, a constant tip amplitude is maintained, and the topography is determined through mechanical interaction, while the electrochemical measurement (dc or ac) is run independently.

Measurements on the gold disk were performed with a dc-bias of 0.0 V vs. OCP, ac-bias of 100 mV, and ac-frequency of 50 kHz. ac-SECM approach curves showed these settings allowed for noticeably different responses at the insulator and conductor. In most cases, an area scan of 150 μm by 150 μm was performed, with a step size of 10 μm and scan velocity of 20 μm/s. For the intermittent contact measurements, an oscillation frequency of 450 Hz (about 15 Hz below resonance) was applied, with an amplitude of 0.1 μm. The set point was 80% of the tip oscillation. For the height tracking experiments, the topography data from the ic-ac-SECM measurement were used to set the *z*-height throughout the ac-SECM experiment. As with the ic-ac-SECM measurement, the result is not convoluted by the sample topography. As the probe is not vibrating in the height tracking measurement, any possible effect of the probe vibration on the result is also ruled out.

A 250 μm × 250 μm area of the LLZO sample was mapped with a 2.5 μm step size while an ac-bias of 100 mV amplitude (sinusoidal wave) with a frequency of 100 kHz was applied to the probe. For mapping of larger areas, a 5 μm step size was used. Unlike more classical ac-SECM approaches where the impedance between the tip and a distant counter electrode is measured and the coupling between the two (or three electrodes, if a reference is used) is studied, here we are measuring the impedance through the sample (1500 μm) and a thin layer of electrolyte above it (<1 μm). The tip intermittent contact settings were: 440 Hz oscillation frequency (about 15 Hz below resonance), 100 nm of free oscillation amplitude, and 80% set point for contact amplitude. The last two parameters define the smallest time-averaged tip-sample distance of 40 nm, which is two orders of magnitude closer than a classical ac-SECM experiment would allow in a study like ours. Furthermore, given that the tip oscillation is almost three orders of magnitude slower than the ac wave applied to the tip (and sample), as well as about two orders of magnitude faster than the per-point data acquisition time, we observed no cross-talk between the topography and electrochemical measurement (each impedance measurement is semi-stationary, and they are averaged over multiple tip oscillation cycles); see Supplementary Material.

Data were processed using Gwyddion 2.40 SPM data analysis and visualization tool and presented in 3D using 3DIsoPlot® software package by Uniscan Instruments. No degradation of the garnet pellet was observed after the experiment, using a Bruker D2-Phaser diffractometer with Cu Kα radiation to determine the phase purity.

RESULTS

Figure 1 shows scanning electron micrographs of large-grained LLZO samples made from powders having the nominal composition $Li_{6.1}Al_{0.3}La_3Zr_2O_{12}$. Pellets made from attrition-milled powders, as described in Cheng et al. (2014) were 92% dense with a majority of grains about 150–200 μm across. The X-ray diffraction data, energy dispersive X-ray spectroscopy (EDS) mapping, inductively coupled plasma optical emission spectrometry (ICP-OES), and laser-induced breakdown spectroscopy (LIBS) results reported in that paper were consistent with the interpretation of a phase-pure, homogeneous garnet sample, once surface impurities were polished away. Total conductivity at room temperature of 2.3×10^{-4} S/cm was measured prior to polishing. A comparison of the ac and dc responses of cells containing LLZO with non-blocking electrodes (i.e., lithium) indicated that the conductivity is primarily ionic and is attributable to lithium transport ($t_{\mathrm{Li}^+} \approx 1$). Typical Nyquist plots for an Au/LLZO/Au cell at different temperatures are shown in **Figure 2**. In cases where the grain boundary resistance is much higher than that of the bulk, two semicircles in the Nyquist plot are frequently observed, with the lower frequency one usually assigned to the grain boundaries (Bauerle,

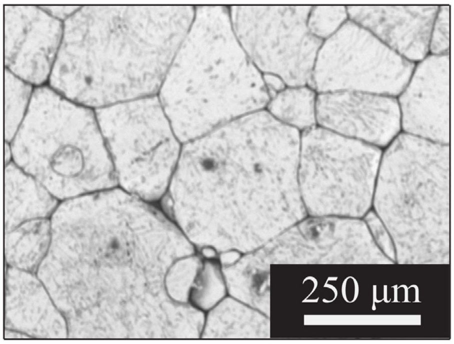

FIGURE 1 | SEM image of the surface of a large-grained LLZO pellet used for this study.

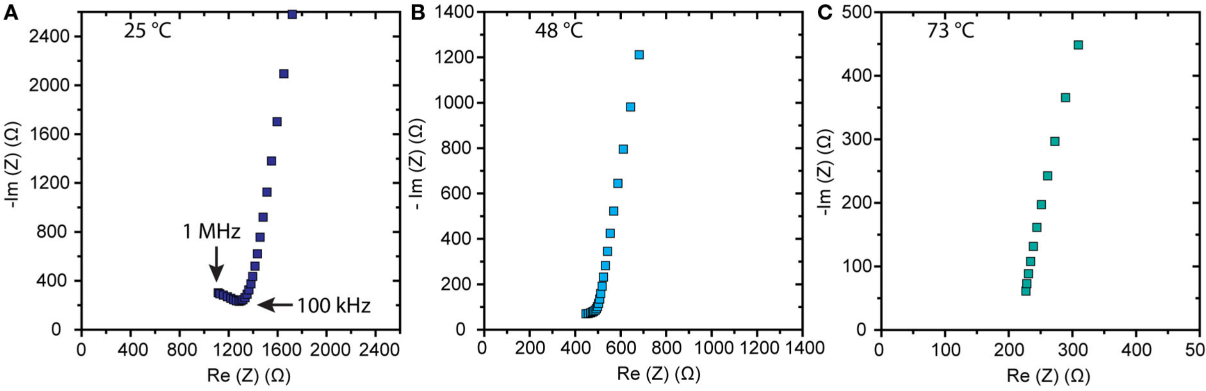

FIGURE 2 | Nyquist plots of impedance data obtained on an Au/LLZO/Au cell at (A) 25, (B) 48, and (C) 73°C.

1969; Fleig, 2002). Their contributions to the total conductivity can then be determined based on geometric considerations [i.e., the bricklayer model (Verkerk et al., 1982)]. However, when grain boundaries are comparable to or more conductive than the bulk, the impedance spectra cannot be readily deconvoluted (Bouchet et al., 2003). At room temperature, the Nyquist plot of the LLZO cell consists of a partial semicircle at high frequency and a spike at low frequency. The diameter of the semi-circle was attributed to the total impedance of the LLZO pellet. At 48°C, as shown in **Figure 2B**, the semicircle diminishes, and it vanishes completely at 73°C (**Figure 2C**). While total conductivities of 5.4×10^{-4} and 1.4×10^{-3} S/cm were determined at 48 and 73°C, respectively, from this data, contributions from the grain and grain boundaries could not be separated.

Several experiments were performed on control samples to verify the capability of the instrumentation to provide meaningful data for the intended characterization of the LLZO sample (e.g., to rule out the possibility of cross-talk between ac vibration and ac measurement channels or tip oscillation affecting the data). Experiments in several different modes were conducted to understand if ic-ac-SECM provided new and useful information. These include constant height ac-SECM, where the probe is scanned in *x* and *y* planes only, constant distance ic-ac-SECM, where the probe maintains partial contact with the surface by adjusting *x*, *y*, and *z* positions, and constant distance ac-SECM by height tracking, where the probe follows a prior recorded topography and again adjusts *x*, *y*, and *z* positions.

The above was first demonstrated on a conductive gold disk to demonstrate the viability of the ic-ac-SECM technique, the results of which are presented in Supplementary Material. These results confirmed that cross-talk between channels was not occurring and that tip oscillation did not influence the output. Additionally, ic-ac-SECM experiments were performed on an insulating PTFE blank in 0.1M TBA-ClO_4 in PC to demonstrate the capability of the instrument to obtain topographic data separately from impedance. For this experiment, the sample was deliberately scratched. **Figure 3** shows the ac current magnitude, the impedance magnitude, and the topography of the blank PTFE sample.

Results from ic-ac-SECM experiments over a wide area (650 μm × 650 μm) were obtained on the LLZO pellet and are shown in Figure S8 in Supplementary Material. **Figure 4** shows results obtained on an unpolished pellet, which had been exposed to air for a prolonged period, over a smaller area (325 μm × 325 μm) in several different modes (ac-SECM, ic-ac-SECM, and ac-SECM mode with height tracking). In the impedance and topography maps using ic-ac-SECM mode, arrows or circles denote areas of interest, which will be discussed in the next section. **Figure 5** shows the same set of experiments on a sample that was polished to remove Li_2CO_3 from the surface. Finally, **Figure 6** shows a 250 μm × 250 μm area of the polished LLZO pellet, which shows a more detailed view.

DISCUSSION

The LLZO sample used in this study had a complex microstructure consisting primarily of large grains that varied considerably in shape and size, as shown in **Figure 1**. The complexity may explain why the impedance data obtained on the large-grained LLZO sample could not be readily deconvoluted into separate grain and grain boundary contributions at any of the temperatures studied, as seen in **Figure 2**. In fact, there have been conflicting reports as to the relative resistances of grains and grain boundaries in LLZO samples [see Tenhaeff et al. (2014) for a more complete discussion of this topic as well as the challenges of interpreting impedance data]. Variations in details of the processing and techniques used to produce dense samples may explain the seemingly contradictory evidence. For example, the properties of a large-grained LLZO sample similar to one used in this study were unlike those of one with smaller (~20 μm) grains, due to possible differences in grain boundary chemistry (Cheng et al., 2015b). This observation illustrates the importance of deeper understanding of the specific nature of the grain and grain boundaries, which may require the use of other techniques sensitive to local grain and grain boundaries besides conventional impedance analysis on the overall sample (Fleig and Maier, 1999; Fleig et al., 2000; He et al., 2011).

Direct observation of local variations in conductivity with simultaneously obtained spatial information can be carried out using SECM (Bard et al., 1989), making it ideal for the study of polycrystalline samples in which the bulk and grain boundary

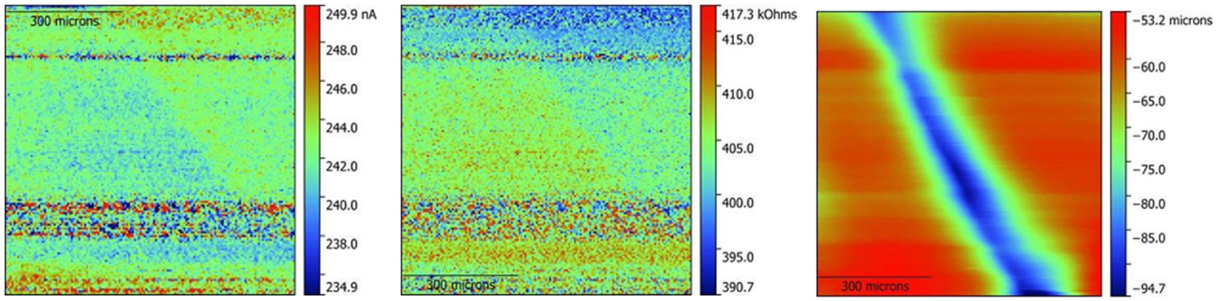

FIGURE 3 | ic-ac-SECM results on a scratched PTFE blank in a 0.1M TBA-ClO_4 PC solution. On the left, ac current magnitude, in the middle, impedance, and, on the right, topography. Note that the absolute scale of the impedance change is ~5% of the signal measured in **Figure 4** (middle) and is dominated by noise in this test.

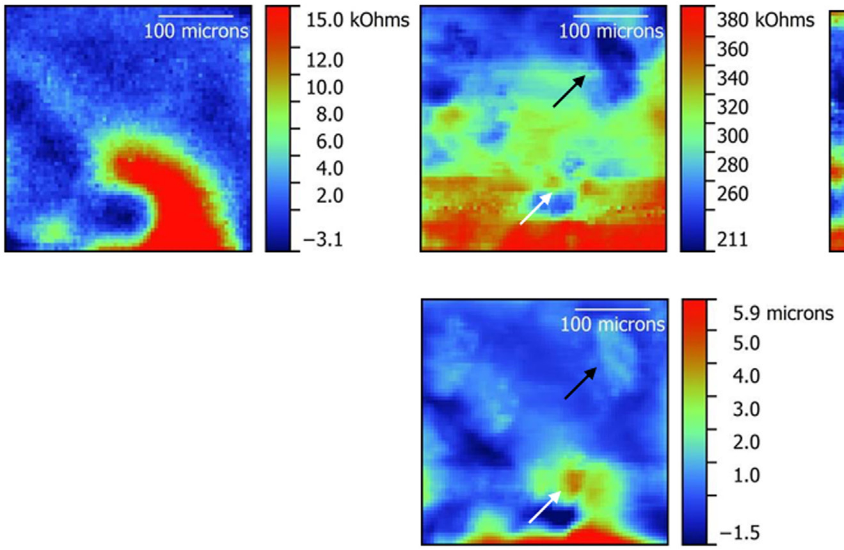

FIGURE 4 | Impedance maps obtained on an unpolished LLZO pellet in ac-SECM mode (left), ic-ac-SECM mode (middle), and ac-SECM mode with height tracking (right). A topography map obtained from the ic-ac-SECM experiment is also shown below the ic-ac-SECM impedance map in the middle. A 325 µm × 325 µm area was studied. White and black arrows in the ic-ac-SECM impedance and topography maps point to areas of interest as explained in the text.

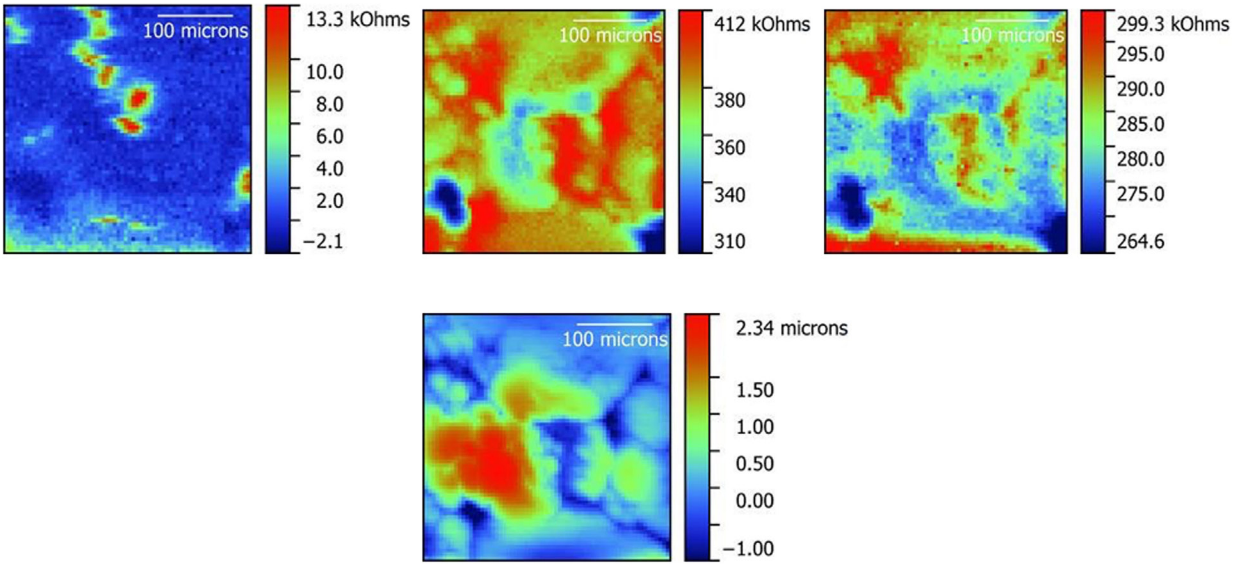

FIGURE 5 | Impedance maps obtained on a polished LLZO pellet in ac-SECM mode (left), ic-ac-SECM mode (middle) and ac-SECM mode with height tracking (right). A topography map obtained from the ic-ac-SECM experiment is also shown below the ic-ac-SECM impedance map in the middle. A 325 µm × 325 µm area was studied.

resistances differ. In SECM, the current response of an ultramicroelectrode tip (probe) as a function of its exact position over a substrate immersed in solution is recorded. This is a function of both the tip-sample distance and the conductivity of the sample. In ac mode, changing the conductivity of the solution or the frequency of the applied potential further alters the response. In intermittent contact (ic) mode, the probe is in intimate proximity to the sample, and that distance is kept uniform throughout the experiment removing or greatly diminishing the influence of sample topography, which is notorious for interfering with SECM measurements. Ideally, this allows information about the electrochemical response of the sample to be obtained independently of the topographical features. There are, however, many technical challenges associated with these experiments, such as the possibility that the vibration of the tip may affect the impedance, or that cross talk may occur between impedance and topography

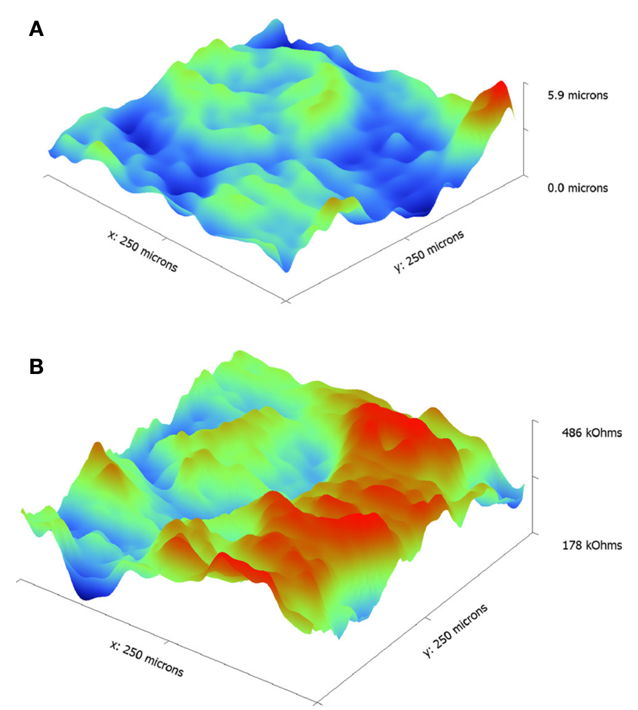

FIGURE 6 | **Topographic (A) and impedance (B) maps obtained on an LLZO pellet using ic-ac-SECM over a 250 μm × 250 μm area**.

channels. To rule out such artifacts as an explanation for what was observed on the LLZO samples, several types of experiments were carried out on a gold disk and are presented in the Supplementary Material. Once these were completed, data were collected on an insulating PTFE sample, which had been deliberately scratched (**Figure 3**). The scratch is clearly visible in the topography image, but the ac current magnitude and impedance responses are not affected by the depth change. A noteworthy feature was the ability to clearly image topographical features only tens of microns deep and less than about 100-μm wide (see upper left of the topography image), in spite of the fact that the total size of the probe, including the encapsulating glass, is estimated to be about 100 μm across. This is possible because the intermittent-contact technique will typically use a part of the probe tip to contact the sample, depending on the exact orientation of the probe relative to the sample. The success of these control experiments lends credence to the results obtained on LLZO samples described below.

Scans in various modes were taken on unpolished (**Figure 4**) and polished (**Figure 5**) LLZO samples over 325 μm × 325 μm areas to show the different information that is obtained. Impedance maps taken in ac-SECM mode (leftmost images in the Figures) are a function of both the sample topography and local differences in impedance. Using height tracking in ac-SECM mode (rightmost images in the Figures) is more informative, but requires that the topography be obtained separately. For this type of experiment, the probe follows a prior-recorded topography, but may still suffer from effects such as sample movement and temperature drift. Finally, the data appear to be better resolved in ic-ac-SECM mode (middle images) as the images show both higher contrast and (subjectively) more detail. Maintaining intermittent contact with the sample helps to remove the interference of temperature drift or sample movement from the measurement as evidenced by the better clarity of the data in **Figures 4** and **5**. Additionally, ic-ac-SECM mode allows topographical information to be obtained simultaneously (bottom images in the middle). In the case of the unpolished sample (**Figure 4**), there is a roughly inverse correspondence between the height and the impedance of the sample at any given location; in other words, where there is a rise in the topography, the impedance appears to decrease and *vice versa*. For example, the light blue patch embedded in a dark blue area on the upper right side of the topography map, indicated by a black arrow, corresponds to a locally raised area with lower impedance than the surroundings. The correlation would normally raise suspicions about cross-talk, but for the fact that the match is not perfect. As one example, the raised spot indicated by the white arrow on the topography image has higher, not lower, impedance than the surroundings. In LLZO samples like this one, grains are raised compared to the grain boundaries; thus, the correlation of raised areas with lower impedance seems to suggest that the grains are more conductive than the grain boundaries, were it not for the anomalous feature pointed out by the white arrow. This feature is much smaller than the grains shown in **Figure 1**. However, large-grained samples of LLZO are somewhat air sensitive and react to form lithium carbonate (Li_2CO_3), particularly when moisture is present (Cheng et al., 2015b). It is likely that the raised spot corresponds to a particle of resistive lithium carbonate on the surface of the unpolished LLZO pellet.

When the LLZO sample was polished to remove lithium carbonate, a clearer picture emerges from the ic-ac-SECM experiment (middle images in **Figure 5**). The topography (bottom, middle in **Figure 5**) is reduced by around 65% compared to **Figure 4**, but still indicates that there are several large raised areas roughly the size of the grains in **Figure 1**, separated by lower narrow regions in dark blue, which could be grain boundaries. Again, there is a rough inverse correspondence between height and impedance despite the reduced topography, with the narrow low regions showing higher impedance compared to the larger higher regions. While the match is not perfect, this suggests that the grain boundaries are more resistive than the grains.

For a more detailed view, a smaller area (250 μm × 250 μm) of a polished sample was studied using a smaller step size. These results are presented in **Figure 6**. A large raised portion about 200 μm across is evident in the topographical map, which is most likely a large grain. This roughly corresponds to the region of lower impedance seen in **Figure 6B**. This grain is surrounded by boundaries of higher impedance. There is, however, significant variation in the impedance of these boundaries with some regions much higher than in others, where it is close in value to that of the grain itself. Several research groups have observed that there is Al enrichment at the grain boundaries of LLZO samples similar to the one in this study (Jin and McGinn, 2011; Li et al., 2012, 2014; Cheng et al., 2014; Ren et al., 2015). Grain boundary conductivities may also vary in polycrystalline samples due to a distribution of grain misorientation angles. Highly mismatched grain boundaries are energetically unstable and can lead to large structural and compositional deviations, as has been observed recently in samples of lithium lanthanum titanate (LLTO) and lithium aluminum titanium phosphate (LATP) (Gellert et al., 2012; Ma et al., 2014). In general, ion transport is more favorable when mismatches are less severe. Synchrotron microdiffraction experiments on the large-grained LLZO sample indicate that the grain boundary misorientation angles are distributed with a mean value of 39.4° ± 13.6° (Cheng et al., 2015a). Thus, it is not unreasonable to observe that the sample contains grain boundaries with different characteristics, a fact that is not revealed using macroscopic impedance analysis, which can only provide averaged information.

CONCLUSION

Deconvolution of impedance data to determine grain and grain boundary contributions to total conductivities of polycrystalline solid electrolytes is not always possible. Furthermore, it can only give averaged information on these samples, which may be very complex in nature (multiple conductive phases and orientation-dependence). In contrast, ic-ac-SECM allows direct observation of both topography and impedance, simultaneously. In this work, it was used to characterize a large-grained LLZO pellet, which showed significant variation not only between grain and grain boundary resistances, but also among the grain boundaries themselves. This is attributed to the distribution of grain misorientation angles in the sample, which lead to differences in the grain boundary structures and chemistries.

AUTHOR CONTRIBUTIONS

LC made LLZO samples and characterized them by SEM and impedance analysis. SC carried out SECM experiments, DL interpreted results and suggested additional SECM experiments, and SC, JS, and DL carried out data analysis. MD supervised the portion of the work carried out at Lawrence Berkeley National Laboratory. All co-authors contributed to the writing of the paper.

ACKNOWLEDGMENTS

This work was supported by the Assistant Secretary for Energy Efficiency and Renewable Energy, Office of Vehicle Technologies of the U.S. Department of Energy under contract no. DE-AC02-05CH11231. SECM measurements were carried out by SC using Uniscan – Bio-Logic equipment at the Uniscan facility in the United Kingdom.

SUPPLEMENTARY MATERIAL

The Supplementary Material for this article can be found online at http://journal.frontiersin.org/article/10.3389/fenrg.2016.00014

REFERENCES

Ban, C. W., and Choi, G. M. (2001). The effect of sintering on the grain boundary conductivity of lithium lanthanum titanates. *Solid State Ionics.* 140, 285–292. doi:10.1016/S0167-2738(01)00821-9

Bard, A. J., Fan, F.-R. F., Kwak, J., and Lev, O. (1989). Scanning electrochemical microscopy. Introduction and principles. *Anal. Chem.* 61, 132–138. doi:10.1021/ac00177a011

Bates, J. B., Dudney, N. J., Neudecker, B., Ueda, A., and Evans, C. D. (2000). Thin film lithium and lithum-ion batteries. *Solid State Ionics.* 135, 33–45. doi:10.1016/S0167-2738(00)00327-1

Bauerle, J. E. (1969). Study of solid electrolyte polarization by a complex admittance method. *J. Phys. Chem. Solids* 30, 2657–2670. doi:10.1016/0022-3697(69)90039-0

Bertoncello, P. (2010). Advances on scanning electrochemical microscopy (SECM) for energy. *Energy Environ. Sci.* 3, 1620–1630. doi:10.1039/c0ee00046a

Bouchet, R., Knauth, P., and Laugier, J.-M. (2003). Theoretical analysis of IS of polycrystalline materials with blocking or conducting grain boundaries: from microcrystals to nanocrystals. *J. Electrochem. Soc.* 150, E348–E354. doi:10.1149/1.1580151

Buechele, A. C., De Jonghe, L. C., and Hitchcock, D. (1983). Degradation of sodium β"-alumina: effect of microstructure. *J. Electrochem. Soc.* 130, 1042–1049. doi:10.1149/1.2119881

Bülter, H., Peters, F., Schwenzel, J., and Wittstock, G. (2014). Spatiotemporal changes of the solid electrolyte interphase in lithium-ion batteries detected by scanning electrochemical microscopy. *Angew. Chem.* 53, 10531–10535. doi:10.1002/anie.201403935

Bülter, H., Peters, F., Schwenzel, J., and Wittstock, G. (2015). Comparison of electron transfer properties of the SEI on graphite composite and metallic lithium electrodes by SECM at OCP. *J. Electrochem. Soc.* 162, A7024–A7036. doi:10.1149/2.0031513jes

Cheng, L., Chen, W., Kunz, M., Persson, K., Tamura, N., Chen, G., et al. (2015a). Effect of surface microstructure on electrochemical performance of garnet solid electrolytes. *ACS Appl. Mater. Interfaces* 7, 2073–2081. doi:10.1021/am508111r

Cheng, L., Wu, C. H., Jarry, A., Chen, W., Ye, Y., Zhu, J., et al. (2015b). Interrelationships among grain size, surface composition, air stability, and interfacial resistance of Al-substituted $Li_7La_3Zr_2O_{12}$ solid electrolytes. *ACS Appl. Mater. Interfaces* 7, 17649–17655. doi:10.1021/acsami.5b02528

Cheng, L., Park, J. S., Hou, H., Zorba, V., Chen, G., Richardson, T., et al. (2014). Effect of microstructure and surface impurity segregation on the electrical and electrochemical properties of dense Al-substituted $Li_7La_3Zr_2O_{12}$. *J. Mater. Chem. A* 2, 172–181. doi:10.1039/C3TA13999A

Chu, M. Y., Visco, S., and De Jonghe L.C. (2002). *Plating Metal Negative Electrodes under Protective Coatings*. U.S. Patent No. 6402795, Washington, DC: U.S. Patent and Trademark Office.

Cussen, E. J. (2010). Structure and ionic conductivity in lithium garnets. *J. Mater. Chem.* 20, 5167–5173. doi:10.1039/b925553b

Diakowski, P. M., and Ding, Z. (2007). Novel strategy for constant-distance imaging using alternating current scanning electrochemical microscopy. *Electrochem. commun.* 9, 2617–2621. doi:10.1016/j.elecom.2007.08.010

Eckhard, K., and Schuhmann, W. (2008). Alternating current techniques in scanning electrochemical microscopy (ac-SECM). *Analyst* 133, 1486–1497. doi:10.1039/b806721j

Fleig, J. (2002). The grain boundary impedance of random microstructures: numerical simulations and implications for the analysis of experimental data. *Solid State Ionics.* 150, 181–193. doi:10.1016/S0167-2738(02)00274-6

Fleig, J., and Maier, J. (1999). Microcontact impedance measurements of individual highly conductive grain boundaries: general aspects and application to AgCl. *Phys. Chem. Chem. Phys.* 1, 3315–3320. doi:10.1039/a902839k

Fleig, J., Rodewald, S., and Maier, J. (2000). Spatially resolved measurements of highly conductive and highly resistive grain boundaries using microcontact impedance spectroscopy. *Solid State Ionics.* 13, 905–911. doi:10.1016/S0167-2738(00)00522-1

Gebala, M., Schuhmann, W., and La Mantia, F. (2011). A new ac-SECM mode: on the way to high-resolution local impedance measurements in SECM. *Electrochem. commun.* 13, 689–693. doi:10.1016/j.elecom.2011.04.010

Geiger, C. A., Alekseev, E., Lazic, B., Fisch, M., Armbruster, T., Langner, R., et al. (2011). Crystal chemistry and stability of "$Li_7La_3Zr_2O_{12}$" garnet: a fast lithium-ion conductor. *Inorg. Chem.* 50, 1089–1097. doi:10.1021/ic101914e

Gellert, M., Gries, K. I., Yada, C., Rosciano, F., Volz, K., and Roling, B. (2012). Grain boundaries in a lithium aluminum titanium phosphate-type fast lithium ion conducting glass ceramic: microstructure and nonlinear ion transport properties. *J. Phys. Chem. C* 116, 22675–22678. doi:10.1021/jp305309r

He, Q., Kusoglu, A., Lucas, I. T., Clark, K., Weber, A. Z., and Kostecki, R. (2011). Correlating humidity-dependent ionically conductive surface area with transport phenomena in proton-exchange membranes. *J. Phys. Chem. B* 115, 11650–11657. doi:10.1021/jp206154y

Jin, Y., and McGinn, P. J. (2011). Al-doped $Li_7La_3Zr_2O_{12}$ synthesized by a polymerized complex method. *J. Power Sources* 196, 8683–8687. doi:10.1016/j.jpowsour.2011.05.065

Jones, S. D., and Akridge, J. (1993). A thin-film solid-state microbattery. *J. Power Sources* 4, 505–513. doi:10.1016/0378-7753(93)80196-V

Kamaya, N., Homma, K., Yamakawa, Y., Hirayama, M., Kanno, R., Yonemura, M., et al. (2011). A lithium superionic conductor. *Nat. Mater.* 10, 682–686. doi:10.1038/nmat3066

Knauth, P. (2009). Inorganic solid Li ion conductors: an overview. *Solid State Ionics.* 180, 911–916. doi:10.1016/j.ssi.2009.03.022

Lai, S. C. S., Macpherson, J. V., and Unwin, P. R. (2012). In situ scanning electrochemical probe microscopy for energy applications. *MRS Bull.* 37, 668–674. doi:10.1557/mrs.2012.146

Lazenby, R. A., McKelvey, K., and Unwin, P. R. (2013). Hopping intermittent contact-scanning electrochemical microscopy (HIC-SECM): visualizing interfacial reactions and fluxes from surfaces to bulk solution. *Anal. Chem.* 85, 2937–2944. doi:10.1021/ac303642p

Li, Y., Han, J.-T., Wang, C.-A., Xie, H., and Goodenough, J. B. (2012). Optimizing Li+ conductivity in a garnet framework. *J. Mater. Chem.* 22, 15357–15361. doi:10.1039/c2jm31413d

Li, Y., Wang, Z., Li, C., Cao, Y., and Guo, X. (2014). Densification and ionic-conduction improvement of lithium garnet solid electrolytes by flowing oxygen sintering. *J. Power Sources* 248, 642–646. doi:10.1016/j.jpowsour.2013.09.140

Lu, Y., and Goodenough, J. B. (2011). Rechargeable alkali ion flow battery. *J. Mater. Chem.* 21, 10113–10117. doi:10.1039/c0jm04222f

Ma, C., Chen, K., Liang, C., Nan, C.-W., Ishikawa, R., More, K., et al. (2014). Atomic-scale origin of the large grain-boundary resistance in perovskite Li-ion-conducting solid electrolytes. *Energy Environ. Sci.* 7, 1638–1642. doi:10.1039/c4ee00382a

McKelvey, K., Edwards, M. A., and Unwin, P. R. (2010). Intermittent contact-scanning electrochemical microscopy (IC-SECM): a new approach for tip positioning and simultaneous imaging of interfacial topography and activity. *Anal. Chem.* 82, 6334–6337. doi:10.1021/ac101099e

Murugan, R., Thangadurai, V., and Weppner, W. (2007). Fast lithium ion conduction in garnet-type $Li_7La_3Zr_2O_{12}$. *Angew. Chem. Int. Ed.* 46, 7778–7781. doi:10.1002/anie.200701144

Nagao, M., Kitaura, H., Hayashi, A., and Tatsumisago, M. (2013). High rate performance, wide temperature operation and long cyclability of all-solid-state rechargeable lithium batteries using Mo-S chevrel-phase compound. *J. Electrochem. Soc.* 160, A819–A823. doi:10.1149/2.058306jes

Ren, Y., Deng, H., Chen, R., Shen, Y., Lin, Y., and Nan, C.-W. (2015). Effects of Li source on microstructure and ionic conductivity of Al-contained $Li_{6.75}La_3Zr_{1.75}Ta_{0.25}O_{12}$ ceramics. *J. Eur. Ceram. Soc.* 35, 561–572. doi:10.1016/j.jeurceramsoc.2014.09.007

Rettenwander, D., Welzl, A., Cheng, L., Fleig, J., Musso, M., Suard, E., et al. (2015). Synthesis, crystal chemistry, and electrochemical properties of $Li_{7-2x}La_3Zr_{2-x}Mo_xO_{12}$ (x=0.1-0.4): stabilization of the cubic garnet polymorph via substitution of Zr^{4+} by Mo^{6+}. *Inorg. Chem.* 54, 10440–10449. doi:10.1021/acs.inorgchem.5b01895

Tenhaeff, W. E., Rangasamy, E., Wang, Y., Sokolov, A. P., Wolfenstine, J., Sakamoto, J., et al. (2014). Resolving the grain boundary and lattice impedance of hot-pressed $Li_7La_3Zr_2O_{12}$ garnet electrolytes. *ChemElectroChem Commun.* 1, 375–378. doi:10.1002/celc.201300022

Thangadurai, V., Narayanan, S., and Pinzaru, D. (2014). Garnet-type solid-state fast Li ion conductors for Li batteries: critical review. *Chem. Soc. Rev.* 43, 4714–4727. doi:10.1039/c4cs00020j

Trinh, D., Keddam, M., Novoa, X. R., and Vivier, V. (2011). Alternating-current measurements in scanning electrochemical microscopy, part 1: principle and theory. *Chemphyschem* 12, 2169–2176. doi:10.1002/cphc.201001084

Ventosa, E., Zampardi, G., Flox, C., La Mantia, F., Schuhmann, W., and Morante, J. R. (2015). Solid electrolyte interphase in semi-solid flow batteries: a wolf in sheep's clothing. *Chem. Commun.* 51, 14973–14976. doi:10.1039/C5CC04767F

Verkerk, M. J., Middelhus, B. J., and Burggraaf, A. J. (1982). Effect of grain boundaries on the conductivity of high-purity ZrO_2-Y_2O_3 ceramics. *Solid State Ionics.* 6, 159–170. doi:10.1016/0167-2738(82)90083-2

Zampardi, G., Ventosa, E., La Mantia, F., and Schuhmann, W. (2015a). Scanning electrochemical microscopy applied to the investigation of lithium (de-) insertion in TiO_2. *Electroanalysis* 27, 1017–1025. doi:10.1002/elan.201400613

Zampardi, G., La Mantia, F., and Schuhmann, W. (2015b). Determination of the formation and range of stability of the SEI on glassy carbon by local electrochemistry. *RSC Adv.* 5, 31166–31171. doi:10.1039/C5RA02940F

Disclaimer: This document was prepared as an account of work sponsored by the United States Government. While this document is believed to contain correct information, the United States Government or any agency thereof, or the Regents of the University of California, or any of their employees, makes any warranty, express or implied, or assumes any legal responsibility for the accuracy, completeness, or usefulness of any information, apparatus, product, or process disclosed, or represents that its use would not infringe privately owned rights. Reference herein to any specific commercial product, process, or service by its trade name, trademark, manufacturer, or otherwise, does not necessarily constitute or imply its endorsement, recommendation, or favoring by the United States Government or any agency thereof, or the Regents of the University of California. The views and opinions of authors expressed herein do not necessarily state or reflect those of the United States Government or any agency thereof or the Regents of the University of Californi.

Conflict of Interest Statement: SC and DL work for Uniscan Instruments, Ltd., the company that makes the commercial ic-ac-SECM instrumentation described in this work. JS works for Bio-Logic USA, which markets this instrument. LC and MD declare no competing interests.

frontiers
in Energy Research

ORIGINAL RESEARCH
published: 31 March 2016
doi: 10.3389/fenrg.2016.00013

Improving NASICON Sinterability through Crystallization under High-Frequency Electrical Fields

*Ilya Lisenker and Conrad R. Stoldt**

Department of Mechanical Engineering, University of Colorado Boulder, Boulder, CO, USA

The effect of high-frequency (HF) electric fields on the crystallization and sintering rates of a lithium aluminum germanium phosphate (LAGP) ion conducting ceramic was investigated. LAGP with the nominal composition $Li_{1.5}Al_{0.5}Ge_{1.5}(PO_4)_3$ was crystallized and sintered, both conventionally and under effect of electrical field. Electrical field application, of 300 V/cm at 1 MHz, produced up to a 40% improvement in sintering rate of LAGP that was crystallized and sintered under the HF field. Heat sink effect of the electrodes appears to arrest thermal runaway and subsequent flash behavior. Sintered pellets were characterized using X-ray diffraction, scanning electron microscope, TEM, and electrochemical impedance spectroscopy to compare conventionally and field-sintered processes. The as-sintered structure appears largely unaffected by the field as the sintering curves tend to converge beyond initial stages of sintering. Differences in densities and microstructure after 1 h of sintering were minor with measured sintering strains of 31 vs. 26% with and without field, respectively. Ionic conductivity of the sintered pellets was evaluated, and no deterioration due to the use of HF field was noted, though capacitance of grain boundaries due to secondary phases was significantly increased.

Keywords: NASICON, field-assisted sintering, high frequency, sintering, grain boundary capacitance

Edited by:
Jeff Sakamoto,
University of Michigan, USA

Reviewed by:
Fatih A. Cetinel,
BASF SE, Germany
Juchen Guo,
University of California Riverside, USA

Correspondence:
Conrad R. Stoldt
stoldt@colorado.edu

Specialty section:
This article was submitted
to Energy Storage,
a section of the journal
Frontiers in Energy Research

Received: *25 January 2016*
Accepted: *21 March 2016*
Published: *31 March 2016*

Citation:
Lisenker I and Stoldt CR (2016)
Improving NASICON Sinterability
through Crystallization under
High-Frequency Electrical Fields.
Front. Energy Res. 4:13.
doi: 10.3389/fenrg.2016.00013

INTRODUCTION

Sodium superionic conducting (NASICON) ceramics are a family of sodium- or lithium-based solids that have been investigated as potential solid-state electrolytes since the 1970s. They offer relatively high room temperature conductivity, improved safety due to their intrinsic stability, and the possibility of assembling mechanically robust monolithic battery cells (Birke et al., 1997; Nagata and Nanno, 2007). Furthermore, as a high modulus and hardness ceramic solid electrolyte, these materials are proposed to inhibit dendrite formation during cycling, thus preventing the possibility of a short circuit, thermal runaway, and ultimately battery cell failure. The leading candidates among this family of ceramics are aluminum substituted lithium titanium and lithium germanium phosphates. Trivalent ion substitution within the NASICON structure requires insertion of additional lithium to maintain charge neutrality. The additional lithium ions, which force a rearrangement of the lithium sublattice, have the effect of dramatically increasing lithium mobility and therefore conductivity. In particular, the $Li_{1+x}Al_xGe_{2-x}(PO_4)_3$ [lithium aluminum germanium phosphate (LAGP)], $x = 0.45$ appears to provide the highest conductivity for Li^+ ions (Li et al., 1988; Francisco et al., 2015), with higher x values resulting in secondary phase formation (Cretin and Fabry, 1999). At a minimum, a dense structure with no interconnected porosity is required to inhibit dendrite propagation in lithium metal battery cells; however, the sintering of LAGP to a consistently high density remains a challenge with densities of 70% to just over 90% of theoretically reported despite sometimes lengthy sintering cycles (Cretin and Fabry, 1999; Yang et al., 2015).

A number of sintering approaches can be utilized to increase densification rates. Raising sintering temperatures is the simplest approach, but for LAGP above 800–825°C, phase separation occurs with formation of insulating phases (Thockchom and Kumar, 2010; Mariappan et al., 2011). The use of high heating rates, for example, by spark plasma sintering (SPS), to increase sintering rates has been well described. In addition to the applied mechanical pressure, the material is in intimate contact with a resistively heated graphite die resulting in heating rates in the hundreds of degree Celsius per minute. In materials for which the bulk diffusion activation energy, responsible for densification, is higher than the activation energy for surface diffusion, responsible for grain coarsening, rapid densification occurs (Stanciu et al., 2001). Resistively heating the sample itself, a process limited to electronically conductive materials is even more effective than traditional SPS but requires an SPS furnace with additional complexity of the die structure (Zapata-Solvas et al., 2015). SPS sintering of LAGP has been reported, but the achieved density was only 87% of theoretical, and the 20°C conductivity was measured to be 3.3×10^{-5} S cm^{-1} (Kubanska et al., 2014), a much lower value than what is commonly reported for such a density (Mariappan et al., 2011). It is notable that an additional, though low intensity, peak appears in the X-ray diffraction (XRD) pattern of the sample after SPS, corresponding to the most intense peak of $AlPO_4$, an insulating secondary phase, though a causal connection was not asserted.

Microwave sintering is another effective approach for rapid sintering of ceramic materials. The alternating electrical field component in microwave processing is used to polarize the ceramic, an inherently lossy process, thereby transferring energy to the crystal lattice with every reversal while rapidly heating the material (Sudiana et al., 2013). Notably, the higher frequencies above about 28 GHz that are needed to prevent formation of standing waves in the chamber and resultant hot spots in the material (Sudiana et al., 2013) may prevent its use in a co-sintering application of a battery device, since the bulk of the device would be effectively shielded by any electronically conductive materials (Bokhan et al., 1995).

Flash sintering methods use DC or lower frequency (up to 1000 Hz) AC electrical current passing directly through the sample to achieve remarkably rapid densification (Cologna et al., 2010). However, the charge carrier drift speed at the currents involved would inevitably cause NASICON phase breakdown due to local changes in stoichiometry resulting from lithium extraction near the anode and lithium accumulation near the cathode, similar phenomena to what has been shown in work with zirconia (Downs, 2013) and thoria (Goldwater, 1961). In addition, flash sintering, with an ohmic conducting path from the electrodes to the component and a dielectric breakdown-like thermal initiation mechanism (Todd et al., 2015; Zhang et al., 2015), presents a formidable engineering challenge in assuring an even current distribution across essentially 2D objects, such as battery components.

Finally, we note that a number of investigations have shown that the manner of material synthesis, and especially crystallization parameters, can substantially influence the conductivity of the final product (Thockchom and Kumar, 2010; Yang et al., 2015). Subjecting amorphous materials to alternating electrical fields, microwave irradiation in particular, has been used to promote uniform crystallization (Mahmoud, 2007).

To the authors' knowledge, frequencies between 1 kHz and 2.4 GHz represent an unexplored frequency range for field-assisted sintering. In this work, we evaluate the use of high-frequency (HF) electrical fields during synthesis, crystallization, and sintering as a means of enhancing sintering rate beyond that found in conventional thermal sintering processes for NASICON type ceramics. The choice of frequencies in the megahertz range represents a compromise between the shallow penetration of microwaves and electrolysis-inducing direct current. We further demonstrate the ability of a HF field to capacitively couple to the sample, eliminating both hot spots, and the need for platinum paints used in flash sintering to achieve a reliable electrical contact to the ceramic specimen.

EXPERIMENTAL PROCEDURE

Experimental Apparatus

A custom built set-up, as shown in **Figure 1**, was designed and fabricated to allow for the application of a variable frequency and variable voltage AC electrical field across the pellet during both crystallization and sintering. The set-up was contained inside a vertical tube furnace (Mellen Co., Concord, NH, USA). The furnace temperature was controlled using a k-type thermocouple embedded within one of the electrodes, approximately 1 mm below the sample, in an attempt to mitigate temperature gradients and sample self-heating. Any sample self-heating was thereby

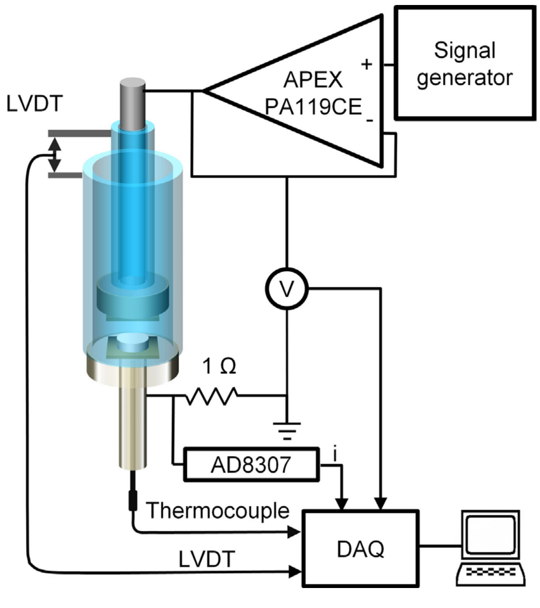

FIGURE 1 | **Sintering and data acquisition set-up**.

compensated by the furnace controller ensuring a stable sample temperature to within 2°C of the target.

Inconel 625 electrodes were separated from the sample pellet by 0.2-mm thick wafers made of Hexoloy SA silicon carbide (Saint-Gobain Ceramics, France) in order to prevent chromium oxide, deriving from Inconel surface oxidation, from contaminating the pellets. A custom built, all-quartz rod-in-tube dilatometer, based on a GTX-1000 LVDT and S7AC transducer (RDP Group, England), was used to monitor shrinkage in real time. The weight of the dilatometer components exerted an effective pressure of 0.2 MPa on the pellet during crystallization and sintering, thus ensuring intimate contact between electrodes and the pellet. The pressure exerted by the dilatometer was sufficiently low to prevent any sinter-forging of the sample, but was sufficient to prevent radial shrinkage of the pellets. An up to 30-V peak-to-peak, 1-MHz AC field can be applied across the pellet using a custom built amplifier based on APEX PA119CE (Apex Microtechnology, Tucson, AZ, USA) op-amp driven by Agilent 33220A signal generator (Keysight Technologies, Santa Rosa, CA, USA), resulting in a field approximately 300 V/cm for a typical 1-mm thick pellet. Note that the capacitor formed by the electrode and the pellet faces acts as a short circuit, inducing a current flow in the sample without any conductive coatings (e.g., platinum) on the pellet faces, as is required for DC and low frequency AC flash sintering experiments. Voltage and current monitoring were provided by a Schottky diode peak detector circuit and AD8307A (Analog Devices, Norwood, MA, USA) logarithmic amplifier to convert high-frequency signal to 0–10 V analog signal. Data acquisition was performed using U3-HV DAQ (Labjack Corp. Lakewood, CO, USA) at 1-s intervals.

Material Synthesis and Crystallization

The entire sample preparation process can be followed by referencing the flowchart in **Figure 2**. Single phase $Li_{1.5}Al_{0.5}Ge_{1.5}(PO_4)_3$ was prepared by coprecipitation from an aqueous mixture of $LiNO_3$ (Alfa Aesar, 99%), $AlNO_3{\cdot}9H_2O$ (Alfa Aesar, 98–102%), $(NH_4)H_2PO_4$ (Sigma-Aldrich, 99.99%), and an ethanol solution of $Ge(EtOH)_4$ (Gelest, 99.99%). The resulting precipitate was thoroughly dried by heating with stirring for 8 h at 80°C followed by an additional 8 h at 120°C. The precipitate was then reground in a mortar and heat treated in an alumina crucible in air for 8 h at 450°C to drive out most of the volatiles, including water and ammonia. The powder was then uniaxially pressed at a pressure of 220 MPa into 70-mg pellets with approximate dimensions of 6.35 mm diameter by 1.3 mm thickness. No binder was used for the pressing.

Two subsequent material crystallization routes were pursued. In both routes, the pellets were heat treated in the experimental furnace according to the schedule shown in **Figure 3**. Half of the material was heat treated under an applied high-frequency (HF) electrical field of 30 V peak-to-peak amplitude and 1.0 MHz frequency. Control samples were heat treated under identical conditions without HF field. The evolution of pellet thickness during the heat treatment is also illustrated in **Figure 3** (note that here positive displacement corresponds to reduction in thickness). The measured volume change coincides with LAGP crystallization peak reported previously by differential scanning calorimetry (Kubanska et al., 2014; Yang et al., 2015). The crystallization process resulted in highly porous bodies of agglomerated crystalline powder that were subsequently reground by hand in a mortar.

Sample Sintering

After crystallization, the respective LAGP powders were again uniaxially pressed (without binder) at a pressure of 220 MPa into 70-mg pellets with approximate dimensions of 6.35 mm diameter by 1.0 mm thickness. All pellets were sintered in a vertical tube furnace in air at 800°C for 1 h with a 10°C/min heating ramp under a 300 V/cm, 1-MHz HF field. The field was applied at the beginning of the heating ramp and was turned off after 4 h, once the sample had cooled below approximately 100°C. A total of five

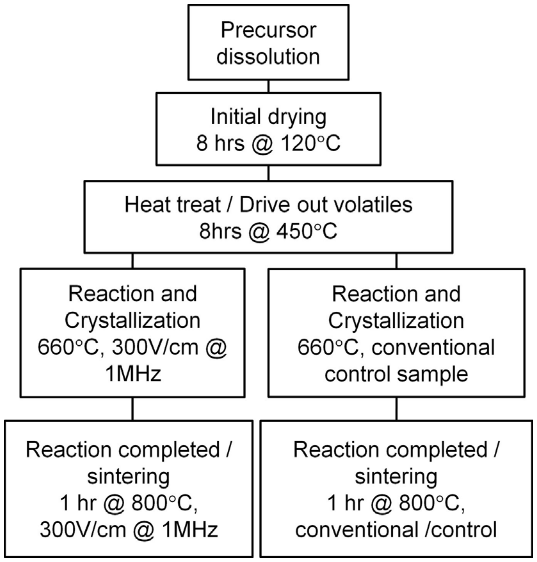

FIGURE 2 | **Sample processing flowchart.**

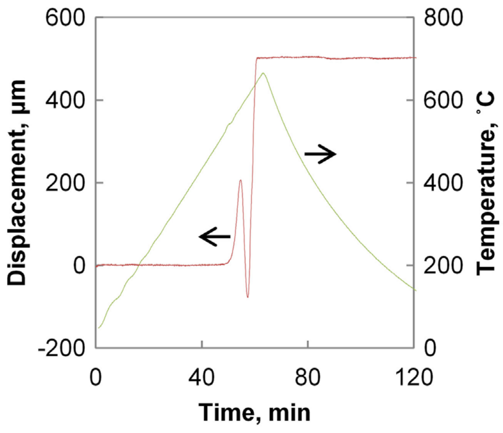

FIGURE 3 | **Sintering schedule and displacement (volume change) during the crystallization process.**

replicates from the two different synthesis runs were made. An additional five replicates using the same batch of material were used as controls with no field applied. Post-sintering sample shrinkage was confirmed using digital calipers.

The shorter time interval, the schedule of which is shown in **Figure 4**, while not allowing for full sintering, serves to accentuate the differences in initial densification rates for the methods used.

Characterization

Powder at every step of preparation and the sintered samples was characterized by XRD using a Bruker D2 Phaser (Bruker GmbH, Germany) using Cu-K_α radiation. Raman spectra, not reported here, on pellet faces was acquired using a Jasco NRS-3100 system (Jasco Corp., Tokyo, Japan) at a 532-nm excitation wavelength with a laser power level of approximately 65 mW and 50× effective magnification to non-destructively confirm material structure. Sample porosity was determined based on geometric measurement of pellet volume using digital calipers and the LAGP theoretical density as calculated from unit cell parameters.

Sample faces were subsequently sputter coated with approximately 500 nm of pure gold and electrochemical impedance spectroscopy (EIS) measurements were conducted using a Solartron 1250B potentiostat with a Solartron 1287 electrochemical interface (Ametek, Inc., Farnborough, UK) with a 100-mV excitation amplitude over a frequency range from 0.1 Hz to 1 MHz. EIS measurements were performed in an airtight enclosure under flowing dry nitrogen in a range of temperatures from room temperature down to −70°C. Fracture surfaces of two of the pellets were sputter coated with carbon and imaged using JEOL JSM-7401F field emission scanning electron microscope (SEM).

Additionally, two samples were prepared using FIB and imaged using a Talos F200S high-resolution transmission electron microscope (HRTEM) (FEI, Hillsboro, OR, USA) with energy dispersive X-ray spectroscopy (EDS) capability for elemental mapping.

RESULTS AND DISCUSSION

A comparison of XRD patterns from as-crystallized powders is shown in **Figure 5**. The powder crystallized under electrical field shows a slightly higher degree of crystallinity with approximately 10% larger grain size as determined by the Scherrer formula, specifically 69 and 63 nm, respectively. With no apparent differences in the timing and temperature of the onset of the crystallization,

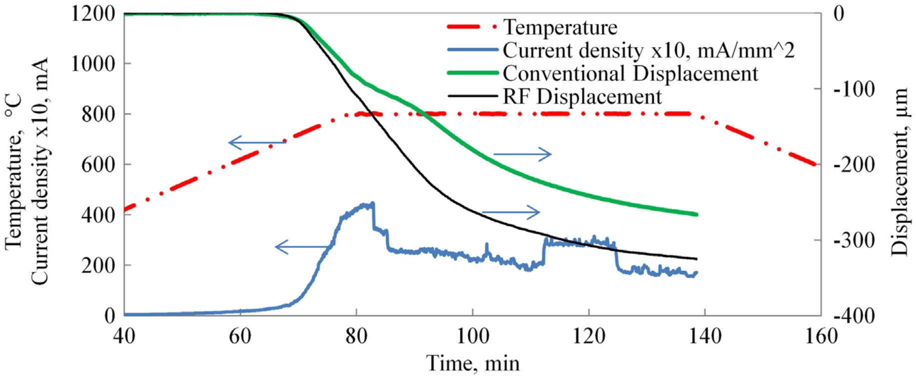

FIGURE 4 | Conventional vs. HF sintering displacement curves. Note that 100-µm displacement corresponds to 10% strain.

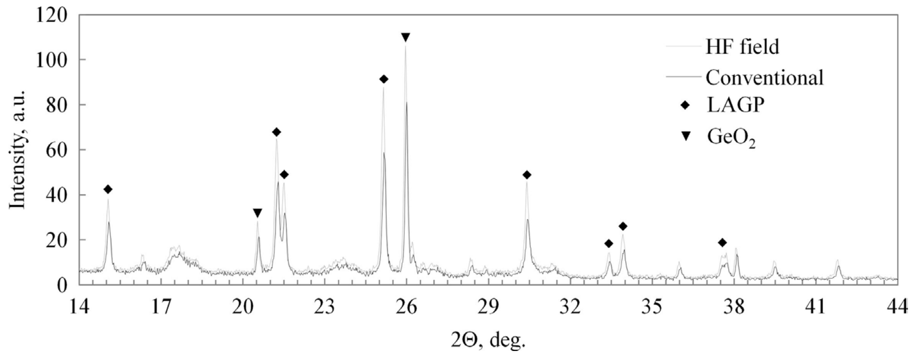

FIGURE 5 | XRD of as-crystallized powders.

it is reasonable to conclude that the field promotes crystallization through a mild non-thermal effect.

A comparison of the conventional and field-assisted final sintering curves is shown in **Figure 4**. Both curves are averages of five samples each. Sintering commences at approximately 630°C with the sintering rate accelerating and rapidly slowing down as some grain growth occurs, thus reducing sintering pressure. Residual thermal expansion of the dilatometer is subtracted from the data shown. The typical current profile is overlaid on the chart in **Figure 4** and illustrates the expected rise in electrical conductivity with temperature. The significant rise in measured current illustrates the effectiveness of using HF fields to achieve capacitive coupling with the material and obviates the need for any added conductive coating. The dramatic fluctuations in current are assignable to secondary phases melting and providing intermittent highly conductive paths until they react with the matrix forming the primary phase. This process can repeat itself many times during HF sintering.

It is notable that any effect on sintering rate is minor. Despite the slightly larger starting grain size, the sintering rate under HF electrical field is only increased by approximately 30% before and 40% after reaching steady state temperature. This brings into question the significance of non-thermally activated matter diffusion mechanisms in the LAGP system. Such effects are widely claimed for a number of electrically assisted sintering processes in other material systems. However, most of the theoretical treatment and experimental work is done on systems where charge carriers simultaneously belong to the crystal lattice. This is not the case for LAGP, and it is possible that polarization of the lattice is a requirement for distinct field effects. The final density of the samples was approximately 80.3 vs. 77.9%, and sintering strain of 30.5 vs. 26.2% for field processed vs. conventionally sintered samples, respectively. With the applied field being in the hundreds of volt per centimeter, a question of why the sample does not flash sinter has to be addressed. Few experimental geometries allow for direct control of the sample temperature by virtue of aspect ratio and electrical connections utilized. By comparison, our experiments embed a shielded thermocouple within the electrode, in intimate contact with the sample itself. This configuration allows for accurate temperature measurement that is not compromised by the applied field. Another benefit is our ability to control the furnace from the same sensor, in effect using the sample temperature for control. Thus, the sample is actively prevented from proceeding into the thermal runaway condition. This is further aided by the very low aspect ratio of the sample, effectively reducing internal thermal gradients and maximizing the intimate thermal contact with the electrodes, thus allowing the electrodes to serve as effective heat sinks. A similar effect has been reported for the flash sintering of zirconia, where the onset of flash was significantly delayed in low aspect ratio samples (Bichaud et al., 2015). To verify that the absence of flash sintering is a result of the thermal sink effect of the electrode configuration in our apparatus, a single sample was pressed from the same powder in the shape of a dog bone using method taught by Francis et al. (2012) and an attempt was made to sinter the sample using the flash sintering technique. The sample flashed immediately upon application of 300 V/cm DC field at a comparatively low temperature of 400°C proving that the material is indeed amenable to flash if allowed to experience thermal runaway. The sample did not densify measurably; however, no further investigation was undertaken since this did not further the current study. Thus, thermal runaway in flash sintering appears to behave similarly to thermal dielectric breakdown (O'Dwyer, 1964).

Typical SEM photographs of fracture surfaces, as shown in **Figure 6**, demonstrate very similar microstructure, consistent with our density measurements. Grain size can be visually estimated to average at 0.3 μm in samples sintered with and without field. It appears that any difference in material that results from crystallization under field is effectively diminished after 1 h at 800°C. No abnormal grain growth was observed.

The XRD spectra, as shown in **Figure 7**, for the two processing methods appear nearly identical with slightly better definition of the weaker peaks, such as [006] and [202] in the HF field sintered material. Besides the primary LAGP phase peaks, only minor features are detected at 26.3° and 20.6°, identified as [101] and [100] peaks of the GeO_2 secondary phase. There is a near consensus in the LAGP community that $AlPO_4$ and some version of lithium phosphate are almost invariably present in amorphous form, and therefore do not produce diffraction peaks in XRD spectra. In order to identify the presence of additional amorphous impurities, HRTEM EDS images of HF field sintered material are shown in **Figure 8**, and contrasted with HRTEM EDS images of conventionally sintered material shown in **Figure 9**. These highlight misalignment of nearly perfectly formed tetragonal crystals

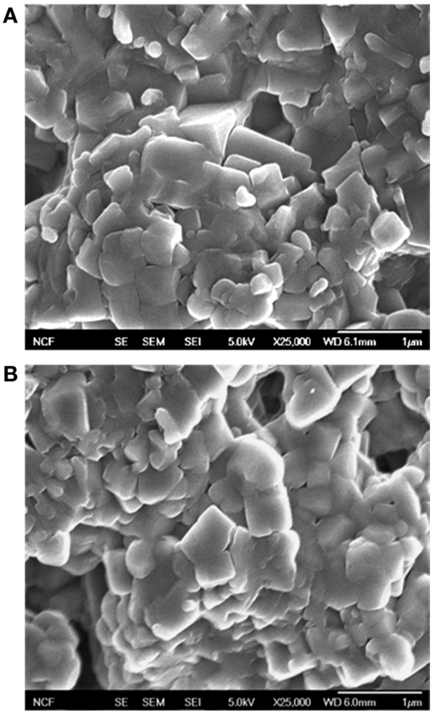

FIGURE 6 | SEM micrographs of selected fracture surfaces. (A) HF sintered and **(B)** conventionally sintered.

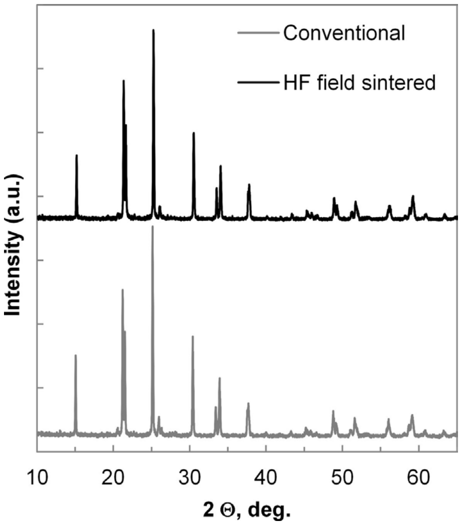

FIGURE 7 | **X-ray diffraction patterns for HF (top) and conventionally (bottom) sintered LAGP**.

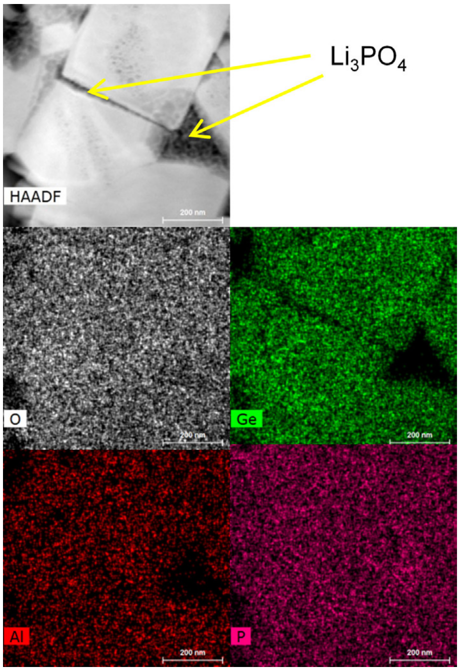

FIGURE 8 | **HRTEM, EDS elemental maps, field-assisted sintered sample**.

of LAGP with relatively little direct grain-to-grain contact. The amorphous phases between grains are identified by elemental mapping as either lithium phosphate, by absence of Al or Ge, or as $AlPO_4$. Precise phase identification is challenging as these phases appear extremely vulnerable to electron beam damage, consistent with previous reports (Mariappan et al., 2011). In general, $AlPO_4$ seems to be more likely to exist as large inclusions or in inter-grain regions with large grain misalignment, whereas lithium phosphate appears to be present in thin layers between mostly aligned grain facets. Due to the much higher 1800°C melting point, $AlPO_4$ has a tendency to segregate and form larger inclusions as shown in the image of conventionally sintered LAGP, **Figure 9**.

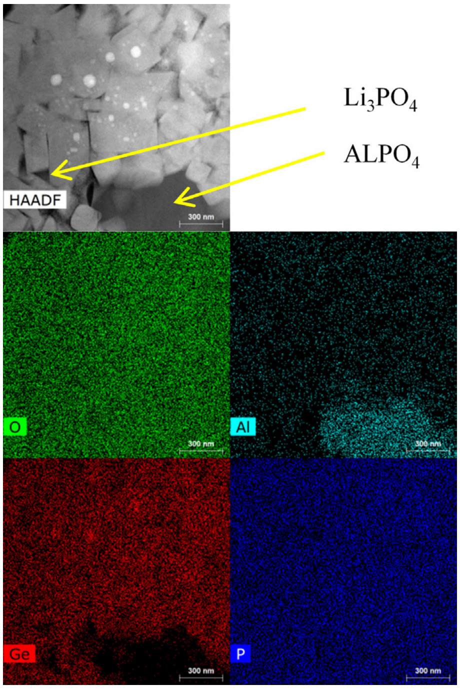

FIGURE 9 | **HRTEM, EDS elemental maps, conventionally sintered sample**.

Impedance spectroscopy results show essentially identical behavior for samples derived from the two processing methods. A typical Nyquist plot is presented in **Figure 10**. The expected contributions from bulk and grain boundary conductivity are clearly visible. An RC network model, as shown in the inset in **Figure 10**, was fit to the data using Zview software (Scribner Associates). Conductivity of the conventional and HF processed material was calculated according to

$$\sigma = \frac{1}{R} \times \frac{t}{A}$$

Although the data exhibit some variation among the five samples of each processing type, the distributions overlap between conventionally and field-assisted sintered samples. Typical results for the bulk and grain boundary conductivity are presented in **Figure 11** in the form of an Arrhenius plot. The calculated activation energies for the grain and grain boundary conductivity are 0.38 and 0.44 eV, respectively, and overall conductivities are on the order of 1.5×10^{-4} S/cm, consistent with values reported in the literature (Kotobuki et al., 2010).

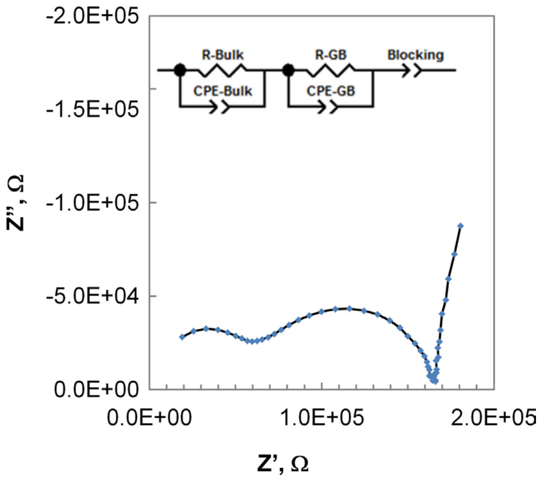

FIGURE 10 | **Typical Nyquist plot of the impedance spectrum for a conventionally sintered sample.**

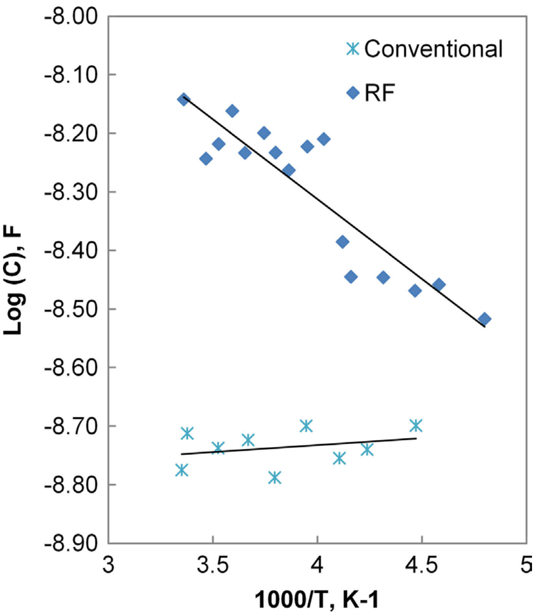

FIGURE 12 | **Grain boundary capacitance of typical conventionally and HF sintered samples.**

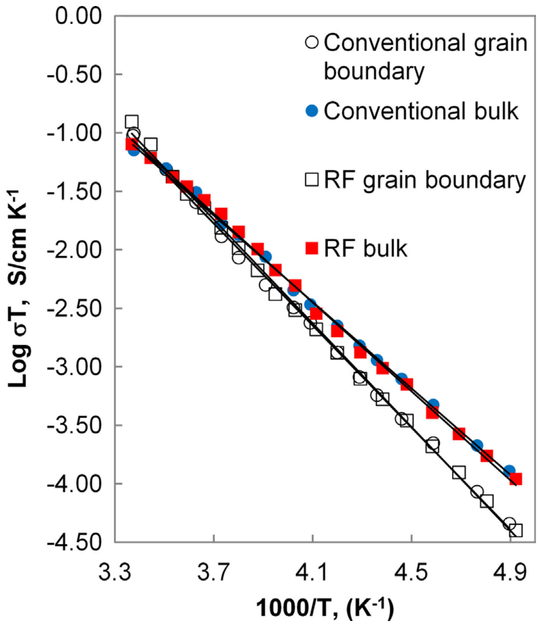

FIGURE 11 | **Arrhenius plot of bulk and grain boundary conductivity for conventional and HF sintered samples.**

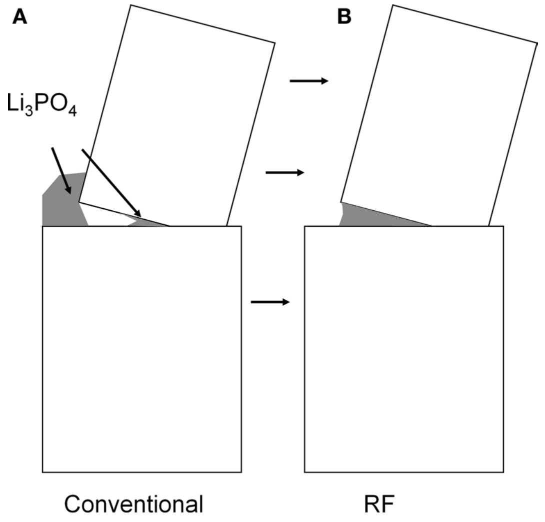

FIGURE 13 | **Proposed geometry of grain boundary electrowetting: (A) conventional sintering and (B) field-assisted sintering.**

A wholly unexpected effect is the significantly increased grain boundary capacitance of the samples processed under electrical field, as illustrated in **Figure 12**. It may be tempting to ascribe this effect to a thinner grain boundary, as thinner grain boundaries were convincingly demonstrated in flash sintered zirconia (M'Peko et al., 2013). However, the nearly identical grain boundary conductivity values between field-assisted and conventional sintering would suggest otherwise. We propose that the cause of the increased grain boundary capacitance is an increased contact area of an insulating intergranular phase adjacent to the actual conducting grain boundary. At least one of the secondary phases, e.g., lithium phosphate, melts at 847°C and might form a lower melting eutectic. If melting of these phases occurs at grain boundaries, application of electrical field would lead to electrowetting, effectively pulling these liquid phases into regions of highest field intensity where they subsequently act as a capacitive element in parallel with the grain boundary resistance, as illustrated in **Figure 13**.

The HRTEM images from our study and other researchers suggest that LAGP itself is fairly resistant to densification with actual grain contact area being substantially lower than the grain facet area (Mariappan et al., 2011). Thus, the classic brick layer model may be inadequate to explain grain boundary behavior in these materials with abundant secondary phases. In addition, since NASICON crystal conductivity is anisotropic, the widely reported grain conductivity is, at best, the average of a randomly oriented ensemble. The presence of intergranular spaces with a random distribution of insulating, e.g., Ge_2O and $AlPO_4$, and ionically conductive phases in addition to substantial porosity complicates the ability to rigorously characterize conduction mechanisms. Our future work will focus on separating the contribution of each phase to sinterability and conductivity with an eventual goal of engineering higher performing materials through intelligent grain boundary control.

CONCLUSION

High-frequency electrical fields by themselves do not appear to have a pronounced effect on sintering rate of LAGP ceramic. However, by allowing the starting material to crystallize under the same field, LAGP does show a moderately increased (+40%) sintering rate when sintered under field, as compared to powders that were conventionally calcined. Providing efficient heat sinks for Joule heating appears to arrest any tendency toward thermal runaway and flash sintering. Microstructure of the ceramic and its ionic conduction properties also show no negative effects from application of HF electric fields. Finally, we demonstrate a HF field's ability to efficiently couple capacitively into ionically conductive ceramics, preserving stoichiometry and foregoing the need for electrically conductive coatings prior to field-assisted sintering.

AUTHOR CONTRIBUTIONS

CS provided guidance in experiment design and sample characterization, contributed to and edited the manuscript, and provided final approval for submission. IL designed and built the experimental set-up, manufactured samples for characterization, performed data analysis, assembled the manuscript, and provided final approval for submission.

ACKNOWLEDGMENTS

Support for instrumentation development was provided under ARPA-E 0869-1584 through a subcontract from Solid Power, Inc. (Louisville, CO, USA). Support for materials characterization was provided under the NSF Sustainable Energy Pathways Program (Project No. DMR-1231048). Additionally, the authors acknowledge the assistance of Dr. David Diercks for the HRTEM analyses and Dr. Brian Francisco for numerous discussions.

REFERENCES

Bichaud, E., Chaix, J. M., Carry, C., Kleitz, M., and Steil, M. C. (2015). Flash sintering incubation in Al_2O_3/TZP composites. *J. Eur. Ceram. Soc.* 35, 2587–2592. doi:10.1016/j.jeurceramsoc.2015.02.033

Birke, P., Salam, F., Döring, S., and Weppner, W. (1997). A first approach to a monolithic all solid state inorganic lithium battery. *Solid State Ionics*118, 149–157. doi:10.1016/S0167-2738(98)00462-7

Bokhan, Yu. I., Komar, V. G., Misyuvyanets, V. Z., Mikhnevich, V. V., and Saraseko, M. N. (1995). High frequency sintering of multilayer ceramic capacitors. *J. Eng. Phys. Thermophys.* 68, 135–137. doi:10.1007/BF00854378

Cologna, M., Rashkova, B., and Raj, R. (2010). Flash sintering of nanograin zirconia in <5sec at 850 degrees C. *J. Am. Ceram. Soc.* 93, 3556–3559. doi:10.1111/j.1551-2916.2010.04089.x

Cretin, M., and Fabry, P. (1999). Comparative study of lithium ion conductors in the system $LiAlA(PO_4)_3$ with A=Ti or Ge and $0 \le x \le 0.7$ for use as Li+ sensitive membranes. *J. Eur. Ceram. Soc.* 19, 2931–2940. doi:10.1016/S0955-2219(99)00055-2

Downs, J. A. (2013). *Mechanisms of Flash Sintering in Cubic Zirconia*. Ph.D. dissertation, University of Trento, Trento.

Francis, J. S. C., Cologna, M., and Raj, R. (2012). Particle size effects in flash sintering. *J. Eur. Ceram. Soc.* 32, 3129–3136. doi:10.1016/j.jeurceramsoc.2012.04.028

Francisco, B. E., Stoldt, C. R., and M'Peko, J.-C. (2015). Energetics of ion transport in NASICON-type electrolytes. *J. Phys. Chem. C* 119, 16432–16442. doi:10.1021/acs.jpcc.5b03286

Goldwater, D. L. (1961). The electrolysis of thorium oxide crystals. *J. Phys. Chem. Solids* 18, 259–260. doi:10.1016/0022-3697(61)90172-X

Kotobuki, M., Hoshina, K., Isshiki, Y., and Kanamura, K. (2011). Preparation of Li1.5Al0.5Ge1.5(PO4)3 solid electrolyte by sol-gel method. *Phosphorus Res. Bull.* 25, 061–063.

Kubanska, A., Castro, L., Tortet, L., Schäf, O., Dollé, M., and Bouchet, R. (2014). Elaboration of controlled size $Li_{1.5}Al_{.5}Ge_{1.5}(PO_4)_3$ crystallites from glass-ceramics. *Solid State Ionics* 266, 44–50. doi:10.1016/j.ssi.2014.07.013

Li, S. C., Cai, J. Y., and Lin, Z. X. (1988). Phase relationships and electrical conductivity of LAGP and LACP systems. *Solid State Ionics* 2, 1265–1270. doi:10.1016/0167-2738(88)90368-2

Mariappan, C. R., Yada, C., Rosciano, F., and Roling, B. (2011). Correlation between micro-structural properties and ionic conductivity of $Li_{1.5}Al_{0.5}Ge_{1.5}(PO_4)_3$ ceramics. *J. Power Sources* 196, 6456–6464. doi:10.1016/j.jpowsour.2011.03.065

Mahmoud, M. M. (2007). *Crystallization of Lithium Disilicate Glass Using Variable Frequency Microwave Processing*. Master's thesis, Virginia Polytechnic Institute and State University, Blacksburg, VA.

M'Peko, J.-C., Francis, J. S. C., and Raj, R. (2013). Impedance spectroscopy and dielectric properties of flash versus conventionally sintered yttria-doped zirconia electroceramics viewed at the microstructural level. *J. Am. Ceram. Soc.* 96, 3760–3767. doi:10.1111/jace.12567

Nagata, N., and Nanno, T. (2007). All solid battery with phosphate compounds made through sintering process. *J. Power Sources* 174, 832–837. doi:10.1016/j.jpowsour.2007.06.227

O'Dwyer, J. J. (1964). *The Theory of Dielectric Breakdown*. Oxford: Clarendon Press.

Stanciu, L. A., Kodash, V. Y., and Groza, J. R. (2001). Effects of heating rate on densification and grain growth during field-assisted sintering of Al_2O_3 and $MoSi_2$. *Metall. Mater. Trans. A* 32, 2633–2638. doi:10.1007/s11661-001-0053-6

Sudiana, I. N., Ito, R., Inagaki, S., Kuwayama, K., Sako, K., and Mitsudo, S. (2013). Densification of alumina ceramics sintered by using submillimeter wave gyrotron. *J. Infrared, Millim. Terahertz Waves* 34, 627–638. doi:10.1007/s10762-013-0011-6

Thockchom, J. S., and Kumar, B. (2010). The effect of crystallization parameters of the ionic conductivity of a lithium aluminum germanium phosphate glass-ceramic. *J. Power Sources* 195, 2870–2876. doi:10.1016/j.jpowsour.2009.11.037

Todd, R. I., Zapata-Solvas, E., Bonilla, R. S., Sneddon, T., and Wilshaw, P. R. (2015). Electrical characteristics of flash sintering: thermal. *J. Eur. Ceram. Soc.* 35, 1865–1877. doi:10.1016/j.jeurceramsoc.2014.12.022

Yang, J., Huang, Z., Huang, B., Zhou, J., and Xu, X. (2015). Influence of phosphorus sources on lithium ion conducting performance in the system of Li_2O-Al_2O_3-GeO_2-P_2O_5 glass-ceramics. *Solid State Ionics* 270, 61–65. doi:10.1016/j.ssi.2014.12.013

Zapata-Solvas, E., Gomez-Garcia, D., Dominguez-Rodriguez, A., and Todd, R. I. (2015). Ultra-fast and energy-efficient sintering of ceramics by electric current concentration. *Sci. Rep.* 5, 1–7. doi:10.1038/srep08513

Zhang, Y., Jung, J., and Luo, J. (2015). Thermal runaway, flash sintering and asymmetrical microstructural development of ZnO and ZnO–Bi_2O_3 under direct currents. *Acta. Mater.* 94, 87–100. doi:10.1016/j.actamat.2015.04.018

Conflict of Interest Statement: The corresponding author CS is a founder and member of the Board of Solid Power, Inc., one of the two sponsors of this research work. IL has no conflict of interest to declare.

frontiers in Energy Research

ORIGINAL RESEARCH
published: 30 March 2016
doi: 10.3389/fenrg.2016.00010

Experimental and Computational Approaches to Interfacial Resistance in Solid-State Batteries

Kazunori Takada[1,2]* and Takahisa Ohno[2,3]

[1] Battery Materials Unit, National Institute for Materials Science, Tsukuba, Japan, [2] Global Research Center for Environment and Energy Based on Nanomaterials Science, National Institute for Materials Science, Tsukuba, Japan, [3] Computational Materials Science Unit, National Institute for Materials Science, Tsukuba, Japan

Solid-state batteries with inorganic solid electrolytes are expected to be an efficient solution to the issues of current lithium-ion batteries that are originated from their organic-solvent electrolytes. Although solid-state batteries had been suffering from low rate capability due to low ionic conductivities of solid electrolytes, some sulfide solid electrolytes exhibiting high ionic conductivity of the order of 10^{-2} S cm^{-1} have been recently developed. Since the conductivity is comparable to or even higher than that of liquid electrolytes, when taking the transport number of unity into account, ion transport in solid electrolytes has ceased from rate determination; however, it has been replaced by that across interfaces. The sulfide electrolytes show high interfacial resistance to the high-voltage cathodes. Our previous studies have demonstrated that oxide solid electrolytes interposed at the interface reduce the resistance, and they also suggest that the high resistance is attributable to a lithium-depleted layer formed at the interface. This study employs the first-principles calculation in order to gain insight into the interface. The interface structure between an oxide cathode/sulfide electrolyte simulated by the first-principles molecular dynamics has disclosed the presence of lithium-depleted layer at the interface, and the electronic structure calculated on the basis of density functional theory strongly suggests that the charge current preferentially removes lithium ions from the sulfide electrolyte side of the interface to deplete the lithium ion there. These calculation results are consistent with the transport mechanism proposed from the experimental results.

Keywords: nanoionics, space-charge layer, electrode/electrolyte interface, solid-state battery, solid electrolyte, first-principles calculation

OPEN ACCESS

Edited by:
Jeff Sakamoto,
University of Michigan, USA

Reviewed by:
Mehmet Kadri Aydinol,
Middle East Technical University,
Turkey
Timothy Sean Arthur,
Toyota Research Institute of North
America, USA

Correspondence:
Kazunori Takada
takada.kazunori@nims.go.jp

Specialty section:
This article was submitted to
Energy Storage,
a section of the journal
Frontiers in Energy Research

Received: *01 February 2016*
Accepted: *14 March 2016*
Published: *30 March 2016*

Citation:
Takada K and Ohno T (2016)
Experimental and Computational
Approaches to Interfacial Resistance
in Solid-State Batteries.
Front. Energy Res. 4:10.
doi: 10.3389/fenrg.2016.00010

1. INTRODUCTION

Lithium-ion batteries predominate in today's rechargeable battery systems because of their high energy densities. They have been used portable electronics devices including cellular phones and notebook PC's and serving as a key component in this information society for more than 20 years. Moreover, they start to be installed in vehicles and smart grids for realizing a low-carbon society; however, some issues including safety originating from the thermal and electrochemical instability of their organic-solvent electrolytes have not gone out completely. Because inorganic solid electrolytes exhibit higher thermal and electrochemical stability, use of the solid electrolytes is expected to be an efficient solution (Tarascon and Armand, 2001), even if the electrochemical stability is attributed to the kinetic stabilization as suggested in Zhu et al. (2015). However, solid-state lithium batteries had been suffering from low power densities.

Essential materials to improve the power densities are, of course, solid electrolytes with high ionic conductivities. Since ions generally diffuse faster in liquids than in solids, the use of solid electrolytes lowers the power densities. However, high ionic conductivities that are comparable to that in liquid systems have been achieved among sulfide solid electrolytes. Sulfide ions are larger in size and higher in polarizability than oxide counterparts. The large ionic radius leaves wide opening for ionic conduction, and the higher polarizability weakens attraction between lithium and sulfide ions to make the lithium ions mobile (Zheng et al., 2003). Therefore, high ionic conductivities have been often observed in sulfides, as reviewed in Minami et al. (2006) and Takada (2013b), and the highest conductivities in sulfide electrolyte systems have recently reached 10^{-2} S cm^{-1} (Kamaya et al., 2011; Seino et al., 2014).

In addition, sulfide solid electrolytes exhibit high processability. They are relatively soft materials (Sakuda et al., 2013) and show low grain boundary resistance only by compression. Therefore, sintering process is not essential to connect the particles, whereas high temperature sintering is inevitable to connect ionic conduction between particles in oxide solid electrolytes, for instance. Besides the high ionic conductivity, this feature is beneficial for developing solid-state batteries, because high temperature sintering promotes mutual diffusion that forms impurity phases at the interface. However, even such solid electrolytes had not improve the power density to be high enough for practical application by themselves.

As reported in Takada et al. (2008), when a sulfide electrolyte is combined with graphite and $LiCoO_2$, which are typical anode and cathode materials, respectively, to assemble a lithium-ion-type solid-state battery, high resistance is found in its cathode. Because the resistance is the highest in the battery to be rate-determining in the battery reaction, power density will not be improved without reducing the cathode resistance. Ohta et al. (2006) integrates a novel interface structure between the sulfide electrolyte and $LiCoO_2$ into the cathode in order to improve the power density to a practical level. In the interface structure, surface of the $LiCoO_2$ particles is coated with $Li_4Ti_5O_{12}$, which act as an oxide solid electrolyte on the surface. This surface coating has reduced the cathode resistance by 1/20 and increased the power density to be as high as that of commercial lithium-ion batteries with liquid electrolytes. The interface is designed on the basis of "nanoionics" (Maier, 1995).

Ionic conductors often exhibit anomalous ionic conduction at their surface or interface. It is explained that the anomalous ionic conduction is induced by the changing concentration of mobile ions to form space-charge layers at the interface. Nanoionics has been often reported as enhanced ionic conduction at interfaces, as reviewed in Maier (2014). On the other hand, Takada (2013a) suggests that the space-charge layer appears as a lithium-depleted layer at the cathode interface in solid-state batteries with sulfide electrolytes. Noble potential of the cathode material depletes lithium ions of the sulfide electrolyte at the interface to the cathode material and makes the interface highly resistive. The surface coating, which interposes the oxide electrolyte between the high-voltage cathode and sulfide electrolyte materials, suppresses the lithium depletion to reduce the interfacial resistance.

Although the changes in the electrode properties upon the surface coating are well explainable by the interface model based on nanoionics, origin of the high interfacial resistance and its reduction are still under debate, because changes in the interfacial structure upon the coating, which are predicted by the interface model, have not been visualized yet. Since the space-charge layer lies between solids with only several nanometers in thickness, it has never shown up even on advanced analyses. This study employs computational science using the first-principle calculations in order to get a clear picture of the interfacial phenomena. Results from density functional theory (DFT) calculation for the interfaces to $Li_{1-x}FePO_4$ cathode materials are combined with experimental results from the interfaces to $Li_{1-x}CoO_2$ and $Li_{1-x}Mn_2O_4$ in Ohta et al. (2007) and Takada et al. (2012) to reveal the validity of the space-charge layer model.

2. MATERIALS AND METHODS

2.1. Experiments

The materials presented in this paper have been already reported in Ohta et al. (2007) and Takada et al. (2012). Thin layer of $LiNbO_3$ was formed on the particle surface of $LiCoO_2$ and $LiMn_2O_4$ from an ethanol solution of alkoxides of Li and Nb by a rolling fluidized coating method. The $LiCoO_2$ and $LiMn_2O_4$ powders are commercially available (D10 and M811, respectively; Toda Kogyo). Average particle size and Brunauer–Emmett–Teller (BET) surface area of the $LiCoO_2$ powder are 11.2 μm and 0.26 m^2 g^{-1}, respectively, while those of the $LiMn_2O_4$ powder are 5 μm and 0.40 m^2 g^{-1}, respectively. Alkoxides used to form $LiNbO_3$ layer are lithium ethoxide and niobium pentaethoxide. The amount of $LiNbO_3$ coated on the surface varies from 0 (uncoated) to 94 mg m^{-2}. The maximum amount corresponds to $LiNbO_3$ layer of 20 nm in thickness, if the surface of active material particles is uniformly covered with the $LiNbO_3$.

The sulfide solid electrolyte to make the interface to the cathode materials in this study is $Li_{3.25}Ge_{0.25}P_{0.75}S_4$ (Kanno and Murayama, 2001). It is mixed with the $LiCoO_2$ and the $LiMn_2O_4$ at weight ratios of 3:7 and 1:1, respectively, to form the interfaces in the composite electrodes. Solid-state cells for the electrochemical measurements are assembled from the mixtures (12.7 mg for the $LiCoO_2$ and 15 mg for the $LiMn_2O_4$) as the working electrodes, In–Li alloy as the counter electrodes and $Li_{3.25}Ge_{0.25}P_{0.75}S_4$ as the separators. Because electrode potential of the In–Li electrode is 0.62 V vs. Li^+/Li, cell voltage is presented by adding 0.62 V in this paper as if the electrode properties were investigated in electrochemical cells with lithium metal anodes. The $LiCoO_2$ cathodes are charged to 4.2 V vs. Li^+/Li, that is, 3.58 V in the cell voltage at a constant current of 127.4 μA cm^{-2}, while the $LiMn_2O_4$ are charged to 4.3 V vs. Li^+/Li at 20 μA cm^{-2}, before the electrochemical impedance spectroscopy to evaluate the electrode impedance.

2.2. Computations

The cathode material used in the computations is $LiFePO_4$. Li_3PO_4 and Li_3PS_4 are selected as oxide and sulfide-based solid electrolytes, respectively, in order to compare cathode/oxide electrolyte and cathode/sulfide electrolyte interfaces. The $LiFePO_4/Li_3PO_4$ interface is constructed between $LiFePO_4$ (010) and γ-Li_3PO_4 (100) planes by the computation method reported in Sumita et al. (2015) and Sumita et al. (2016).

On the other hand, because lattice mismatch between $LiFePO_4$ and Li_3PS_4 is too large to form a coherent interface, Li_3PS_4 is amorphized on the $LiFePO_4$ (010) plane by first principles molecular dynamics simulation (FP-MD) to form the interface as follows. The amorphous Li_3PS_4 is constructed from 16 Li_3PS_4 units stacked on (010) plane of a 1 × 3 × 2 supercell of $LiFePO_4$. The interface is stabilized by FP-MF calculation with a constant-temperature, constant-pressure (NPT) ensemble at the temperature of 400 K, and the pressure of 1.0 atom with the valuable cell dimension perpendicular to the interface. The interface structure is equilibrated under the temperature control by canonical sampling through velocity rescaling thermostat (Bussi et al., 2007) for 40 ps.

In this study, cathode interfacial structures during the cell operation are also investigated. Fully charged $LiFePO_4$, i.e., $FePO_4$, is stacked onto Li_3PO_4 and Li_3PS_4, respectively, and the interface structures are relaxed by FP-MD simulations with an NPT ensemble at 400 K under 1.0 atom for *ca.* 200 ps. These interfaces are connected to lithium metal in order to calculate energies relative to its Fermi level.

Computational analyses for these interfaces are according with the procedures in Sumita et al. (2015) and Sumita et al. (2016). Total energies are calculated at the Γ point in the super cell approach within DFT implemented in CP2K at www.cp2k.org. The Goedecker, Teter, and Hutter (GTH) pseudopotentials are selected for PBE functional (Perdew et al., 1996) with the local spin density approximation in this study. Valence pseudowave functions are expanded in Gaussian-type orbitals, and the density is represented in a plane wave auxiliary basis in the hybrid Gaussian (MOLOPT DZVP) and plane-wave (240 Ry for cutoff energy) basis set. The $+U$ strategy is applied to include the electronic correlation within the *d* orbital of Fe, in which the effective U is set to 4.3 eV as in Wang et al. (2007).

3. RESULTS

3.1. Changes in the Electrode Properties upon the $LiNbO_3$ Coating in the Experiments

The surface coating reduces the cathode impedance, as demonstrated in **Figure 1**. Each Nyquist plot consists of an arc followed by a tail in the low frequency region. The impedance at the high frequency limit agrees with the resistance of the solid electrolyte layer calculated from the cross section and the thickness of the electrolyte layer and the ionic conductivity of the solid electrolyte. It is, in general, very difficult to derive intrinsic interfacial resistance from impedance data of composite electrodes; however, it is clear that the surface coating decreases the interfacial resistance. The impedance including the interfacial resistance, which draws an arc in the Nyquist plot, is decreased from 670 to 10 Ω cm^2 for the $Li_{1-x}CoO_2$ cathode and from 8000 to 150 Ω cm^2 for the $Li_{1-x}Mn_2O_4$ cathode, that is, by almost two orders of magnitude.

The surface coating has another effect on the electrode properties. Lithium ions are deintercalated from $LiCoO_2$ and $LiMn_2O_4$ in potential plateaus at 4 V vs. Li^+/Li. However, they exhibit additional potential slopes prior to the 4 V plateaus in the sulfide solid electrolyte during the charging, as shown in the top panels of **Figure 2**. The surface coating changes the length of the slopes. Before surface coating, both of the $LiCoO_2$ and $LiMn_2O_4$ show potential slopes with almost the same length of 0.2 μAh cm^{-2}. The increasing amount of $LiNbO_3$ gradually shortens the potential slopes, and the slopes finally disappear at the $LiNbO_3$ amount of 94 mg m^{-2}.

The capacities in the potential slopes are very small. For example, the capacity of 0.2 μAh cm^{-2} based on the BET surface area corresponds only to 0.5 mAh g^{-1} for the $LiCoO_2$ and 0.8 mAh g^{-1} for the $LiMn_2O_4$. However, the slopes are not artifact. They appear both in $LiCoO_2$ and $LiMn_2O_4$ with almost the same capacity based on the BET surface areas of the materials and fade to the same degree with increasing amounts of $LiNbO_3$.

3.2. Electronic and Interface Structures Obtained from the Computations

Figure 3 plots density of states (DOS) in $LiFePO_4$, Li_3PO_4, and Li_3PS_4 against energy relative to Fermi level of lithium metal. They are semiconductors with band gap energies of 3.7, 5.9, and 2.4 eV, respectively. The valence band maximum (VBM) of the $LiFePO_4$, which mainly consists of Fe 3*d* orbital, is located at −3.5 V, indicating that charge reaction of $LiFePO_4$ extracts electrons from the 3*d* orbitals at 3.5 V to give the electromotive force in a $Li/Li_{1-x}FeO_4$ cell. The VBM's in Li_3PO_4, and Li_3PS_4, where contribution of O 2*p* and S 3*p* orbitals is predominant, are located at −4.0 and −2.0 V, respectively.

Figures 4B and **5B** show the crystallographic structures of the interfaces during the cell operation, which are computed by relaxing $FePO_4/Li_3PO_4$ and $FePO_4/Li_3PS_4$ stacks displayed in **Figures 4A** and **5A**, respectively, by the FP-MD. It shows a clear difference between the interfaces. The structure relaxation leads to little change in the $FePO_4/Li_3PO_4$ interface, while it transfers a significant amount of lithium ions residing in the interface region of Li_3PS_4 to the $FePO_4$. As a result, $FePO_4$ has become $Li_{1-x}FePO_4$. At the same time, the interface region of the Li_3PS_4 becomes low in the lithium-ion concentration, while that in the bulk region is not changed significantly, as can be seen in **Figure 5B**.

4. DISCUSSION

4.1. Formation of Lithium-Depleted Layer at Cathode/Sulfide Solid Electrolyte Interface

Origin of the high interface resistance at oxide cathodes/sulfide electrolytes can be found in **Figure 5B**. The FP-MD, which leads the interface to the equilibrium, transfers lithium ions from Li_3PS_4 to $FePO_4$ and depletes lithium ions on the Li_3PS_4 side of the interface. This result reveals that the space-charge layer appears as a lithium-depleted layer at the $Li_{1-x}FePO_4/Li_3PS_4$ interface, which should make the interface highly resistive owing to the absence of charge-carrying lithium ions.

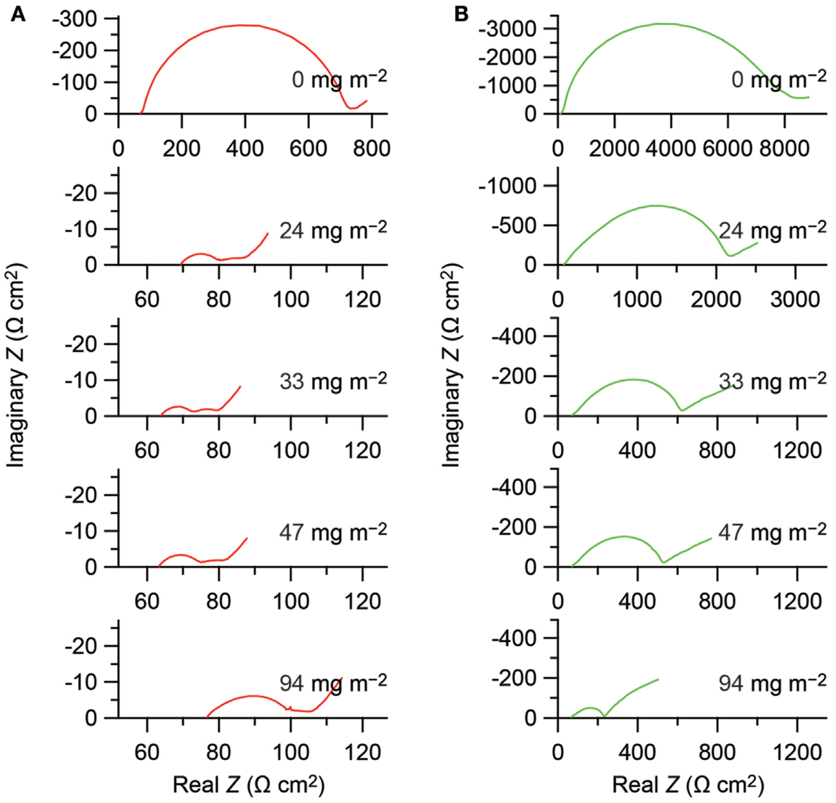

FIGURE 1 | Nyquist plots obtained from the solid-state electrochemical cells with configuration of In–Li$_x$/Li$_{1-x}$CoO$_2$ (A) and In–Li$_x$/Li$_{1-x}$Mn$_2$O$_4$ (B). Horizontal and vertical axes indicate real and imaginary parts of the complex impedance based on the projection areas of the cathodes, respectively. The amounts of the $LiNbO_3$ coating on the active materials are indicated on the basis of the BET surface areas of the active materials in the figures. Impedance date reported in Ohta et al. (2007) and Takada et al. (2012) are replotted in this figure, copyright © 2007 and 2012, with permission from Elsevier.

This computational results demonstrate that the ion concentration on the electrode surface will be a critical factor governing the interfacial resistance. It is needless to mention that the ion concentration is related to the electrode potential through a Nernst equation.

$$E = E^0 + \frac{RT}{zF}\ln\frac{a_{\mathrm{Ox}}}{a_{\mathrm{Red}}} \tag{1}$$

In the Nernst equation, electrode potential, E is connected to activities of oxidant and reductant, a_{Ox} and a_{Red}, respectively, with the standard electrode potential, E^0; the gas constant, R; the absolute temperature, T; the number of transferred electrons, z; and the Faraday constant, F. Because activities are related to ion concentration through activity coefficient, the concentrations of oxidant and reductant determine the E and *vice versa*. In solid electrolytes, only lithium ions are mobile to change the concentration; therefore, presence and absence of lithium should be regarded as the reductant and oxidant, respectively. That is, lithium-ion concentration at the interface is governed by the electrode potential, and noble potential of the oxide cathodes will decrease it.

E^0 in sulfide will be much lower than that in oxides, because lithium ions are much more loosely bonded to the lattice framework in sulfides. Therefore, $a_{\mathrm{Ox}}/a_{\mathrm{Red}}$, which corresponds to concentration of lithium vacancies, should become very large in order to make the E reach the redox potential of the cathode and start the charge reaction. In other word, the oxidation current in the beginning of charging is spent to remove lithium ions from the sulfide solid electrolyte side of the cathode/sulfide electrolyte interface to increase the $a_{\mathrm{Ox}}/a_{\mathrm{Red}}$ in equation (1) before E reaches the redox potential. After the E becomes equal to the redox potential of the cathode, lithium deintercalation from the cathode material begins.

This classical picture may be rough but seems reasonable. The preferential removal of lithium ions from the sulfide electrolyte side can be seen as potential slopes appearing for the uncoated materials in **Figure 2**, which are distinguishable from the following potential plateaus originated from lithium deintercalation from the cathode materials. Moreover, because E determines the lithium-ion concentrations on the electrode surface in equation (1), the potential slopes should have the same capacity between the $LiCoO_2$ and $LiMn_2O_4$ due to the same electrode potential of 4 V, which is also evidenced by the top panels in **Figure 2**.

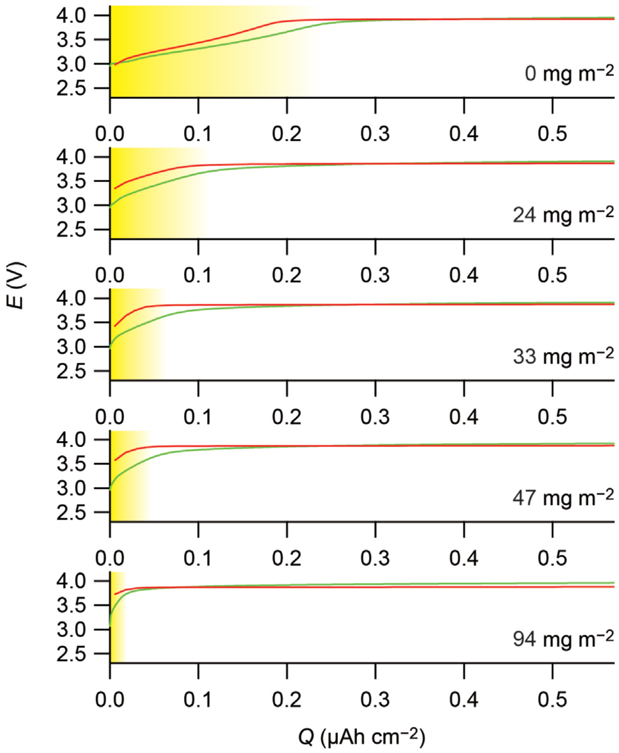

FIGURE 2 | The beginning parts of the charge curves of the cathodes. The curves for the In–Li_x/$Li_{1-x}CoO_2$ and In–Li_x/$Li_{1-x}Mn_2O_4$ are shown in red and green, respectively. The horizontal axes indicate the charge capacities normalized by the BET surface areas of the active materials, and the vertical axes indicate the cathode potential calculated by adding 0.62 V, which is the electrode potential vs. Li^+/Li of the In–Li_x counter electrodes, to the cell voltage. The amounts of the $LiNbO_3$ coated on the active materials are indicated on the basis of the BET surface areas of the active materials in the figures. The potential slopes described in the text are shaded in yellow. Charge curves reported in Ohta et al. (2007) and Takada et al. (2012) are replotted in this figure, copyright © 2007 and 2012, with permission from Elsevier.

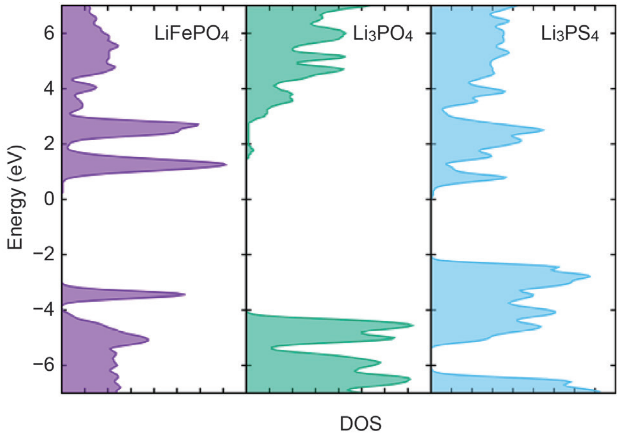

FIGURE 3 | Density of states calculated for $LiFePO_4$, Li_3PO_4, and Li_3PS_4. Zero in energy is set to the Fermi level of Li metal.

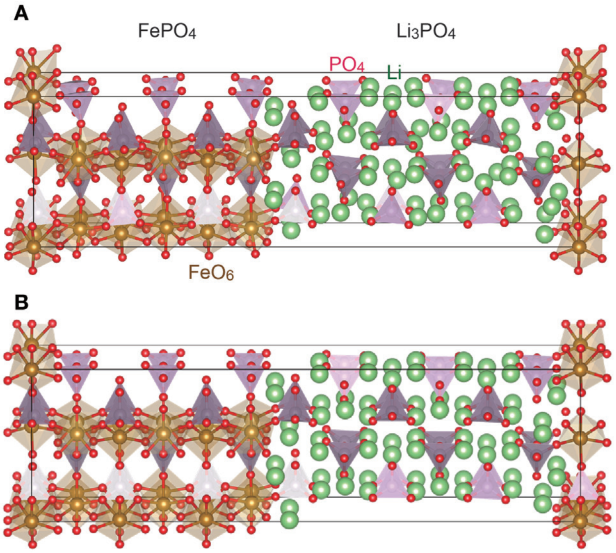

FIGURE 4 | Interface structure between $FePO_4$ and Li_3PO_4 before (A) and after (B) the FP-MD. The crystal structures are drawn by a computer program, VESTA (Momma and Izumi, 2011).

In addition, equation (1) suggests that change in the electrode potential changes lithium-ion concentration exponentially; that is, increasing *E* results in the drastic decrease of lithium ions. A buffer layer in the first report on the reduced interfacial resistance (Ohta et al., 2006) is $Li_4Ti_5O_{12}$. Although it decreases the interfacial resistance at $Li_{1-x}CoO_2$/$Li_{3.25}Ge_{0.25}P_{0.75}S_4$ by 1/20, its ionic conductivity is only 10^{-13}–10^{-10} S cm^{-1} (Wilkening et al., 2007; Fehr et al., 2010), while ionic conductivity of the sulfide electrolyte, $Li_{3.25}Ge_{0.25}P_{0.75}S_4$, is as high as 2.2×10^{-3} S cm^{-1} (Kanno and Murayama, 2001). A reasonable explanation for the reduced resistance inferred from the Nernst equation is that the high bulk conductivity of $Li_{3.25}Ge_{0.25}P_{0.75}S_4$ becomes so low at the interface due to the exponential decrease in the carrier concentration that even the $Li_4Ti_5O_{12}$ with low ionic conductivity reduces the resistance.

The DFT calculation results shown in **Figure 3** gives a clear explanation for the preferential removal of lithium ions from the Li_3PS_4 side upon charging. Charge reaction in $LiFePO_4$ is lithium deintercalation accompanied by the extraction of electrons in 3*d* orbitals of $LiFePO_4$ located around −3.5 V. On the other hand, VBM of the Li_3PS_4 is located at −2.0 eV, which is higher than the 3*d* orbital of $LiFePO_4$. Therefore, electrons will be extracted not from the $LiFePO_4$ but from the Li_3PS_4 at the beginning of the charge reaction, and simultaneously lithium ions will be extracted from the Li_3PS_4 to keep charge neutrality.

4.2. Reduction of Interfacial Resistance by Surface Coating

High interfacial resistance at oxide cathodes/sulfide electrolytes is considered to come from lithium-depleted layer formed at the interface, as discussed above. Therefore, reduction of the interfacial resistance by interposing oxide electrolytes observed in the

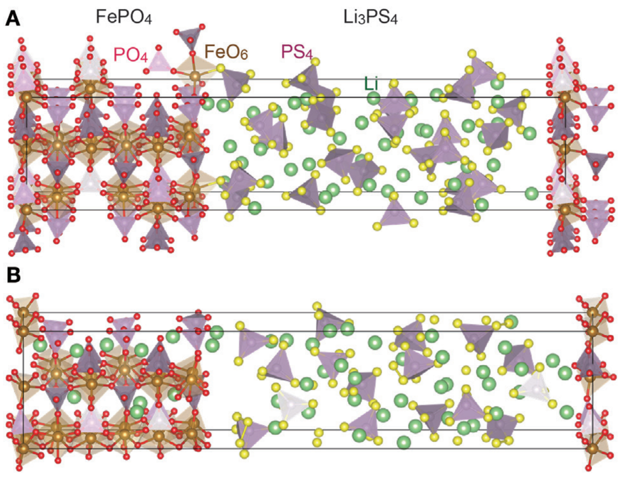

FIGURE 5 | Interface structure between $FePO_4$ and Li_3PS_4 before (A) and after (B) the FP-MD. The crystal structures are drawn by a computer program, VESTA (Momma and Izumi, 2011).

experiment should be attributed to the suppression of lithium depletion; that is, lithium-depleted layer is not formed at oxide cathode/oxide solid electrolyte interfaces.

In fact, the FP-MD to relax the interfacial structure does not change distribution of lithium ions around the $FePO_4/Li_3PO_4$ interface, as demonstrated in **Figure 4**. The Li_3PO_4 keeps its original structure at the interface to the $FePO_4$, and lithium depletion is not recognized there. Moreover, the DOS's calculated for $LiFePO_4$ and Li_3PO_4 indicate that lithium ions are not preferentially removed from the solid electrolyte. VBM of the Li_3PO_4 is located above 3*d* orbital of $LiFePO_4$ as shown in **Figure 3**, and thus charging current should be electrons removed from $LiFePO_4$ even at the beginning. That is, lithium deintercalation from the $LiFePO_4$ takes place at the interface to Li_3PO_4 from the beginning of charging.

Because lithium ions are not preferentially removed from the oxide electrolyte side of the interface, cathode/oxide electrolyte interfaces do not provide a potential slope to the charging curves. In fact, **Figure 2** indicates fading of the potential slopes for the $LiCoO_2$ and $LiMn_2O_4$ observed in the $Li_{3.25}Ge_{0.25}P_{0.75}S_4$ interfaces upon the $LiNbO_3$ coating. The increasing amount of $LiNbO_3$ coated on the cathode materials gradually shortens the potential slope, which is attributable to the increasing coverage by the coating layer. It decreases the interface area, where the cathode materials are directly contacted to the sulfide solid electrolyte, to eliminate the potential slope. Simultaneously, it increases the cathode/oxide electrolyte interface area, where lithium-depleted layer is not formed, to decrease the interfacial resistance.

The above discussions have revealed that the high interfacial resistance and the effects of surface coating on the electrode properties are explainable by the space-charge model. On the other hand, Sakuda et al. (2010) has proposed another mechanism for the interfacial resistance and its reduction. It reports that transition metals and anions, as well as lithium ions, diffuse across a $Li_{1-x}CoO_2/Li_2S–P_2S_5$ to form an impurity phase. The impurity phase is concluded to be the reason for the high interfacial resistance, and the surface coating suppresses the mutual diffusion and reduces the interfacial resistance. On the other hand, such mutual diffusion is not observed in the present computations. **Figure 5B** exhibits that the structure relaxation changes the lithium-ion distribution around the interface without changing the flamework structure. However, it is premature to deny the mutual diffusion, because the relaxation time in the FP-MD simulations is only 200 ps.

It should be noted that $Li_{1-x}FePO_4$ is used as the cathode material in the computations instead of $Li_{1-x}CoO_2$ in the experiments in this study. $LiFePO_4$ forms a coherent interface to Li_3PO_4, as reported in Sumita et al. (2015). In addition, the surface spin-state of $LiCoO_2$ is complicated, although the manifold spin-states may not affect the band alignment at the interface significantly (Sumita and Ohno, 2016). That is, $Li_{1-x}FePO_4$ is better than $Li_{1-x}CoO_2$ to eliminate ambiguities in the computation models, and thus is used in this study. Although computations using $Li_{1-x}CoO_2$ is preferable to provide an accurate picture on the interfacial phenomena observed in the experiments, coincidences in the electrode properties between the $LiCoO_2$ and $LiMn_2O_4$ in the $Li_{3.25}Ge_{0.25}P_{0.75}S_4$ and the effects of the surface coating to the interfaces, which are displayed in **Figures 1** and **2**, and the above discussions strongly suggest that electrode potential of cathode materials dominates the lithium-ion concentration at the interface and the interfacial resistance. Of course, electrode potential of $Li_{1-x}FePO_4$ is 3.5 V and lower than 4.0 V for $Li_{1-x}CoO_2$ to a certain extent; however, both of them are far enough from the VBM of Li_3PS_4 not to give significant differences. Therefore, the picture given from the $Li_{1-x}FePO_4$ will be valid also for the interface to $Li_{1-x}CoO_2$. Computations on $Li_{1-x}CoO_2$ are in progress, and the results will appear in near future.

However, some differences may be found between the interfaces to $Li_{1-x}FePO_4$ and $Li_{1-x}CoO_2$. These cathode materials are quite different in the electronic conduction: $Li_{1-x}CoO_2$ exhibits metallic conduction, while $Li_{1-x}FePO_4$ is poor in electronic conduction and moreover insulating at $x = 0$. When they come into contact with a sulfide electrolyte, part of lithium ions in the electrolyte move into the cathode materials, as displayed in **Figure 5B**. By the way, $Li_{1-x}FePO_4$ is a two-phase system. Roughly speaking, $Li_{1-x}FePO_4$ is a mixture of $FePO_4$ and $LiFePO_4$. Therefore, the movement of lithium ions from the electrolyte into the material may form a $LiFePO_4$ layer at the electrode surface. Consequently, $Li_{1-x}FePO_4$ particles become to have a core–shell structure in sulfide electrolytes, where the core is a mixture of $FePO_4$ and $LiFePO_4$, while the shell mainly consists of $LiFePO_4$. Because the $LiFePO_4$ is electronically insulating, the lithium depletion may be suppressed at the surface of $Li_{1-x}FePO_4$, and thus the $Li_{1-x}FePO_4$ may work relatively well even without surface coating in sulfide electrolytes. That is, $Li_{1-x}FePO_4$ may have a self-origanized core–shell structure for high power, which is similar to that proposed in Xu et al. (2011), where the coating layer is formed only by compositional change in the cathode material.

AUTHOR CONTRIBUTIONS

KT and TO are responsible for the experimental and computational studies, respectively.

ACKNOWLEDGMENTS

The authors thank Dr. Narumi Ohta and Dr. Masato Sumita for their collaboration in the experiments and computations, respectively. This work was partially funded by the Ministry of Economy, Trade and Industry (METI), New Energy and Industrial Technology Development Organization (NEDO), ALCA-SPRING project of Japan Science and Technology Agency, and Ministry of Education, Culture, Sports, Science and Technology (MEXT).

REFERENCES

Bussi, G., Donadio, D., and Parrinello, M. (2007). Canonical sampling through velocity rescaling. *J. Chem. Phys.* 126, 014101. doi:10.1063/1.2408420

Fehr, K., Holzapfel, M., Laumann, A., and Schmidbauer, E. (2010). DC and AC conductivity of $Li_{4/3}Ti_{5/3}O_4$ spinel. *Solid State Ionics.* 181, 1111–1118. doi:10.1016/j.ssi.2010.05.026

Kamaya, N., Homma, K., Yamakawa, Y., Hirayama, M., Kanno, R., Yonemura, M., et al. (2011). A lithium superionic conductor. *Nat. Mater.* 10, 682–686. doi:10.1038/nmat3066

Kanno, R., and Murayama, M. (2001). Lithium ionic conductor thio-lisicon: the Li_2S–GeS_2–P_2S_5 system. *J. Electrochem. Soc.* 148, A742–A746. doi:10.1149/1.1379028

Maier, J. (1995). Ionic conduction in space charge regions. *Prog. Solid State Chem.* 23, 171–263. doi:10.1016/0079-6786(95)00004-E

Maier, J. (2014). Pushing nanoionics to the limits: charge carrier chemistry in extremely small systems. *Chem. Mater.* 26, 348–360. doi:10.1021/cm4021657

Minami, T., Hayashi, A., and Tatsumisago, M. (2006). Recent progress of glass and glass-ceramics as solid electrolytes for lithium secondary batteries. *Solid State Ionics.* 177, 2715–2720. doi:10.1016/j.ssi.2006.07.017

Momma, K., and Izumi, F. (2011). VESTA 3 for three-dimensional visualization of crystal, volumetric and morphology data. *J. Appl. Crystallogr.* 44, 1272–1276. doi:10.1107/S0021889811038970

Ohta, N., Takada, K., Sakaguchi, I., Zhang, L., Ma, R., Fukuda, K., et al. (2007). $LiNbO_3$-coated $LiCoO_2$ as cathode material for all solid-state lithium secondary batteries. *Electrochem. commun.* 9, 1486–1490. doi:10.1016/j.elecom.2007.02.008

Ohta, N., Takada, K., Zhang, L., Ma, R., Osada, M., and Sasaki, T. (2006). Enhancement of the high-rate capability of solid-state lithium batteries by nanoscale interfacial modification. *Adv. Mater.* 18, 2226–2229. doi:10.1002/adma.200502604

Perdew, J. P., Burke, K., and Ernzerhof, M. (1996). Generalized gradient approximation made simple. *Phys. Rev. Lett.* 77, 3865–3868. doi:10.1103/PhysRevLett.77.3865

Sakuda, A., Hayashi, A., and Tatsumisago, M. (2010). Interfacial observation between $LiCoO_2$ electrode and Li_2S–P_2S_5 solid electrolytes of all-solid state lithium secondary batteries using transmission electron microscopy. *Chem. Mater.* 22, 949–956. doi:10.1021/cm901819c

Sakuda, A., Hayashi, A., and Tatsumisago, M. (2013). Sulfide solid electrolyte with favorable mechanical property for all-solid state lithium batteries. *Sci. Rep.* 3, 2261. doi:10.1038/srep02261

Seino, Y., Ota, T., Takada, K., Hayashi, A., and Tatsumisago, M. (2014). A sulphide lithium super ion conductor is superior to liquid ion conductors for use in rechargeable batteries. *Energy Environ. Sci.* 7, 627–631. doi:10.1039/C3EE41655K

Sumita, M., and Ohno, T. (2016). Multi-spin-state at Li_3PO_4/$LiCoO_2$ (104) interface. *Phys. Chem. Chem. Phys.* 18, 4316–4319. doi:10.1039/C5CP07735D

Sumita, M., Tanaka, Y., Ikeda, M., and Ohno, T. (2015). Theoretically designed Li_3PO_4 (100)/$LiFePO_4$ (010) coherent electrolyte/cathode interface for all solid-state Li ion secondary batteries. *J. Phys. Chem. C* 119, 14–22. doi:10.1021/jp5060342

Sumita, M., Tanaka, Y., Ikeda, M., and Ohno, T. (2016). Theoretical insight into charging process in a Li_3PO_4 (100)/$LiFePO_4$ (010) coherent interface system. *Solid State Ionics.* 285, 59–65. doi:10.1016/j.ssi.2015.09.029

Takada, K. (2013a). Interfacial nanoarchitectonics for solid-state lithium batteries. *Langmuir* 29, 7538–7541. doi:10.1021/la3045253

Takada, K. (2013b). Progress and prospective of solid-state lithium batteries. *Acta Mater.* 61, 759–770. doi:10.1016/j.actamat.2012.10.034

Takada, K., Ohta, N., Zhang, L., Cu, X., Hang, B. T., Ohnishi, T., et al. (2012). Interfacial phenomena in solid-state lithium battery with sulfide solid electrolyte. *Solid State Ionics.* 225, 594–597. doi:10.1016/j.ssi.2012.01.009

Takada, K., Ohta, N., Zhang, L., Fukuda, K., Sakaguchi, I., Ma, R., et al. (2008). Interfacial modification for high-power solid-state lithium batteries. *Solid State Ionics.* 179, 1333–1337. doi:10.1016/j.ssi.2008.02.017

Tarascon, J.-M., and Armand, M. (2001). Issues and challenges facing rechargeable lithium batteries. *Nature* 414, 359–367. doi:10.1038/35104644

Wang, L., Zhou, F., Meng, Y. S., and Ceder, G. (2007). First-principles study of surface properties of $LiFePO_4$: surface energy, structure, wulff shape, and surface redox potential. *Phys. Rev. B* 76, 165435. doi:10.1103/PhysRevB.76.165435

Wilkening, M., Amade, R., Iwaniak, W., and Heitjans, P. (2007). Ultraslow Li diffusion in spinel-type structured $Li_4Ti_5O_{12}$ – a comparison of results from solid state nmr and impedance spectroscopy. *Phys. Chem. Chem. Phys.* 9, 1239–1246. doi:10.1039/B616269J

Xu, X., Takada, K., Watanabe, K., Sakaguchi, I., Akatsuka, K., Hang, B. T., et al. (2011). Self-organized core–shell structure for high-power electrode in solid-state lithium batteries. *Chem. Mater.* 23, 3798–3804. doi:10.1021/cm103665w

Zheng, N., Bu, X., and Feng, P. (2003). Synthetic design of crystalline inorganic chalcogenides exhibiting fast-ion conductivity. *Nature* 426, 428–432. doi:10.1038/nature02159

Zhu, Y., He, X., and Mo, Y. (2015). Origin of outstanding stability in the lithium solid electrolyte materials: insights from thermodynamic analyses based on first-principles calculations. *ACS Appl. Mater. Interfaces* 7, 23685–23693. doi:10.1021/acsami.5b07517

Conflict of Interest Statement: The authors declare that the research was conducted in the absence of any commercial or financial relationships that could be construed as a potential conflict of interest.

Advantages of publishing in Frontiers

OPEN ACCESS
Articles are free to read
for greatest visibility
and readership

FAST PUBLICATION
Around 90 days
from submission
to decision

HIGH QUALITY PEER-REVIEW
Rigorous, collaborative,
and constructive
peer-review

TRANSPARENT PEER-REVIEW
Editors and reviewers
acknowledged by name
on published articles

Frontiers
Avenue du Tribunal-Fédéral 34
1005 Lausanne | Switzerland

Visit us: www.frontiersin.org
Contact us: info@frontiersin.org | +41 21 510 17 00

REPRODUCIBILITY OF RESEARCH
Support open data
and methods to enhance
research reproducibility

DIGITAL PUBLISHING
Articles designed
for optimal readership
across devices

FOLLOW US
@frontiersin

IMPACT METRICS
Advanced article metrics
track visibility across
digital media

EXTENSIVE PROMOTION
Marketing
and promotion
of impactful research

LOOP RESEARCH NETWORK
Our network
increases your
article's readership